AN ANALYSIS OF BUBBLE PLUMES IN UNSTRATIFIED STAGNANT WATER

A Dissertation

by

CHUNG KEI CHRIS LAI

Submitted to the Office of Graduate and Professional Studies of
Texas A&M University
in partial fulfillment of the requirements for the degree of

DOCTOR OF PHILOSOPHY

Chair of Committee,	Scott A. Socolofsky
Committee Members,	Kuang-An Chang
	Hamn-Ching Chen
	Mohsen Pourahmadi
Department Head,	Robin Autenrieth

December 2015

Major Subject: Civil Engineering

ABSTRACT

Multiphase flows are ubiquitous in nature and engineering scenarios; examples include volcanic eruption, cloud formation, land reclamation and subsea oil well blowout. In these flows, one or more heterogeneous materials is/are transported by a turbulent carrier fluid (fluid, hereafter). Their interactions, as embodied in the fluid velocities, determine the final fate and transport of the heterogeneous materials. This dissertation investigates how turbulent kinetic energy (TKE) is created and injected into surrounding fluid by the rising bubbles in an air-water bubble plume. This analogue flow shares many similar fluid mechanical properties with oil well blowout plumes whose knowledge is important in disaster management. A comprehensive experimental program using acoustic Doppler velocimetry (ADV) and planar particle image velocimetry (PIV) has been carried out to measure fluid velocities inside the time-steady two-phase plume. Radial profiles of diffusion of TKE and turbulent dissipation rate are reported for the first time. From the fluid-phase TKE budget, it is found that approximately 55-60% of the total work done by bubbles is used to create turbulence in the carrier fluid. Results on the auto-spectral density function of velocity fluctuations reveal a -8/3 spectral slope instead of the classic Kolmogorov-Richardson value of -5/3, suggesting a fundamental difference in spectral energy transfer in this two-phase flow when compared to other simple boundary-layer shear flows, such as a singe-phase jet. This is supported by the subgrid scale (SGS) dissipation computed from the PIV data where it can be seen that the direction of energy cascade is always forward for a simple jet whereas it can be backward for the two-phase plume. On the other hand, a data interpolation method based on first-order autoregressive processes is developed to replace faulty or missing data in

a time series of turbulent velocities. The method is shown to preserve both spectral slopes and energies of frequency components, for the range of slopes between -7/6 to -8/3. Further, the classical sample and hold interpolation is shown to be the limiting behavior of a first-order autoregressive process and therefore has theoretical underpinnings hitherto unknown in the literature.

DEDICATION

Dedicated to you, the *Reader*.

"My aim is to put down on paper what I see and what I feel in the best and simplest way." - Ernest Hemingway

ACKNOWLEDGEMENTS

The financial support offered by a grant from British Petroleum/Gulf of Mexico Research Initiative, administered through the Gulf Integrated Spill Research (GISR) Consortium, to the author is gratefully acknowledged.

I would like to first thank my advisor, Dr. Scott A. Socolofsky, for giving me this opportunity to carry out research on oil spill-related problems; the field is packed with exciting phenomena and mechanisms, waiting to be observed and uncovered. In particular, his trust on my ideas, judgement and work has enabled me to complete a dissertation that I can be proud of in years to come. I enjoy the idea exchange and constructive criticism he has poured into my active research life in the past three years at A&M. His financial support for my professional development is also appreciated; this includes the attendance of summer schools on Fluid Dynamics of Sustainability and the Environment at École Polytechnique (Paris, France) and on Particle-Turbulence Interactions in Planktons at the Darling Marine Center (Maine, the United States). Numerous discussions from members of my degree committee and from my research group are acknowledged.

I thank former members of the Croucher Laboratory of Environmental Hydraulics at the University of Hong Kong for their suggestions given to this research work; this includes Drs. David Choi, Anthony Thoe and Simon Wong. Although Professor Joseph Lee is not involved in this dissertation, I hope it would be something that he approves of.

I thank my friends, Chris Siu, Jakin Chow, Tat Leung, Chak Lee and Jerry Yiu, living at the College Station area for their companionship, joy, good humor and laughter throughout these three years of research. The care and encouragement of Amy Pan is much appreciated. Her constant support has kept the author in high spirits.

Lastly, I thank my mother for her love and unwavering support in my entire life. Without her patience and understanding, this work could not have come to its fruition. Although it seems I have earned the title of a PhD, much is still left to be learnt from the wisdom of a loving mother. I hope she will be proud of me and of my accomplishment.

This dissertation is type-setted using LaTeX 2_ε.

NOMENCLATURE

ADV	Acoustic Doppler Velocimetry
FLUENT	Commercial Fluid Dynamics Code (CFD) by Ansys, Inc.
(T)KE	(Turbulent) Kinetic Energy
PIV	Particle Image Velocimetry
SGS	Subgrid scale
Vectrino II	Profiling velocimeter manufactured by Nortek
$\mathbf{x}$	Vector position in Cartesian coordinates (x,y,z)
$\tilde{\mathbf{u}}(\mathbf{x})$	Instantaneous velocity vector at $\mathbf{x}$ with components ($\tilde{u}$,$\tilde{v}$,$\tilde{w}$)
$\mathbf{U}(\mathbf{x})$	Time-averaged velocity vector at $\mathbf{x}$ with components (U,V,W)
$\mathbf{u}(\mathbf{x})$	Fluctuating velocity vector at $\mathbf{x}$ with components (u,v,w)
b_g	Gaussian radius of a jet/plume
k	Time-averaged turbulent kinetic energy
l_M	$= \frac{M_o^{3/4}}{F_o^{1/2}}$, Jet/plume momentum length scale
u_s	Slip velocity of bubbles relative to water
β	Spreading rate of a jet/plume
ϵ	Turbulent dissipation rate
ν	Kinematic viscosity of water
Q_b	Volume flowrate of air at in-situ pressure
Q_o	Volume flowrate of air at standard atmospheric pressure
D	Eq. 2.1, dynamic length scale of air-water bubble plumes
$D(\lambda)$	Dissipation spectrum
$E_{ii}(\lambda)$	Spatial auto-spectral density function of velocity $\tilde{u}_i$
F_o	Kinematic buoyancy flux

L	Unit of length in dimension analysis
M_o	Kinematic momentum flux
T	Unit of time in dimension analysis
$< \cdot >$	Volume average
$\overline{(\cdot)}$	Time average

TABLE OF CONTENTS

Page

LIST OF FIGURES

FIGURE Page

LIST OF TABLES

TABLE Page

1. INTRODUCTION

"I do not pretend to start with precise questions. I do not think you can start with anything precise. You have to achieve such a precision as you can as you go along."

- Bertrand Russell.

The convection of one fluid in another where both are miscible is ubiquitously found in both natural and man-made environment. From the spectacular volcanic eruption cloud that extends several kilometers into the upper troposphere to exhaust gas stacks from coal-fired power plant then to the smoke plume of a burning cigarette, these flows span a wide range of spatial and temporal scales. They owe their motions to their density difference with the surrounding ambient and the induced flow usually turns fully turbulent a short distance from the starting position. Turbulent motions are often seen to be bounded by a convoluted surface which can be considered as the juxtaposition of eddies (concentrated regions of turbulence) of different sizes. They are strongly diffusive, transport great amount of mass and heat along their paths and bring intense mixing to the environment (Tennekes & Lumley 1972). In many practical engineering scenarios, it is imperative to understand and predict this mixing. Some examples are air ventilation in buildings (Lin & Linden 2005), disposal of wastewater into water bodies (Fischer, List, Koh, Brooks & Imberger 1979), application of dispersants in oil well blowout events (Socolofsky, Adams & Sherwood 2011), and heat exchange between upper and lower atmosphere (Shrinivas & Hunt 2014).

When the density difference (buoyancy) is between contacting regions of the same material/composition, it is termed a single-phase flow; examples include the cigarette plume and ocean disposal of domestic wastewater into salty seawater. The former

involves localized heated region of air rising in a cooler ambient whereas the latter is primarily due to a difference in salt content in water. At distances sufficiently far from source the injected fluid will become indistinguishable from the ambient, forming a homogeneous solution. On the contrary, buoyancy can be due to the addition of heterogeneous materials into a fluid; an engineering example is that of a dredging sediment thermal (Lai, Zhao, Law & Adams 2013) induced by falling heavy particles in water, like sand that on average has a specific gravity of 2.65. The turbulent motions set up in the receiving fluid will lead to mixing in the sediment cloud but the cloud will remain distinctive from the ambient throughout its descend. This flow is termed as a two-phase flow; sand, the *dispersed* phase, and water, the *carrier* phase. The term *phase* has a broader meaning in this context; instead of referring to the three physical states, solid, liquid and gas, it now distinguishes composition as well. For instance, oil droplets dispersed in water constitute a separate phase despite both being liquids. In general, there can be more than two phases, thus giving rise to multiphase flows.

The research described in this dissertation focuses on one particular case of two-phase flows - an air-aerated bubble plume in water. This is an idealized setup for the oil/gas multiphase plume formed during an oil well blowout event. Figure 1.1 shows a schematic of the *DeepHorizon* blowout plume in Gulf of Mexico in 2010. The plume was subject to a strong ambient stratification and weak crossflows whence multiple horizontal intrusions of dissolved oil and gas were detected at different elevations above the well head (Socolofsky et al. 2011). Some of the largest droplets may escape the intrusion layers and rise in the water column. However, they are eventually dissolved into seawater. These transport processes depend on the details of fluid turbulence inside the two-phase plume that are currently limited to measurements of

the turbulent stresses. In particular, the pathways by which the droplets create, and hence transfer, turbulence into surrounding fluid have not been elucidated. In this study, air bubbles of a few millimeters in diameter dispersed in water are considered; in the terminology defined above, air and water are respectively the dispersed and carrier phase. The air bubbles are introduced at a steady rate into the receiving water via a small orifice, i.e. a localized source, and the water body is assumed to have a much larger physical dimension than the orifice such that the resultant flow is unbounded. Variables of interest are dilution (mixing) and turbulent characteristics inside the bubble plume. Obtained results will be relevant to the modeling of oil/gas plume. Only the fluid mechanical aspects of the flow will be considered; chemical and biological transformations of oil/gas droplets, both of which affect the final transport of dispersed phases, are beyond the present scope of study. It is instructive to first review the research and solution techniques used on single-phase plume flow as they are also used in the two-phase problem.

1.1 Single-phase jets/plumes in a stagnant fluid

To fix ideas, we consider a source discharged from a circular orifice of diameter D into a stagnant ambient. The flow is incompressible and fully turbulent (jet Reynolds number $Re > 2000$, see figure 1.2). Fluids are miscible at all proportions. A jet is the flow created by a maintained source of momentum while that of a plume is created by a maintained source of buoyancy (Lee & Chu 2003). A forrest fire plume is an example of the latter. In practice, however, pure sources of momentum/buoyancy are rarely seen and the discharge usually have both to varying degrees, leading to buoyant jets. Close to the source, the discharge is dominated by its source momentum whereas the source buoyancy governs the flow at large downstream distances. Consequently, the buoyant jet will exhibit characteristics pertaining to a pure jet and

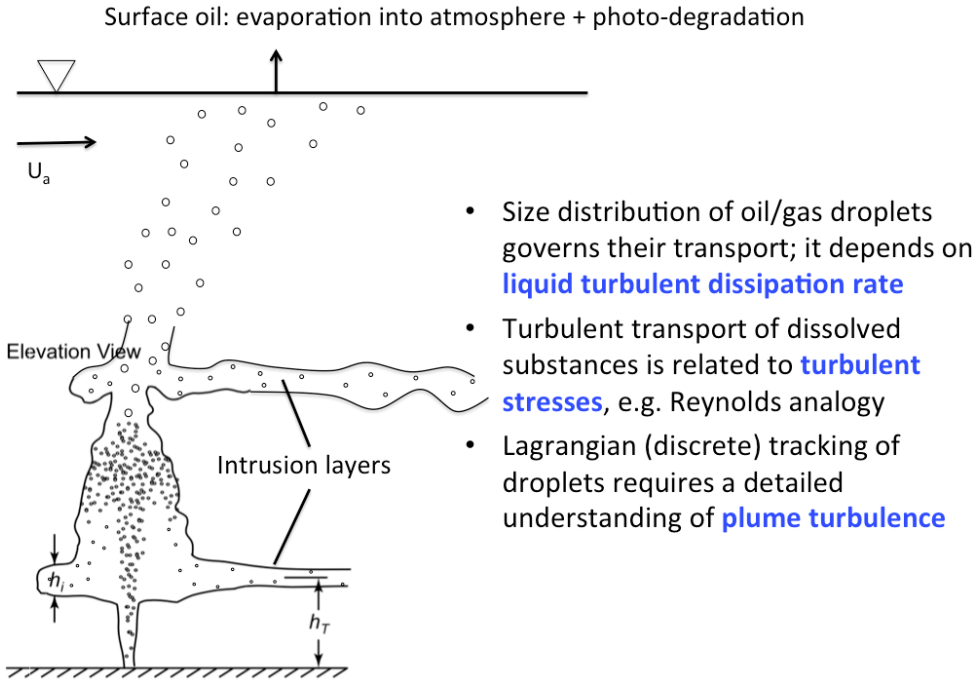

Figure 1.1: A schematic sketch of the subsea oil well plume formed during *Deep Horizon oil spill* (20 April - 15 July 2010); a oil/gas droplet plume in a water column dominated by density-stratification

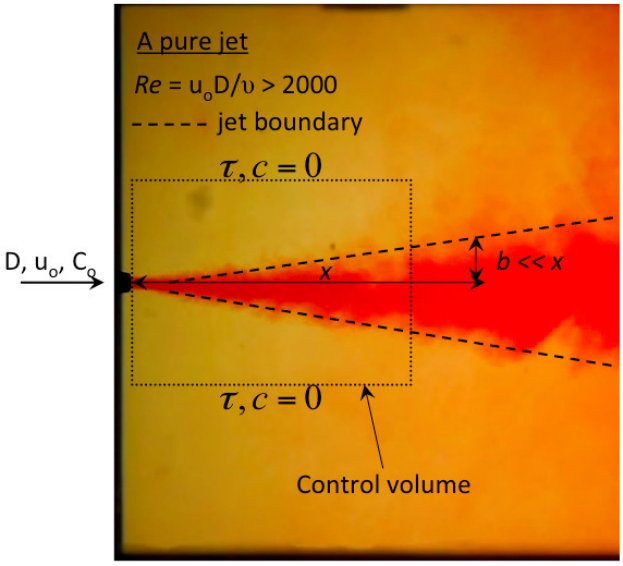

Figure 1.2: Illustration of a pure momentum water jet (dyed red) in a large water tank that is initially motionless; D = jet diameter, u_o = jet discharge velocity, C_o = discharge tracer concentration, x = distance downstream from source, b = jet width, τ = horizontal shear stress and c = tracer concentration

a pure plume at different distances from source. Figure 1.2 shows a momentum jet injected horizontally into a water tank; the source fluid is dyed red for visualization. It can be seen that the jet is fanning out; its width b grows linearly with downstream distances x at a small spreading angle $\beta = b/x \approx 0.1$. The jet spread is indicative of an increasing volume flux, and hence, the engulfment of ambient fluid into the jet. If a rectangular control volume is drawn (dotted box in figure 1.2) with one of its vertical face at the source and the other at any downstream position, one can see that the jet velocity must decrease with the distance from source by virtue of conservation of horizontal momentum. At each downstream position, it is of interest to predict the local jet width and distributions of velocity and passive tracer across the jet. In the following, we describe a number of approaches used in calculating these quantities.

1.1.1 Solution methods

As in the studies of other types of flow, the average flow field or global properties can often be characterized by dimensional analysis and experiments. To predict flow transitions, the governing equations of motion must be referred to and depending on the level of approximations applied varying details of the flow will be obtained. A comprehensive description of these different approaches attempted on single-phase jets/plumes is not intended; rather the aim is to provide enough pointers relevant to the proposed research on air bubble plumes.

First, we go over dimensional analysis. Without resorting to the governing equations of motion, jet/plume properties can be predicted by a combination of dimensional analysis and a finite set of laboratory experiments. Employing the point source concept, i.e. consider distances away from source, typically $x > 10D$, a pure jet is dynamically governed by its source kinematic momentum flux $M_o = Q_o U_o$ whereas a pure plume is governed by its source kinematic buoyancy flux $F_o = Q_o g'_o$, where $Q_o = \frac{\pi}{4} D^2 U_o$ = source volume flux, D = jet diameter at source, U_o = jet velocity at source, $g'_o = \frac{\triangle \rho_o}{\rho} g$ = source reduced gravity, $\triangle \rho_o = \rho - \rho_j$ = density difference at source, ρ = reference fluid density and g = acceleration due to gravity. It should be noted that the Boussinesq approximation for small density differences has been invoked here. Then, in functional form, any jet properties ϕ can be written as,

$$\phi = f(M_o \text{ or } F_o, x) \tag{1.1}$$

We immediately see that the jet width b_g (subscript g stands for Gaussian and is related to profile assumption in integral models) must depend linearly on x and the spreading rate $\beta = \frac{b_g}{x}$ is observed to be constant in experiments; $\beta = 0.114$ for jets

and 0.105 for plumes (Lee & Chu 2003). Using this line of argument, Zeldovich (1937) was the first to give the empirical relationships for time-averaged centerline velocity W_c and volume flux Q (hence average dilution $= \overline{S} = \frac{Q}{Q_o}$) in pure plumes; $W_c = C_1 F_o^{1/3} x^{-1/3}$ and $\overline{S} = C_2 F_o^{1/3} x^{5/3} Q_o^{-1}$ where C_1 and C_2 are experimentally determined constants. The approach has been extended into more demanding situations, including ambients with a linearly stratification or with a uniform horizontal current; a comprehensive summary can be found in Lee & Chu (2003).

The major difficulty in applying the empirical formulae to general situations is that they describe jets/plumes behaviors asymptotically when either M_o or F_o dominates; they cannot model regions of flow transition. To overcome this problem, the governing equations must be solved.

Second, we go over jet integral models. This approach is versatile and is widely used in engineering designs. The time-averaged flow field is governed by the boundary-layer approximated Reynolds-averaged Navier-Stokes equations (RANS); the streamwise gradients of flow variables are an order of magnitude smaller than the radial ones such that they can be dropped from the full RANS equations (Lee & Chu 2003). The approximated governing equations admit a self-similar solution for fully turbulent jets/plumes (Chen & Rodi 1980). A physical intuition for this is apparent in figure 1.2; β is a constant and the jet only evolves gradually with x, reflecting the small spreading angle. This self-similarity has been confirmed in the measurements of the radial distributions of velocity $U(x, r)$ and tracer mass $c(x, r)$; both exhibit a Gaussian distribution and profiles taken along the trajectory collapse onto the same curve when normalized by the local centerline velocity U_c and jet width b_g. This demonstrates that the turbulent eddies inside single-phase jets/plumes are

characterized by one length scale and one velocity scale only, which is different from multiphase flows (see later discussions).

$$\frac{U(x,r)}{U_c} = e^{-(r/b_g^2)} \text{and } \frac{c(x,r)}{C_c} = e^{-(r/\lambda b_g^2)} \tag{1.2}$$

where $U_c = U(x,0)$, $C_c = c(x,0)$, λ = spreading ratio of tracer mass to velocity = 1.2 (Lee & Chu 2003); $\lambda > 1$ means that the transport of mass is faster than momentum.

By substituting equation (1.2) into the approximated governing equations and integrating radially from $r = 0$ to $r = \infty$, one obtains a set of coupled ordinary differential equations (ODE) from the original partial differential equations (PDE). The effort required in solving the system is thus greatly reduced since there are efficient solvers for ODEs, e.g. the family of Runge-Kutta methods. Turbulence closure is achieved by specifying the rate at which ambient fluid is entrained into the jet/plume flow in the continuity equation (Lee & Chu 2003). To this end, the celebrated entrainment hypothesis put forward by Morton, Taylor & Turner (1956) is used, which states that the radial inflow velocity v_e into the jet/plume at the periphery is equal to αu_c; α is known as the entrainment coefficient and encapsulates the net effect of jet turbulence. For a pure jet, $\alpha_j = 0.057$. For a pure plume, $\alpha_p = 0.088$ (Lee & Chu 2003). A larger α for plumes indicates that buoyancy is a more effective agent in creating mixing. As mentioned earlier in dimensional analysis, a discharge usually have both momentum and buoyancy and so its behavior will be intermediate between a pure jet and a pure plume; M_o dominates small values of x whereas F_o governs large values of x. The entrainment coefficient must then transit from α_j to α_p along the jet path. This transition can be analytically derived under the integral framework using the

governing equations; for a 2D plane buoyant jet (Jirka & Harleman 1979) and for a 3D axisymmetric round buoyant jet (Lai & Lee 2012*b*). All of the above have been incorporated into commercially available jet integral models; CorJet (Jirka 2004) and VISJET (Lee & Chu 2003). The comparison of model results with basic laboratory and field data under a wide range of ambient and source conditions is excellent. Model extension into a flowing ambient can be made by adding additional terms to the continuity and momentum equations (e.g. Jirka 2004, Lee & Chu 2003).

Third, we go over computational fluid dynamics (CFD). The integral model only predicts time-averaged values of velocity and tracer mass; it gives no information on jet/plume turbulence. To predict turbulent quantities, such as turbulent kinetic energy k (TKE), dissipation rate ϵ and Reynolds stresses $\overline{u_i u_j}$, the governing equations must be solved numerically together with an appropriate turbulence closure model. Some details of the RANS approach are described here as it will be used to simulate the flow of a two-phase bubble plume in section 2, and, in particular, we consider the $k-\epsilon$ closure model. The $k-\epsilon$ model is a two-equation closure for fluid turbulence in which the transport equations of k and ϵ are solved alongside the continuity and momentum equations. It is based on the Boussinesq turbulent viscosity model and uses a modeled ϵ equation, which is of similar form to the exact k equation, because of the intractable higher velocity moment terms that arise during its exact derivation; the modeling is based on the concept of eddy overturning time (Shih, Liou, A., Yang & Zhu 1995). Empirical constants of the model have been obtained from a number of basic flows (Pope 2000). One major assumption is that the fluid turbulence is isotropic; in an x,y,z Cartesian coordinate system, this leads to a equal partitioning of total energy k among its three components $\overline{u^2} = \overline{v^2} = \overline{w^2} = \sqrt{2k/3}$, where $k = (\overline{u^2} + \overline{v^2} + \overline{w^2})/2$. The transport of Reynolds stresses is thus the same

in all directions. It should be noted that a universal theory for turbulence is yet to exist and all sorts of model are phenomenological, i.e. derived from physical evidence. Fluid turbulence is a flow specific property and is not a thermodynamical parameter, like molecular viscosity, of the fluid (Tennekes & Lumley 1972). When a model is applied to a flow that is different from its calibration database, a recalibration of the model constants is required. An example is the pure jet; the $k-\epsilon$ model with standard coefficients predicts a larger jet spread than measured and the model constant C_μ has to be reduced, i.e. a smaller turbulent viscosity/diffusivity (Lee & Kuang 1999). Once this is done, the prediction can be used to explore flow properties that is unavailable or cannot be easily measured in physical experiments.

In RANS, none of the turbulent scales/eddies are solved explicitly; their cumulative effects on the mean flow are represented by k and ϵ. The simulated flow field is always smooth and without any turbulent structures. Hence, this does not allow a detailed study of the momentum and energy transfer in fluid turbulence. Large eddy simulation (LES) offers a solution to this problem. Instead of time-averaging out all turbulent eddies, the Navier-Stokes equations are filtered in space in LES. Any scales smaller than the size of filter are removed and their effects on the large, resolved scales are modeled via a subgrid-scale (SGS) model. The filtered velocity field is inherently unsteady in time and therefore LES is able to simulate the temporal evolution of turbulent structures such as hairpin vortices, billows and blobs (Davidson 2015). For example, one can extract auto-spectral density function (section 3 and 5) of the velocity fluctuations from LES and investigate turbulent energy cascade (with some limitations due to the cut-off size of spatial filter). In simple terms, LES simulations are closer to physical measurements in a turbulent flow than RANS.

The empirical nature of turbulence closure models remains as the source of discrepancy among different simulations and different flows. In a direct numerical simulation (DNS) of the Navier-Stokes equations, such a model is completely abandoned where all flow scales are resolved and tracked in time. It is analogous to performing "physical" measurements in a numerical space. The required computational resources, however, limit its usage to homogeneous isotropic turbulence in a periodic box and simple shear flows like that of a jet (Taub, Lee, Balachandar & Sherif 2013).

1.2 Two-phase air bubble plumes in a stagnant fluid

Plume buoyancy is due to collective drag exerted by dispersed bubbles on surrounding fluids. The drag force causes motions in the ambient fluid and sets up a velocity gradient across the plume which eventually triggers turbulent entrainment into the plume via shear-layer instabilities. Figure 1.3 shows a laboratory bubble plume in a 1m^3 water tank. Similar to a single-phase jet/plume, the plume flow, as visualized by air bubbles, is fanning out at a small spreading angle with distance from source. Without the induced plume flow, air bubbles could only rise vertically like a column. An example is the air bubble column where the void fraction α_{air} (not to be confused with the entrainment coefficient α) is everywhere uniform in the domain. It should be noted that bubbles are not perfect passive tracer like the red dye in figure 1.2; a significant relative velocity exists between them and plume fluid. The ability of a dispersed phase to response to velocity fluctuations in the carrier fluid is characterized by the dimensionless Stokes number St (Crowe, Schwarzkopf, Sommerfeld & Tsuji 2012); a small St indicates a rapid response. For air bubbles of a few millimeters in water, St is on the order of 10^{-3}.

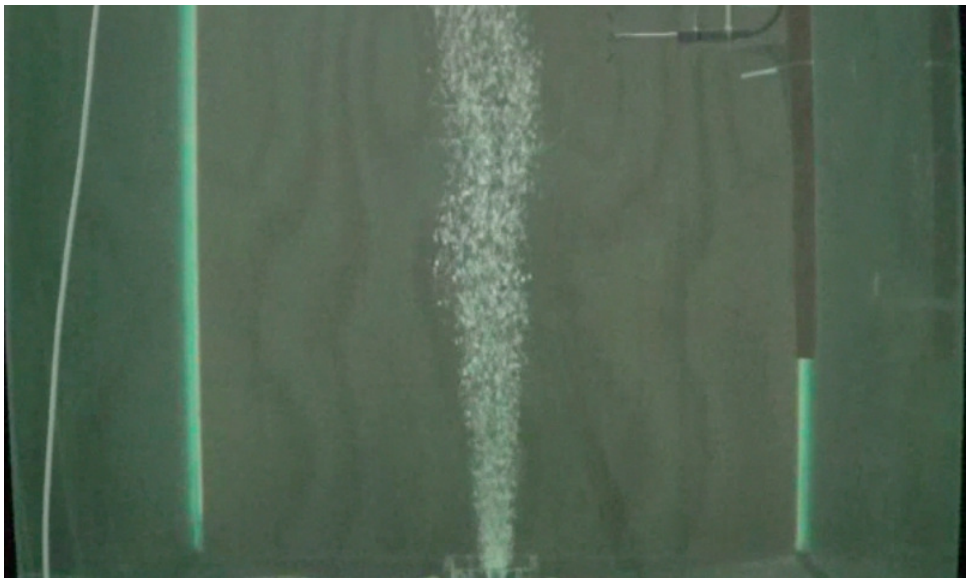

Figure 1.3: Illustration of an air-aerated bubble plume in a $1m^3$ water tank that is initially motionless; air injection is made through an aquarium airstone located at the bottom of the figure and the generated bubbles have a narrow distribution of diameters, 2.4 ± 0.2mm

The integral approach is also applied to predict the time-averaged values of fluid velocity, fluid spread and dispersed phase void fraction at different plume elevations. Individual bubble is not tracked and the collective action of bubbles on the plume is effected by their kinematic buoyancy flux at source. The air void fraction is tracked by a conservation equation. Cederwall & Ditmars (1970) gave the first model of this sort and numerous improvements have been made in the ensuing decades in which the model has been extended into situations with ambient stratifications (e.g. McDougall 1978, Asaeda & Imberger 1993, Socolofsky, Bhaumik & Seol 2008). In a density-stratified fluid, bubble plumes exhibit multiple layers of lateral intrusion. The ascending part of plume is shrouded by a descending curtain of denser ambient fluid entrained from elevations below. This phenomenon is modeled by the double-integral plume approach. Comparison between model predictions and measurements

in the laboratory and field is good (Socolofsky et al. 2011).

1.2.1 Unresolved issues

Despite laboratory efforts and success of integral models, there remain several unresolved problems.

1. Budget of turbulent kinetic energy inside a bubble plume - Experimental measurements of turbulent stresses have been made using particle image velocimetry (PIV) in a number of previous studies (e.g. Simiano, Zboray, de Cachard, Lakehal & Yadigaroglu 2006, Duncan, Seol & Socolofsky 2009). One major difficulty of applying the technique to the two-phase flow, apart from discriminating air bubbles from seeding particles, is the existence of shadows behind the bubbles. This lack of illumination in the immediate vicinity of rising bubbles may lead to absence of computed velocity vectors in these high-velocity regions and therefore an underestimation of stresses when the missing data are filled by interpolation using neighboring vectors of lower velocities. It would be beneficial to use another measuring technique to confirm the PIV results. In addition, no data exist for the third order moments of velocity and dissipation rate, both of which are required in performing a turbulent kinetic energy budget across the bubble plume. Obtaining these measurements will enhance our understanding of the turbulence in this two-phase plume.

2. Turbulent signatures of bubbles - Because of the presence of air bubbles, TKE is created at the scale of the bubble diameter ($d_{50} = 2.4$mm in this study). This gives rise to a different situation than that in single-phase jets/plumes where energy is cascaded down from the largest eddies, of the size of jet width, to the dissipative scales, i.e. the Kolomogorov scale; the longitudinal wavenumber spectra shows a -5/3 slope over a range of intermediate wavenumbers before

ending with an exponential decay in the dissipative range (Pope (2000), see also section 5). On the other hand, laboratory measurements on air bubble columns (without turbulent entrainment and with void fraction $\alpha_{air} < 10\%$) have revealed a distinctive -8/3 or -3 spectral slope that is interpreted as the signature of bubble interactions (e.g. Lance & Bataille 1991, Riboux, Risso & Legendre 2010). Depending on actual experimental conditions, this -3-slope may then revert back to the classical -5/3 slope before the spectra ends with a dissipative range (on the order of 0.1mm) or extends to scales smaller than the bubble diameter (< 1mm). For bubble plumes, no such measurements exist which are important in turbulence modeling, e.g. in LES, a correct spectra is needed to ensure a correct dissipation rate.

Regarding point 1, the simple case of an isolated spherical bubble can be called upon to illuminate the energetics inside a bubble plume. Suppose an air bubble of diameter d is brought to a depth h in an initially quiescent water column of uniform density ρ_w. For time $t \leq 0$, it is kept at the depth h by some restraining force and has a zero velocity. It has a stored potential energy $PE = \rho_w \delta V g h$ where δV = volume of bubble and g = acceleration due to gravity. At $t = 0$, the restraining force is removed and the bubble rises because of its buoyancy; the buoyancy force B is almost equal to $\rho_w \delta V g$. The bubble's kinetic energy KE thus increases at the expense of the stored PE. After a transient period (at a height on the order of d from its release point), the bubble attains a constant terminal speed V, which is an outcome of the force balance between buoyancy and fluid drag $D = \frac{1}{2}\rho_w V^2 A C_D$ where $A = \pi d^2/4$ = projected area of bubble in the fluid flow direction and C_D = drag coefficient. In this steady regime, the KE of bubble remains constant. This means that the loss of PE is all extracted by the surrounding water through the fluid drag. This can be

made more mathematically precise by considering time rate of change of PE, $\frac{dPE}{dt}$, and the workdone W by fluid drag $W = DV$. First, $\frac{dPE}{dt} = \rho_w \delta V g \frac{dh}{dt} = -\rho_w \delta V g V$; the negative sign comes from the fact that the vertical axis is defined top-down from the water surface. Second, $W = DV = BV = \rho_w \delta V g V = -\frac{dPE}{dt}$. So, the stored potential energy of bubble is continuously converted into the energy of fluid and one observes from experiments that the created fluid energy is kinetic due to fluid motions set up by the rising bubble. Further, the induced fluid flow of bubbles of a few millimeters large in water is usually turbulent and therefore the pertaining question is to determine the fraction of PE or W that is directly used to create turbulent kinetic energy. Section 2 is devoted to answer this question.

1.3 Outline of thesis

Section 2 deals with the first unresolved issue by a set of original laboratory experiments. It will be shown that the fluid velocities inside the two-phase flow can be successfully measured by a profiling acoustic Doppler velocimeter. Profiles of time-averaged turbulent dissipation rate and the amount of TKE production by bubbles are reported for the first time.

Section 3 presents a method to obtain from gappy datasets reliable spectral estimate of the auto-spectral density function of turbulent velocities. It will be shown that velocity signals from classic turbulence, i.e. with the -5/3 isotropic slope in their spectra, are well described by a first-order autoregressive model; the model can be used to fill-in missing data. Through numerical experiments, the method is also shown to work with signals that exhibit a range of spectral slopes, [-7/6, -8/3], observed in multiphase flows.

Section 4 develops a balance equation for the conservation of bulk kinetic energy (mean + turbulent) inside a single-phase jet/plume. The integral framework is used to derive the equations. Extension to the two-phase bubble plume is also given; it is used to give an overall check of accuracy of the measurements in section 2.

Section 5 deals with the second unresolved issue by performing a set of planar particle image velocimetry (PIV) experiments on the residual flow left behind a bubble plume. Here, measurements of the flow field following an abrupt shut-off of a time-steady bubble plume are taken. Properties of embedded vortices and energy flux at different spatial scales are investigated using swirl strength and subgrid scale dissipation. Evidence for the peculiar -8/3 or -3 spectral slope observed in bubbly flows is presented.

Finally, section 6 gives a summary of present findings and a list of recommendations for future work.

Appendix D presents a method to estimate the variance of noise from measured time series of velocity. Broadly speaking, the method is applicable to any types of signal that follow a *signal* + *noise* model. It will be shown that an approximate pointwise estimate of the noise is given by the difference between the raw signal and its two-point moving average. The quality of this estimate improves with increasing values of signal-to-noise ratio and sampling frequency f_s; in fact, a theoretical limit can be derived in the limit of large f_s.

2. BUDGET OF TURBULENT KINETIC ENERGY IN BUBBLE PLUMES BY ACOUSTIC DOPPLER VELOCIMETRY (ADV)

"Everything is theoretically impossible, until it is done." - Robert A. Heinlein

"Nothing has such power to broaden the mind as the ability to investigate systematically and truly all that comes under thy observation in life."
- Marcus Aurelius

2.1 Introduction

Bubble plumes encompass a wide range of natural phenomena and engineering applications. Although bulk properties of the multiphase plume have been measured (e.g. Milgram 1983, Simiano et al. 2006, Seol, Bhaumik, Bergmann & Socolofsky 2007, Duncan et al. 2009, Simiano, Lakehal, Lance & Yadigaroglu 2009) and predicted by integral models (e.g. Wüest, Brooks & Imboden 1992, Zheng, Yapa & Chen 2003, Socolofsky et al. 2008), measurements are mostly limited to first- and second-order velocity moments. Fluxes of turbulent kinetic energy (TKE), which are third-order velocity moments and important components in a TKE budget, have not been reported. This budget is needed for the verification of modeling approaches in computational fluid dynamics (CFD) codes and the purpose of present work is to account for them by using velocity data obtained from an original set of experiments.

The dynamics of air-water bubble plumes in an unstratified and initially motionless ambient is governed by the length scale D, which can be derived from the governing equations of a two-fluid model (Bombardelli, Buscaglia, Rehmann, Rincon & Garcia 2007).

$$D = \frac{gQ_b}{4\pi\alpha^2 u_s^3} \tag{2.1}$$

where gravitational acceleration $g = 9.81\text{m}^2/\text{s}$, Q_b = air volume inflow at in-situ pressure, α = plume entrainment coefficient (= 0.083) and u_s = bubble slip velocity. For non-dimensional source heights $z/D < 5$ (adjustment phase), the plume flow is still dependent on source conditions and its local Froude number is adjusting towards the asymptotic value at about 1.7 which is a constant when $z/D \geq 5$ (asymptotic regime). In subsea oil well blowout events, D is comparable to the water depth ($O(10^3 m)$); the bubble plume almost never reach the asymptotic regime in practice. However, properties of the regime are worth quantifying as they provide a basis on which the adjustment phase can be gauged. Experiments in this study have covered z/D = 2-11. From dimensional analysis, the time-averaged plume centerline velocity $W_c(z)$, Gaussian plume radius $b_g(z)$ and fluid phase volume flux $Q(z)$ have the following functional dependence,

$$\frac{b_g(z)}{D} = f(\frac{z}{D}),\ \frac{W_c(z)}{u_s} = f(\frac{z}{D}),\ \frac{Q(z)}{u_s D^2} = f(\frac{z}{D}), \tag{2.2}$$

The functional form $f(z/D)$ will be investigated in the experiments and compared to published data. It is noted that bubble plumes in the two papers by Simiano *et al.* experienced significant contraction of the plume diameter above source level, a phenomenon known as "necking" that was also observed in forest fire plumes (Lee & Chu 2003). W_c initially increased and became constant with z in their reported data. This is in contrast to present and previous experimental datasets where a decay of W_c is found. As such, a quantitative comparison between data therein and those of this study will not be made.

At the outset, three types of fluid velocities can be expected inside a bubble plume: (i) bulk entrained flow, (ii) bubble wakes and (iii) return flow due to rising bubbles. All must be registered by the chosen instrument for correct quantification of plume turbulence. The instrument must also have moderately high spatio-temporal resolutions, and preferably with all three components of the velocity vector available. This naturally rules out all intrusive single-point devices and suggests the use of particle image velocimetry (PIV). In multiphase flows, the technique is complicated by the need to discriminate between continuous liquid phase and dispersed gas phase. To this end, phase-discriminating PIV that uses fluorescent seedings and optical filters for phase selection has been developed. Two cameras are needed for the synoptic measurements of both phases. In Simiano et al. (2006), the method is applied in the center plane of bubble plumes but only fluid velocities are captured. A simplified technique that uses only a single camera and standard algorithms of PIV and particle tracking velocimetry PTV for the calculation of phase velocity is proposed in Seol et al. (2007). Inherent to this is the removal of bubble wake velocities that leads to an underestimation of the streamwise velocity and hence its stresses (see § 5). In general, the major challenge in applying PIV to bubbly flows is the existence of shadowy regions behind bubbles which could render the measured velocities uncertain and inaccurate. It would be helpful if the PIV results can be compared against data measured by another instrument that has a different operating principle.

In this study, we have selected the Nortek *Vectrino II* for three-dimensional fluid velocity measurements. It is the latest generation of acoustic Doppler velocimeter (ADV) and is capable of synoptic measurements along a 35mm strip (as of present writing) at temporal frequencies up to 100Hz and at spatial resolutions from 4mm down to 1mm. Being calibration-free on the part of the experimenter, it is convenient.

The coherent- pulse technology of ADVs is well understood and its performance in probing energetic turbulent flows has been well-documented. We are therefore led to explore its capabilities in probing the bubble plume, as an alternative to PIV. A concern arises on whether the returned measurements are correct in the presence of bubbles which are strong acoustic scatterers. It has long been considered that bubbles cause outliers to appear in the time series which have to replaced by some in-range values. Surprisingly, it turns out that no such replacement is necessary for the Vectrino II data obtained from our flow field (void fraction $< 2\%$) and we have been able to verify the validity of all data.To provide a baseline for comparison, we simulate the time-steady bubble plume flow using the commercial CFD software FLUENT (Ansys, Inc.). A mixture model is used and turbulence closure for the continuous liquid phase is achieved using the standard $k - \epsilon$ model. To our knowledge, there are no published CFD results on the steady-state bubble plume under present settings.

The section is structured as follows. First, the laboratory set-up, experimental conditions and some operational details of Vectrino II are given in §2.2 and §2.3. Those details are included because they aid the understanding of our verification process on the ADV data. Second, we give the numerical details of the FLUENT simulations in §2.4. Some results that guide our choice of model parameters are also presented. Third, we present the empirical probability density function PDF of velocities at the start of the results section §2.5. It will be shown that all outliers are really valid data points and correspond to either bubble wakes or return flow caused by rising bubbles. In order words, the data consists of three different stochastic processes instead of one as is commonly presumed in any outliers detection algorithms. The section continues by presenting time-averaged profiles for mean flow, turbulent quantities and dissi-

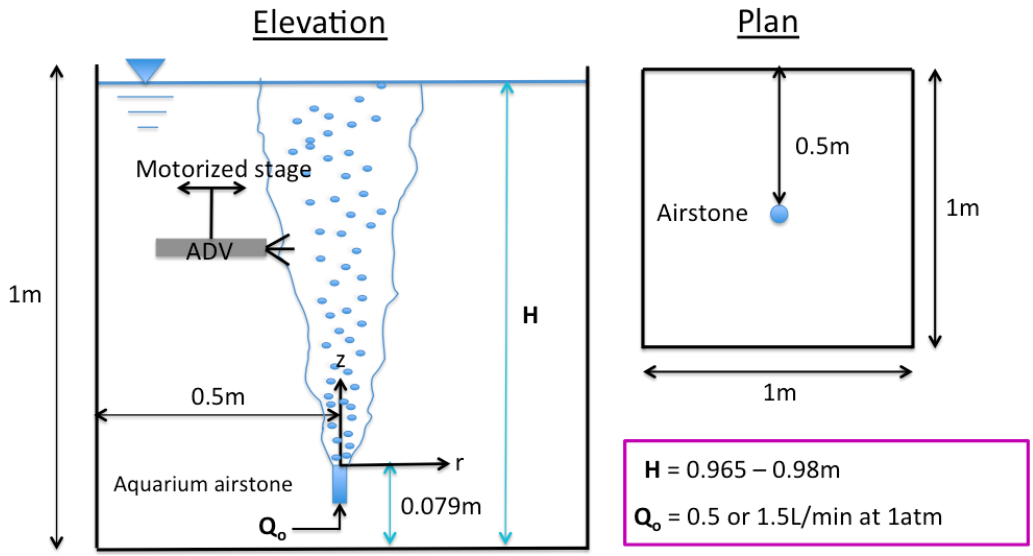

Figure 2.1: Schematic diagram of the laboratory setup in present study

pation rate; a TKE budgets across the plume is performed using data-fits of these results. Lastly, a summary of present findings and some generalized conclusions are given in §2.6.

2.2 Laboratory experiments

2.2.1 Set-up

Experiments were carried out in the Fluid Dynamics Laboratory in the Ocean Engineering Program at Texas A&M University. To establish an almost symmetric flow field, a $1m^3$ cube compartment was partitioned from a glass-walled rectangular water tank. A definition diagram of the experiment setup is shown in figure 5.1. Compressed air was injected into the cube through an aquarium airstone located at the center of the bottom face. The volume inflow of air Q_o at standard atmospheric pressure was monitored by a calibrated gas flowmeter and the air bubbles generated had a median diameter d_{50} of 2.4mm (figure 2.2) with a corresponding slip velocity of 24cm/s (Clift, Grace & Weber 1978). A Cartesian coordinate (x, y, z) system is

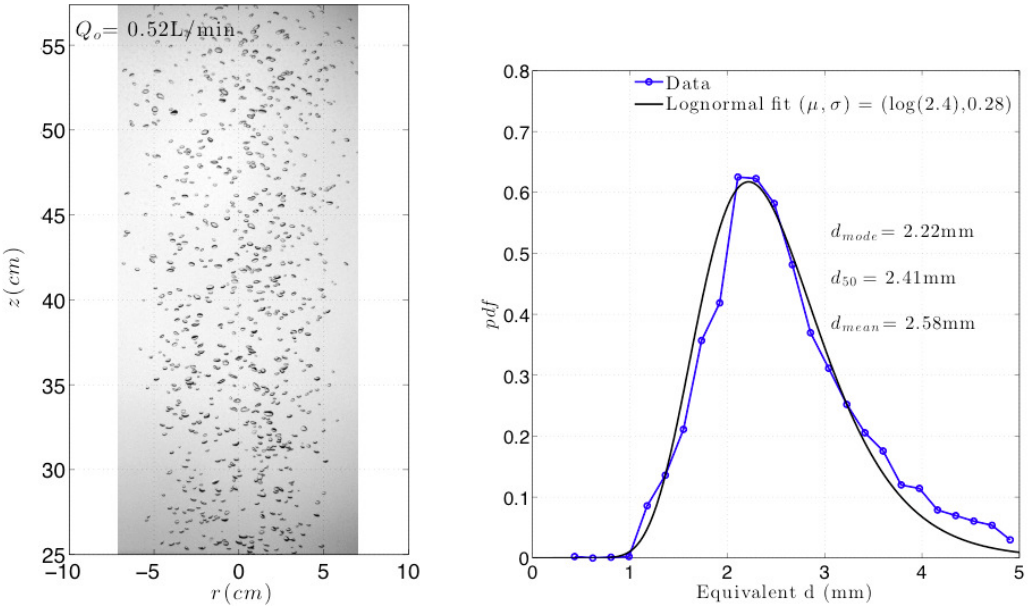

Figure 2.2: Bubble size distribution for case A

adopted with z being the vertical (streamwise) axis, x the horizontal (radial) axis and y the out-of-plane axis. The corresponding velocity components are respectively, w, u and v.

A *Vectrino II* profiler mounted on a motorized linear stage (Zaber Technologies) was used to measure fluid velocities at different source elevations. Measurements were obtained at 1mm intervals in the radial direction along a 35mm-long strip and at each measurement height, twenty-three strips were used to cover the bubble plume width. Although a minimum of five strips would suffice, this high number is used to ensure that the same portion (most sensitive) of the strip is used to obtain the data; a decision based on the varying sensitivity of the probe (see §2.2.3). Each 1mm-thick sampling disc has a diameter of 6mm and therefore has a sampling volume equal to $9\pi\text{mm}^3$, which is equivalent to that of a 3mm cube.

Case	Q_o (L/min)	D (cm)	z/D
A	0.5	6.8	6.6-11.0
B	1.5	20.4	2.2-3.7

Table 2.1: Experimental conditions; D = dynamic length scale defined in equation (1.1), z/D = non-dimensional height, bubble slip velocity $u_s = 24$cm/s

For an ADV, Garcia, Cantero, Nino & Garcia (2005) showed that if the dimensionless frequency $F = f_s L/U_c > 20$ where f_s = sampling frequency, L = size of energy containing eddies and U_c = convective velocity, over 90% of the total turbulent kinetic energy is captured and the energy aliased from frequencies larger than the Nyquist frequency is negligible. This criterion was satisfied in the experiments by choosing $f_s = 50$Hz with $L \sim 0.1m$ and $U_c \sim 0.2m/s$ (table 2.3). The two-phase bubble plume is known to exhibit large scale oscillations (Milgram 1983). Using the empirical relationship given in Seol, Duncan & Socolofsky (2009), the wandering period is estimated at 1.5mins for case A in our tank. Therefore, the plume flow was sampled for 15mins at one measurement strip, which covered about ten wandering periods, and a total of 5.75hrs was required to complete the twenty-three profiles at one source height. Table D.1 shows the experimental conditions and relevant quantities.

2.2.2 Velocities measured by an ADV

Along the directions of its receiver beams that intersect to form a sampling volume, the four-receiver bistatic ADV probe measures velocities of seeding particles. The beam velocities $\mathbf{b}$ are converted into Cartesian velocities $\mathbf{u}$ via a probe geometry transformation matrix $\mathbf{T}$ that is unique to each sampling cell i.e. $\mathbf{u} = \mathbf{T}\mathbf{b}$. An example is given below.

$$\begin{bmatrix} w \\ v \\ u1 \\ u2 \end{bmatrix} = \begin{bmatrix} 2.1589 & -0.0195 & -2.1292 & 0.0193 \\ -0.1521 & 2.2529 & 0.1499 & -2.2607 \\ 0.4514 & 0.0022 & 0.5764 & -0.0022 \\ 0.0034 & 0.5295 & -0.0034 & -0.4961 \end{bmatrix} \begin{bmatrix} b_1 \\ b_2 \\ b_3 \\ b_4 \end{bmatrix} \tag{2.3}$$

Elements in **T** are determined empirically in the laboratory by the manufacturer. From the system (2.1), one can see that each Cartesian velocity is predominantly determined by a pair of beam velocities, for example, (b_1, b_3) on w and $u1$. As we shall see later, this explains why $u1$ has slightly more fluctuations than its independent measurement $u2$ in § 5. Another other point to note is the collinearity between the two beams (b_1, b_3) and (b_2, b_4). The line joining $b1$ and b_3 is perpendicular to that of b_2 and b_4. This implies that a high correlation should exist between collinear beams while low correlations can be expected for perpendicular beams, e.g. between b_1 and b_2. The work of Voulgaris & Trowbridge (1998) gives a more in-depth discussion on the pulse-coherent technology and its performance in probing turbulent flows.

2.2.3 Some experiences working with the profiling ADV - Vectrino II

The *Vectrino II* was introduced by Nortek into the fluid mechanics community in 2011 (Craig, Loadman, Clement, Rusello & Siegel 2011). It brings several technological advancements over its point-wise predecessors: (i) simultaneous profiling capability along a 35mm strip (as of present writing) at moderately high temporal (10-100Hz) and spatial (1-4mm) resolutions, (ii) extended velocity range up to 3m/s afforded by dual pulse repetition frequency (PRF), (iii) adaptive ping-algorithm for the elimination of weak-spots, and (iv) reduced integrated circuit noise which would otherwise contribute to measurement uncertainties. Our experience with the instrument in a

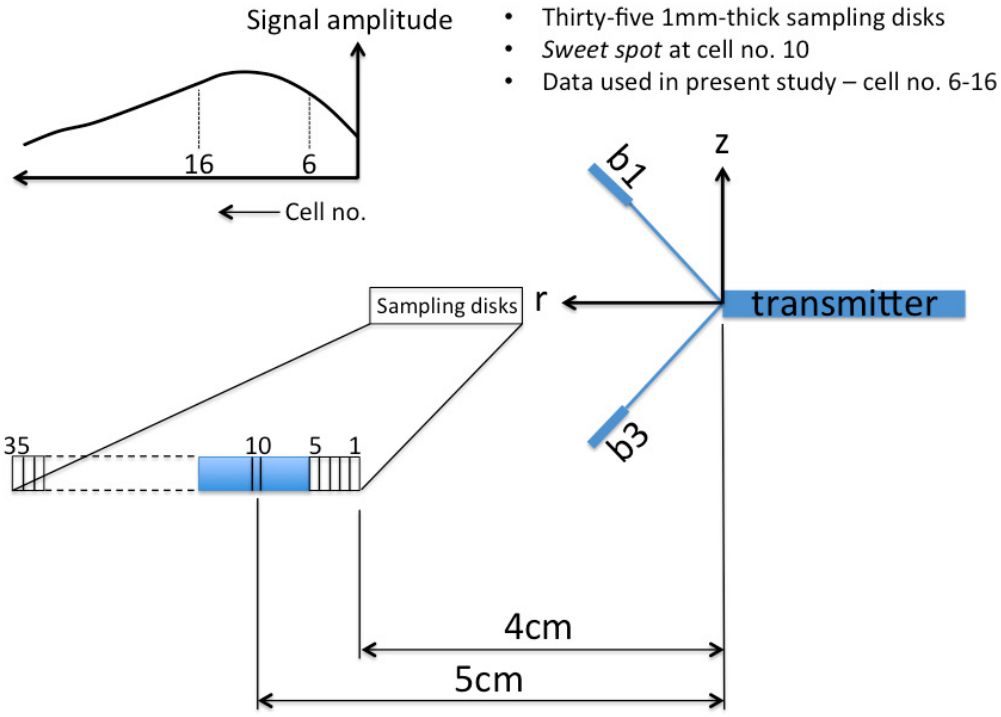

Figure 2.3: Characteristics of the sampling disks of *Vectrino II*; showing the varying measurement sensitivity and the positions of data considered in present study

bubbly flow revealed the following. Pulse interference, i.e. weak spot, is common because of a tight bubble core and item (iii) above must be turned on. Failing to do so, say using the standard minimum ping-algorithm suited for single-phase turbulent flows, will result in exceptionally high velocities that are unphysical at plume edges. Further, deploying multiple profilers in the same plane should be avoided as mutual interference will occur. It is, however, observed that the interference reduces if the probes are farther apart; flow conditions probably play a role as well.To ensure the highest possible data quality (constrained by probe capabilities), two precautionary steps were taken. First, the water tank was adequately seeded with neutrally buoyant polyamide particles such that the background (without bubble plume flow) signal-to-noise ratio SNR and correlation coefficient Corr were better than 30 and 98% and that their profiles were parabolic with a peak at the *sweet spot* (see below and user manual, Nortek (2013)). Second, probe check was performed with the plume flow turned on before each experiment run. The amplitude profiles of each receiver should overlap and be smooth across the measuring strip, and again with a distinct maximum at the *sweet spot*. A schematic sketch of the thirty-five sampling disks is shown in figure 2.3. The probe's *sweet spot* is about 5cm from the transmitter head and corresponds to the tenth cell in the measurement strip. In this study, only data from the sixth to sixteenth cell are considered due to the decaying sensitivity, hence accuracy, at both ends of the strip. These eleven cells were repeatedly used to sample the plume flow at different radial positions. The data quality will be further assessed and discussed in the result section §2.5.4.

2.3 Post-processing of raw ADV data

A word of caution is warranted here when one considers removing extreme values from any raw datasets. Extremities in a population are usually conceptualized as

those that lay far away from the population mean, for example, tails in a probability density function PDF. Naturally, there is no universal rejection criterion for extreme values in a dataset as the physical mechanism(s) that generate(s) the data varies from one situation to another. A proper interpretation of a given dataset requires careful inquiry to the underlying physics; *how many types of forcing are present? how would they manifest themselves in the empirical PDF?* In recent literature on ADV data despiking - a term coined to mean outliers removal - the class of phase-space despiking methods, as an objective rejection algorithm first advocated by Goring & Nikora (2002), is commonly used. The method is based on a classical statistical result of the normal (Gaussian) distribution; extreme values cannot appear more often than a certain limit. The presumed Gaussian behavior appears to apply in many turbulent fluid flows although non-Gaussianity of the small dissipative scales is recognized (Pope 2000). More importantly, this implicitly assumes there is only one underlying forcing responsible for the data which is probably true for flows characterized by a single length scale e.g. a single-phase jet. In multiscale flows, there can be more than one forcing and each may have a different PDF and represents a different data fraction, leading to incorrect identification of outliers by the usual algorithm. Cea, Puertas & Pena (2007) recognized the issue and applied their modified phase-space algorithm to an ADV dataset obtained from the highly-aerated flow behind a sluice gate. However, they were not able to provide a complete characterization of the raw data because of the highly chaotic interactions between air entrainment and supercritical flow. Our bubble plume experiments are more amenable to such analysis because of a low void fraction ($< 2\%$) and because of the predominant vertical rise of the gas phase at a significant slip velocity. It turns out that all extreme data points in our raw ADV time-series are actually valid and corresponds to different physical forcings. Our heuristic arguments will be given and discussed in the results section

(§2.5).

2.3.1 Doppler noise estimation and noise-reduced estimates of the stress tensor

It is known that raw ADV data obtained from flows without any physical obstructions is accurate in computing the mean flow field while turbulent statistics are highly biased by Doppler noise which must be estimated and removed from measurements (e.g. Voulgaris & Trowbridge 1998, Garcia et al. 2005). For a four-receiver bistatic probe like *Vectrino II* employed here, the redundant vertical (along transmitter direction) velocity $w2$ can be used together with $w1$ to estimate directly the Doppler noise. Noise-reduced estimates of the stress tensor can then be obtained after accounting for probe geometry (Hurther & Lemmin 2001). More details of the correction procedure can be found in Appendix A.

2.4 Reynolds-averaged numerical modeling of bubble plumes

Only half of the experimental tank (figure 2.1) is modeled; the flow field is symmetric with respect to the central vertical plane. The computational domain is shown in figure 2.4; grid refinement in near wall regions has not been carried out as the present objective is to only model the bubble plume flow. No-slip boundary conditions are applied to the side walls and the bottom face. Inflow of air is initiated through a 10mm-diameter circular orifice located at the center of bottom face. The top boundary is designated as a pressure-outlet where air and water are allowed to leave the domain without back flow; surface boil is not modeled. A mixture model is employed where a single set of governing equations is solved for the mass-weighted mixture properties. The continuous fluid phase (designated as the primary phase) and the discrete bubble phase (secondary phase) are modeled as two interpenetrating fluids and each is tracked by a volume fraction such that their sum is equal to

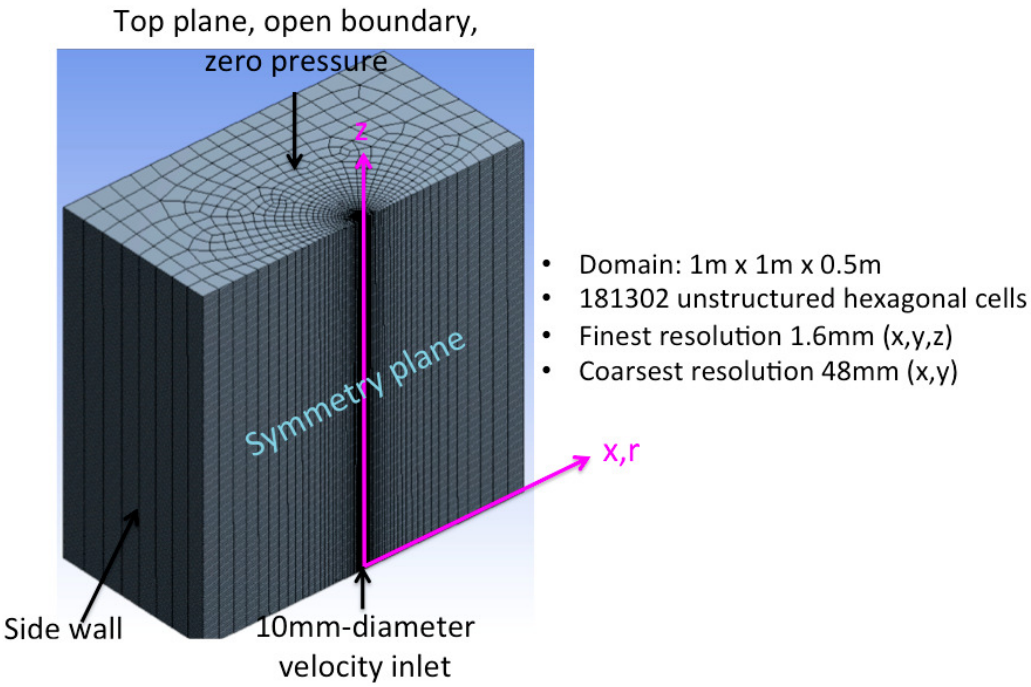

Figure 2.4: Computational domain of a single bubble plume in stagnant ambient in FLUENT

one everywhere in the domain. As such the volume fraction is a conservative passive scalar whose transport is calculated from a transport equation. The action of air bubbles on the fluid phase is effected through the slip velocity, calculated by a dynamic drag law (Schiller and Naumann, see Clift et al. (1978)) that depends on local velocities of both phases. The standard $k-\epsilon$ model is used for closure of the fluid phase turbulence. These choices are consistent with the very low Stokes number ($O(10^{-3})$) of air bubbles.

Even for a single-phase jet, the standard $k-\epsilon$ model with standard coefficients is known to predict a larger jet spread i.e. diffusion of jet turbulence into surrounding ambient is faster than reality. Rodi (1993) pointed out that the coefficient C_μ is not constant across the jet and should be adjusted from the standard value of 0.09; he

subsequently proposed a formulation for C_μ based on local jet turbulence properties. This *ad hoc* adjustment reflects the fact that jet turbulence is not isotropic, contrary to the tenant of the $k-\epsilon$ model. For a similar reason, the computed transport of mass across the jet, which is α_{air} in our case, is also different from measurements (Lee & Kuang 1999). The mass transport is modeled by Reynolds analogy, expressed through a turbulent Schmidt number σ. In this study, C_μ and σ are kept as constants for simplicity and their choice is guided by matching the predicted spreading rates of the jet and the bubble core with measured data. The default values of C_μ and σ in FLUENT are, respectively, 0.09 and 0.75.

To ensure the simulation results are independent of grid resolution, a finer grid with half the step size in all directions has been tested. The comparison reveals that the high- resolution results are visually indistinguishable from that of the coarse grid (figure 2.4) when plotted. All results shown below are those of the coarse grid.

First, details of the boundary conditions used for the simulations are give here. At the circular inlet, velocity and volume fraction of the fluid phase are set to zero. The inflow of air perpendicular to the inlet face is set via an artificial velocity $u_{artificial} = \alpha_{inlet}\frac{Q_o}{Area}$ where inlet volume fraction of air is $\alpha_{inlet} = 1$ and inlet area is $Area = \frac{\pi}{4}(0.01^2) = 7.85 \times 10^{-5} m^2$. For $Q_o = 0.5$ and 1.5L/min, $u_{artificial} =$ 0.1061 and 0.3183m/s respectively. At the pressure-outlet, the backflow air volume fraction is set to zero. It remains to specify the inlet and outlet conditions for fluid turbulence; the values of k and ϵ. Both need to be non-zero to initiate the calculation of turbulent field but because of a zero inlet fluid phase velocity they are equal to zero. To circumvent the difficulty, we use the results of a single phase jet emanating from a fully-developed smooth pipe flow. The jet exit velocity is taken as $u_{artificial}$

and the turbulent intensity I related to the Reynolds number $Re = \frac{u_{artificial}(10mm)}{\nu}$ via the Blassius equation is $I = 0.16Re^{-1/8}$. Then, for $u_{artificial} = 0.1061$m/s, $k = \frac{3}{2}(u_{artificial}I)^2 = 0.0000757m^2/s^2$ and $\epsilon = C_\mu^{3/4}\frac{k^{3/2}}{l} = 0.000155m^2/s^3$ where the mixing length $l = 0.07(10) = 0.7$mm. At the outlet, k and ϵ are taken as 1% of their respective inlet values. Sensitivity tests (not shown) show that the simulated steady plume flow does not significantly depend on the exact values of k and ϵ at these magnitudes.

Second, details of the computation are give here. Convergence criteria for the scaled residuals of the following variables are set to 10^{-6}: continuity, x-,y-,z-velocity, k and ϵ. The criteria is taken as 10^{-3} for the volume fraction of air. Under-relaxation factors are taken as follows: 1.0 for density and body force, 0.1 for slip velocity, 0.4 for volume fraction, 0.8 for k and ϵ, 0.8 for turbulent viscosity. Coefficients used in the $k-\epsilon$. model are: $C_1 = 1.44$, $C_2 = 1.92$, k Prandtl number = 1.0 and ϵ Prandtl number = 1.3. The governing equations are solved using the coupled scheme for velocity-pressure coupling. Typical number of iterations required for converged results is about 14,000-15,000.

2.4.1 Numerical results - the selection of C_μ and σ

As mentioned above, the appropriate choice of C_μ and σ are made based on a comparison between predicted and measured mean-flow properties; these include (i) plume centerline velocity W_c decay, (ii) fluid phase spreading rate β and (iii) the ratio λ of spreading rates between bubble phase and fluid phase. For illustration, these results are shown in figure 2.5 for $C_\mu = 0.15$ and $\sigma = 0.1$. In general, there is a close agreement on the decay of W_c but the numerical results appear to suggest a faster decay above z =10cm, i.e. with a slope larger than -1/3. To take a closer look into this

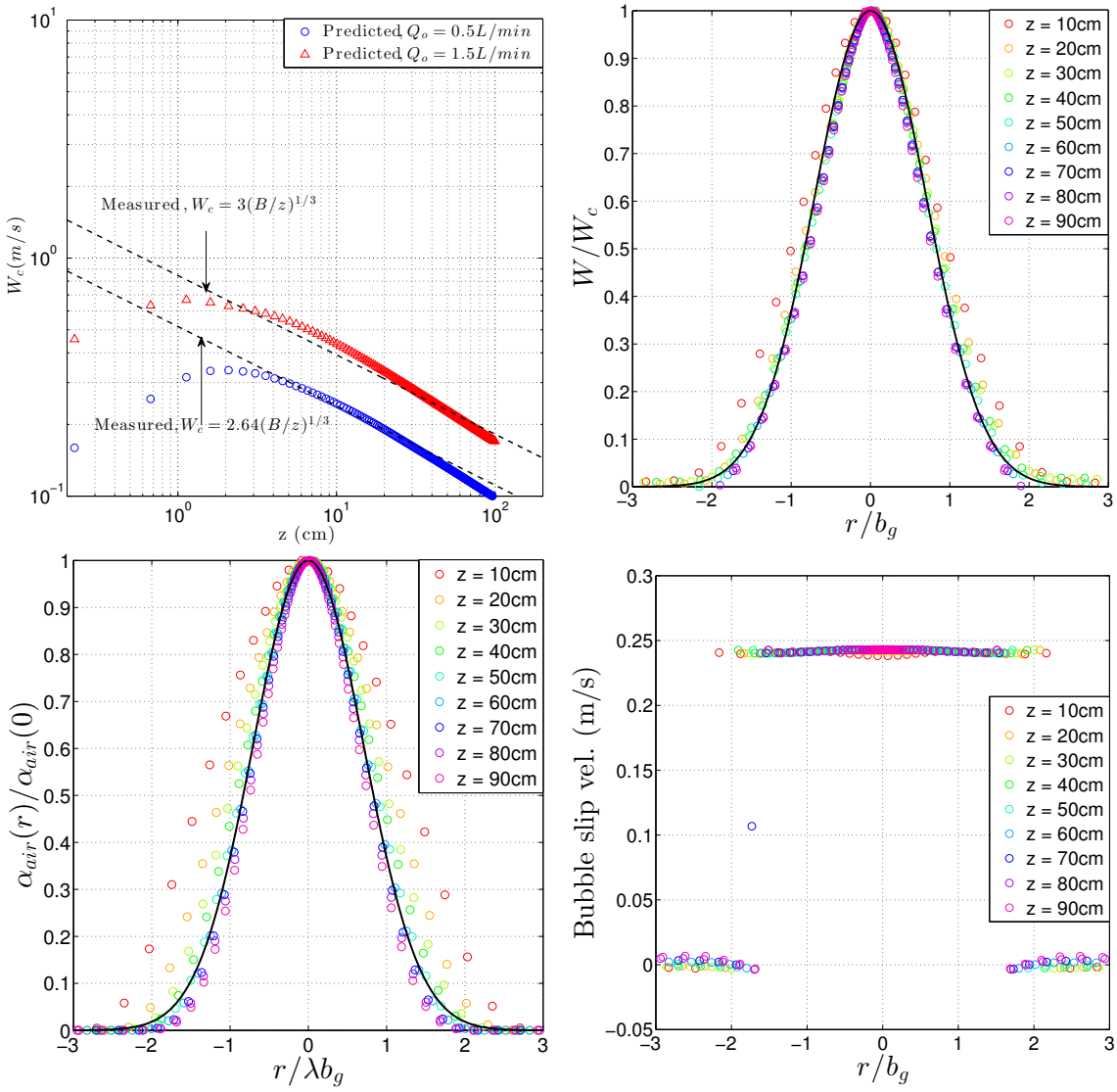

Figure 2.5: Comparison between FLUENT predicted and measured plume mean-flow; $C_\mu = 0.15$, $\sigma = 0.1$ and $\lambda = 0.7$; measurements in Seol *et al.* (2007)

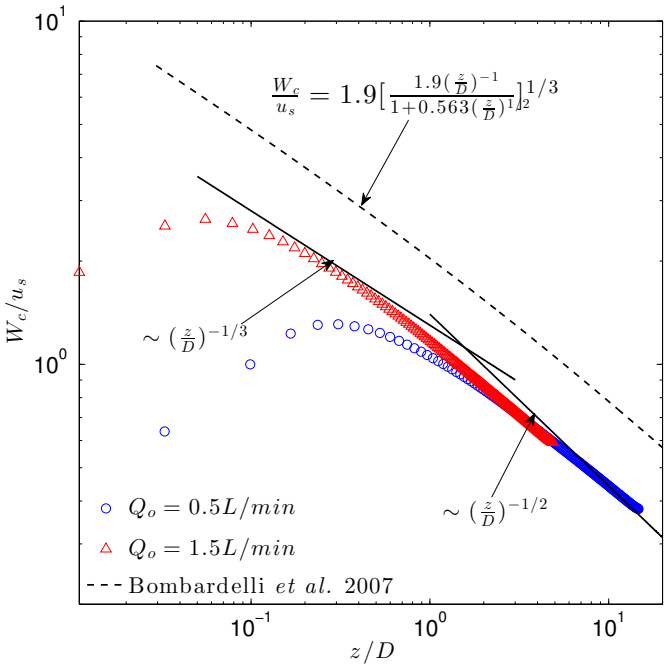

Figure 2.6: Comparison between FLUENT prediction and the semi-analytical solution of W_c given in Bombardelli *et al.* (2007); the prefactor of 1.9 appearing in front of the square bracket term converts top-hat velocity into plume centerline velocity and is calculated by $\sqrt{\frac{4}{\gamma}}$ where $\gamma = 1.1$ is the momentum amplification factor (Socolofsky *et al.* (2008)

behavior, W_c is replotted in figure 2.6 using the functional form given in equation 2.2. It can be notice that predictions from both flowrates collapse onto each other when $z/D > 1$. There is an apparent steepening of decay slope from -1/3 to one that is somewhat milder than -1/2 around $2 < z/D < 3$. Based on the results of their integral plume model, Bombardelli et al. (2007) derived a semi-analytical expression for the top-hat plume velocity $\frac{W_{th}}{u_s} = [\frac{1.9(\frac{z}{D})^{-1}}{1+0.563(\frac{z}{D})^{1/2}}]^{1/3}$ that has the following limiting behavior,

$$\frac{W_{th}}{u_s} = \begin{cases} 1.24(\frac{z}{D})^{-1/3}, & \frac{z}{D} \to 0 \\ 1.5(\frac{z}{D})^{-1/2}, & \frac{z}{D} \to \infty. \end{cases} \tag{2.4}$$

The critical transition occurs at $z/D = 3.15$ (by equating the two limiting equations). Two comments can be made here. First, Bombardell's integral model was rigorously derived from a mass-weighted two-fluid model whose governing equations were solved in the RANS simulations. The observed subtle steepening of the W_c decay slope in both approaches suggest the change is probably real. Second, scalings borrowed from single-phase plumes are not adequate in describing the behavior of multiphase plume; by neglecting the slip velocity u_s, which characterizes the bubbles, one is presuming the flow to behave like a pure buoyancy point source. The only velocity scale to non-dimensionalize W_c is then $(B_o/z)^{1/3}$ where B_o is the source kinematic buoyancy flux. This predicts $W_c \sim z^{-1/3}$. Decay slopes other than -1/3 are only possible when u_s is included in the dimensional analysis (equation 2.2).

The normalized streamwise velocity $W(r)$ assumes a Gaussian profile across the plume (figure 2.5); the fluid-phase spread width b_g is defined at the radial position r where $W = W_c/e \approx 0.37W_c$. The cross-sectional distribution of α_{air} can also be similarly normalized by a bubble spread width b_b where $b_b = \lambda b_g$; λ is the spread

	$Q_o = 0.5$L/min		$Q_o = 1.5$L/min	
C_μ	$\beta = b_g/z$	λ	$\beta = b_g/z$	λ
0.15	0.132	0.7	0.132	0.9
0.13	0.126	0.7	0.126	0.9
0.12	0.122	0.7	0.126	0.9
0.11	0.118	0.7	0.117	0.9
Measured $\beta = 0.132$ (Seol et al. (2007))				
Measured $\lambda = 0.7$-0.8 (Seol et al. (2007))				

Table 2.2: Variations of fluid-phase spreading rate β and ratio of spreading rates λ with C_μ; turbulent Schmidt number $\sigma = 0.1$ in all cases

width ratio. It can be seen that the air void fraction profile is predicted to be Gaussian; λ =0.7 in the figure. At elevations closer to the source (10-30cm), a larger λ (0.9-1) is needed to collapse the profiles which reflects the influence of source conditions. The variations of β and λ with C_μ are tabulated in table 2.2. As expected, a larger C_μ represents faster diffusion of plume turbulence, hence, a larger β. For $Q_o = 0.5$L/min, the spread width ratio λ (=0.7) shows no dependence on C_μ as it is only dependent on σ. The ratio is larger and equal to 0.9 for $Q_o = 1.5$L/min. These results are nearly the same for $\sigma = 0.1$-0.15. In Seol et al. (2007), λ can be inferred from their figure 8 to be in the range of 0.7-0.9; λ increases with Q_o. This is consistent with the simulations and we are therefore content with these results and choose $C_\mu = 0.15$ and $\sigma = 0.1$ in our simulations. Finally, we note that the computed bubble slip velocity is 24cm/s.

Figure 2.7 shows the computed profiles of TKE and dissipation rate ϵ in normalized ordinates. Also shown in the figure are parametric fits to the data using a superposition of two Gaussian profiles to approximate the computed double-peak structure, i.e.

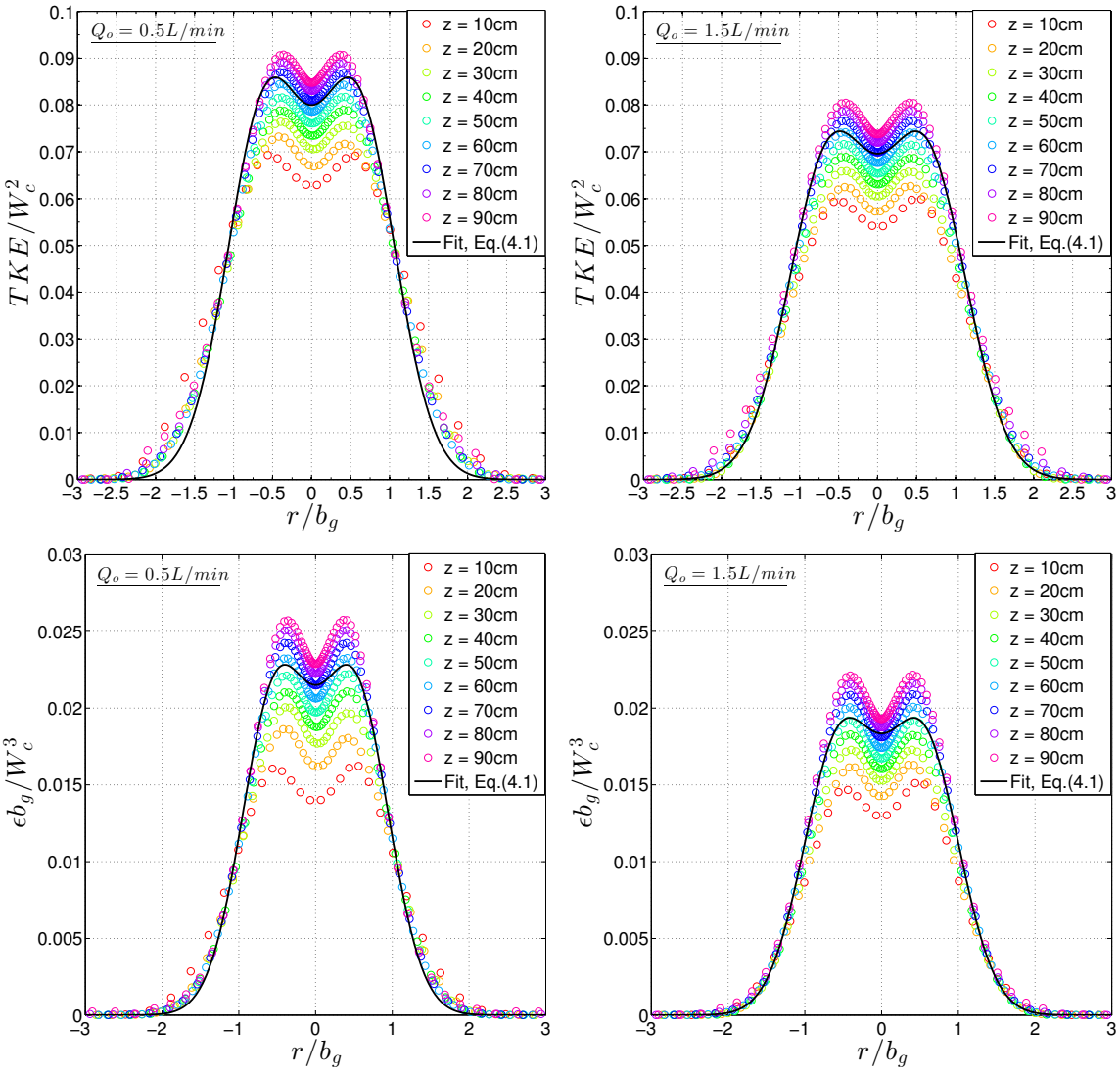

Figure 2.7: Computed profiles (FLUENT) of TKE and dissipation rate ϵ; $C_\mu = 0.15$, $\sigma = 0.1$

$$\frac{y(r)}{y(0)} = exp(-\frac{(r-\alpha b_g)^2}{(\gamma b_g)^2}) + exp(-\frac{(r+\alpha b_g)^2}{(\gamma b_g)^2}) \tag{2.5}$$

where $y(r)$ = normalized values of TKE or ϵ, $y(0)$ = peak value at αb_g, αb_g = position of off-centre peaks, and γb_g = spread of profile. α and γ are fitting constants and they are equal to (0.58,0.70) for TKE and (0.51, 0.63) for $\bar{\epsilon}$.

It is seen that self-similarity is not fully obeyed across the plume by using the velocity scale W_c and length scale b_g. This occurs for $|r/b_g| < 0.5$. Referring to the air void fraction in figure 2.5, $r/b_g = 0.5$ corresponds to the radial position where α_{air} drops to about 60% of the centerline value. This suggests that the usual single phase jet/plume scalings are not adequate in the multiphase plume core, which is not a surprising result as the bubble slip velocity u_s characterizes the motions of bubbles.

Finally, we remark on the difference between the simulations and our experimental data to be presented next. The simulations followed an Eulerian-Eulerian approach where the discrete bubble phase had been modeled as a fluid continuum. Consequently, wakes behind individual bubbles and their interactions with each other were not simulated; only the average bubble drag responsible for ambient fluid entrainment was included. These interactions in reality determine the local turbulent conditions inside the bubble plume and it is the present objective to measure them, and indeed they have been captured, in the experiments. As such, the simulations represent the bulk entrained flow and provide a baseline for comparison.

2.5 Results

We first inspect the empirical PDFs of the raw velocities to get an overall impression of the data. A decomposition of the streamwise velocity w's PDF into three

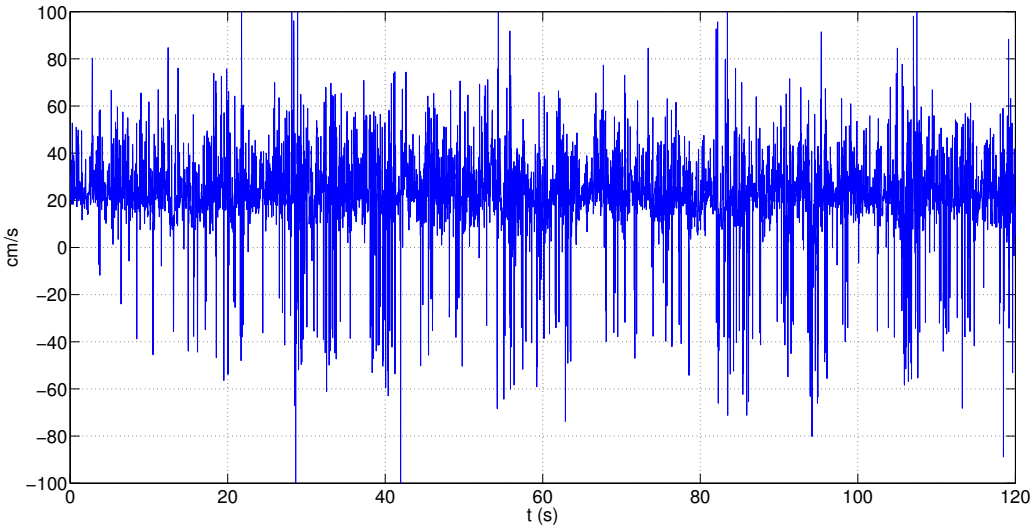

Figure 2.8: Raw data for streamwise velocity $\tilde{w}$ at plume core $r = 0$ (case A, $z/D = 6.6$)

Gaussians will allow us to identify the underlying forcings that generate the data and thereby shows that it is unnecessary and indeed incorrect to filter out the extreme values. Further, a wavelet analysis will be carried out to investigate the non-stationary characteristics of the velocity; it should be remembered that gas bubbles only intermittently force the fluid flow at any fixed point. Useful references are drawn from published laboratory and numerical data on bubble columns with similar void fractions (<4%). We then move on to present normalized profiles of mean flow, second- and third-order turbulent statistics and dissipation rate. A TKE budget will be performed using data fits derived from the measured ADV data.

2.5.1 Empirical probability density function of $\mathbf{w}(\mathbf{x},t)$

Figure 2.8 shows a two-minute segment (out of a full 15-min record) of the raw streamwise velocity w at the plume core $r = 0$ for a single sample volume along the strip. When viewed over the entire segment the series is stationary in time but is also interlaced with intermittent large negative and positive values. This means that the

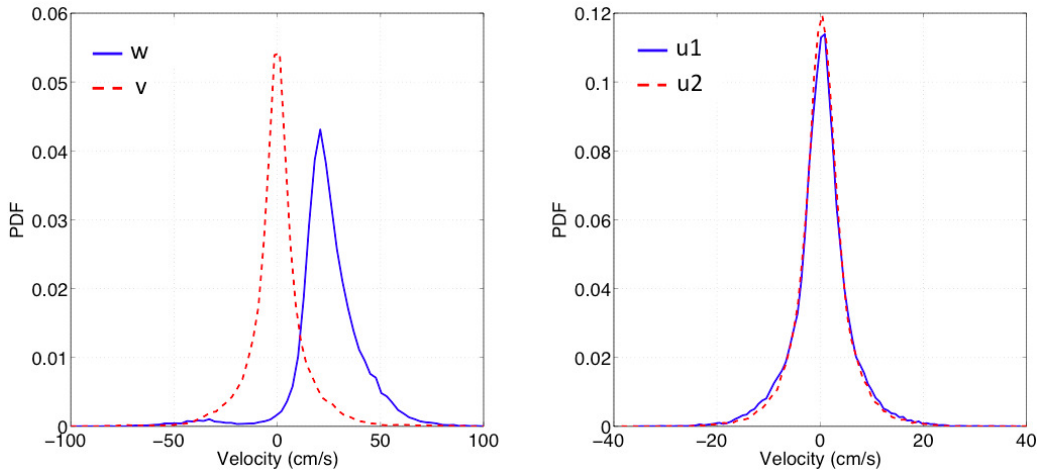

Figure 2.9: Empirical PDF of raw velocities at plume core $r = 0$ (case A, $z/D = 6.6$)

series is not locally stationary i.e. over small time intervals. It can be seen from the figure that fluctuations of drastically higher frequencies than those present during "quieter" times occur when w attains extreme values. The corresponding empirical PDF is shown in figure 2.9. For the streamwise velocity w, we can see that there are two peaks; a primary peak at about 25cm/s characterized by a distribution of positive velocities that is right-skewed and a secondary peak at -35cm/s characterized by a distribution of negative velocities. The latter represents the passage of air bubbles and is a consistent feature of the ADV measurements; large negative velocities are always observed in the presence of bubbles. At first, we thought that this may be due to phase-wrapping inherent to the pulse-coherent technique of the ADV but the same result had been obtained by doubling the velocity range to 1m/s, which was higher than the expected peak bubble rise velocity at 0.6m/s. The interpretation on this observation is given in more details in § 5.2. On the contrary, the radial velocity $u1$ contains only one peak in its PDF. The PDF is symmetric with respect to zero velocity as can be expected from the flow symmetry at plume core. Similar observations can be found from the PDFs of $u2$ and v. The rapid vertical rise of air

bubbles created definite signatures in w only. This is the first piece of evidence that indicates the instrument was returning meaningful measurements; if the data had been biased by false bubble signatures, all PDFs should share the same set of features.

Evolution of the PDFs across the plume is shown in figures 2.10-2.11 for radial distances r = 16-70mm. First, we note the narrowing of PDFs with increasing r that indicates a decreasing TKE away from the plume core; $\langle u_i^2 \rangle$ equals the second moment of PDF. This is an expected result. Second, a tertiary peak with positive velocities appears in w at around r = 25mm. The tertiary peak becomes more and more separated from the primary peak with r until r becomes larger than 80-90mm at which point it disappears altogether. Such phenomenon is not observed in other velocity components. Third, the cluster of negative velocities in w's PDF disappears gradually with increasing r. The above suggests that the measurements have captured some key processes inside a bubble plume; if the ADV data had been all wrong then the PDFs should be nearly the same at different r as the time-averaged void fraction is uniform across the plume (Seol et al. 2007). This leads us to the decomposition of w-PDF in next section.

To quantitatively characterize the w-PDFs, we separate extreme values of w into two groups by a median filter:

$$C_2 \lambda \text{median}(|w_i - \text{median}(w_i)|) \tag{2.6}$$

where $C_2 = 1.35$, $\lambda = \sqrt{2log(N)}$ and N = no. of data points in a time series (see Goring & Nikora 2002, Cea et al. 2007).

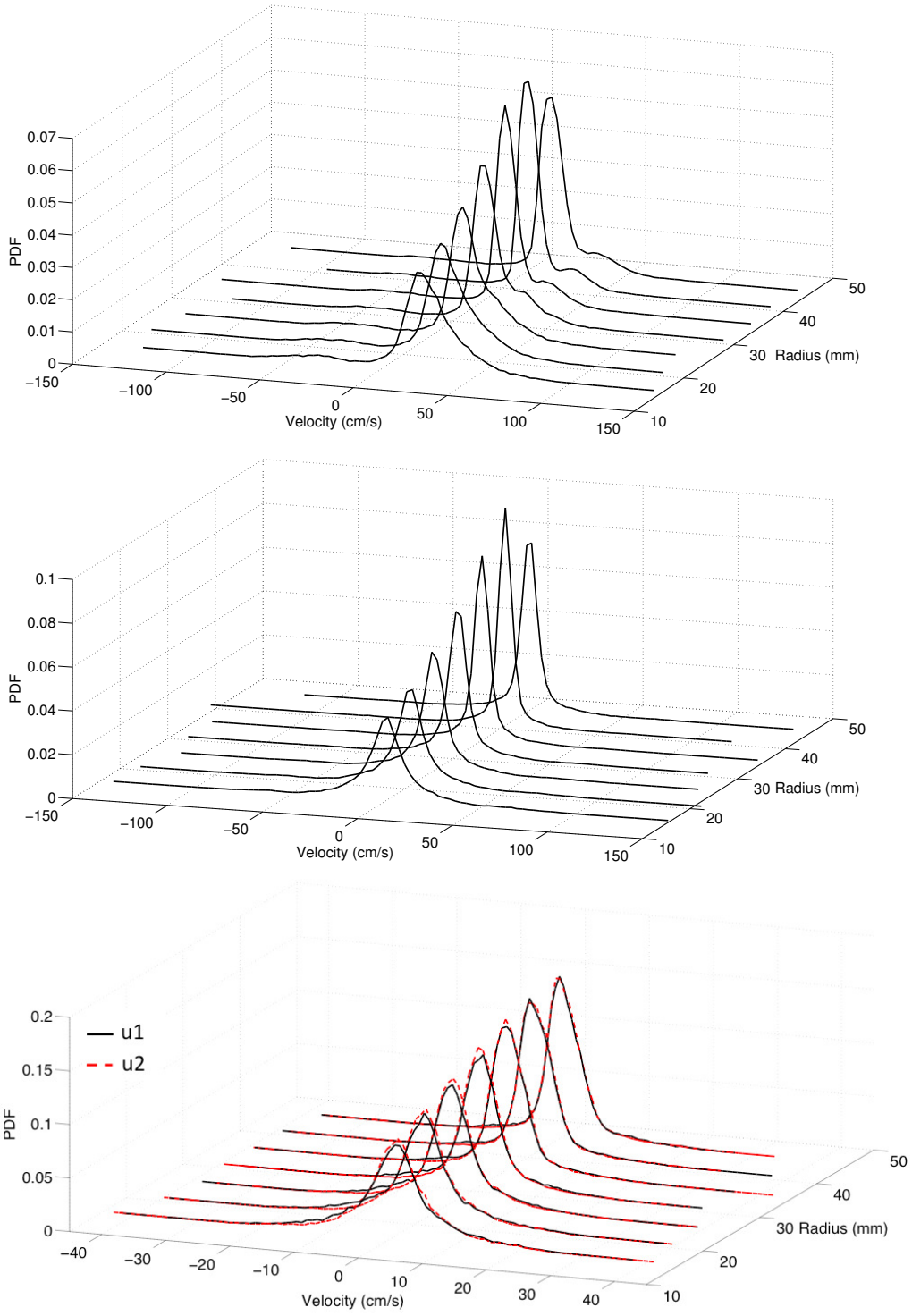

Figure 2.10: Evolution of empirical PDF of raw velocities r = 16-50mm (case A); $\tilde{w}$ (top), $\tilde{v}$ (middle) and $\tilde{u}$ (bottom)

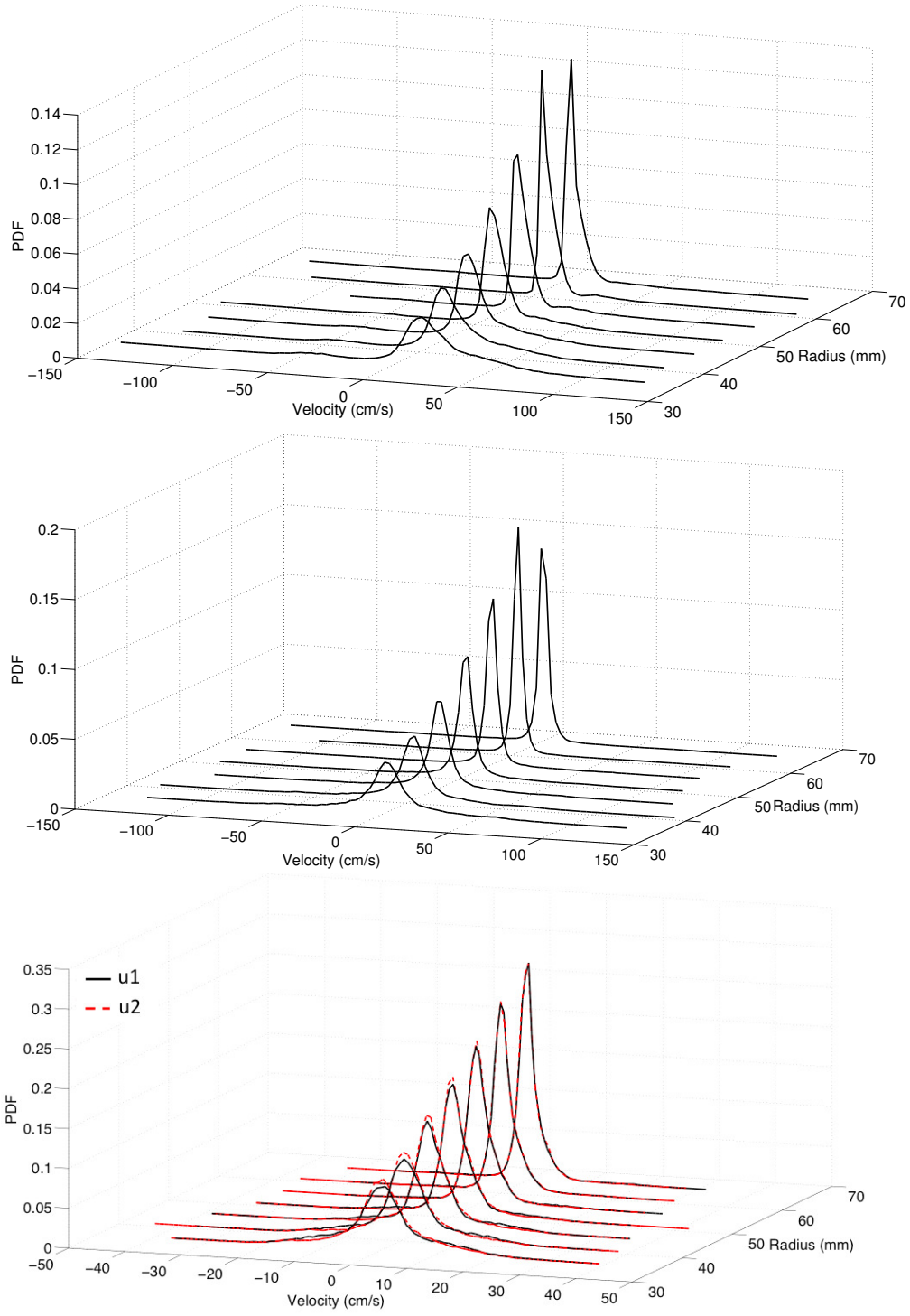

Figure 2.11: Evolution of empirical PDF of raw velocities r = 36-70mm (case A); $\tilde{w}$ (top), $\tilde{v}$ (middle) and $\tilde{u}$ (bottom)

This set of constants is applied to all data which are presumed to have a Gaussian PDF as mentioned in § 3. Referring to figure 2.9, the median filter identifies outliers relative to the central primary peak which is assumed to take on a Gaussian shape. We then label the outliers as follows; those with positive values of w are termed the *wake* (tertiary peak) and those with negative w termed the *return flow* (secondary peak), and calculate their data fraction n_i in the total population. The results for both cases are shown in figure 2.12. The radial distance r (horizontal axis) has been normalized by the Gaussian radius b_g (see §2.5). For $r/b_g < 1$, the return flow accounts for less than ($n_1 =$) 2% of the data whereas the wake contributes a significant portion at ($n_3 =$) 5-25%. As one moves away from $r = 0$, n_3 decreases steadily to low values. Previous void fraction measurements (Seol et al. 2007) of the same flow have shown that the time-averaged α_{air} is in the range 0.7-1.8%. This correlates very well with our n_1 and indicates that large negative values of w are related to the passage of air bubble through the ADV sampling volume. Further, the wake fraction is much larger than that of the return flow since the latter is a very localized process. In their numerical simulations on bubble columns ($\alpha_{air} < 4\%$), Riboux, Legendre & Risso (2013) show that bubble wakes have lengths ten times the bubble diameter. It is therefore reasonable to see a significant wake contribution to the total data.

2.5.2 Decomposition of streamwise velocity w

The evolution of the w-PDFs identified in the previous section leads to the hypothesis that outliers, relative to the primary peak in figures 8-9, are not erroneous but the results of different physical mechanisms. There are three mechanisms to consider: (1) return fluid flow caused by rising bubbles, (2) bulk entrained fluid and (3) bubble wakes. The boundary between (2) & (3) is not distinct because plume entrainment

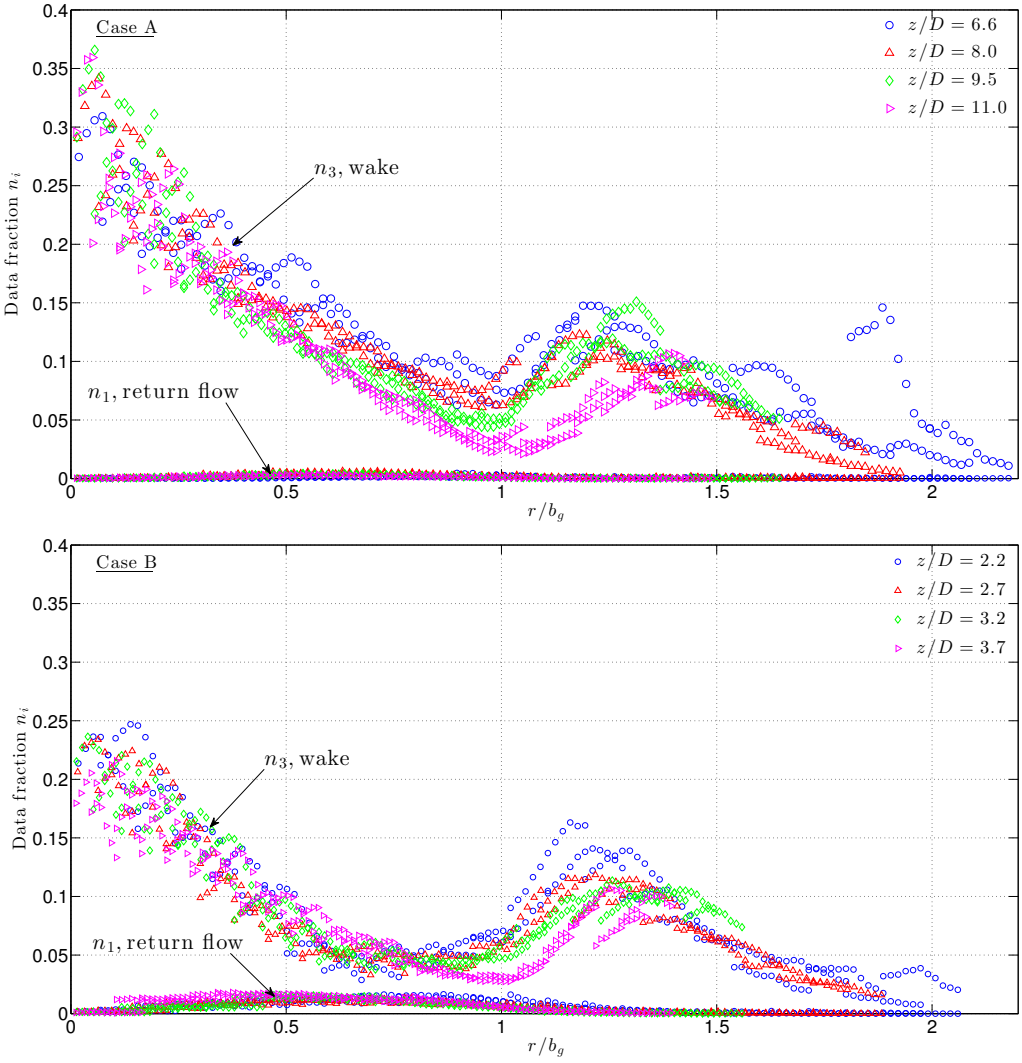

Figure 2.12: Data fraction identified as *return flow* n_1 or *wake* n_3 by the median filter in equation 2.6

is a collective result of the bubble wakes. Nonetheless, this classification is useful as the two rise at different velocities with the expectation that the latter is rising faster and the time-averaged velocity differential is near the bubble slip velocity. As for (1), it stems from the necessity of mass conservation of the liquid fraction. Let us consider the return flow caused by the rise of a single bubble inside a cylinder of diameter D where the ambient fluid is originally motionless. If d is the bubble diameter and u_{rise} is the bubble rise velocity, a volume void is created at a rate equal to $\frac{\pi}{4}d^2u_{rise}$ which must be filled by a downflow of ambient water. The average velocity of this downflow is $\overline{u_d} = \frac{d^2u_{rise}}{D^2-d^2}$ which shows that $\overline{u_d}$ can attain very large values as $D \to d$. In previous section (see also figure 7), we interpret large negative velocities as the return flow which in this case has a mean value of 40cm/s i.e. $u_d =$ 40cm/s. The rise velocity $u_{rise} = 50$cm/s which is the sum of local bulk fluid velocity ($\sim$ 30cm/s) and slip velocity (24cm/s, Clift et al. (1978)). Solving for D, we get D = 3mm, meaning that the periphery gap that allows drainage of the return flow is a 0.5mm-thick annular ring. This is on the same order of the 1mm radial resolution and therefore one can expect the return flow be captured by the ADV probe.

With these heuristic arguments in mind, we postulate that w comprises velocities generated by all three mechanisms, each has a Gaussian PDF $p_i(w)$ of which their sum is equal to the total (raw) PDF $p_{total}(w)$. A nonlinear curve-fitting is then done to calculate the mean and variance of each PDF i.e. (μ_i,σ_i). A constraint that must be satisfied is,

$$\int_{-\infty}^{\infty} p_{total}(w) = \int_{-\infty}^{\infty} (p_1(w) + p_2(w) + p_3(w))dw = 1 \tag{2.7}$$

To satisfy equation (2.7), the individual PDF takes the following form.

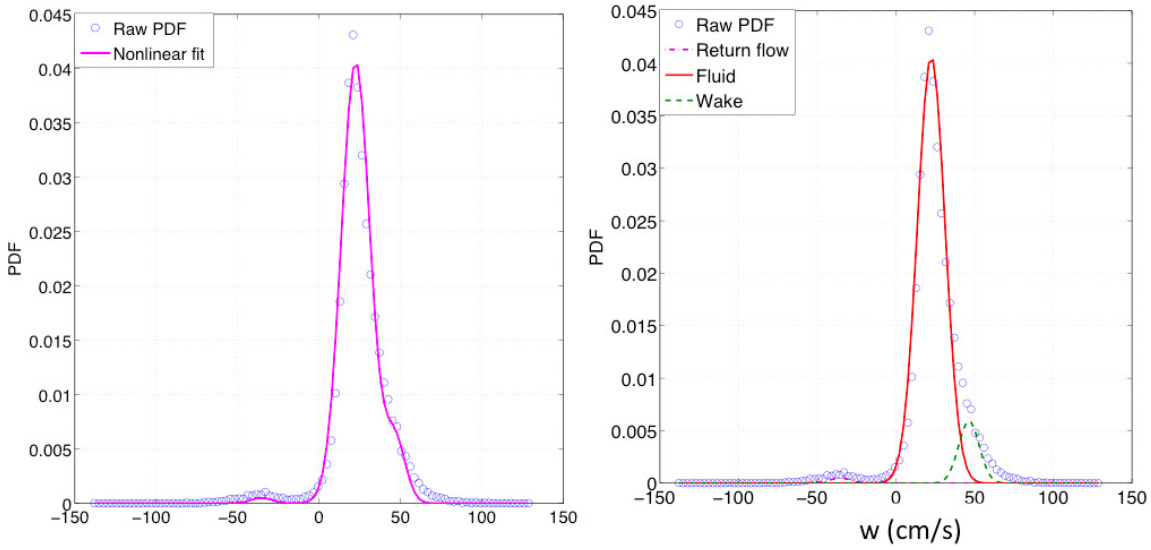

Figure 2.13: Decomposition of the streamwise velocity $\tilde{w}$ into the return flow of bubbles, entrained fluid and bubble wake (case A, $r = 0$)

$$p_i(w) = \frac{1}{\sqrt{\pi}} \frac{n_i}{\sigma_i} e^{-(\frac{w-\mu_i}{\sigma_i})^2} \tag{2.8}$$

where n_i is the data fraction corresponding to mechanism i and $\sum_{i=1}^{3} n_i = 1$; it is straightforward to verify $\int_{-\infty}^{\infty} p_i(w) = n_i$. n_i is calculated from experimental data by the median filter introduced in previous section.

An example of the decomposition is shown in figure 2.13. It can be seen that the total PDF is reasonably fitted by the sum of three Gaussians. Notably, the return flow is well separated from the rest of the flow and the upper end of the bulk entrained fluid flow is indistinguishable from the wake. To substantiate our heuristic arguments, the velocity differential $\triangle\mu = \mu_3 - \mu_1$, which in principle should equal to u_s, across the plume for both cases is plotted in figure 2.14. The radial distance (horizontal axis) has been normalized by the fluid phase Gaussian radius b_g (see later result sections). At all source heights, a velocity plateau can be found for $r/b_g < 0.8 - 0.9$; $\triangle\mu =$

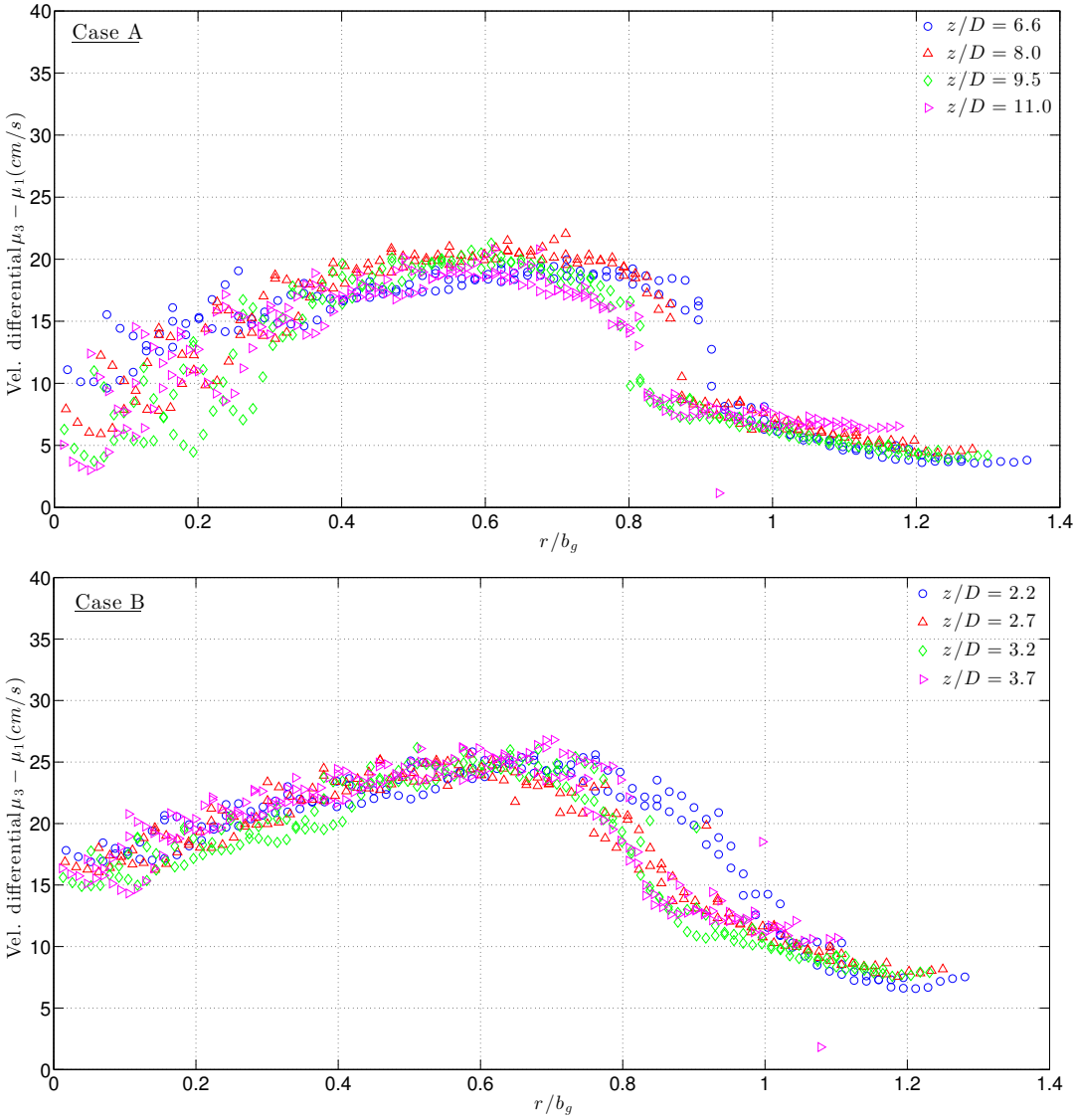

Figure 2.14: Velocity differential $\mu_3 - \mu_1$

20cm/s in case A and 20-25cm/s in case B. The velocity differential then drops off sharply and attains low values beyond $r/b_g = 1$. The values of velocity plateau are comparable to the terminal velocity (24cm/s) of a single bubble in a quiescent ambient; the observed variations are caused by group effects of bubbles and local state of fluid turbulence both of which are known to increase/decrease the terminal velocity. From the figure, a possible definition of the bubble core radius is $b_b = 0.9b_g$ and this will be used to calculate the plume spread ratio λ in §2.5.4. Analysis above shows that the wake identified by the median filter in previous section is indeed physical and the ADV data contain this key flow component.

2.5.3 Wavelet analysis on streamwise velocity $\tilde{w}$

A wavelet analysis has been carried out on w to elucidate the nature of fluctuations caused by rising bubbles through the ADV sampling volume. The wavelet method has a solid mathematical foundation and has been widely used to analyze time series with non-stationary statistics (Daubechies 1990). It is particularly relevant here since the injection of bubble-induced energy into the bulk plume flow occurs only intermittently in time; the void fraction is at most 2% inside the plume. Conventional Fourier transform, which is opted for stationary time series, is not applicable for characterizing the rapid and short-lived velocity fluctuations caused by the bubbles because of its poor time localization property (Farge 1992). We elected to use the Morlet wavelet in our analysis; its strengths in decomposing turbulent velocity signals have been discussed in Farge (1992). We employ the continuous wavelet transform and follow the recommendations in Torrence & Compo (1998) in choosing the wavelet parameters. The parameters were chosen such that at least 98% of the energy (variance) in the original time series is captured by the wavelet coefficients. Although it is beyond our scope to give a complete discussion on the wavelet transform, we would

like to explain briefly the connection between the wavelet scale and the usual Fourier period (frequency). Wavelet transform, like any other L_2-decomposition, projects a signal onto a set of complete basis functions such that the partial sums formed by a linear combination of the basis functions converge uniformly to the original signal in L_2-sense. In Fourier analysis, the orthonormal set of periodic trigonometric functions on the interval $[-\pi, \pi]$ is chosen as the basis functions. The notion of period (frequency) is well-understood since they are sines and cosines. On the contrary, basis functions in wavelet transform are scaled and shifted versions of a mother wavelet that is not periodic in itself. It is therefore necessary to convert the wavelet scale into its equivalent Fourier period so that one can interpret the results in the usual frequency sense. Such a conversion is provided in Torrence & Compo (1998) and it is unique for each type of wavelet. For a Morlet wavelet, the scale is almost equal to the Fourier period.

Figure 2.15 shows the results at two locations (i) r = 5mm (plume interior) and (ii) r = 65mm (plume exterior). First, we note that there are many needle-like signatures of high frequencies in the time-frequency plot of r = 5mm. They are set against the backdrop of a band of energetic low frequencies that persists throughout the entire time record. By contrast, the plume exterior contains only the low-frequency band which is expected as there are few bubbles. Second, a zoom-in of time at r = 5mm (shown in the same figure) reveals that the needle-like signatures are short-lived patches of high energy content. They span a range of frequencies, 1-20Hz, but many of them have frequencies of about 10-15Hz. The two most energetic patches are indicated by arrows and they may represent the direct passage of bubbles through the ADV sampling volume, thus leaving behind strong signatures. In their model of bubble-induced turbulence based on large-scale wake interactions, Riboux et al.

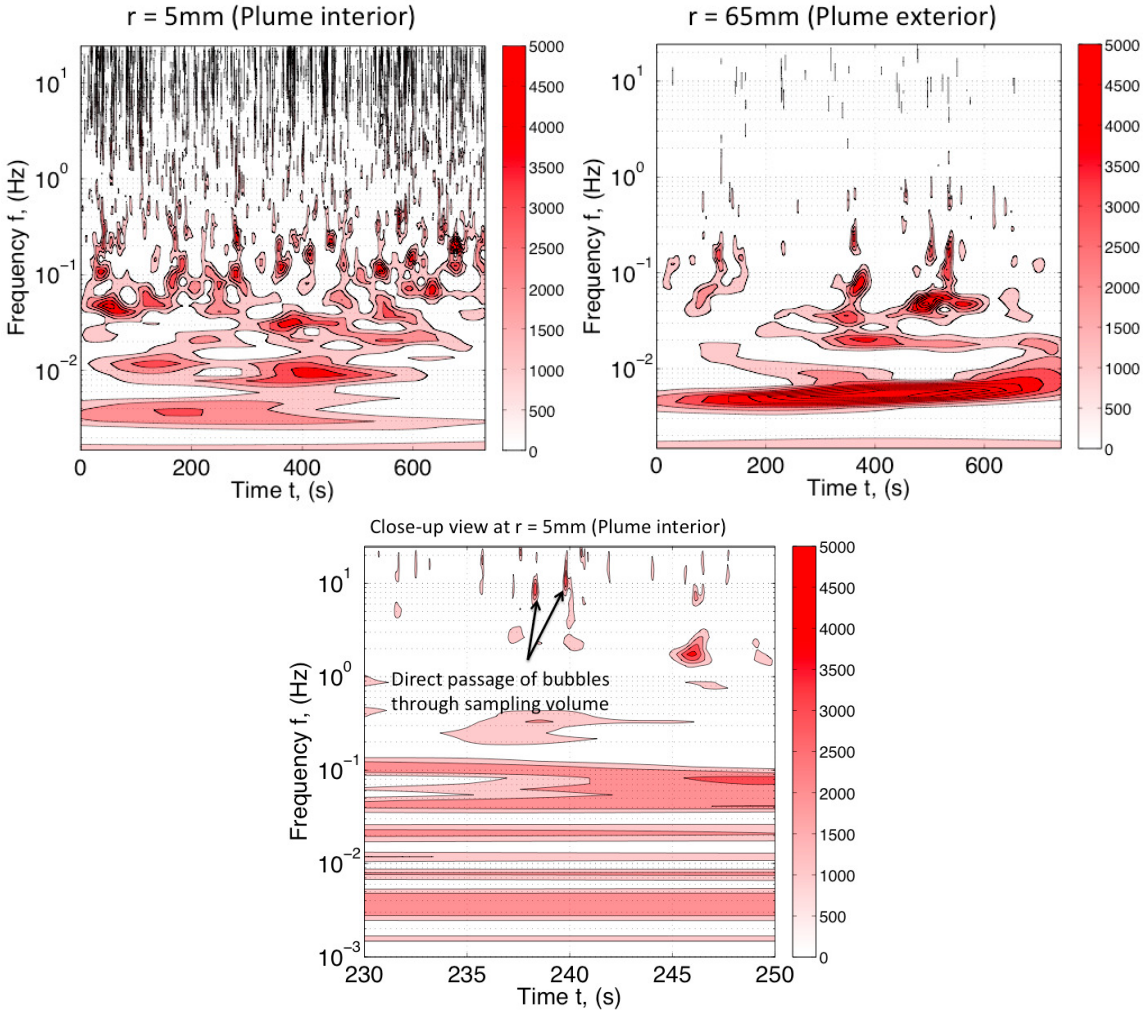

Figure 2.15: Continuous wavelet transform of streamwise velocity $\tilde{w}$ using the Morlet wavelet; no. of scale analyzed = 71, smallest scales $s_o = 2dt = 0.04$s, largest scale $J = 655$s

$z(cm)$	$D(cm)$	z/D	$W_c(cm/s)$	$b_g(cm)$	$b_b = 0.9b_g(cm)$	$\lambda = b_b/\sqrt{2}b_g$	$\beta = b_g/z$
44.7	20.4	2.2	30.01	5.78	5.20	0.64	0.129
54.7	20.4	2.7	27.05	6.32	5.69	0.64	0.116
64.7	20.4	3.2	25.92	7.63	6.87	0.64	0.118
74.7	20.4	3.7	25.14	8.53	7.68	0.64	0.114
44.7	6.8	6.6	20.64	5.46	4.91	0.64	0.122
54.7	6.8	8.0	19.43	6.18	5.56	0.64	0.113
64.7	6.8	9.5	17.81	7.23	6.51	0.64	0.112
74.7	6.8	11.0	17.90	8.00	7.20	0.64	0.107

Table 2.3: Measured mean flow properties of bubble plumes in present study; the $\sqrt{2}$ appearing in λ accounts for the difference between top-hat and Gaussian profiles

(2013) obtained a scaling relationship, $f_{cwi} = 0.14u_s/d$, for the frequency f_{cwi} at which energy generated by the collective wake instability of a group of rising bubbles is injected into the surrounding fluid. Using present values of u_s and d, $f_{cwi} = 14$Hz which corresponds to that of the short-lived energetic patches. This comparison is not exact since the simulations were on bubble columns where there is no entrainment of ambient fluid; the overall turbulent characteristics are different from our bubble plume. Nonetheless, it at least supports that our ADV data captured the collective effects of bubble wakes on the plume proper which is sufficient for performing a TKE budget.

2.5.4 Mean flow and turbulent stresses

Instantaneous velocity $\tilde{\mathbf{u}}(\mathbf{x}, t)$ is decomposed into a time-averaged part $\mathbf{U}(\mathbf{x})$ and a fluctuating part $\mathbf{u}(\mathbf{x},\mathrm{t})$, e.g. in the streamwise direction $\tilde{w} = W + w$. Figure 2.16 shows W in normalized ordinates. A Gaussian profile was fitted to the data and the centerline streamwise velocity W_c and Gaussian jet radius b_g were obtained as a result of the curve fitting. In both cases, the profile $\frac{W}{W_c} = e^{-(r/b_g)^2}$ fits the data reasonably well; at $r = b_g$, $W = e^{-1}W_c$. The relatively large discrepancy that occurs when $r \geq 1.5b_g$ is probably due to large-scale recirculation cells induced by the time-steady

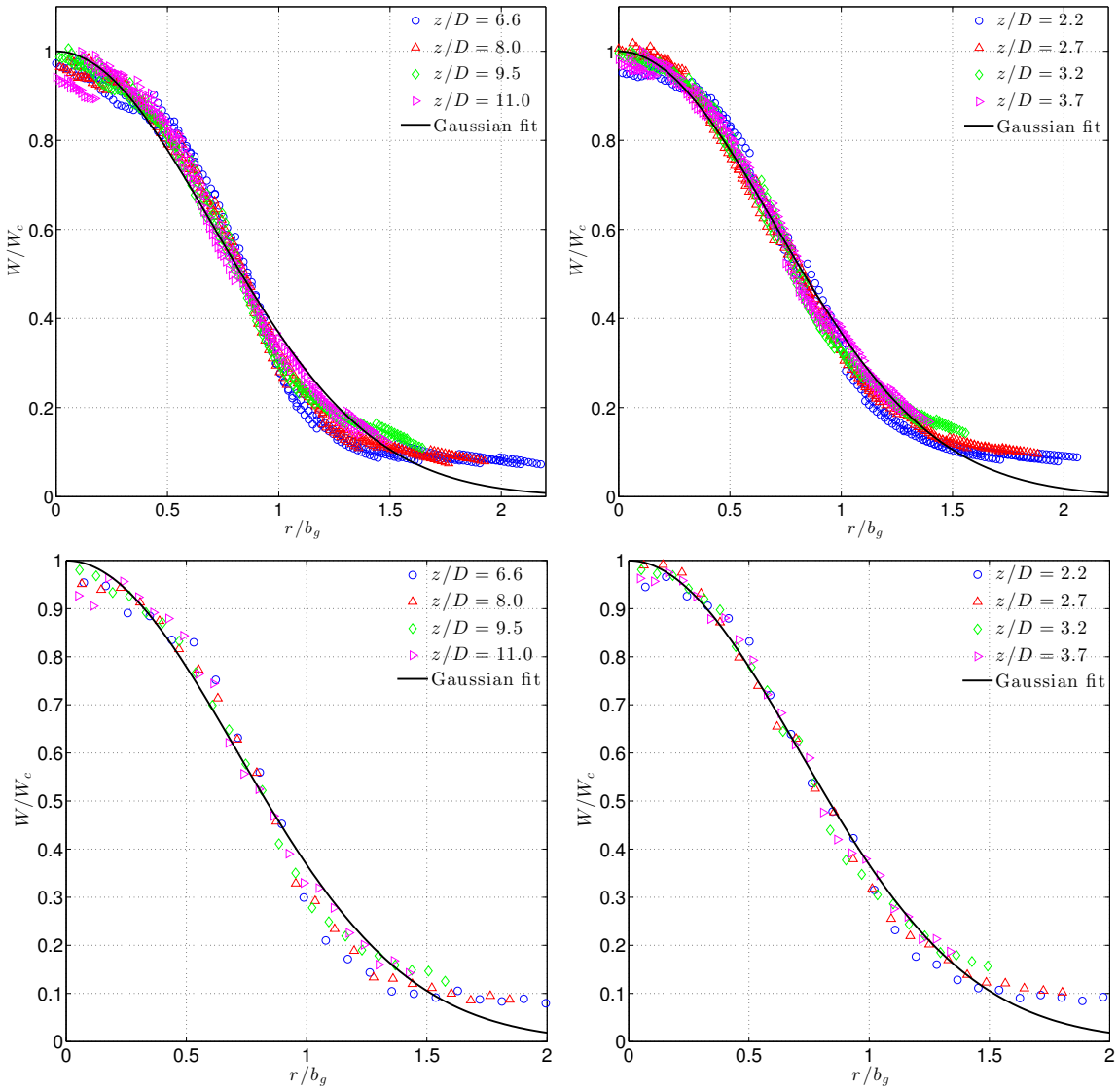

Figure 2.16: Normalized radial profiles of time-averaged vertical velocity W; a comparison between data in the center portion of the ADV's measurement strip (top row) and the data point at *sweet spot* (bottom row); $Q_o = 0.5$L/min (left column), $Q_o = 1.5$L/min (right column)

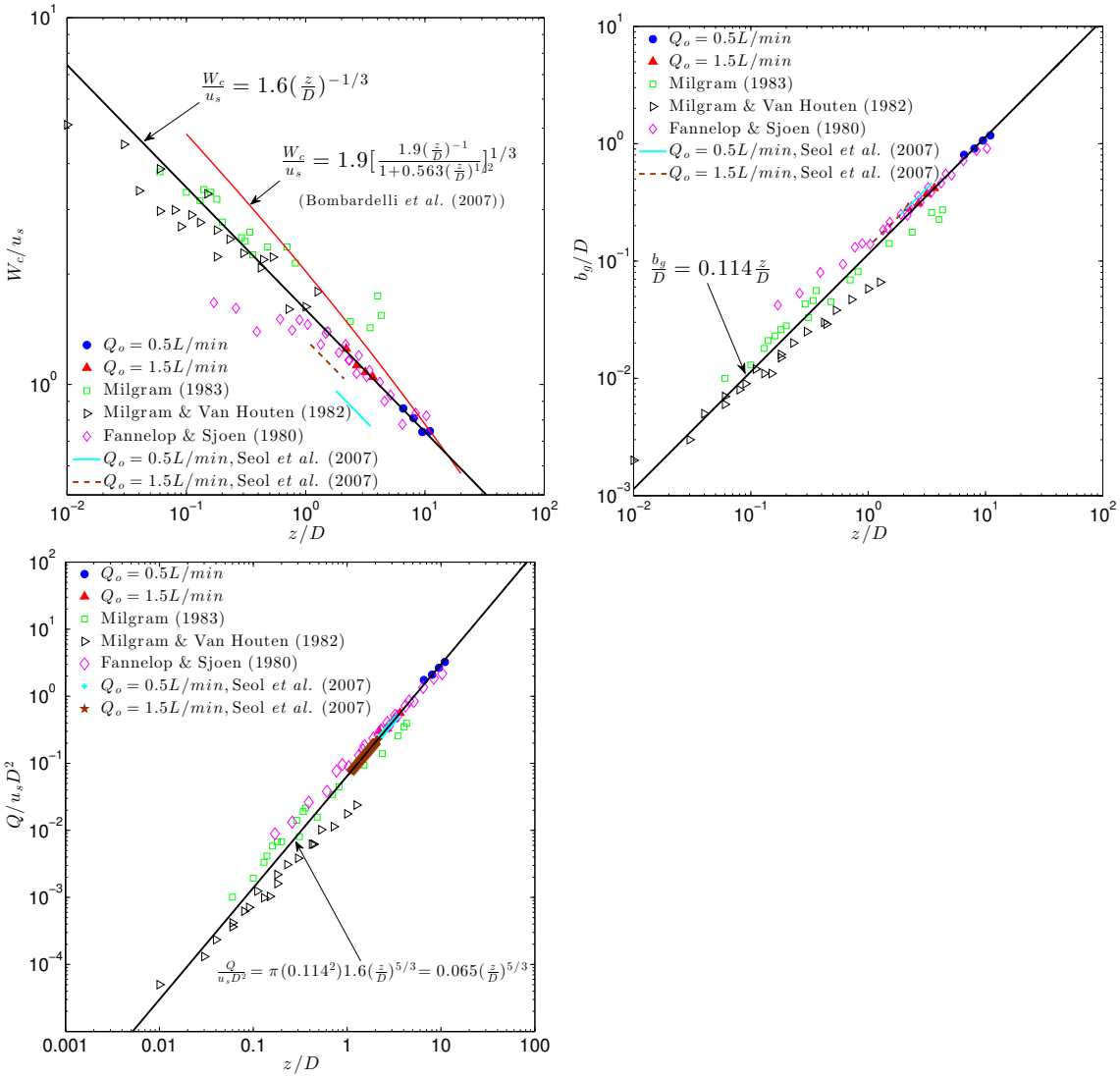

Figure 2.17: Comparison of measured plume centerline velocity W_c (top left), Gaussian plume radius b_g (top right) and fluid phase volume flux Q (bottom left) with published data

plume inside the tank (Fraga, Stoesser, Lai & Socolofsky 2015). Figure 2.17 shows a comparison on W_c, b_g and the fluid phase volume flux Q with previous experimental data in Seol et al. (2007) and datasets compiled in Milgram (1983). The data compiled in the latter reference were obtained from bubble plumes of much large scales than present study; the water depth was 50m, 10m and 3.66m in Milgram (1983), Fannelop & Sjoen (1980) and Milgram & Van Houten (1982), respectively. Results are shown using the functional forms in equation (2.2). A remarkable agreement can be seen between the empirical relationships (black solid lines) derived from present small-scale plume data and past large-scale plume data. For W_c, the PIV data in Seol et al. (2007) are about 20-30% lower than the empirical fit and appear to lay further away from the rest of other datasets. As mentioned in introduction, wake velocities could not be captured by their PIV technique which led to an underestimation of the fluid phase velocities inside the plume core. Earlier studies like that of Milgram (1983) employed mechanical current meters that had no phase-discrimination problem and so W_c was probably not underestimated. If it is assumed that the velocities at plume edge are only slightly underestimated, a lower W_c would probably lead to a larger b_g. Indeed, b_g in Seol et al. (2007) is 18% ($0.132z$) larger than the presently derived value ($0.114z$). This interpretation is further supported by the measurements of Q; despite the difference in W_c and b_g, the data on Q agree excellently with the empirical fit. Since for very diluted plumes, $Q = \pi b_g^2 W_c$, if Q is to remain the same when b_g is increased by 20%, W_c must decrease by 30%. This reduction compares very well with their W_c data. On the other hand, the steepening of decay slope of W_c described in §2.4 is not clearly discernible in the combined dataset that spans $0.01 < z/D < 11$. Further experiments are needed in the range $10 < z/D < 100$ to explore the $(z/D)^{-1/2}$ decay suggested in Bombardelli et al. (2007).

Table 2.3 tabulates the numerical values of various mean flow properties. The bubble core radius b_b is estimated from figure 2.14 in the manner described in §2.5.2. It is interpreted as the top-hat radius and so a factor of $\sqrt{2}$ is multiplied to b_g in the calculation of spread width ratio λ. A value of 0.64 is obtained, which is somewhat smaller than data in Seol et al. (2007). The fluid phase spreading rate β appears to decrease with z/D and attains an asymptotic value of 0.11 for $z/D > 8$. Overall, our ADV data on the plume mean flow are consistent with other experimental datasets and exhibit the following dependence on z; $W_c \sim z^{-1/3}$, $b_g \sim z$ and $Q \sim z^{5/3}$. Integral properties of bubble plumes are adequately described by the independent parameters u_s and D. As a further comparison, the entrainment coefficient α in the asymptotic regime ($z/D > 8$) of a bubble plume can be computed from the integral equation of conservation of fluid volume flux, $\frac{dQ}{dz} = 2\pi b_g^2 W_c$, using the three empirical fits. The coefficient α can be written as,

$$\alpha = \frac{5}{3}\frac{1}{2\pi}\frac{C_3}{C_2 C_1} = 0.095 \tag{2.9}$$

where $C_1 = 0.114$, $C_2 = 1.6$ and $C_3 = 0.065$ are the empirical-fit constants for $b_g(z)$, $W_c(z)$ and $Q(z)$ respectively. This value is somewhat larger than the generally accepted value of 0.083 for a single-phase plume (Fischer et al. 1979) but is well within the range of published data. It should be noted that the spreading rate β for a pure plume is equal to $\frac{6}{5}\alpha_p$ (Lee & Chu (2003, p.95)) by the equivalence of spreading hypothesis and entrainment hypothesis. Using $\alpha_p = 0.095$, this relation gives β= 0.114 which is in excellent agreement with the measured value C_1. Finally, the asymptotic plume densimetric Froude number Fr_p can be computed from $Fr_p = \frac{1}{\sqrt{2}}\sqrt{\frac{5}{4\alpha_p}}\lambda$ (Lee & Chu 2003, p.99); the factor of $\frac{1}{\sqrt{2}}$ is used to convert jet radius into diameter so that the definition of Fr_p becomes identical to that in Wüest et al. (1992) and

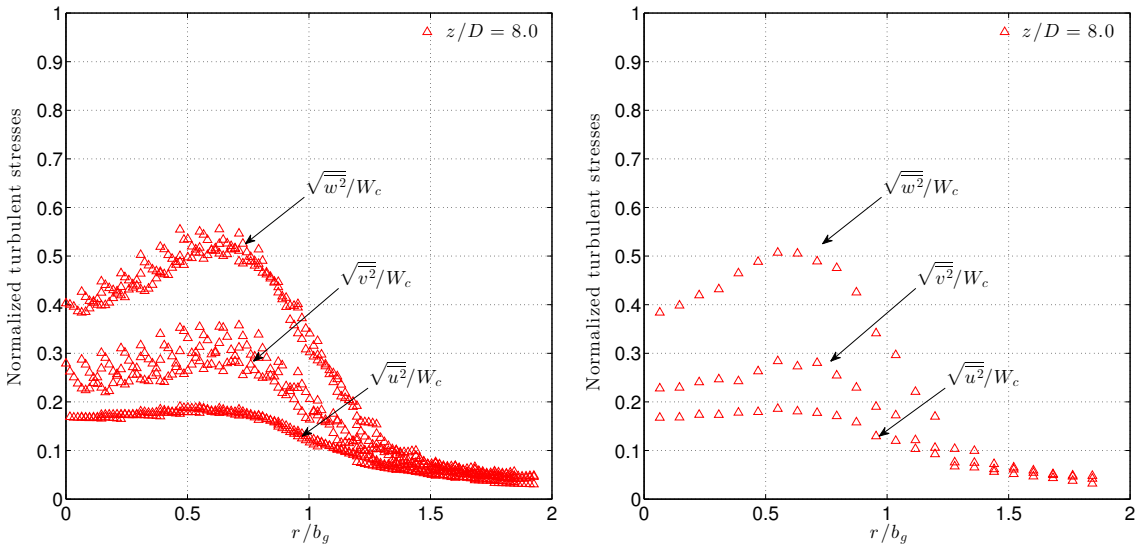

Figure 2.18: Raw ADV data on turbulent stresses; raw data (left) and data at sweet spot (right)

Bombardelli et al. (2007). Using $\lambda = 0.64$ from our experiments, Fr_p equals to 1.63, which is in agreement to the suggested value of 1.6 in Wüest et al. (1992) and the analytical value of 1.7 in Bombardelli et al. (2007).

Before moving on to the results of time-averaged turbulent stresses, figure 2.18 (left panel) shows the raw data at $z/D = 8$ in Case A. In the plume core, $r/b_g < 1$, a clear peak is seen around $r/b_g = 0.5$ but a non-physical distribution is observed in each measurement strip; data points closer to the plume center ($r = 0$) have higher stress magnitudes than points further away. This is due to the varying sensitivity mentioned in §2.2.3; the probe is more sensitive (accurate) at locations closer to the transmitter head which, in the experiments, were located further away from plume center. In the right panel, the data point corresponding to the *sweet spot* in each measurement strip is shown and the profiles are seen to be smooth across the plume. The comparison is representative of all other data in present experiments and the

sweet spot data will be shown and used in curve-fitting in later section.

Figure 2.19 shows the time-averaged turbulent stresses of case A. It can be seen that all stresses (streamwise, radial and shear) possess self-similarity in normalized ordinates; the local streamwise velocity W is used as the velocity scale to facilitate comparison with the PIV data (sampled at 125Hz) in Duncan et al. (2009). The gradual increasing trend from plume center towards the edge is congruent with PIV measurements. In particular, both techniques measured very close $\overline{wu}$ and $\overline{u^2}$. For $\overline{w^2}$, much higher values are given by the ADV data which is a result of wake and return flow velocities in $\tilde{w}$. Some conclusions can be drawn here. First, the 15min-average produces converged and repeatable turbulent statistics. Second, because some seeding particles inside bubble wakes had been removed during image processing in (Duncan et al. 2009) the rapid velocity fluctuations associated with the wakes could not be obtained from their PIV cross-correlation. In reality, the flow is much more agitated in the streamwise direction. Third, the bubbly flow is clearly not isotropic contrary to the PIV data; $\sqrt{\overline{w^2}}$ is 2.2-2.6 times as large. This strong anisotropy has also been reported in Simiano et al. (2009); a direct comparison is, however, not possible because of the strong plume contraction in their experiments as described in §2.1. Results for case B are very similar to those in A as can be seen in figure 2.20.

Case A of this study has very recently been simulated by a large-eddy simulation (LES) code in Fraga et al. (2015). A Eulerian-Lagrangian approach is used to predict bubble plume dynamics. The Smagorinsky subgrid scale (SGS) model with a constant Smagorinsky constant of 0.1 is used to model the unresolved fluid turbulence. Applicability of the LES code has been demonstrated for a variety of flows, including

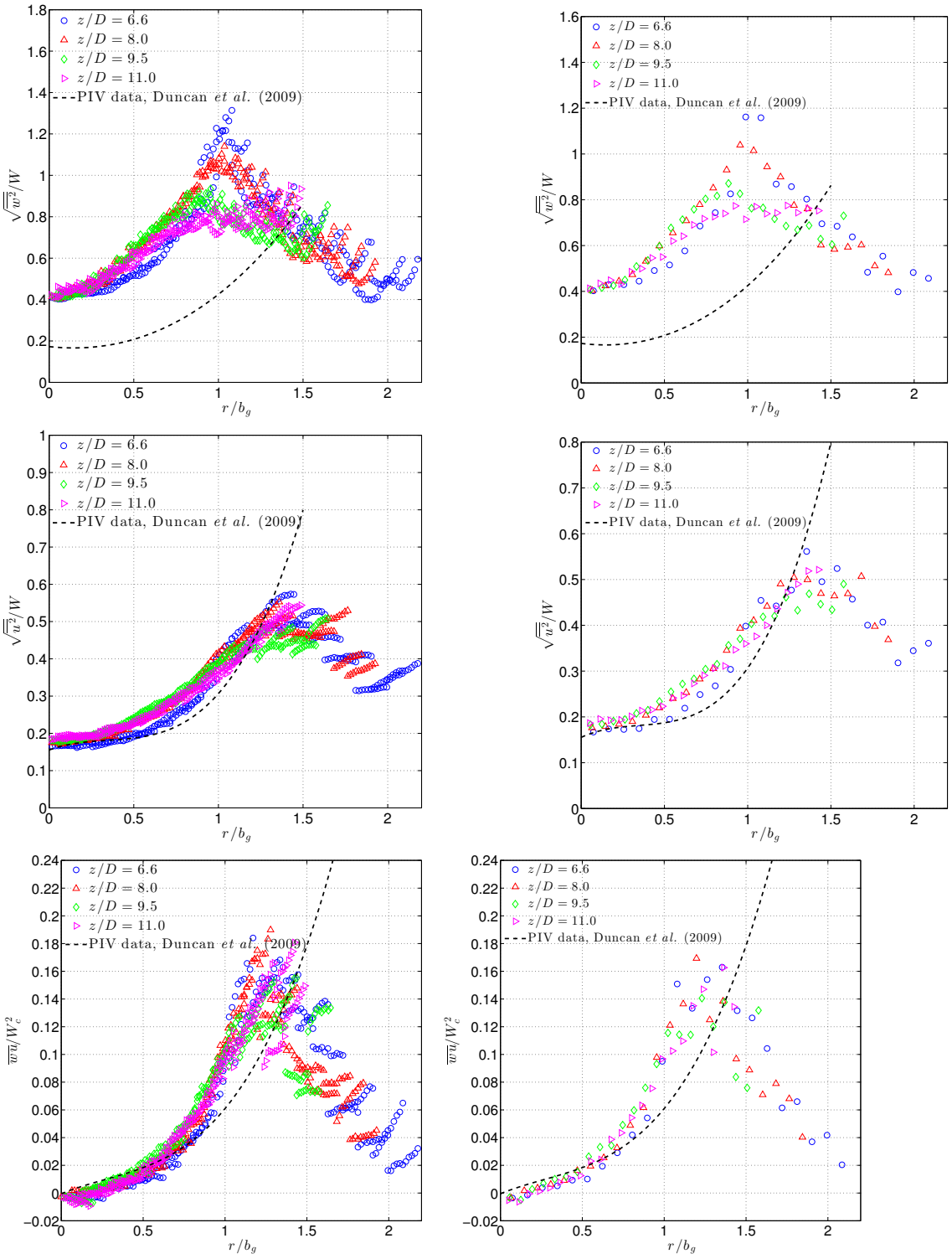

Figure 2.19: Comparison on measured turbulent stresses by ADV and PIV data in Duncan *et al.* (2009); $Q_o = 0.5$L/min (Case A), from data strip defined in §2.2.3 (left column) and from sweet spot (right column)

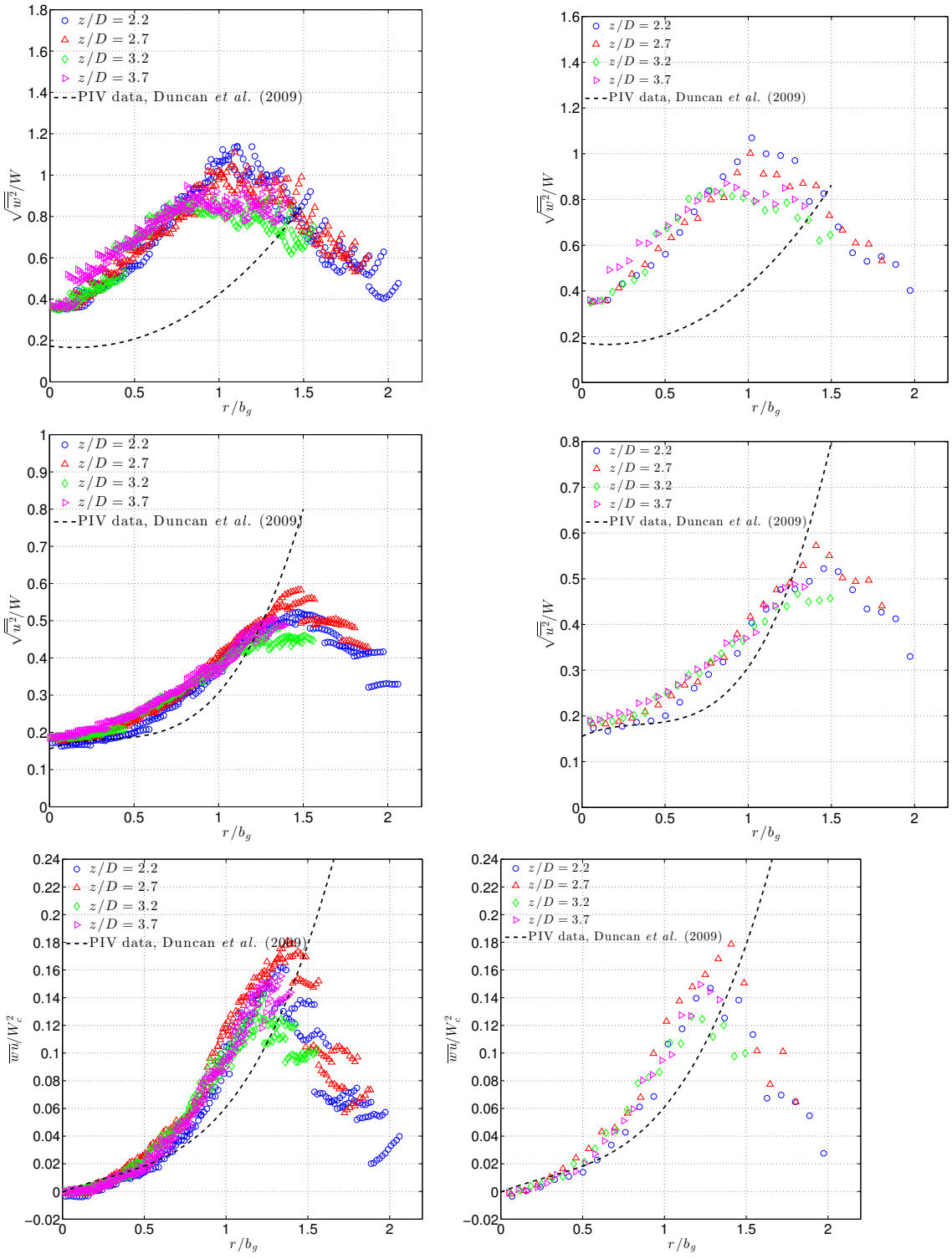

Figure 2.20: Comparison on measured turbulent stresses by ADV and PIV data in Duncan *et al.* (2009); $Q_o = 1.5$L/min (Case B), from data strip defined in §2.2.3 (left column) and from sweet spot (right column)

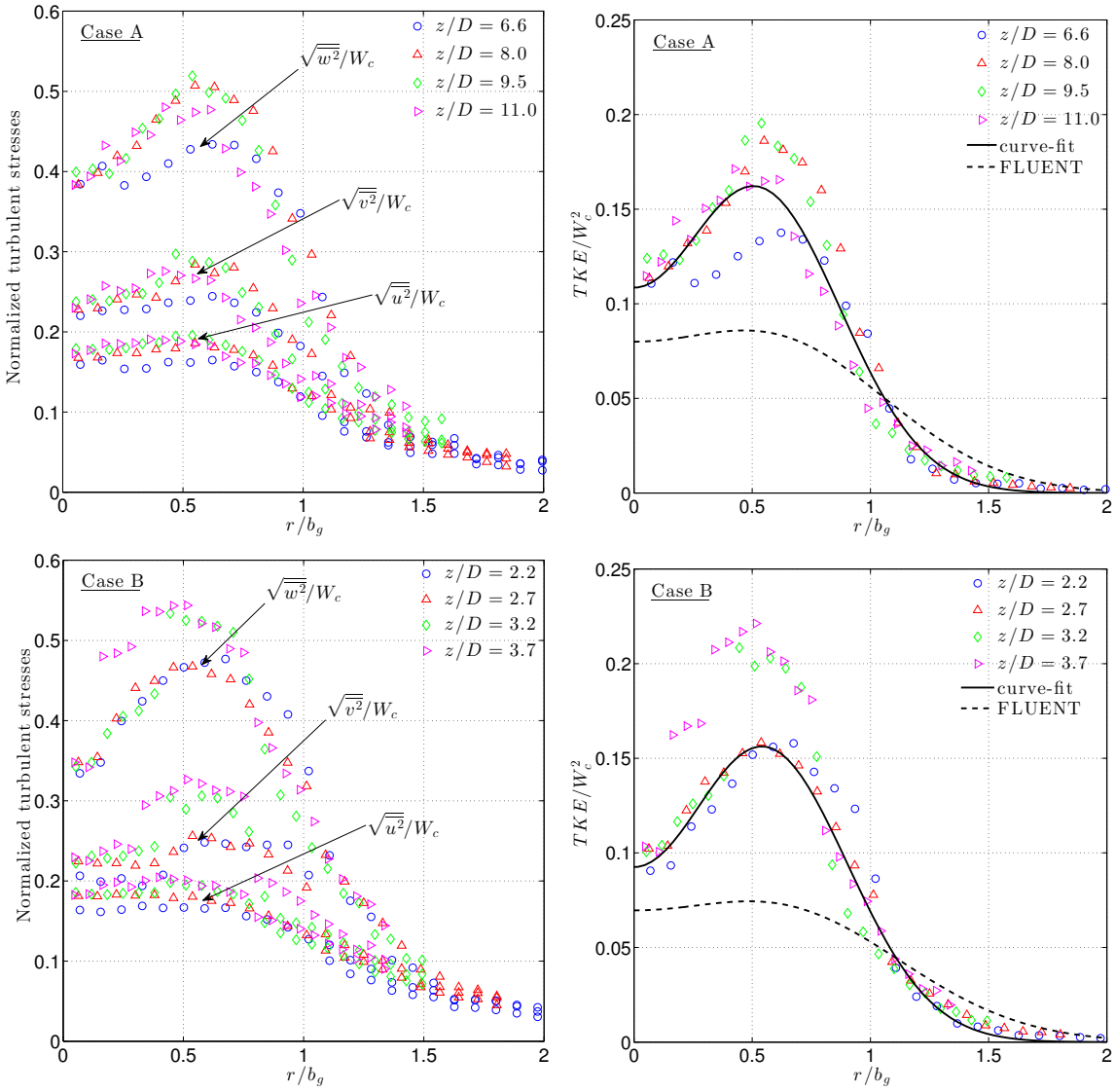

Figure 2.21: Normalized radial profiles of turbulent stresses and turbulent kinetic energy TKE = $\frac{1}{2}(\overline{w^2} + \overline{u^2} + \overline{v^2})$; a double Gaussian profile (equation (2.10)) is fitted to the TKE data

open-channel flows over a rough bed, compound channel flow, vegetated flows and transport and deposition of fine sediments in open-channels (references to be found in Fraga et al. (2015)). Albeit the under-prediction of $\sqrt{\overline{w^2}}$ for $r/b_g < 1$, model predictions for case A show good agreement on W_c, $\sqrt{\overline{u^2}}$ and $\overline{wu}$ in terms of magnitude and shape of normalized profile. This is because bubble-induced turbulence is not included in the SGS model. The purpose of this study is to quantify this production term in bubble plumes via a TKE budget.

Figure 2.21 shows the same data but the stresses are normalized by W_c instead; the out-of-plane stress $\overline{v^2}$ is also shown. Anisotropy of the stresses is evident where the normalized centerline values of $\sqrt{\overline{w^2}}$, $\sqrt{\overline{v^2}}$ and $\sqrt{\overline{u^2}}$ are 0.38, 0.23 and 0.18 respectively. Both $\overline{w^2}$ and $\overline{v^2}$ show a peak around $r/b_g = 0.55$ whereas $\overline{u^2}$ remains level across the plume core. The TKE $= \frac{1}{2}(\overline{w^2} + \overline{u^2} + \overline{v^2})$ profiles have a peak at $r/b_g = 0.55$ and appear to be well-fitted by a double Gaussian profile given by the following equation,

$$TKE(r,z) = 0.18W_c^2(z)exp(-\frac{(r-0.55b_g)^2}{(0.5b_g)^2}) + exp(-\frac{(r+0.55b_g)^2}{(0.5b_g)^2}) \qquad (2.10)$$

When compared to the results of FLUENT in §2.4, both exhibit a off-centre peak at $r/b_g = 0.5$. The RANS simulations, however, predict only 50-70% of the measured TKE inside the plume core. Beyond the core, $r/b_g > 1$, the predictions become comparable in magnitude with the measurements but are higher. The double Gaussian fit is also applied to individual profiles of turbulent stresses and these are shown in Appendix B and used in the TKE budget.

2.5.5 Triple velocity correlation - turbulent transport of components of TKE

The triple-velocity correlations $\overline{u_i u_j^2}$ normalized by W_c^3 are shown in figure 2.22 for case A. Note that a similar correction for Doppler noise is possible but could not be made because the skewness factor $\overline{\sigma_D^3}$ cannot be estimated (see Appendix A). Despite the larger scatter in data when compared to those of turbulent stresses, a reasonably good collapse of profiles from different source heights is observed; a clear trend is identifiable and a curve-fit in the form $P_k(r/b_g)exp(-C(r/b_g)^2)$, where $P_k(r/b_g)$ is a polynomial of degree k and C is a constant, is applied to each profile. This follows from the work in (Hussein, Capp & George 1994) and full expressions of each curve-fit are given in Appendix B. Data for case B (Q_o =1.5L/min) did not yield sufficiently converged profiles and hence they are not considered further. It can be seen that all profiles are practically zero beyond $1.2b_g$, suggesting that turbulent transport of TKE is confined within the plume core. This is quite different from a single-phase jet (Hussein et al. 1994).

2.5.6 Turbulent dissipation rate estimates

Following Pope (2000, p.132), we evaluate the pesudo-dissipation rate by $\epsilon = \nu\langle\frac{\partial u_i}{\partial x_j}\frac{\partial u_i}{\partial x_j}\rangle$ where angle brackets $\langle\cdot\rangle$ denote an ensemble average and $\nu = 0.935\times10^{-6}\mathrm{m}^2/\mathrm{s}$ is the kinematic viscosity of water at 23^oC (the temperature in experiments). In cylindrical polar coordinates, the full second-order velocity gradient tensor is given by

$$\nabla\mathbf{u} = \begin{bmatrix} \frac{\partial u}{\partial r} & \frac{1}{r}\frac{\partial u}{\partial \theta} & \frac{\partial u}{\partial z} \\ \frac{\partial u_\theta}{\partial r} & \frac{1}{r}\frac{\partial u_\theta}{\partial \theta} & \frac{\partial u_\theta}{\partial z} \\ \frac{\partial w}{\partial r} & \frac{1}{r}\frac{\partial w}{\partial \theta} & \frac{\partial w}{\partial z} \end{bmatrix} \tag{2.11}$$

where $\nabla = \frac{\partial}{\partial r}\mathbf{e_r} + \frac{1}{r}\frac{\partial}{\partial r}\mathbf{e}_\theta + \frac{\partial}{\partial r}\mathbf{e_z}$ and $\mathbf{u} = (u, u_\theta, w)$.

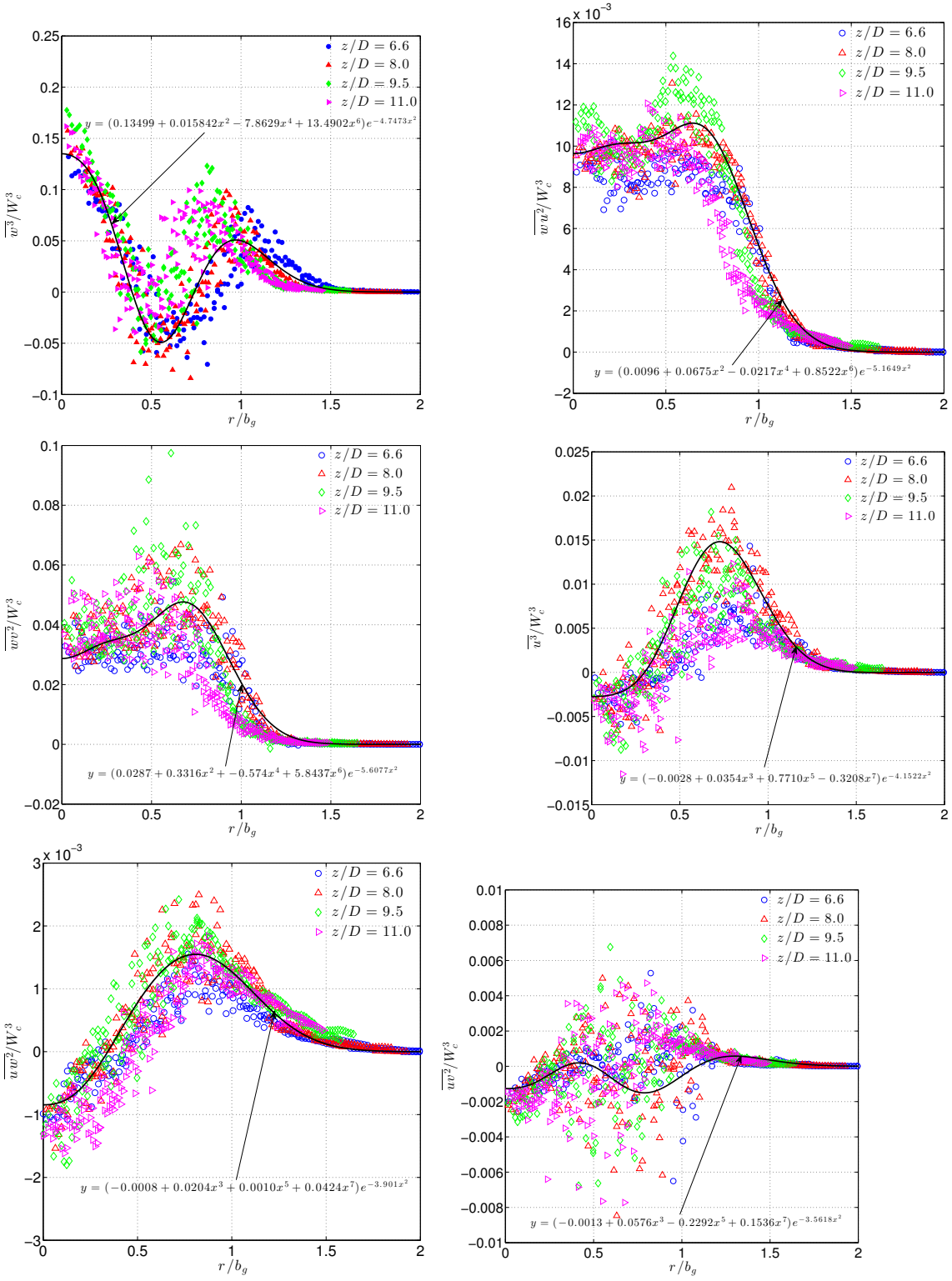

Figure 2.22: Normalized radial profiles of turbulent transport of TKE; Q_o = 0.5L/min (Case A)

Assuming an axially symmetric flow, the azimuthal terms are omitted and the full tensor reduces to its two-dimensional form. Correction for Doppler noise contamination in the first two terms is carried out straightforwardly using the technique in Hurther & Lemmin (2001); details in Appendix A. For the correlation term, no correction is needed as beam velocities $\mathbf{b}$ and Doppler noise are statistically independent among different sampling cells.

$$\nabla \mathbf{u_{2D}} = \begin{bmatrix} \frac{\partial u}{\partial r} & \frac{\partial u}{\partial z} \\ \\ \frac{\partial w}{\partial r} & \frac{\partial w}{\partial z} \end{bmatrix} \tag{2.12}$$

From (2.12), it can be seen that gradients of w and u in both radial and axial direction are needed. The former can be directly evaluated from the ADV data whereas the latter can only be indirectly evaluate for one of the axial gradient term $\frac{\partial w}{\partial z}$, which is equal to $\frac{-1}{r}\frac{\partial ru}{\partial r}$ by incompressiblity. The remaining term $\frac{\partial u}{\partial z}$ is assumed to be zero as the flow satisfies the boundary-layer approximation and u is small in magnitude. The following expression for ϵ is finally derived as,

$$\epsilon = \nu\big\langle 2(\frac{\partial u}{\partial r})^2 + 2(\frac{\partial w}{\partial z})^2 + (\frac{\partial w}{\partial r})^2 \big\rangle \tag{2.13}$$

The first derivative is replaced by a central difference that is second-order accurate. For instance, the mean-square radial gradient of streamwise velocity w at cell i is

$$\big\langle (\frac{\partial w}{\partial r})^2 \big\rangle \approx \frac{1}{4(\triangle r)^2}[\langle w_{i+1}^2 \rangle + \langle w_{i-1}^2 \rangle - 2\langle w_{i+1} w_{i-1} \rangle] \tag{2.14}$$

where $\triangle r = 1$mm and the equation involves second-order moments of w at cell $i+1$ and $i-1$ and also their correlation. Correction for Doppler noise contamination in

the first two terms is carried out using the technique in Hurther & Lemmin (2001); details in Appendix A. No correction is need for the correlation term as beam velocities **b** and Doppler noise are statistically independent among different cells.

It is instructive to first inspect the magnitudes of each contributor in the mean dissipation rate equation. A representative example at $z/D = 6.6$ (case A) is shown in figure 2.23. It is seen that all profiles exhibit a flat region inside the plume core after which the gradients decrease by about two order of magnitudes at the plume edge. In terms of relative magnitude,

$$(\frac{\partial w}{\partial r})^2 \approx (\frac{\partial v}{\partial r})^2 = 10(\frac{\partial u}{\partial r})^2 = 10(\frac{\partial w}{\partial z})^2 \tag{2.15}$$

The largest contributor to ϵ is thus $(\frac{\partial w}{\partial r})^2$ that accounts for 70% of the dissipation; the remaining 30% is equally split between $(\frac{\partial u}{\partial r})^2$ and $(\frac{\partial w}{\partial z})^2$. This is not surprising as the plume flow satisfies the boundary-layer equations. The equivalence of the latter two is also expected since from continuity $\frac{\partial w}{\partial z} = \frac{u}{r} + \frac{\partial u}{\partial r} \rightarrow \frac{\partial u}{\partial r}$, when r becomes large. As $|u| \leq 1$cm/s, the limit is reached rapidly beyond $r = 0$.

The time-averaged dissipation rate profiles for case A and B are shown in the right panel of figure 2.23. It should be noted that these values have not been corrected for under-resolved mean square velocity gradients due to limited spatial resolution. A correction method based on the universality of small scales (e.g. Pope 2000) will be presented in section 5, section 5.3. Using the proposed method, a correction factor equals to $1/0.65 = 1.54$ should be multiplied to data in case A; the ratio l/η, where l is the smallest resolvable spatial scale, is 2mm /0.135mm = 14.8. Going back to the figure, the radial profile of $\overline{\epsilon}$ is again well-fitted by a double-Gaussian curve whose

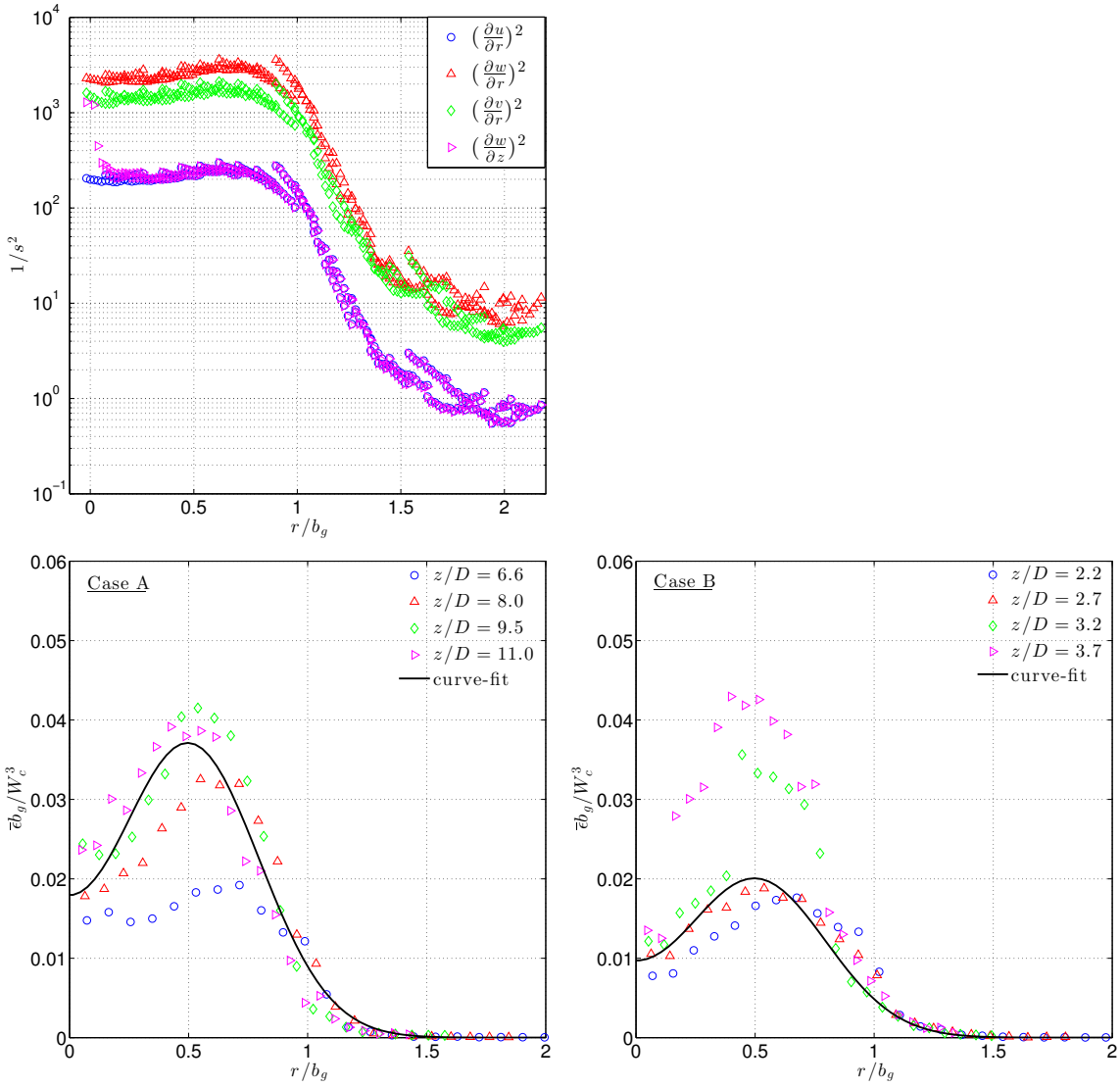

Figure 2.23: Time-averaged dissipation rate ϵ; profiles of mean-squares gradients at $z/D = 6.6$ (top left) and normalized profiles of unadjusted ϵ (bottom left and right)

equation is given in Appendix B.

2.5.7 Conservation of bulk kinetic energy

One way to check the overall accuracy of the measured TKE and dissipation is to perform a bulk kinetic energy balance. Such balance equation follows directly from the full unsteady Navier-Stokes equations and is derived for round jets/plumes using the integral framework in section 4. The equation for a two-phase bubble plume is given below.

$$(\frac{1}{2}I_1 + C_{I_2}I_2)[b_g^2(z)W_c^3(z)]_{z_1}^{z_2} = -b_g(z_1)W_c^4(z_1)(C_{I_3}I_3)\frac{\triangle z}{\overline{W}} + 1.36F_o \triangle z$$

The constants appearing in the equation are $(I_1, I_2, I_3) = (1.0472, 1.8128, 1.8691)$ and $(C_{I_2}, C_{I_3}) = (0.18, 0.037 \times 1.54)$ (the factor 1.54 accounts for underestimated $\overline{\epsilon}$); they are derived from the fitted curves to data. Consider a plume in its asymptotic regime, i.e. case A, at two elevations $z_1 = 8D$ and $z_2 = 9.5D$. This gives a difference in elevation $\triangle z = 10$cm, a plume kinematic buoyancy flux $F_o = 8165 \times 0.954 = 7789\text{cm}^4/\text{s}^3$ (the factor 0.954 accounts for compressibility of air at a water depth of 0.5m) and a mean advection velocity $\overline{W} = W_c/1.9$. The ratio formed by RHS/LHS of the equation equals $(-59565.5 \times 1.54 + 105936)/12876 = 14297/12876 = 1.11$; the energy budget is satisfied to within 11%.

2.5.8 Time-averaged TKE equation

In cylindrical polar coordinates, the balance equation for $k = \frac{1}{2}(\overline{w^2} + \overline{u^2} + \overline{v^2})$ reads

$$
\begin{aligned}
\underbrace{W\frac{\partial k}{\partial z}+U\frac{\partial k}{\partial r}}_{\text{Mean convection}} = & - \underbrace{\frac{1}{r}\frac{\partial}{\partial r}[r(\overline{ku}-\nu\frac{\partial k}{\partial r})]-\frac{\partial}{\partial z}[\overline{kw}-\nu\frac{\partial k}{\partial z})]}_{\text{TKE diffusion}} \\
& - \underbrace{\frac{1}{r}\frac{\partial}{\partial r}[r(\frac{1}{\rho}\overline{pu})]-\frac{\partial}{\partial z}[\frac{1}{\rho}\overline{pw}]}_{\text{Pressure diffusion}} \\
& - \underbrace{[\overline{wu}(\frac{\partial U}{\partial r}+\frac{\partial W}{\partial z})+\overline{w^2}\frac{\partial W}{\partial z}+\overline{u^2}\frac{\partial U}{\partial r}+\overline{v^2}\frac{U}{r}]}_{\text{Production due to fluid shear}} \\
& - \underbrace{P_B}_{\text{Production due to bubbles}} \\
& - \underbrace{\epsilon}_{\text{Dissipation}}
\end{aligned}
\tag{2.16}
$$

The physical interpretation of each term is labeled beneath the equation. All but the pressure-velocity correlation term have been measured in the experiments; the model put forward in Lumley (1978) is used to represent the missing pressure transport terms, $\overline{pv}=-\frac{2}{5}\overline{kv}$ and $\overline{pu}=-\frac{2}{5}\overline{ku}$. In their recent direct numerical simulation (DNS) on a round turbulent jet ($Re=2000$), Taub et al. (2013) assessed the model's validity and found that the predicted profile shape and magnitude (except for a shift of the profile peak) matched well with the simulated results.

The production of TKE due to bubbles is modeled by,

$$
P_B = C_B\alpha_g[\frac{3}{4}\frac{C_D}{d_{50}}(\overline{w_g-w_l})^2](\overline{w_g-w_l}) \tag{2.17}
$$

where C_D is the quasi-steady state drag coefficient, α_g the time-averaged air void fraction and $\overline{w_g-w_l}$ the time-averaged relative (slip) velocity of the two phases (subscript g and l refer to air and water respectively). The coefficient C_B is smaller than 1 and determines what fraction of total work done (energy) by bubbles is used to

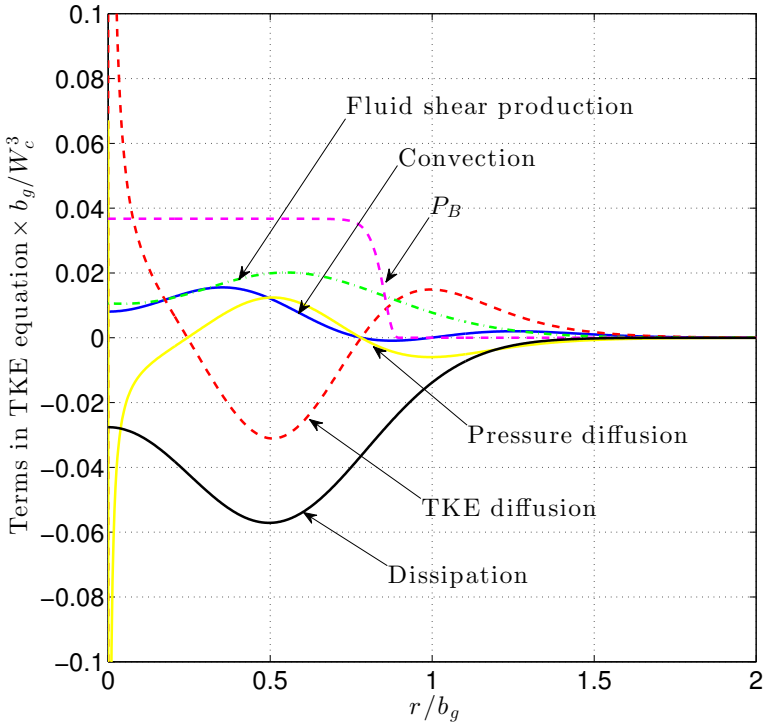

Figure 2.24: TKE budget of a bubble plume in the asymptotic regime ($z/D = 8$)

create fluid velocity fluctuations, hence, TKE. Its value is found from balance of the TKE equation. The relative velocity between phases is taken as the velocity differential $\mu_3 - \mu_2$ in §2.5.2; a curve-fit is applied to the data at $z/D = 8.0$. A constant value of 0.5% is taken for α_g across the plume. For C_D, a value of 0.634 is calculated for the ellipsoidal bubble based on a balance between fluid drag and bubble buoyancy force; the bubble Reynolds number Re_B based on terminal velocity and d_{50} is 576 (Clift et al. 1978).

Figure 2.24 shows the TKE balance at $z/D = 8.0$; a value between 0.55 and 0.6 is found for C_B. It can be seen that production by P_B is almost two times that by fluid shear inside the plume core. For $r/b_g < 1$, all contributing terms are relevant in the balance. Beyond $r/b_g > 1$, the balance is mainly between TKE diffusion, pressure

diffusion and dissipation.

2.6 Summary and discussions

This section has investigated experimentally the turbulent kinetic energy budget inside a time-steady air-water bubble plume in an unstraifitied and initially stationary ambient. The required three-dimensional fluid velocities have been measured by a new generation of acoustic Doppler velocimeters - Nortek's *Vectrino II* with profiling capability. It is heuristically shown that the measurements are physical and correspond to one of the following types, (i) bulk entrained flow, (ii) bubble wakes and (iii) return flow due to rising bubble. Across the plume, the entrained flow accounts for over 80% of the data while the remaining 20% is mostly contributed by the wake with the return flow being less than 1%. A wavelet analysis applied on the time series of streamwise velocity $\tilde{w}$ shows that bubbles are intermittently forcing the plume flow at frequencies of 10-15Hz. This range is in good agreement with Riboux's model on bubble-induced turbulence based on large-scale wake interactions (Riboux et al. 2013).

Empirical relationships relating the time-averaged streamwise centerline velocity W_c, the fluid phase Gaussian plume radius b_g and fluid phase volume flux Q to the source height z have been derived from present data. A remarkable collapse of data from different datasets, which include facilities one order of magnitude larger than present laboratory, is achieved when the gas phase slip velocity u_s and the dynamic length scale D (equation 2.1) are used to non-dimensionalize the variables. In the asymptotic regime ($z/D > 5$), the Gaussian plume entrainment coefficient equals 0.095 and the asymptotic plume Froude number takes the value of 1.63. Turbulence inside the multiphase bubble plume core ($r/b_g < 1$) is highly anisotropic with the stream-

wise intensity $\sqrt{\overline{w^2}}$ being 2.2-2.6 times as large the radial intensity $\sqrt{\overline{u^2}}$. Beyond $r/b_g = 1.5$, the turbulence appears to become globally isotropic, i.e. with equal variance among the three velocity components. The transport of TKE across the plume width is largely confined to $r/b_g = 1.2$. From the TKE budget, it is found that about 55-60% of the total work done by bubbles, P_B, is used to create fluid turbulence. The production by fluid shear and P_B are comparable across the plume.

The limitations of present study are the following. Our profiling ADV data mostly quantify the large-scale turbulent statistics; the second- and third-order velocity moments are controlled by large eddies (Pope 2000). Due to the high turbulence anisotropy, streamwise velocity spectra could not be easily obtained via Taylor's frozen turbulence approximation without an elaborate correction for the decay of turbulence (e.g. Hill 1996). The distribution of TKE in wavenumber space remains unknown. Further, because the data are limited to one-dimension in space the inter-scale energy transfer, which requires an evaluation of the third-order velocity structure function, could not be investigated. To circumvent these shortcomings, a new experimental program is reported in section 5. Specifically, a two-dimensional PIV system with a small camera field-of-view is used to measure the residual flow field left behind a bubble plume after an abrupt shut-off of the gas inflow. In this manner, no phase-discrimination is needed and computed velocity vectors are solely that of the liquid water; this has been used to study wake-wake interactions in a bubble column (Riboux et al. 2013). Obtained 2D data can then be used to study the velocity spectra and inter-scale energy transfer.

3. IMPLICATIONS OF SAMPLE AND HOLD INTERPOLATION ON SPECTRAL ESTIMATE OF GAPPY TURBULENT VELOCITY DATA

"Simplicity is the ultimate sophistication." - Leonardo da Vinci

3.1 Introduction

[1] Estimation of the turbulent dissipation rate ϵ is important in predicting sediment transport in the surf zone (Feddersen 2012), oxygen concentration in aeration projects (Wüest et al. 1992), initial bubble/droplet size distribution in bubble plumes and sub- sea oil well blowouts (Bandara & Yapa 2011), and in general turbulent mixing in the environment (Pope 2000). Analytically, determination of ϵ requires all nine components of the velocity gradient tensor to be measured at resolutions sufficient to resolve the smallest scales of turbulence, which is a daunting task even in well-controlled laboratory experiments. To overcome this obstacle, the assumption of isotropic turbulence together with Taylor's hypothesis is often made to infer ϵ from single point velocity measurements. This requires estimating the auto-spectral density function, hereafter referred as "spectrum", of the turbulent fluctuations; the spectrum is uniquely linked to the autocorrelation function ACF of the fluctuating velocities via the Fourier Transform and is evaluated numerically on a computer by the Fast Fourier Transform (FFT) algorithm. However, it often occurs in the screening of raw data that some outliers are identified that need replacement prior to FFT. The motivations for the present work originate from the authors' own laboratory velocity measurements in an air-aerated bubble plume using acoustic Doppler

[1]This work is a spin-off from the data analysis in section 2. In the early stage of research, despiking was thought to be necessary with data acquired by *Vectrino II* and the resultant gappy time series were ought to be filled by some form of data interpolation. The section presents an interpolation method that would preserve the underlying attributes of a turbulent velocity signal.

velocimetry (ADV). The current understanding within the ADV community is that bubbles cause erroneous velocity spikes to appear in the data, and the time series has to be reconstructed following removal of the spikes (this was shown not to be the case with *Vectrino II* in the section 2). It is important to ensure that the underlying true spectrum is unaltered after data replacement for otherwise reliable estimates of ϵ are not possible. We will demonstrate that the classical sample & hold (S&H) method is the simplest yet general and robust way to replace faulty data in order to obtain reliable estimates of the velocity spectra.

A related issue in data reconstruction is the creation of pseudo-turbulence – a white noise process appears to have a power-law dependence on frequency, an artifact well-known in the laser Doppler velocimetry (LDA) community(e.g. Adrian & Yao 1987). An LDA measures velocity only when a seeding particle is present inside the intersecting volume of laser beams, and since the arrival time of seeding particles follows a Poisson distribution, the sampling rate is non-uniform in time. Pseudo-turbulence is injected into the time series when these data are resampled to a constant sampling frequency by some form of aggregation or interpolation; velocity spectra estimation suffers from a filtering effect imposed by the mean particle arrival rate that leads to a biased spectral estimate (Adrian & Yao 1987). For measurement systems that uniformly sample in time, such as ADV and particle image velocimetry (PIV), such data resampling is not required. Data reconstruction, however, is needed when gaps exist in the record due to a poor measurement (e.g. outliers) or fluid voids (e.g. multiphase flows). The artificial autocorrelations introduced into the reconstructed time series then result in pseudo-turbulence whose form depends on the interpolation scheme adopted.

The simplest interpolation method is to substitute missing values by their preceding valid values, which is equivalent to the classical S&H method in the LDA literature. Because neighboring valid data points are combined in some manner to produce a value for the gap, this creates correlations that may or may not exist/agree with those in the original signal. The main task is then to select a scheme that approximates as close as possible to the true correlations, i.e. to preserve the ACF. This is, however, not a trivial task because usually one does not have prior knowledge on the true spectrum but only of the gappy data. Fortunately, turbulent signals usually show a power-law dependence on frequency over some intermediate range, e.g. the inertial subrange -5/3 scaling for isotropic behavior of the small scales (Pope 2000). A milder, -7/6, to a steeper, -8/3 slope are observed in bubbly flows (Bolotnov, Lahey Jr., Drew & Jansen 2008). We hypothesize that it is possible to preserve the true ACF using an interpolation scheme that gives a slope in the range of -7/6 to -8/3 provided that the fraction of gaps is not too excessive (here, limited to less than 25% of the measured time series).

This section is structured as follows. In § 3.2, we introduce the 1D wavenumber spectrum by (Pope 2000) to shed light on the properties of interpolation needed. Autoregressive modeling of stationary stochastic processes is then described and the first order AR(1) model is proposed as an appropriate interpolation scheme. It will be shown that the classical S&H method can be viewed as the limit of an AR(1) process with zero noise and its interpolation properties, thus, have theoretical underpinnings. Synthetic velocity signals based on the Pope spectrum are generated to illustrate the spectral-slope-preserving property of the full AR(1) model. In § 3.3, we outline the details of a more sophisticated interpolation method - POD-reconstruction ((Venturi & Karniadakis 2004)); it will be used here to compare with the AR(1) modeling. In

§ 3.4, we give the details of isotropic turbulence experiments performed in an open channel. Velocity measurements have been made with a profiling acoustic Doppler velocimeter (ADV). In § 3.5, we insert random gaps into the real ADV data and subsequently fill in the data gaps by both interpolation methods. The effects of data gap fraction and gap duration are investigated. Comparison of their performance is made with the ACF as it has a one-to-one correspondence to the spectra via FFT. S&H will be shown to be the simpler yet robust method to preserve the shape and magnitudes of the spectra in situations where gaps occur in isolation. For gap clusters, the full AR(1) model should be used instead. This section ends with a discussion on the S&H method in relation to other commonly used interpolation schemes.

3.2 Velocity spectra estimation from gappy data

3.2.1 Spectrum of turbulent flows and its ACF

To gain insight into the kind of interpolation sufficient to preserve the ACF attributes of a data time series, we consider a model spectrum representative of turbulent flows. The 1D wavenumber spectrum by Pope (2000) shows a clear -5/3 power scaling over intermediate frequencies and an exponential decay in the high frequencies, i.e. in the dissipation range. A synthetic time series can be generated based on the model and we follow the approach given in Garcia et al. (2005) (details in Appendix). The sample spectrum is shown together with the model in figure 3.1(a); good agreement is observed up to the Nyquist frequency, as expected. The corresponding ACF, which is the inverse Fourier transform of the model spectrum, is shown in 3.1(b), and it can be seen that it is on the whole well-fitted by a first-order exponential decay of the form $e^{-h\triangle t/I_t}$, where h = 0, $\pm$1, $\pm$2, ..., $\triangle t = 1/f_s$, f_s = sampling frequency, and I_t = integral time scale. It should be understood that the exponential fit in 3.1(b) does

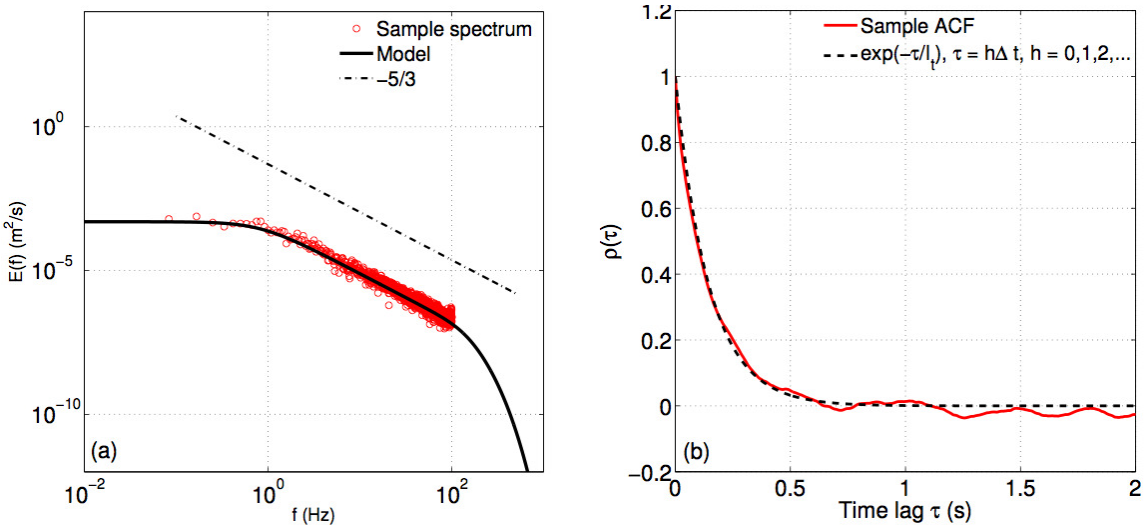

Figure 3.1: (*Left panel*) Sample spectrum of a synthetic time series generated based on the 1D wavenumber model spectrum in Pope (2000); model inputs L=0.1m, η=10^{-4}m, U_c=0.2m/s, f_s=200Hz (*Right panel*) Corresponding ACF of the time series

not conform to a parabola near the origin, i.e. small time lags, and as a result the dissipation range cannot be approximated. This is, however, not a serious constraint because only the power-law dependence over intermediate frequencies is needed to be preserved for dissipation rate estimations.

3.2.2 Data interpolation with autoregressive AR(1) models

The class of autoregressive (AR) models is used extensively in time series analysis. Its ability and flexibility to approximate the underlying autocorrelation function (ACF) of a given real, stationary time series render model forecasting possible (Shumway & Stoffer 2010). Data interpolation is effectively the same as in-sample forecasting. Here, we consider the class of causal and invertible AR models because they have (i) stationary statistics for all moments and (ii) an explicit expression of the ACF. The general expression of an AR(p) process is,

$$y_i = \phi_1 y_{i-1} + ... + \phi_p y_{i-p} + w_i \tag{3.1}$$

where y_i is the data point at the i-th time step and $w_i \approx (0, \sigma_w^2)$ is a white noise process with zero mean and variance σ_w^2 . The model (constant) coefficients ϕ_i have to lay inside the unit circle centered at the origin to give property (i) and (ii) ((Shumway & Stoffer 2010)).

When p = 1, we have a causal AR(1) process. Its expression and ACF $\rho(h)$ are,

$$y_i = \phi_1 y_{i-1} + w_i, |\phi_1| < 1 \tag{3.2}$$

$$\rho(h) = \phi_1^h, h = 0, \pm 1, \pm 2, ... \tag{3.3}$$

Note that the superscript h denotes the power of ϕ_1. The ACF decays exponentially to zero at large values of h as $|\phi_1|$ <1. Equation (3.3) can be rewritten in the equivalent form $\rho(h) = e^{-h\triangle t/I_t}$ and it follows immediately that ϕ_1 is exactly equal to correlation at the first lag $e^{-\triangle t/I_t}$, which is an analytical result of the AR(1) model (Shumway & Stoffer 2010). It remains to determine the analytical form of its spectrum which is readily found from the Fourier transform of the exponential function $g(t) = e^{-at}$. This yields $F(f) = \frac{2a}{a^2+4\pi^2 f^2} \sim f^{-2}$ which is only slightly steeper than the isotropic scaling i.e. a -5/3 slope. $F(f)$ = Fourier transform at the frequency f and $a = \frac{\triangle t}{I_t}$. Note that the multiplicative constant 2 is different for different definitions of the Fourier transform, which is here defined as $F(f) = \int_{-\infty}^{\infty} e^{-2\pi i f t} g(t) dt$.

An interesting result appears if the noise term is dropped in equation (3.2); this is equivalent to in-sample forecasting using the AR(1) model. The model then becomes $y_i = \phi_1 y_{i-1}$, which says the current value is some fraction of the preceding value as $|\phi_1| < 1$. As $\phi_1 \to 1$, the sample and hold (S&H) method is recovered in the limit

- that is, the simple zeroth order interpolation can be interpreted as the application of AR(1) modeling. From equation (3.3), we showed that $\phi_1 = e^{-\triangle t/I_t}$ = correlation at the first lag. The limit of applicability then implies $\triangle t/I_t < 1$. This meets our physical intuition; when a flow is sampled at a frequency much higher than its rate of evolution it appears to be frozen in consecutive data points. This is indeed the basis of the S&H method originally adopted for LDA. In sections that follow, the efficacy of the AR(1) model as an interpolation scheme is investigated with synthetic gappy times series having known spectra. We will call the full AR(1) model the one for which ϕ_1 is the true correlation at lag 1 and the S&H method the limit of an AR(1) model with $\phi_1 = 1$. We will show that AR(1) models are general and robust methods in preserving spectral slopes commonly observed in turbulent signals. Higher order models i.e. $p > 2$ will not be considered as they have sharp spectral peaks; they are more like a narrow-banded spectrum when compared to the broad-banded Pope spectrum.

As a heuristic justification for the above, autoregressive modeling of the synthetic turbulent time series has been done with the statistical package R (official website at www.r- project.org). AR models of order p = 1-5 were tested. The best model is one that has a high goodness-of-fit while limiting the number of independent variables at a minimum i.e. to avoid over-parametrization. For this purpose, the Akaike information criterion (AIC) and Bayesian information criterion (BIC) are two commonly used metrics (Shumway & Stoffer 2010). Table 3.1 shows the values of each indicator for the models tested; the smaller (more negative) the value, the better the model. It can be concluded that the model only improves very marginally when one more variable i.e. $y_{i-(p-1)}$ is added. The AR(1) model stands out as the simplest method.

Model order p	AIC	BIC
1	-6.966	-7.965
2	-6.979	-7.978
3	-6.996	-7.995
4	-6.996	-7.995
5	-6.997	-7.996

Table 3.1: Comparison of AR(p) models for representing turbulent flows - values of AIC and BIC indicators

3.2.3 Verification of the proposed AR(1) interpolation

3.2.3.1 Generation of synthetic ADV time series with known spectra

Raw ADV data follow a simple *signal + noise*, $u(t) = v(t) + w(t)$ model as the major noise component, the Doppler noise, is white and uncorrelated with the velocity (Voulgaris & Trowbridge 1998). To simulate such data, the signal $v(t)$ with known spectral characteristics is generated from the Pope model spectrum (details given in Appendix C). The noise $w(t)$ is calculated based on a signal-to-noise ratio that compares variance (energy) of the signal to that of noise i.e. SNR $= \frac{\overline{v^2}}{\overline{w^2}}$. To obtain $w(t)$, a Gaussian white noise $w_G(t)$ with zero mean and unit variance $\sigma^2 = 1$ is first generated which has a variance different from the required value defined by $\frac{\overline{v^2}}{SNR}$. The difference can be SNR made up for if $w_G(t)$ is multiplied by a constant factor C. For $w_G(t)$, its variance is $\overline{w_G^2} = \frac{1}{T}\int w_G^2(t)dt$ where T = sampling duration. Then, C can be found by the equation $C = \sqrt{\frac{\frac{\overline{v^2}}{SNR}}{\overline{w_G^2}}}$, and we have $w(t) = Cw_G(t)$.

To mimic data drop-out, gaps are inserted into the synthetic time series based on a random number uniformly distributed between zero and one. Let s denote the percentage of gaps required, say 20%, then whenever the value of the random number is less than 0.2 at a data point, a gap will be inserted. It is recognized that this

algorithm is the simplest form possible; it generates isolated data gaps with a brief duration that spread out across the full record. This can happen in actual flows when strayed individual air bubbles pass through the sampling volume of an ADV. For the sake of presentation, the comparison shown in the rest of this section will employ this simple algorithm. The harder problem of clustering data gaps with an expected mean duration will be treated in § 3.5 using measured ADV data.

3.2.3.2 Comparison

We first demonstrate the pseudo-turbulence caused by an AR(1) or sample and hold interpolation scheme. Figure 3.2(a) shows the comparison of spectra obtained from a continuous white noise process (zero spectral slope) and from its discontinuous version with 50% of gaps added, and then filled by S&H. It can be seen that the interpolation scheme causes a spurious spectral slope resembling the -5/3 at high frequencies; whereas, it increases the energies at low frequencies. The latter is the result of holding a preceding valid value for gap filling which acts to create a non-zero mean flow. Note that according to Eq.(2.4) the artificial slope should equal to -2 but may not be distinguishable from the -5/3 due to the randomness of data. Similar comparison for a 25% gap is shown in (b). In this case the spurious spectral slope is much attenuated, suggesting that a good approximation can be achieved if the fraction of bad data is low. However, the energy is still increased by gap filling.

The comparison for the synthetic ADV time series with spectral slopes -7/6, -5/3 and -8/3 is shown in figure 3.3. The case of a 25% data gap is adopted as the worst case scenario; actual laboratory data has gaps $\geq$ 20% (see later sections). It can be seen that all of the actual spectral slopes are preserved and only a small bias is introduced into the high frequencies in the case of a -8/3 slope. The energy at

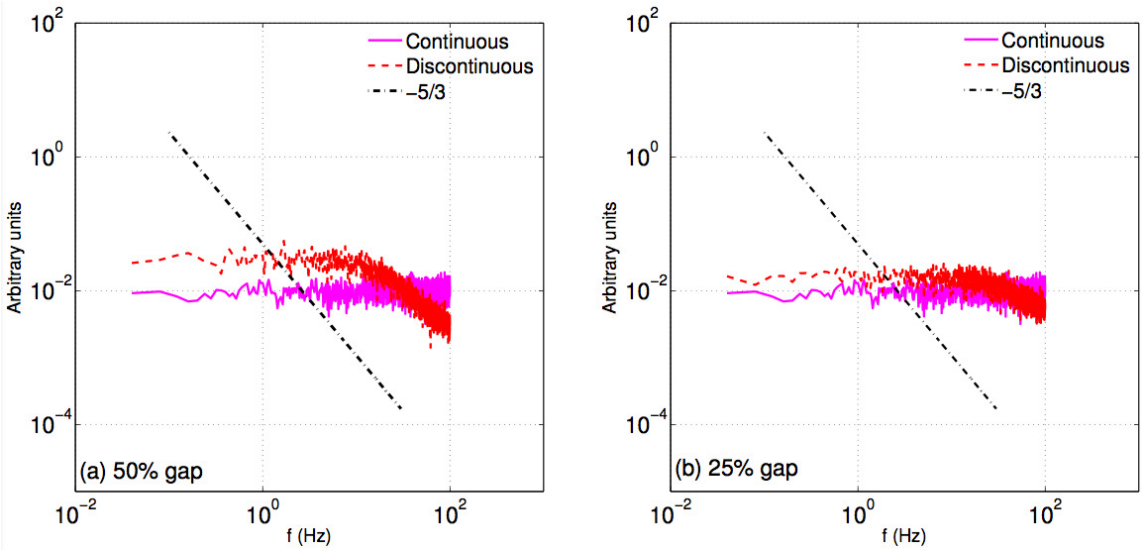

Figure 3.2: Spectrum of a Gaussian white noise process, continuous *Vs* reconstructed series by AR(1) modeling; time series shown are not physical quantities and thus have arbitrary units

each frequency also remains approximately the same. Returning to figure 3.2, this may seem a bit surprising at first since the AR(1) model injects energy to the low frequency end of a white noise process but does not result in a discernible increase for turbulent signals. This can be understood by acknowledging that a white noise has absolutely no (zero) correlation with itself at lags larger than zero. Holding a preceding value changes this property entirely and results in much augmented energy levels at the low frequency end. However, in a turbulent signal, non-zero correlations exist at all lags and it shares a similar ACF with an AR(1) process, and hence, the energy injection is not significant. More details can be found in the Result section, below.

3.3 Interpolation based on proper orthogonal decomposition

In this section we contrast our proposed AR(1) interpolation scheme with a more sophisticated interpolation method. For this purpose, we have elected to use the reconstruction method based on proper orthogonal decomposition POD (Everson &

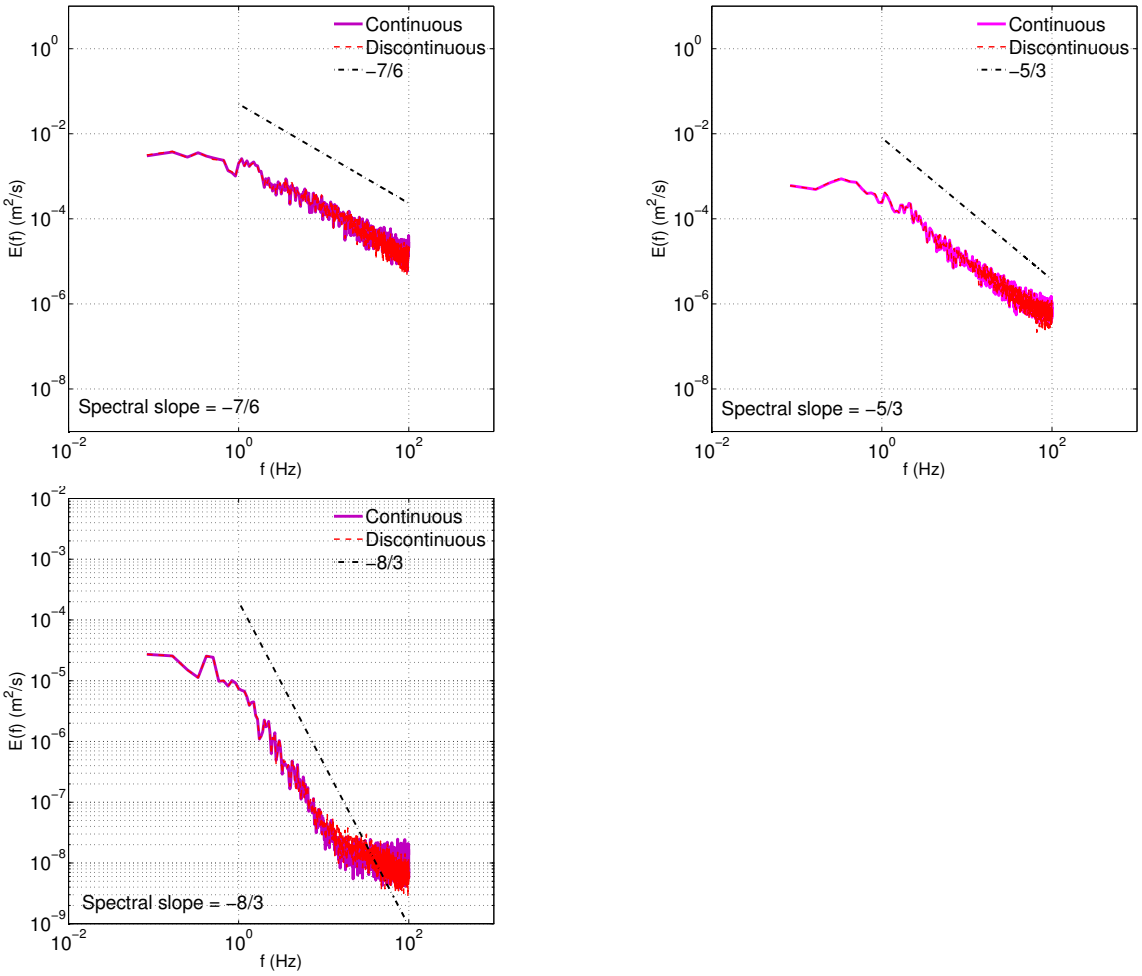

Figure 3.3: Spectra of turbulent signals with known spectral slopes, continuous Vs reconstructed series by AR(1) modeling (25% gap, SNR = 20, L=0.1m, η=10^{-4}m, U_c=0.2m/s and f_s=200Hz)

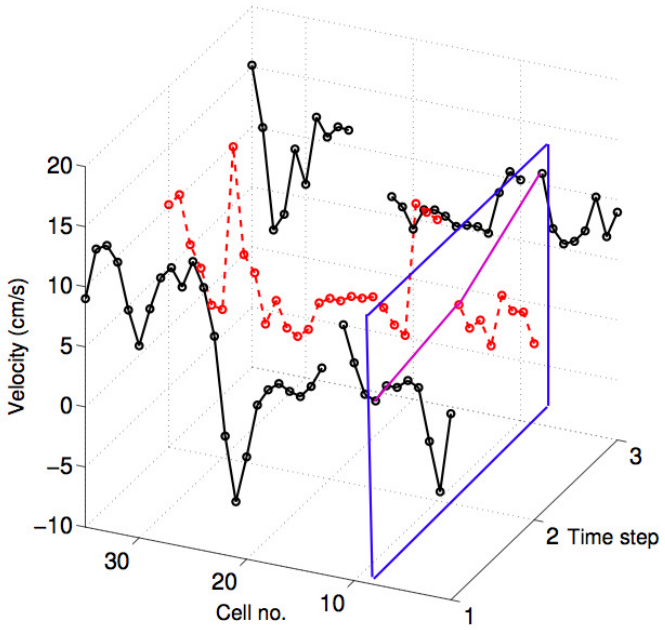

Figure 3.4: POD-reconstruction - deterministic data interpolation using both space and time information; rectangular box indicates a time series measured at a fixed point in space

Sirovich 1995). A reconstruction of the incomplete (created artificially from full data) velocity field is possible because of the spatio-temporal data measured by *Vectrino II* (see figure 3.4 and details are given in §3.4) and we apply the extended procedure proposed in Venturi & Karniadakis (2004). A brief outline of the extended POD reconstruction procedure is described below.

In the standard Everson-Sirovich procedure, the gappy spatio-temporal data are first filled by a local time-average after which the complete dataset is subjected to a POD analysis to obtain the initial guessed spatial modes $\{\phi(\mathbf{x})\}$. The next step is to reconstruct the whole date field with the first M eigenmodes along with their unknown time-varying coefficients $\{\xi(t)\}$. The $\{\xi(t)\}$ are solved via a least squares (LS) minimization on the difference between the original dataset and the reconstruction at

those points that are known and valid. A new vector field $w(\mathbf{x}, t)$ is obtained and is used to substitute the initial guess. The procedure is repeated until a predefined level of convergence has been achieved. It should be noted that the procedure will not work if data are missing in the entire spatial domain or if there exists subregions where data are absent for all times. Venturi & Karniadakis (2004) pointed out that the procedure's accuracy and effectiveness relies undesirably on the initial guess. They proposed an extension such that M at each iteration increases stepwise, starting from 2 then 3 and so forth, until the eigenspectrum does not change any further. Using a set of DNS data, their results show that the maximum number of accurately resolved modes is higher and independent of the initial guess. In addition, the extension performs better than local Kriging methods in minimizing the L^2-norm of the reconstruction error.

During LS minimization, the covariance matrix of predictors, whose elements are correlations of the orthonormal POD modes, can at times become ill-conditioned, i.e., close to being singular because of the gappy data points. Solving the linear system in the usual way will cause $\{\xi(t)\}$ to take on non-physical extreme values and hence a wild reconstruc- tion of the velocity field. To eliminate this problem, the ridge regression also known as the Tikhonov regularization is used (Horel & Kennard 1970). A small positive trace $k\mathbf{I}$ is added to the covariance matrix where k $\geq$ 0 and $\mathbf{I}$ = identity matrix. This amounts to impose an upper bound to the square norm of the $\{\xi(t)\}$ column vector which effectively limits their possible range of values. Larger k imposes a stronger bound and kills off all $\{\xi(t)\}$ in the limit; a zero solution will be obtained. We have chosen k = 0.01 after some trial and error such that the reconstructed velocity data is within three standard deviations from the mean estimated from the probability density function of the valid data points.

A similar approach is also implemented in local Kriging methods (Lophaven, Nielsen & Sondergaard 2002).

3.4 Laboratory experiments

Real data of approximate decaying grid turbulence have been obtained in a recirculating water flume located in the Fluid Dynamics Laboratory at Texas A&M University.The flume is 30 m-long, 0.9 m-wide and is filled to a water depth of h = 25.5 cm. Flow inside the flume is driven by a centrifugal pump. To create a reasonably uniform current, two arrays of straight PVC pipes were placed at the beginning section of the flume. Each pipe has a length of 0.75 m and a diameter of 3 cm, forming a 1.5 m-long flow straightening region. A horse-hair mat was also placed in front of the flow straighteners to further break down the flow structures at the flume inlet. The downstream end of the flume is a sloping beach lined with dissipative elements to damp out reflected surface waves. The painted steel bottom of the flume is estimated to have a roughness height of 1-3 mm.

Three-dimensional velocity measurements have been made using a Norterk *Vectrino II* ADV at the mid-section of the flume. This ADV is capable of measuring velocity profiles over a stretch of 35 mm (as of present writing) at a user-defined spatial resolution of 1-4 mm and at a temporal frequency up to 100 Hz (Craig et al. 2011). The probe was mounted on a motorized vertical traverse (Zaber technologies) for making measurements at different elevations above the flume bottom. Six vertical profiles, with a 5 mm overlap, were made to cover the water depths between 0.7 to 20 cm. For an ADV, Garcia et al. (2005) showed that if the dimensionless frequency $F = f_s L/U_c > 20$, where f_s = sampling frequency, L = size of energy containing eddies and U_c = convective velocity, over 90% of the total turbulent kinetic energy

is captured and the energy aliased from frequencies above the Nyquist frequency is negligible. This criterion was satisfied in the experiments by choosing $f_s = 100$ Hz with $L \approx h$, the water depth, and $U_c \sim 0.3$ m/s. These values give a dimensionless frequency $F = 85$. During the experiments, the two metrics correlation and signal-to-noise ratio, that indicate the quality of ADV measurements were always better than 95% and 15, respectively.

Figure 3.5 shows the vertical profile of mean streamwise velocity U in both natural and wall coordinates. The shear velocity U_τ was estimated from the velocity profile by a curve fit using the log-law of wall; only data in the inner region were included (see right panel in figure 3.5). U_τ was found to be 1.34 cm/s which gives a Reynolds number $Re_\tau = \frac{U_\tau h}{\nu} = 3800$. The profile of normalized Reynolds shear stress $-\overline{uv}/U_\tau^2$ is shown in figure 3.6; a reasonably good agreement can be seen between the data and the theoretical linear profile of fully-developed 2D open-channel flows (Nezu & Nakagawa 1993). It is noted that these results were obtained using a sampling duration of about 5.5 mins.

3.4.1 Doppler noise estimation and noise-reduced estimates of the stress tensor

It is known that raw ADV data obtained from flows without any physical obstructions are accurate in computing the mean flow field while turbulent statistics are highly biased by Doppler noise which must be estimated and removed from measurements (e.g. Voulgaris & Trowbridge 1998, Garcia et al. 2005). For a four-receiver bistatic probe like the *Vectrino II* employed here, the redundant vertical (along transmitter direction) velocity $v2$ can be used together with $v1$ to compute directly the Doppler noise. Noise-reduced estimates of the stress tensor can then be obtained after accounting for probe geometry (Hurther & Lemmin 2001) and such correction has been

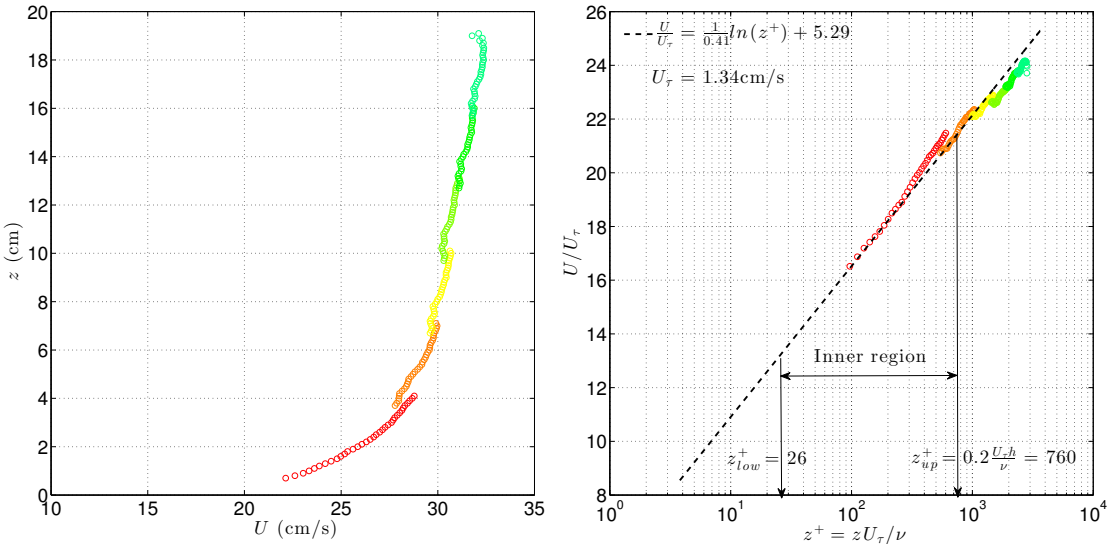

Figure 3.5: Mean streamwise velocity U at flume mid-section (water depth $h = 25.5$cm)

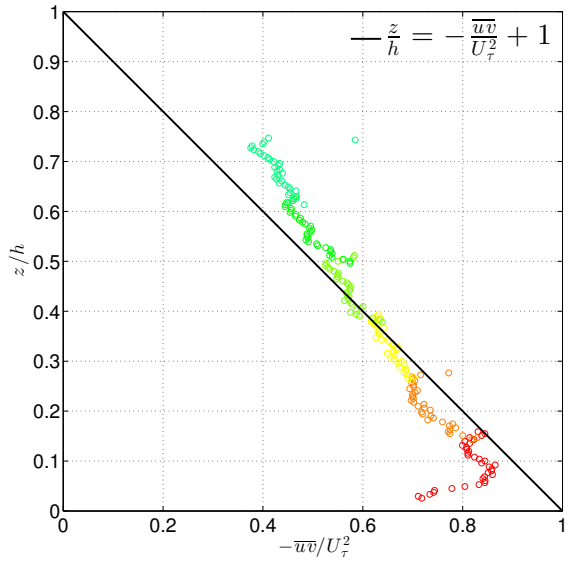

Figure 3.6: Vertical profile of turbulent shear stress

applied to our raw data.

3.5 Results

In order to obtain converged velocity spectra in isotropic turbulence, measurements at elevations 9.7-13.1 cm (0.38<z/h<0.52) were repeated for a sampling duration of 22.5 mins. These elevations were well above the wall region and the flow could be considered approximately as that of decaying turbulence. The time series at z = 12.1 cm that corresponds to a single bin in the velocity profile is used here since this bin is the "sweet spot" of the ADV where data quality is the best. The full record was subdivided into 240 equal segments in time, each measuring 5.63 s in duration. This time space is 13 times and 42 times the Eulerian integral time scale in the streamwise and vertical direction, respectively (see later discussion). Using FFT, estimates of the velocity spectra in time were calculated from each time interval, which were then ensemble averaged to give the final result. The averaging gives a degree-of-freedom of 480 for the chi-square distributed spectral energy density, $E_{ii}(f)$, which is sufficient to yield well converged spectra.

Invoking Taylor's hypothesis, wavenumber spectra can be obtained from the measured temporal spectra. Figure 3.7(a) and (b) show respectively the velocity spectra $E_{ii}(k_1)$ and their normalized compensated forms in the longitudinal (streamwise) wavenumber space k_1. In the streamwise direction, the latter reads (Pope 2000)

$$\epsilon^{-2/3} k_1^{5/3} E_{11}(k_1) = 0.5 \tag{3.4}$$

In both vertical and cross stream directions, it reads

$$\epsilon^{-2/3} k_1^{5/3} E_{22or33}(k_1) = (4/3)0.5 = 0.67 \tag{3.5}$$

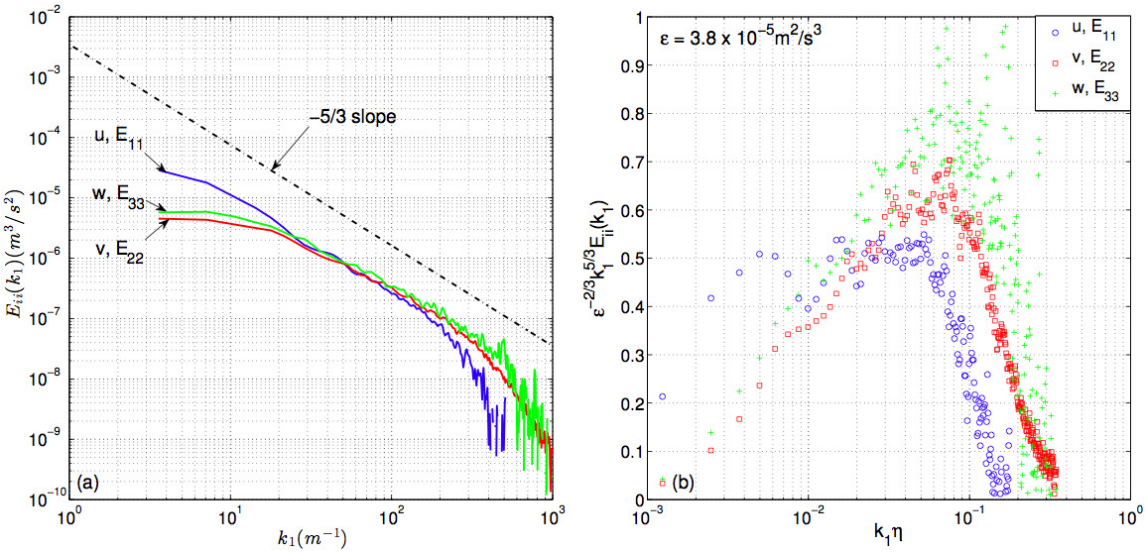

Figure 3.7: Turbulent velocity spectra of approximate isotropic turbulence in a re-circulating water flume at z = 12.1cm

It is clear that an inertial sub-range exists in all three components of velocities and that the stated isotropic relationships are largely satisfied by a turbulent dissipation rate $\epsilon = 3.8$ x $10^{-5}m^2/s^3$. The Kolmogorov length scale $\eta = (\frac{\nu^3}{\epsilon})^{1/4}$ is 0.37 mm.

In § 3.2, we demonstrated that S&H can be viewed as a simplified version of the full AR(1) model and its accuracy, relative to AR(1), is dependent on the ratio $1/f_s I_t$; the simplification is less accurate for a larger ratio. Physically, this means that as the sampling frequency decreases the flow can no longer be assumed to take on its preceding value. To illustrate these ideas and to explore how robust S&H can be, the original velocity time series sampled at 100 Hz have been down-sampled to 50 Hz, 25 Hz and 10 Hz; this is done by removing every second, fourth and tenth data point in the original dataset. It should be noted that the artificial time series obtained in this manner would be different from actual ADV measurements taken at these sampling frequencies because the actual internal sampling rate is different. The instantaneous velocities would be different but the flow structures would remain the same. Random

and isolated data gaps are then created in these time series in a fashion similar to the synthetic series in § 2.3. The gaps are subsequently filled by either the full AR(1) model or S&H; the full model refers to $y_i = \phi_1 y_{i-1}$ where $\phi_1 = e^{-1/f_s I_t}$ whereas S&H takes $y_i = y_{i-1}$. In the result comparison below, only the autocorrelation function will be shown since the auto-spectral density of velocity is uniquely linked (a one-to-one correspondence) to it via the FFT.

Figures 3.8 and 3.9 show the down-sampled (at $f_{artificial}$) ACF of the streamwise and vertical velocity respectively. The Eulerian integral time scale It is calculated as the area under the curve up to the first zero-crossing on the time lag axis; numerical integration is carried out by the rectangle rule (midpoint rule). As expected, It increases with decreasing sampling frequency due to a coarser representation of the full ACF. Except for the extreme case of 10 Hz sampling rate, the relative difference with reference to I_t at 100 Hz is within +12%. I_t in the vertical is about one-third of the corresponding value in the streamwise direction and is equal to 0.134s.

Because $\phi_1 = e^{-\triangle t/I_t}$ deviates more from unity for a smaller I_t, the vertical velocity v represents a more demanding test to the proposed AR(1) model. Figure 3.10 shows the ACFs computed from gap-filled time series of v. First, we note that as the sampling frequency $f_{artificial}$ decreases the difference in the correlation value computed by each interpolation scheme increases. This is most evident for small lags i.e. rapid turbulent fluctuations. The values for large lags, i.e. energy containing scales, are essentially the same across all $f_{artificial}$ and methods. This is easily understood by noting that rapid fluctuations that appears as spikes in the time series have negligible contributions in the correlation integral evaluated at large time lags. Second, we can see that at 25 and 10 Hz the full AR(1) model actually performs better than S&H

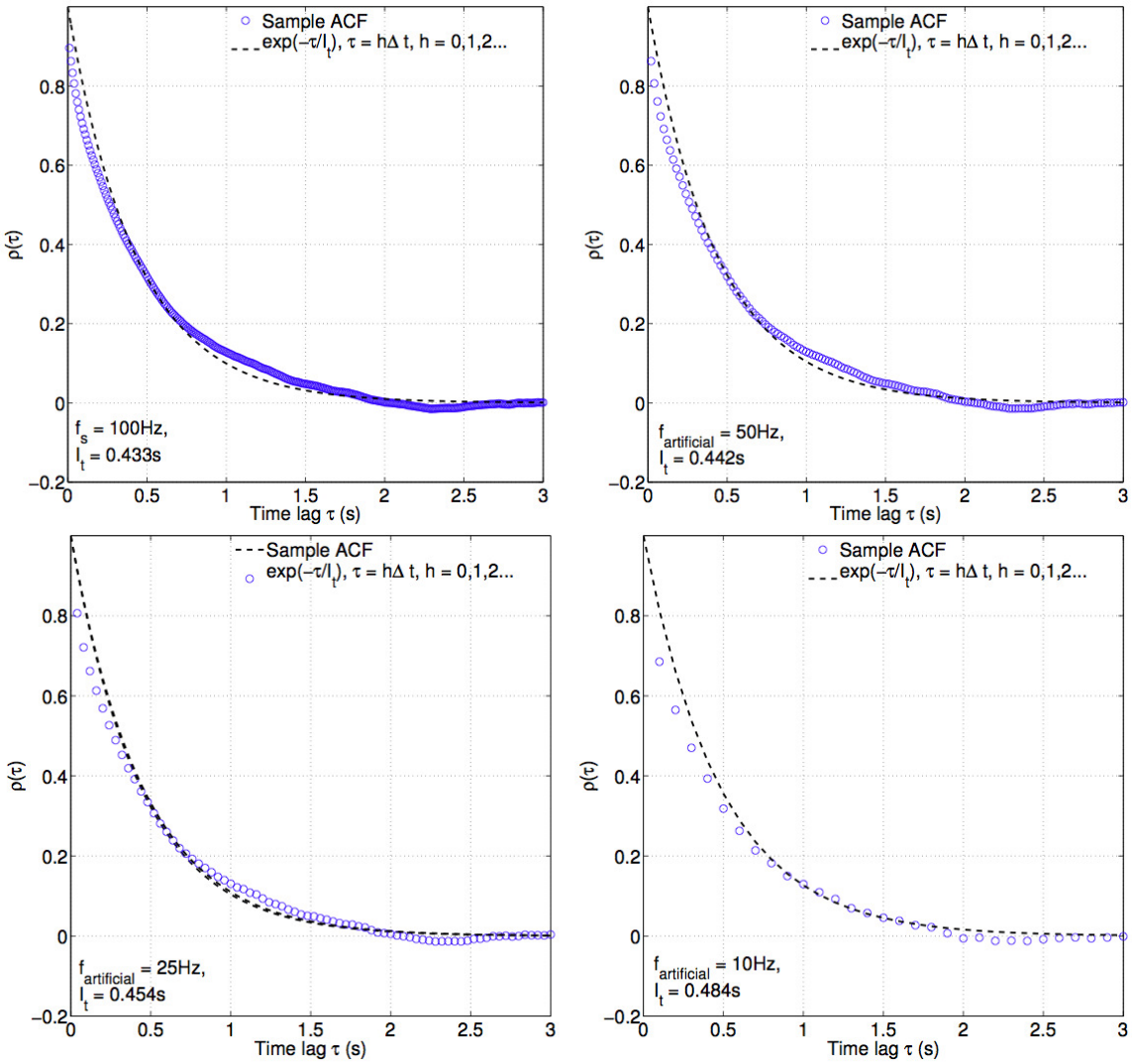

Figure 3.8: Autocorrelation function (ACF) of streamwise velocity u as a function of sampling frequency f_s ($f_{artificial}$)

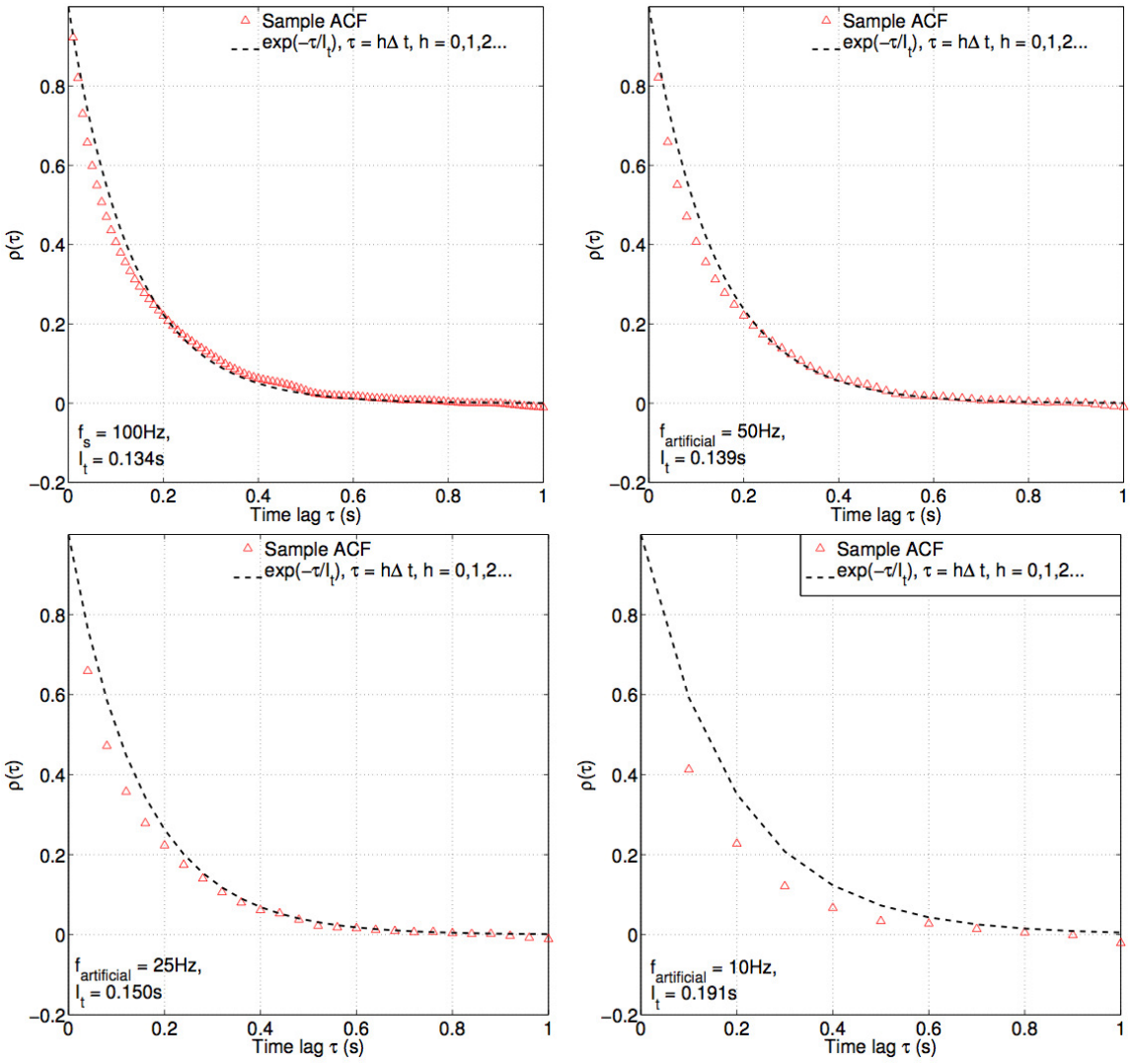

Figure 3.9: Autocorrelation function (ACF) of streamwise velocity v as a function of sampling frequency f_s ($f_{artificial}$)

in preserving the correlation values (being closest to the no-gap result); the case at 50 Hz presents no visual difference at all between the two. This reflects the fact that velocities will have changed between consecutive samples when the sampling frequency is low. The AR(1) model allows for this change and, hence, gives better agreement, although it is not perfect. Third, it can be concluded that S&H can be used safely in lieu of the full model in most, if not all, situations, its performance improves as the sampling rate increases.

Comparisons shown in figure 3.10 are for isolated data gaps that occur randomly throughout the full record. A more complicated situation arises when data gaps come in clusters, blocking a considerable duration of the flow. To investigate this possibility, the data gap generation algorithm in section §3.2 is modified. A Poisson distribution with the parameter λ is used to characterize the cluster durations. The beginning of a cluster is decided based on a seed set by a random number in [0,1]. To facilitate comparison with the results of isolated gaps, the total percentage of gaps added was set at 19%. For $\lambda = 6$, a seed is set at a data point whenever the random number is larger than 0.95; a larger λ requires a larger random number so as to maintain the total gap fraction. Figure 3.11 shows the effects of interpolation on the ACF of data sampled at 100 Hz with clustering data gaps added. It can seen that for a mean gap duration less than one integral time scale (λ = 6,12), both S&H and the full AR(1) model perform about the same. In contrast, when the mean gap duration is larger than one integral scale (λ = 24, 48), the performance of the full model is superior. This difference can be better appreciated by looking at an example of the reconstructed time series shown in figure 3.12; S&H cannot adjust for the decorrelation between consecutive samples when the mean gap duration is larger than I_t.

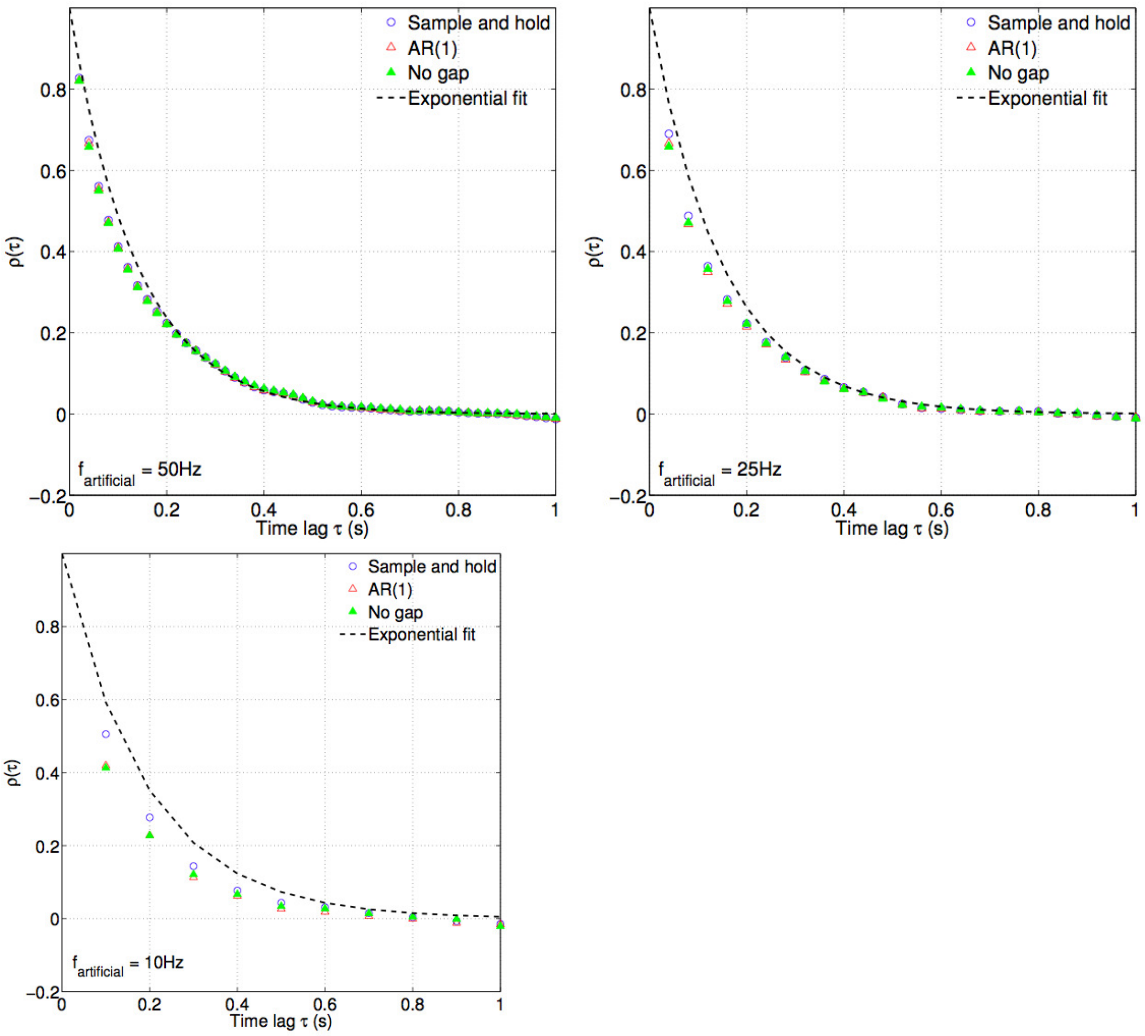

Figure 3.10: Autocorrelation function (ACF) of v with 20% artificial data gaps occurring in isolation as a function of sampling frequency f_s ($f_{artificial}$)

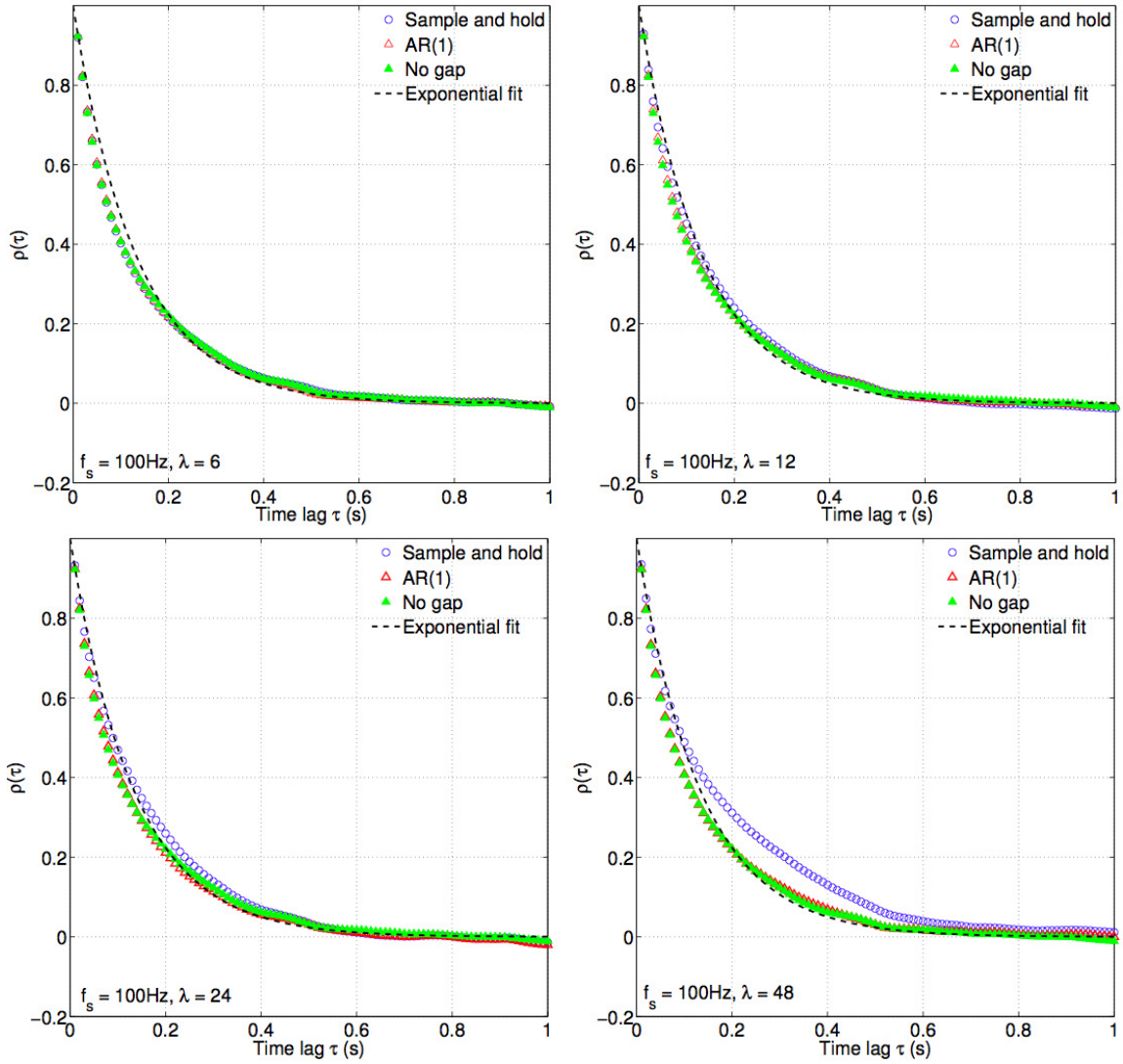

Figure 3.11: Autocorrelation function (ACF) of v with 19% artificial data gaps occurring in clusters as a function of the mean gap duration = ($0.45I_t$, $0.90I_t$, $1.79I_t$, $3.58I_t$) for λ = (6,12,24,48)

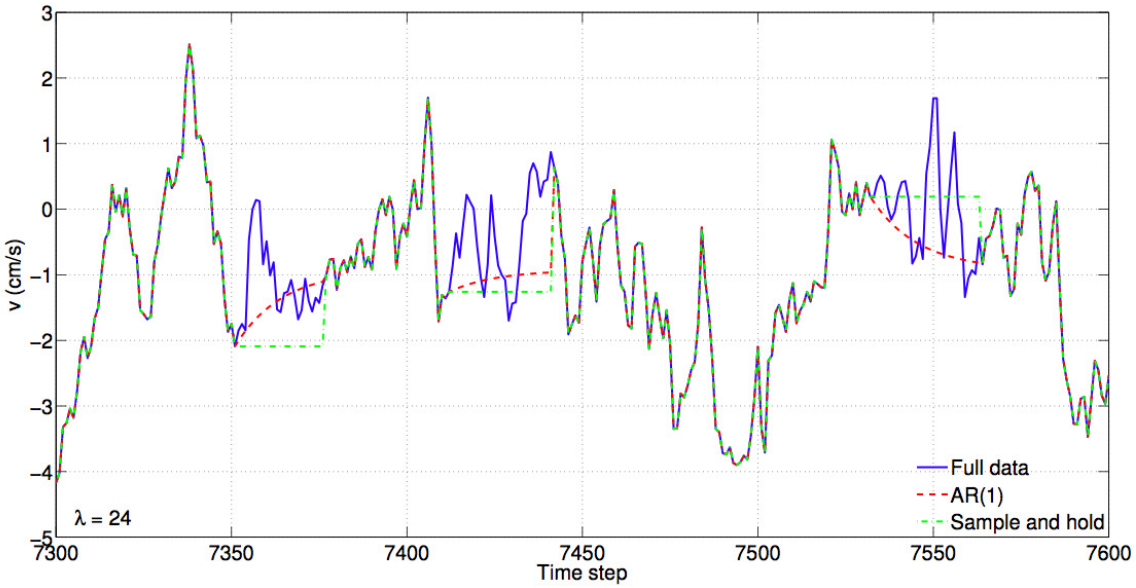

Figure 3.12: Reconstructed vertical velocity v with 19% artificial data gaps occurring in clusters; mean gap duration characterized by $\lambda = 24$

3.5.1 Gappy data reconstruction - POD-reconstruction Vs sample and hold

Figure 3.13 shows a one-second segment of the velocities, u and v, to illustrate the performance of both the S&H and POD interpolation schemes at reconstructing the observed but randomly removed data (at a gap rate of 20%). Isolated data gaps with brief interruption periods are considered. The POD-reconstruction uses both spatial and temporal information across the whole velocity profile to fill in the artificial data gaps. Only the single bin corresponding to the "sweet spot" of the ADV probe had been added with gaps whereas the rest of the bins in the profile contained full records of the data. It is apparent that both schemes give realistic velocities; nothing too small or too large had been inserted into the gaps. This is natural for S&H as it uses a preceding value. The advantage of POD-reconstruction is also evident in the figure; it generally reconstructs the instantaneous fluctuations better in terms of both magnitude and direction. This is a consequence of its deterministic nature in using both spatial and temporal information obtained from the *Vectrino II* to reconstruct

the missing flow field.

Figure 3.14 shows a comparison of the autocorrelation functions derived from the reconstructed time series and the full record (ridge regression coefficient $k = 0.01$ in the POD-reconstruction). It can be seen that both methods give virtually identical results although the POD-reconstruction appears to perform slightly better at very small time lags (see streamwise velocity u). The relative difference over the entire range of time lags is, however, well within $\pm 0.5\%$. This insignificant difference can be understood by reckoning the fact that ACF is an ensemble (time) averaged quantity. Since the true ACF of u and v are exponentially decaying (figure 3.8 and 3.9) and S&H or AR(1) models are tailored to give such an ACF, it is not surprising to see the models perform almost the same as POD-reconstruction which, as shown in figure 3.13, reconstructs better the instantaneous velocities.

3.6 Summary and conclusions

The reconstruction of gappy velocity time series is not a new problem in the research of fluid mechanics and many interpolation methods are routinely in use; from simple linear algebraic methods, such as S&H, to non-linear methods, such as polynomial fits and spline curves, then to sophisticated methods that account for correlation structures of the field variable, such as Kriging and POD-reconstruction. It is difficult to compare the performance of these different methods of varying complexities due in large part to (i) a lack of an objective function and (ii) different definitions on the degree of success; for example, while Kriging and POD-reconstruction minimize the error in the mean-square sense (L^2-norm) across the whole flow field, interpolation using polynomials like those of Lagrange can be shown to be exact (L^1-norm of error is zero) under appropriate conditions. Compounding with these reasons is that

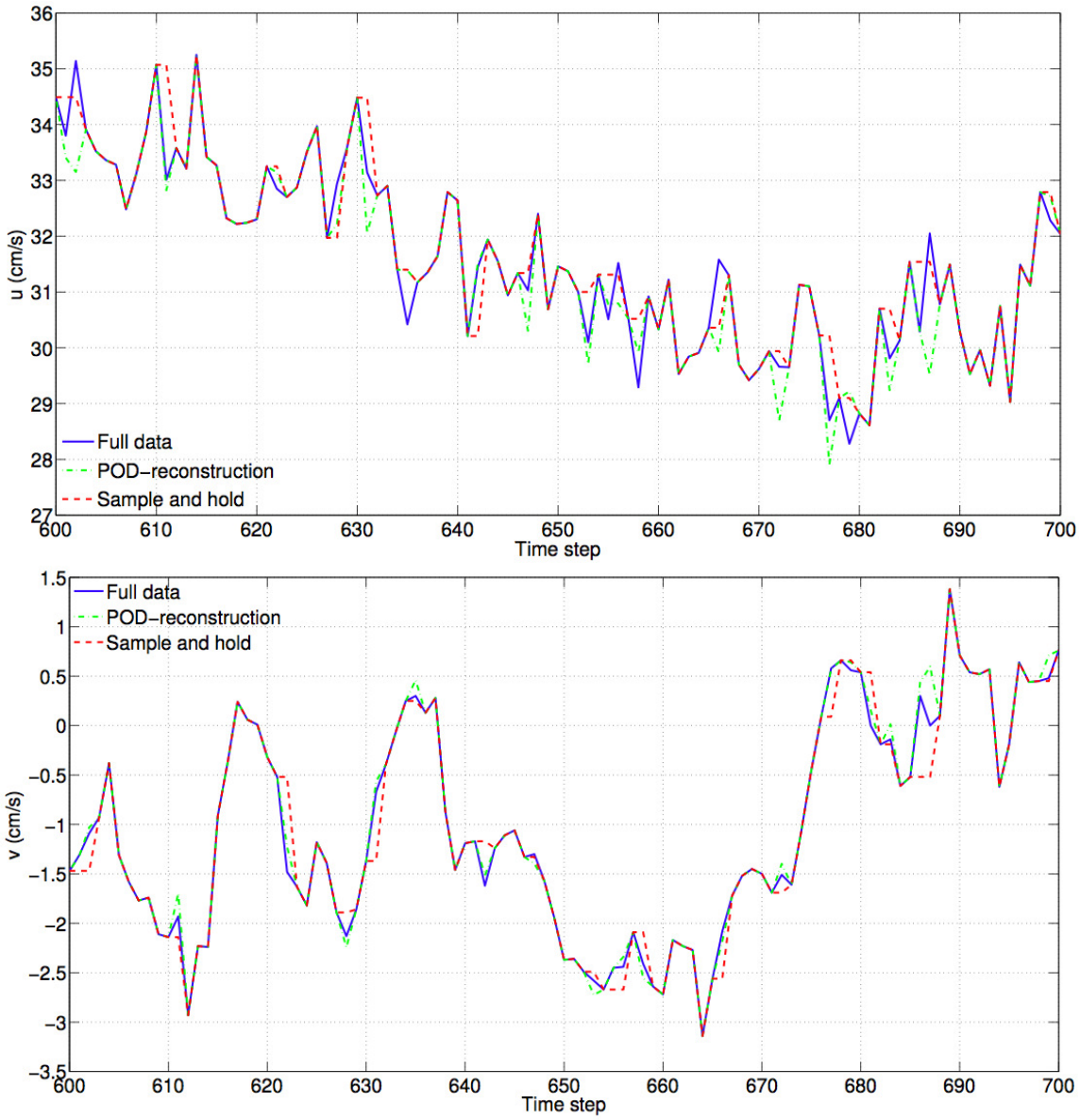

Figure 3.13: Comparison on different data interpolation schemes; S&H *Vs* POD-reconstruction

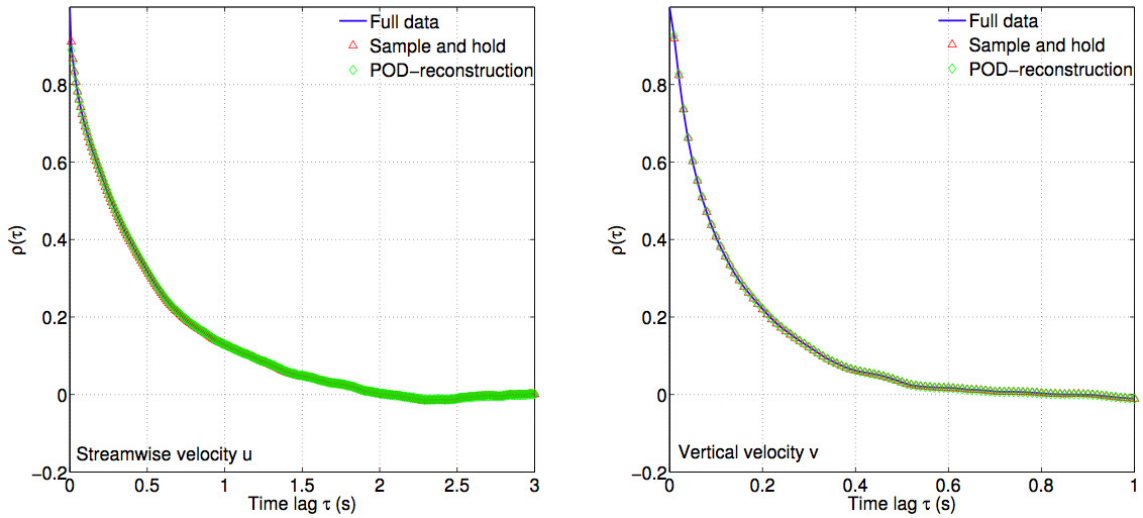

Figure 3.14: Comparison on ACF derived from reconstructed data; S&H *Vs* POD-reconstruction

very similar results are produced by the methods when the fraction of data gaps is small, rendering the choice of interpolation scheme immaterial and arbitrary.

In this section methods to recover accurate spectral estimates of the velocity spectra from gappy data have been considered. It is found that the classical S&H interpolation is sufficient to achieve this goal when the underlying velocity measurements are at a constant sampling rate. We have shown that S&H is the limiting behavior of an autoregressive AR(1) process when the sampling frequency is much faster than the evolution rate of the underlying stochastic process. The spectrum of an AR(1) process has a power-law dependence on frequency over an intermediate range and the spectral slope is -2. Since real turbulent velocity signals show similar spectral slopes, it is possible to use the AR(1) model as a proxy. This hypothesis has been tested and confirmed with laboratory ADV data obtained in an open-channel flow. Two types of data gap are considered, (i) isolated gaps of short durations and (ii) gap clusters of longer durations. For isolated gaps, S&H performs closely to the full

AR(1) model except when the ratio $\frac{\triangle t}{I_t} = \frac{1}{f_s I_t}$ is large; present test case suggests a limiting value of 0.75. It therefore can be used in almost all situations, and if increased accuracy is needed, the full model can be employed. For gap clusters, S&H only achieves comparable results as the full AR(1) model when the mean gap duration is less than one integral time scale I_t. The full model must be used if the gap duration is larger than I_t. This behavior reflects the fact that the decorrelation between consecutive samples cannot be handled by the simple S&H interpolation. To decide between S&H and the full AR(1) model, first compute I_t from the empirical ACF derived from the gappy data. Missing data must be removed from the calculation of correlation coefficients. Then if the data gaps can be considered as isolated and also if $\frac{1}{f_s I_t} < 0.75$, use S&H, otherwise, use the full model. For gaps occurring in clusters, the full AR(1) model always produces better results than S&H.

It is finally remarked that the comparison on synthetic time series with spectral slopes equal to -7/6 and -8/3 also supports the use of the AR(1) model. These slopes, other than the -5/3 isotropic scaling, have been observed in multiphase flows. The proposed method is originally aimed for one-dimensional data only; this can be space or time. Extension into 2D or even 3D is possible but it remains to define what a preceding value is. In this regard, the Kriging method and POD-reconstruction handle naturally the multidimensional problem.

4. BULK KINETIC ENERGY BUDGET INSIDE A ROUND JET/PLUME

"He who loves practice without theory is like the sailor who boards the ship without a rudder and compass and never knows where he may cast." - Leonardo da Vinci

4.1 Introduction

This short section derives a conservation equation for the bulk kinetic energy of a jet/plume flow. The aim is to provide an overall accuracy check on the measured profiles of TKE and dissipation rate of a bubble plume in section 2. It is, however, emphasized that the method is applicable to other types of flow.

4.2 A turbulent round jet

A bulk kinetic energy balance for a round jet can be easily understood in the Lagrangian framework sketched in figure 4.1. The streamwise (Eulerian) evolution of the jet is viewed as the time-evolution of a Lagrangian element along the jet path. At time t, the element has a mass ρV where $V = \pi B(t)^2 h(t)$ is the volume; B and h are radius and thickness of the element, respectively. ρ is the fluid density inside the element. As the element moves along the jet path, external fluid is incorporated into it due to jet entrainment Q_e. At the time $t + \triangle t$, the element acquires a new set of B, W_{th} and h. Let us now consider the kinetic energy at the time t; given an instantaneous velocity vector $\mathbf{u}$(t) the kinetic energy per unit fluid mass is

$$(KE)_t = \frac{1}{2}\frac{M}{\rho}|\mathbf{u}(t)|^2 = \frac{1}{2}(\pi B(t)^2 W_{th}(t))|\mathbf{u}(t)|^2 \triangle \tau \sim [\frac{L^5}{T^2}] \tag{4.1}$$

where L has the dimension of length and T has the dimension of time. During the time interval $\triangle t$, part of this energy is removed (dissipated) from the element by fluid viscosity at a rate dictated by the dissipation rate ϵ; it has the unit $[\frac{L^2}{T^3}]$ and

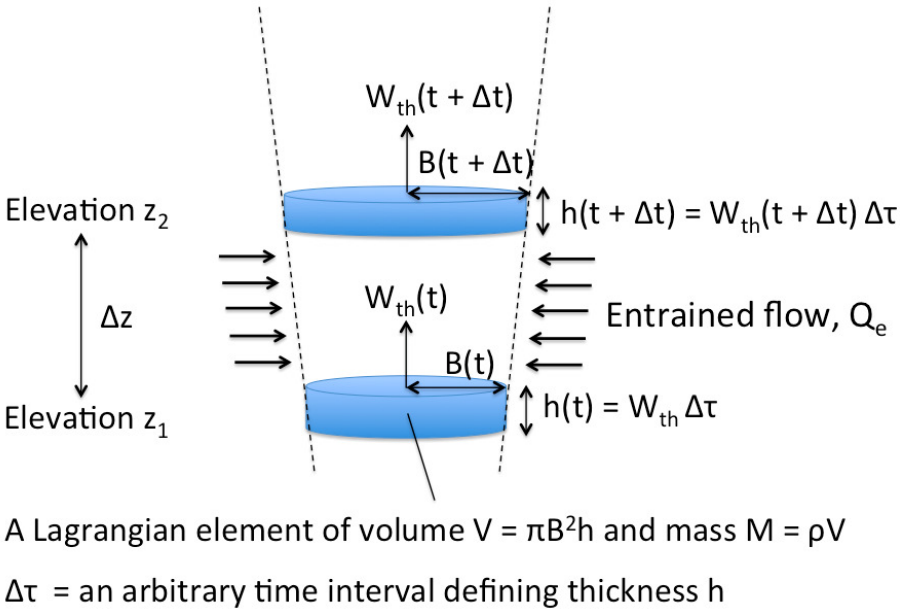

Figure 4.1: Bulk kinetic energy balance of a jet - a Lagrangian analysis

reads as energy removal per unit fluid volume per unit time. The loss of kinetic energy during $\triangle t$ is then given by

$$(KE)_{loss} = V\epsilon(t) \triangle t = (\pi B(t)^2 W_{th}(t))\epsilon(t) \triangle t \triangle \tau \sim [\frac{L^5}{T^2}] \tag{4.2}$$

The difference in kinetic energy between the times $t + \triangle t$ and t is equal to this loss, i.e. $(KE)_{t+\triangle t} - (KE)_t = (KE)_{loss}$. The Eulerian version of this statement is $\frac{D\langle \frac{1}{2}\mathbf{u}\cdot\mathbf{u}\rangle}{Dt} = -\nu\langle \nabla\mathbf{u} : \nabla\mathbf{u}\rangle = -\langle\epsilon\rangle$ where $\langle\cdot\rangle$ represents a volume average. This energy equation is obtained by first dotting $\mathbf{u}$ to the full Navier-Stokes equation and subsequently perform a volume average (Pope 2000, p.123) the average removes (via Gauss divergence theorem) the gradient flux term that only redistributes the energy in space by pressure and viscous diffusion. To use the Eulerian PIV data (to be presented in section 5) that are taken at fixed points in space the Galilean transformation $\triangle t = \triangle z/\overline{W}$ is invoked. Time t corresponds to an elevation z_1 and $t + \triangle t$ becomes $z_2 = z_1 + \triangle z$. The energy at z_1 is,

$$(KE)_{z_1} = \int_0^\infty 2\pi r W(\frac{1}{2}|\mathbf{u}(z_1)|^2)dr \sim [\frac{L^5}{T^3}] \tag{4.3}$$

Note the change in unit to $[\frac{L^5}{T^3}]$ because of the Eulerian nature of measurements. Similarly, the volume-averaged energy loss is,

$$(KE)_{loss,z_1} = (\int_0^\infty 2\pi r W \epsilon dr)\frac{\triangle z}{\overline{W}} \sim [\frac{L^5}{T^3}] \tag{4.4}$$

where $\overline{W}$ is some average advection velocity between the two elevations z_1 and z_2. The data has been time-averaged and decomposed into a mean $\mathbf{U}(\mathbf{x})$ and a fluctuating part $\mathbf{u}'(\mathbf{x})$. Hence, the total kinetic energy is $\frac{1}{2}\overline{|\mathbf{u}(\mathbf{x})|^2} = \frac{1}{2}|\mathbf{U}(\mathbf{x})|^2 + \frac{1}{2}\overline{|\mathbf{u}'(\mathbf{x})|^2}$. Contributions from radial and out-of-plane velocity to $|\mathbf{U}(\mathbf{x})|^2$ can be neglected when compared to the streamwise velocity because they are only a few percent of the latter (entrainment coefficient of a jet = 0.057); the error committed is well below 1%. W is taken as the mean streamwise velocity and curve-fits to the radial profiles of $\frac{1}{2}\overline{|\mathbf{u}'(\mathbf{x})|^2}$ and ϵ are used in evaluating the integrals.

The mean streamwise velocity is self-similar and assumes a Gaussian radial profile, $W = W_c(z)e^{-(r/b_g(z))^2}$. The total kinetic energy $\frac{1}{2}|\mathbf{u}(\mathbf{x})|^2$ equals to $\frac{1}{2}|\mathbf{U}(\mathbf{x})|^2 + \frac{1}{2}\overline{|\mathbf{u}'(\mathbf{x})|^2}$ where $\frac{1}{2}|\mathbf{U}(\mathbf{x})|^2 \approx \frac{1}{2}W^2 = \frac{1}{2}W_c^2(z)e^{-2(r/b_g(z))^2}$. Because out-of-plane velocity is not available from the planar PIV measurements, the turbulent kinetic energy is approximated by $\frac{1}{2}\overline{|\mathbf{u}'(\mathbf{x})|^2} = \frac{1}{2}(\overline{u^2} + 2\overline{v^2})$. The approximation $\overline{v^2} = \overline{w^2}$ (out-of-plane stress) has been shown to be valid in Hussein et al. (1994). Curve-fits for turbulent kinetic energy and time-averaged dissipation rate are,

$$\frac{1}{2}\overline{|\mathbf{u}'(\mathbf{x})|^2} = 0.085W_c^2(z)(e^{-(\frac{r-0.6b_g}{0.6b_g})^2} + e^{-(\frac{r+0.6b_g}{0.6b_g})^2})$$

$$\overline{\epsilon} = 0.015\frac{W_c^3(z)}{b_g(z)}(e^{-(\frac{r-0.65b_g}{0.55b_g})^2} + e^{-(\frac{r+0.65b_g}{0.55b_g})^2})$$

The equations become

$$(KE)_z = b_g^2(z)W_c^3(z)[\frac{1}{2}\overbrace{\int_0^\infty 2\pi\eta e^{-3\eta^2}d\eta}^{I_1=1.0472} + 0.085\overbrace{\int_0^\infty 2\pi\eta e^{-\eta^2}(e^{-(\frac{\eta-0.6}{0.6})^2} + e^{-(\frac{\eta+0.6}{0.6})^2})d\eta}^{I_2=2.1148}]$$

$$(KE)_{loss} = b_g(z)W_c^4(z)[0.015\overbrace{\int_0^\infty 2\pi\eta e^{-\eta^2}(e^{-(\frac{\eta-0.65}{0.55})^2} + e^{-(\frac{\eta+0.65}{0.55})^2})d\eta}^{I_3=2.0204}]\frac{\triangle z}{\overline{W}}$$

I_1, I_2 and I_3 are shape factors that only depend on the shapes of fitted profile; their values are evaluated by the Matlab function integral.m that employs an adaptive quadrature. Overall, the bulk energy balance can be written down as

$$\underbrace{(\frac{1}{2}I_1 + 0.085I_2)[b_g^2(z)W_c^3(z)]_{z_1}^{z_2}}_{\text{Change in KE}} = \underbrace{-b_g(z)W_c^4(z)(0.015I_3)\frac{\triangle z}{\overline{W}}}_{\text{Dissipation}} \tag{4.5}$$

Using the data in section 5, $b_g = 0.106x$ and $U_c(x) = 6U_j(x/D)^{-1}$, and numerical values of the shape factors, the equation above can be simplified to

$$\frac{0.703(0.106)}{z_1 z_2} = 6(\frac{D}{z^3})(0.0303)\frac{U_j}{\overline{W}} \tag{4.6}$$

where $z_2 = z_1 + \triangle z$. The elevation z is taken as the average of z_1 and z_2. The advection velocity $\overline{W}$ is taken as the jet top-hat velocity at z, i.e. $\overline{W} = W_c/2$.

4.3 A turbulent round plume

Extension to a pure plume requires the kinetic energy production term by buoyancy on the RHS of energy equation (equation 4.5). This is given by the expression

$$(KE)_p = (\int_0^\infty 2\pi r W^2 g' dr)\frac{\triangle z}{\overline{W}} \sim [\frac{L^5}{T^3}] \tag{4.7}$$

where $g' = \frac{\triangle \rho}{\rho}$ = reduced gravity. Using the self-similar solutions of W and $g' = g_c(z)e^{-(r/\lambda b_g)^2}$, where the spread ratio $\lambda = b_{gc}/b_g$, the integral can be written as

$$\int_0^\infty 2\pi r W^2 g' dr = b_g^2(z) W_c^2(z) g_c'(z) \overbrace{[\int_0^\infty 2\pi\eta e^{-2\eta^2} e^{-(\frac{\eta}{\lambda})^2} d\eta]}^{I_4}$$

The kinematic buoyancy flux $F_o = \int_0^\infty 2\pi r W g' dr = \frac{\pi\lambda^2}{1+\lambda^2} b_g^2 W_c g_c'$ can be used to recast the above into the following form,

$$b_g^2(z) W_c^2(z) g_c'(z) I_4 = W_c F_o (I_4 \frac{1+\lambda^2}{\pi\lambda^2})$$

Using $\overline{W} = W_c/\sqrt{4/\gamma}$, where γ is the momentum amplification factor, the final form of the KE production term due to buoyancy becomes,

$$(KE)_p = [(I_4 \frac{1+\lambda^2}{\pi\lambda^2})\sqrt{4/\gamma}] F_o \triangle z$$

Defining $C = [(I_4 \frac{1+\lambda^2}{\pi\lambda^2})\sqrt{4/\gamma}]$ as a prefactor, its variation with λ and γ is plotted in figure 4.2; increasing values of λ lead to a decrease in C while small values of γ increase C. The bulk KE balance equation for a pure plume is,

$$\underbrace{(\frac{1}{2}I_1 + C_{I_2}I_2)[b_g^2(z)W_c^3(z)]_{z_1}^{z_2}}_{\text{Change in KE}} = \underbrace{-b_g(z)W_c^4(z)(C_{I_3}I_3)\frac{\triangle z}{\overline{W}}}_{\text{Dissipation}} + \underbrace{CF_o \triangle z}_{\text{Buoyancy production}} \tag{4.8}$$

Using $W_c = 4.47(F_o/z)^{1/3}$, $b_g = 0.104z$ and $\overline{W} = W_c/1.9$, the dissipation term can be re-written in terms of F_o; $-b_g(z)W_c^4(z)(C_{I_3}I_3)\frac{\triangle z}{\overline{W}} = -1.9\beta(4.47^3)(0.011I_3)F_o \triangle z = -0.46F_o \triangle z$. The energy equation becomes,

$$(\frac{1}{2}I_1 + C_{I_2}I_2)[b_g^2(z)W_c^3(z)]_{z_1}^{z_2} = 0.74F_o \triangle z$$

This equation shows that the change in total kinetic energy (mean + turbulent fluctuation) increases linearly with height z for a given F_o. A similar result has been derived in Lai & Lee (2012*a*, Appendix C); however, their derivation begins with the Reynolds-averaged kinetic energy equation of the mean flow. There is no dissipation term but the transfer of energy from mean flow to turbulence is represented by an interaction term between mean axial velocity and radial gradient of shear stress. Nonetheless, both approaches give the important result $\int W^3 dA \sim F_o z$ that allows one to compute plume group velocity field by superposing kinetic energy flux of individual plume.

Equation 4.8 can be further simplified by using the plume spreading rate β and the centerline velocity decay constant C_1 of a plume,

$$(\frac{1}{2}I_1 + C_{I_2}I_2)\beta = -2(C_{I_3}I_3) + \frac{CF_o}{\beta W_j^3(C_1(\frac{\pi}{4})^{1/3}(\frac{1}{Fr})^{2/3})^3 D}$$

where C_{I_2} and C_{I_3} are fitting constants associated with the respective double Gaus-

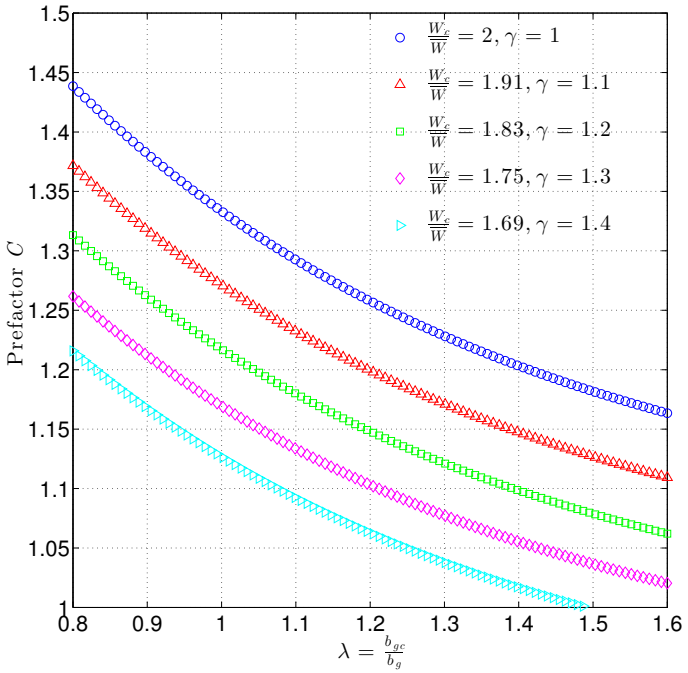

Figure 4.2: Prefactor C to the buoyancy production term of kinetic energy; $W_c =$ jet/plume centerline velocity, $\overline{W} =$ top-hat velocity and $\gamma =$ momentum amplification factor

sian profiles of TKE and $\bar{\epsilon}$. Fr = jet densimetric Froude number, W_j = jet exit velocity and D = jet diameter at exit. In this form, the apparent dependence of the energy balance with height z is removed. This is rightly expected because an energy equilibrium must be attained when the plume enters its asymptotic state $z > 5l_M$. To illustrate the equation's applicability, the required constants have been extracted from the results of a numerical simulation using the $k - \epsilon$ model for turbulence closure. The commerical computational fluid dynamics (CFD) code FLUENT (Ansys, Inc.) was used. A buoyant jet of $Fr = 5$ was injected vertically upward at $W_j = 25$cm/s from a circular orifice of diameter D =1cm at the center of the bottom face of a 1m^3 cubic computational domain; the domain height was 100cm. It had an initial kinematic buoyancy flux $F_o = 490.874$cm^4/s^3 and a jet/plume momentum length scale of $l_M \approx FrD = 5$cm. Figure 4.3 shows the relevant time-averaged properties of the plume needed in the energy equation. The double Gaussian profile is also fitted to the predicted radial profiles of TKE and $\bar{\epsilon}$. The constants are; $(I_1, I_2, I_3) = (1.0472, 2.5105, 2.3940)$, $(C_{I_2}, C_{I_3}) = (0.060, 0.011)$ and $(\beta, C_1) = (0.104, 4.47)$. The prefactor C equals 1.2 since $\lambda = 1.2$ in the simulation and also since $\gamma = 1.1$ as measured in the experiments of Wang & Law (2002). Using these values the ratio, RHS/LHS of the equation, equals $(-0.0527 + 0.1296)/0.07012 = 1.0975$; the energy budget is accurate to within 10% in this dataset.

4.4 A turbulent round bubble plume

Extension to the two-phase bubble plume is straightforwardly obtained by allowing $\lambda < 1$ in figure 4.2; reported range of λ is between 0.7-1.0 (e.g. Socolofsky et al. 2008). Adopting $\lambda = 0.8$ and $\gamma = 1.1$, the prefactor $C = 1.36$ and therefore the bulk energy balance becomes the following.

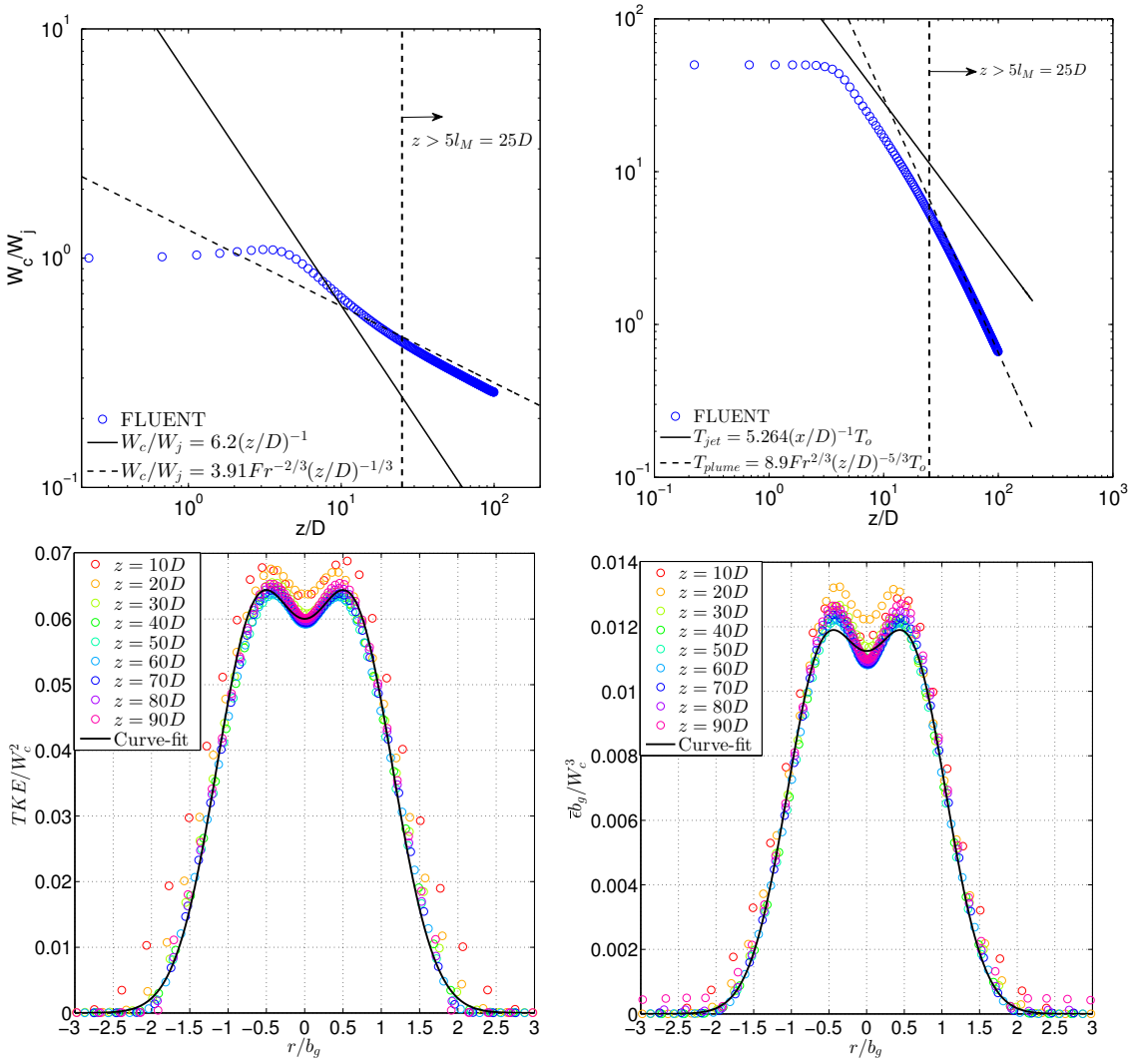

Figure 4.3: Properties of a buoyant jet ($Fr = 5, D = 1$cm) as predicted by FLUENT ($C_\mu = 0.09, \sigma_{Sc} = 0.6$); the curve-fits (black solid lines) to TKE and $\bar{\epsilon}$ are based on a double-Gaussian profile

$$(\frac{1}{2}I_1 + C_{I_2}I_2)[b_g^2(z)W_c^3(z)]_{z_1}^{z_2} = -b_g(z)W_c^4(z)(C_{I_3}I_3)\frac{\triangle z}{\overline{W}} + 1.36F_o \triangle z \qquad (4.9)$$

This equation is used in section 2 to verify the overall measurement accuracy for the case $Q_o = 0.5\text{L/min}$, where the plume is in its asymptotic regime.

5. PARTICLE IMAGE VELOCIMETRY (PIV) MEASUREMENTS OF THE RESIDUAL FLOW FIELD FOLLOWING THE ABRUPT SHUT-OFF OF A BUBBLE PLUME

5.1 Introduction

Modulation of single-phase fluid turbulence due to the presence of heterogeneous material such as solid particles and liquid bubbles has received much attention in the past two decades. For air bubbles in water, previous studies have focused on the bubble column; a homogenous swarm of bubbles rising through a walled-container. Because of the confinement there is no lateral entrainment into the swarm and the average fluid upwelling velocity is close to zero (depends, to a certain degree, on the sampling volume since water is dragged upward by bubbles in a thin boundary layer). Lance & Bataille (1991) was the first to report detailed measurements of the fluid phase velocity spatial auto-spectral density function. They considered bubbles of 5mm in diameter and found that the bubble-fluid interactions resulted in a -8/3 spectral slope in the spectra. The velocity fluctuations showed no sign of return to local isotropy; the -5/3 slope did not reappear at the high wavenumber end. Riboux et al. (2010) performed planar particle image velocimetry (PIV) to quantify the residual flow field left behind by the bubble swarm (diameter $d = 1.6 - 2.5$ mm) after the gas supply was abruptly shutoff. Contrary to Lance & Bataille (1991) who obtained their results from single point hot wire data and Taylor's frozen turbulence approximation (Pope 2000), a direct evaluation of the wavenumber spectra was made with the PIV data. Their results showed a slightly steeper -3 spectral slope which transits into the isotropic -5/3 slope near the high wavenumber end of spectra; this happened in both velocity components. To collapse their spectra with those in pre-

vious investigations, they introduced the wake attenuation length scale $L = d/C_d$, where C_d is the steady state drag coefficient, to account for the difference in bubble diameters and drag force.

Risso (2011) introduced a one-dimensional theoretical model to explain the peculiar -3-spectral slope. The model starts by considering the fluid velocity induced by each bubble as a localized burst in space; the velocity distribution is Gaussian. The combined velocity field is then obtained from a linear superposition of contributions of all bubbles. Provided that maximum velocity, position and Gaussian width of each burst are statistically independent of each other's and of the number of bubbles considered, the resulting ensemble averaged spatial spectrum possesses the desired -3-spectral slope in the wavenumber range bounded by the inverse of maximum and minimum Gaussian burst width and an exponential decay ensues beyond this range. One important model prediction is that velocity spectrum, once normalized by its energy (variance), is independent of air void fraction, which is an experimental fact observed in Riboux et al. (2010). It should be noted that the assumption of Gaussian bursts is not essential in deriving the results; any regular and smooth functions that decay to zero with distance from their center would suffice.

While the induced fluid flow inside a bubble column is almost free of Reynolds shear stress (horizontal gradient of the mean fluid vertical velocity is close to zero, see Riboux et al. (2010)), the air bubble plume is a free-boundary layer flow with significant shear stresses. Globally, it behaves similarly to a single-phase plume; in both cases, the plume growth rate is about 0.1 and the initial kinematic buoyancy flux is the dynamical quantity that governs the flow. Even with this single-phase counterpart, fluid turbulence is not isotropic as shown in many previous studies (Gibson 1963, Wyg-

nanski & Fiedler 1967, Papanicolaou & List 1988)e.g.. Simiano et al. (2006) reported fluid velocity measurements, obtained from phase-discriminating 2D PIV, in a developing bubble plume (in the sense that centerline velocity did not decay with elevation) and showed that the vertical normal stress is 2.1-2.8 times the radial (horizontal) stress (their figure 17); in comparison, the ratio ($\overline{w^2}/\overline{u^2}$) in single-phase plumes is only about 1.96. In terms of spatial velocity spectra, results in Duncan et al. (2009) show a -7/6 spectral slope at the plume center but it reverts to the classic -5/3 slope at the plume edge. Their spectra, however, did not extend into high enough wavenumbers to reveal the full spectrum due to an insufficient temporal resolution; Taylor's frozen turbulence hypothesis was used to convert frequencies into wavenumbers.

The objective of present research is to use an original experimental dataset to resolve the large disparity in observed spectral slopes in bubbly flows. The chosen flow for investigation is the bubble plume because it allows one to study rising bubbles in a shear flow. There coexist two regions of low shear, the plume core and the plume edge. While the former has a high degree of bubble-fluid interactions, the latter is entirely made up of fluid motions. This permits one to inquire into the interaction among bubbles in a shear flow.

This section is structured as follows. In §5.2, details of the laboratory setup, settings of camera and PIV system and experimental design are given. The results of a single-phase round jet and a single-phase round plume are first presented in §5.3 and §5.4. These two experiments bear two purposes: (i) to verify the adequacy of present PIV system in resolving the details of fluid turbulence; the single-phase jet/plume is chosen because they have a similar global behavior of a bubble plume and (ii) to

provide a comparison with the results of a bubble plume. A correction method for underestimated turbulent dissipation rate is proposed and is shown to be valid for jets and plumes using the bulk kinetic energy balance equation derived in section 4. Subsequently, turbulent structures in the residual flow behind a bubble plume are elucidated using swirl strength and subgrid scale energy flux in §5.5. And, finally a summary of present findings and conclusions are given in §5.6.

5.2 Laboratory experiments

Experiments were carried out in the Fluid Dynamics Laboratory in the Ocean Engineering Program at Texas A&M University. To establish a symmetric flow field, a 1m^3 cube compartment was partitioned from a glass-walled rectangular water tank. A definition diagram of the setup is shown in figure 5.1. Compressed air was injected into the cube through an aquarium airstone located at the center of the bottom face. The volume flux of air Q_o at standard atmospheric pressure was monitored by a calibrated gas flowmeter and the air bubbles had a median diameter $d_{50} = 2.4\text{mm}$ with a corresponding slip velocity of 24cm/s (Clift et al. 1978); the distribution of bubble diameters has already been shown in section 2.

The plume center plane was illuminated by a laser sheet generated by directing a 5W Ar-ion laser beam through laser optics consisting of a cylindrical lens and reflecting mirrors. A high-speed (at a maximum pixel resolution 1024 by 1024) SRCMOS camera (Phantom v5.1, LaVision Co.) was used for image capturing; it was fitted with a macro-Nikkor 200mm lens and positioned 75cm from the illuminated plane. The camera had a pixel resolution d_r of 0.016mm/pixel, a magnification M_o of 0.356 and a f-number of 4. Fifty microns polyamide-12 particles were used as seeding. The diffraction-limited particle image size d_e was found to be 0.0192mm and thus the

ratio $d_e/d_r = 1.2$ fell in the range of 1-3 recommended in Adrian (1997), implying a negligible mean bias error due to the digital camera's discrete sampling. The temporal sampling frequency f_s was set at 200Hz and the velocity field was calculated by a multipass PIV cross-correlation algorithm with Gaussian-weighted interrogation windows (IW). For consecutive images, the temporal resolution was thus f_s. The velocity computation was made by the DaVis 8.2 software (LaVision Co.) with decreasing IW size from 64 x 64 to 32 x 32, each with a 50% overlap and two iterations. The final vector spacing is 0.72mm. Spurious vectors were removed by the universal outlier detection algorithm (median filter of normalized residual) inWesterweel & Scarano (2005) and the resulting data gaps were filled by a local neighbor average. In general, less than 0.5% of the total data was identified as faulty. The final-pass (raw) velocity field was low-pass filtered using a narrow 2D Gaussian kernel (a 3-by-3 square with a standard deviation of 0.5) to remove *jitters* caused by high-frequency PIV noise. Inspection of the empirical histogram of particle displacements reveals no peak-locking phenomenon.

Measurements of the vertical $\tilde{w}$ and horizontal $\tilde{u}$ velocity were taken in two regions, named A and C respectively, in figure 5.1. Region A spans the bubble core with the plume axis right at the middle of the image. It has low values of Reynolds shear stress $\overline{wu}$ but with a high degree of bubble-fluid interactions. Contrarily, region C is outside the plume where interactions are small. The level of shears stress is also low. The camera field-of-view (FOV) is a 4.6 by 4.6 cm square in all experiments; length-to-pixel factor = 0.0045cm/pixel. In each region, three values of Q_o were tested, 0.5, 1.0 and 1.5L/min. For A, image acquisition had already begun before Q_o was abruptly turned off; the first few hundreds of image containing rising bubbles were discarded and the remaining images were used in subsequent analysis. For C, the

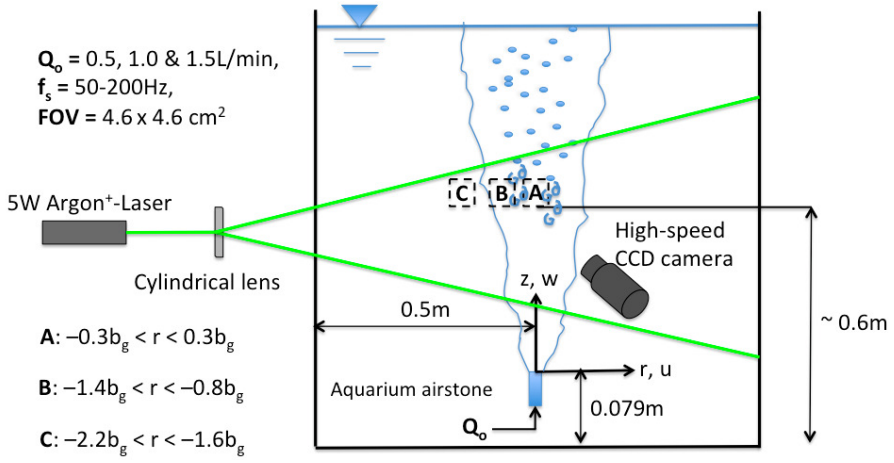

Figure 5.1: Laboratory setup of present PIV experiments

gas inflow was kept on the whole time as the area did not contain any air bubbles.

5.3 Single-phase round jet

To test the fidelity of present PIV setup and selected camera parameters, measurements of a free turbulent round jet have been obtained in the same water tank depicted in figure 5.1. The time-steady jet was issued vertically upward from a 11mm-diameter nozzle into the initially quiescent ambient. Jet fluid was fed by a constant water head tank whose flow rate was regulated by a calibrated Tokyo Keiso rotameter. Particle images were taken for the downstream distances $18< x/D <30$. Figure 5.2 shows the profiles of jet velocity and turbulent intensities on exit; the time-averaged axial velocity profile is close to top-hat and the jet flow is turbulent on exit with intensities between 1-2%. The time-averaged centerline dissipation rate $\overline{\epsilon_c}$ was measured (see figure 5.8) between 1-10cm^2/s^3. Therefore, the ranges of Kolmogorov length and time scale, $\eta = (\nu^3/\epsilon)^{1/4}$ and $\tau_\eta = (\nu/\epsilon)^{1/2}$, are respectively, 0.18-0.32mm and 0.032-0.1s. Since the images had been sampled at 50Hz ($\triangle t$ = 0.02s), the most rapid velocity fluctuations were captured. In terms of spatial resolution, the vector spacing is 1.584mm which means that the smallest resolvable scale

is 3.168mm, as demanded by the Shannon-Nyquist theorem. This is about ten times the Kolmogorov scale.

Figure 5.3 shows the measured linear decay of centerline axial velocity U_c with downstream distance and the normalized radial profiles of axial velocity U. A value of 6.0 is found for the centerline velocity decay coefficient, which is well-within the range of previously reported values, 5.60-6.48 (see, for example, Wang & Law (2002)). Self-similar property of the jet can be seen in the normalized radial profiles from which the jet spreading rate, $\beta = b_g/x$, is determined to be 0.106. Figure 5.4 shows the time-averaged second-order moments of velocity fluctuations which include the two normal stresses , $\overline{u^2}$ and $\overline{v^2}$, and the Reynolds shear stress $\overline{uv}$. Curve-fits of the PIV data in Wang & Law (2002) are added for comparison; they were taken in the range $40 \leq x/D \leq 70$. A downstream distance of $50D$ is required for the jet to reach a fully self-similar state where turbulent statistics becomes independent of x (Wygnanski & Fiedler 1967). It can be seen in the figure that the radial profiles of stresses exhibit self-similarity but the stress magnitudes are lower than those in a fully self-similar state. The turbulent viscosity of the jet can be computed from $\nu_{tur} = -\overline{uv}/(\partial U/\partial r)$ and the results are shown in the lower right hand panel in figure 5.4. Normalized ν_{tur} is approximately constant within one jet width, b_g, from the jet axis, taking a value of 0.024. It decreases beyond one b_g and is close to zero at the jet edge ($r = 2b_g$). A reasonable agreement with hot-wire data in Hussein et al. (1994) is found (presented as a curve-fit in Pope (2000)).

Figure 5.5 shows the non-dimensional spatial longitudinal (streamwise) density $E_{11}(\lambda_1)/(\bar{\epsilon}\nu^5)^{1/4}$ derived from present data; symbols are data at jet axis ($r = 0$) and jet edge ($r = b_g$). The solid line is a curve-fit of previous experimental datasets compiled

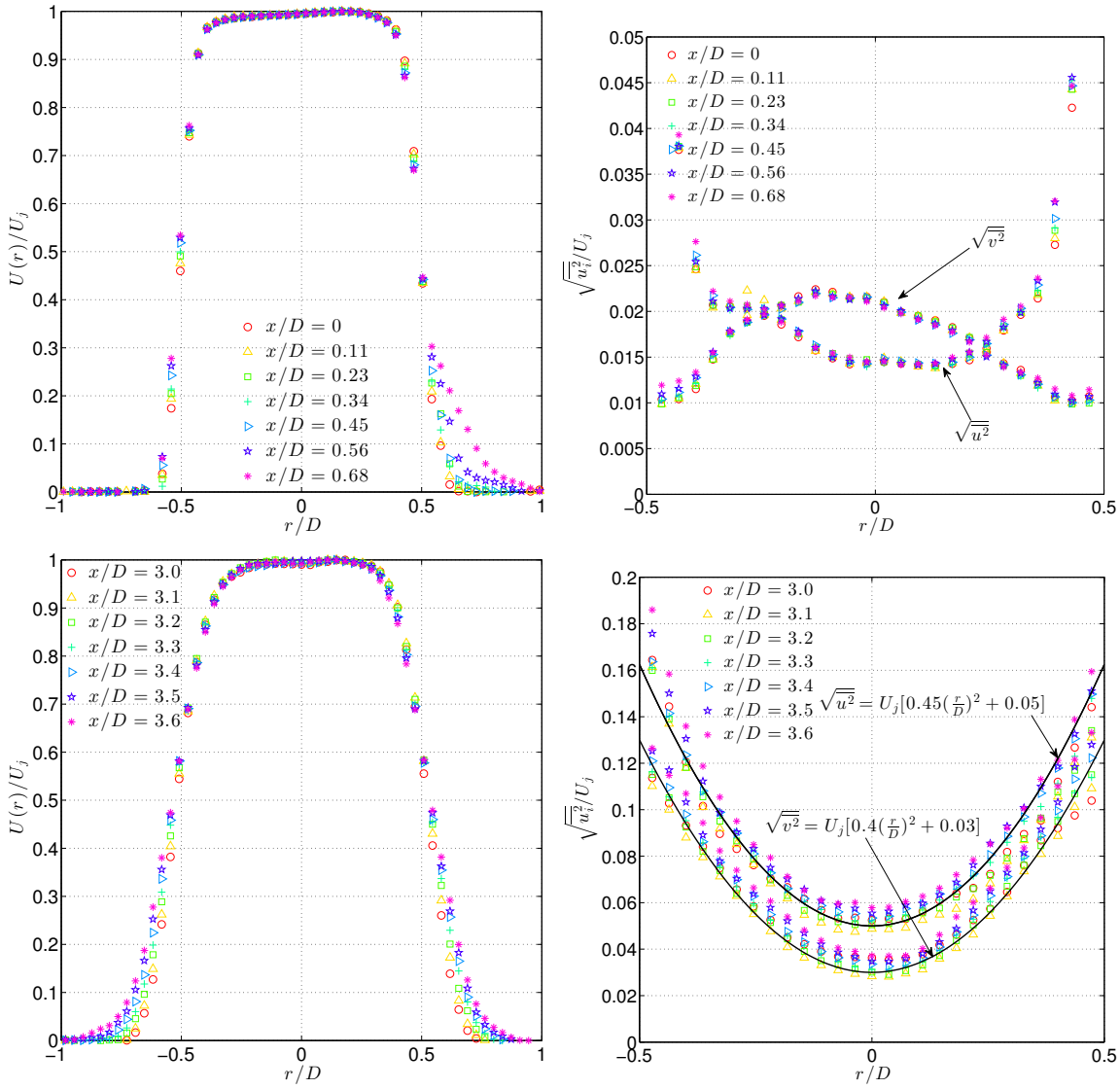

Figure 5.2: Time-averaged axial jet velocity U at jet exit (left panel) and associated turbulent intensities (right panel); D= 11mm, U_j = 30.4cm/s and Re = 3344

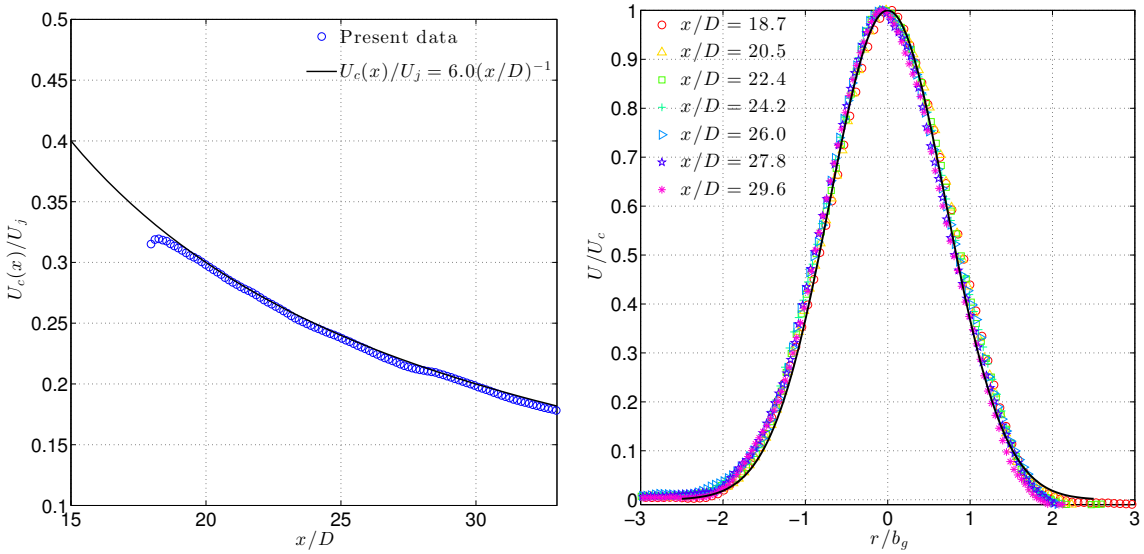

Figure 5.3: Decay of centerline axial velocity $U_c(x)$(left panel); normalized axial velocity profile (right panel) in which $b_g = 0.106x$

in Pope (2000); the compilation encompasses a wide range of flows, e.g. wakes, jets, grid turbulence and boundary layers, with Taylor Reynolds numbers R_λ varying from 23 to 3180. It can be seen that the present data agree very well with the curve-fit; an inertial subrange is apparent and at $\lambda_1\eta \sim 0.02$ the energy of velocity fluctuations start to decay as $(\lambda_1\eta)^{-11/3}$. The transition marks the beginning of dissipative scales where the fluid kinematic viscosity acts as the energy sink to fluid turbulence. It should be noted that there are no theoretical grounds or dimensional arguments that predict a power-dependence on λ_1 in the dissipation range; the actual decay is exponential. It is merely a convenience to identify the range by steeper spectral slopes of -11/3 or 7, an indication that is however borne out by many previous measurements. The longitudinal dissipation spectrum $D(\lambda_1) = 2\nu\lambda_1^2 E_{11}(\lambda_1)$ is shown in the right panel of the figure. Although in this set of low magnification experiments the smallest resolvable spatial scale is only 10-12 times η ($\lambda_1\eta = 0.08$-0.1), it can be seen that a significant portion of the dissipation spectrum has been covered.

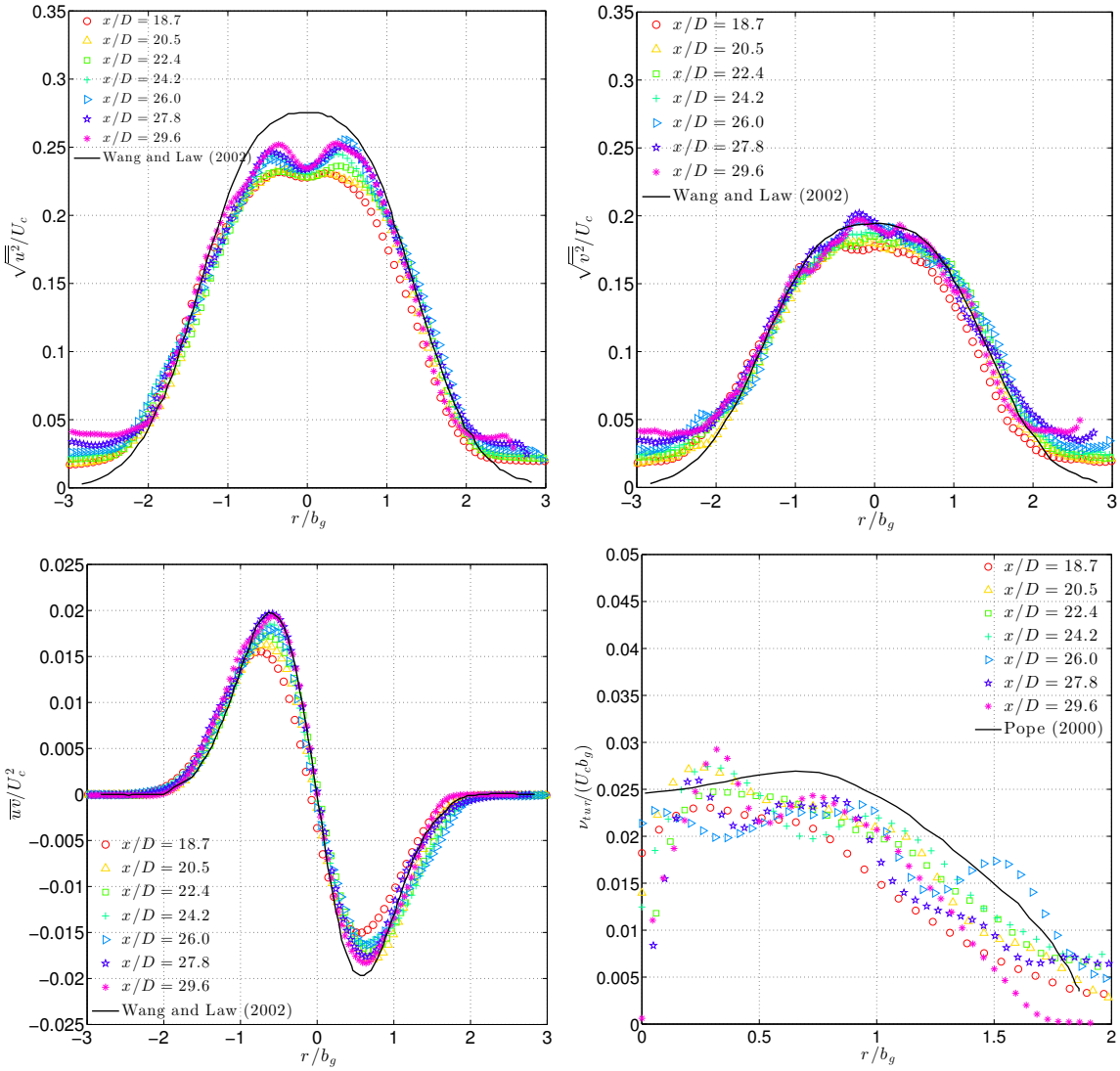

Figure 5.4: Time-averaged second-order moments of fluctuating velocity; $\overline{u^2}$, $\overline{v^2}$, $\overline{uv}$ and computed turbulent viscosity ν_{tur}; solid black lines are curve-fits to PIV data in Wang and Law (2002); Pope (2000) extracted hot wire anemometry (HWA) data from Hussein *et al.* (1994)

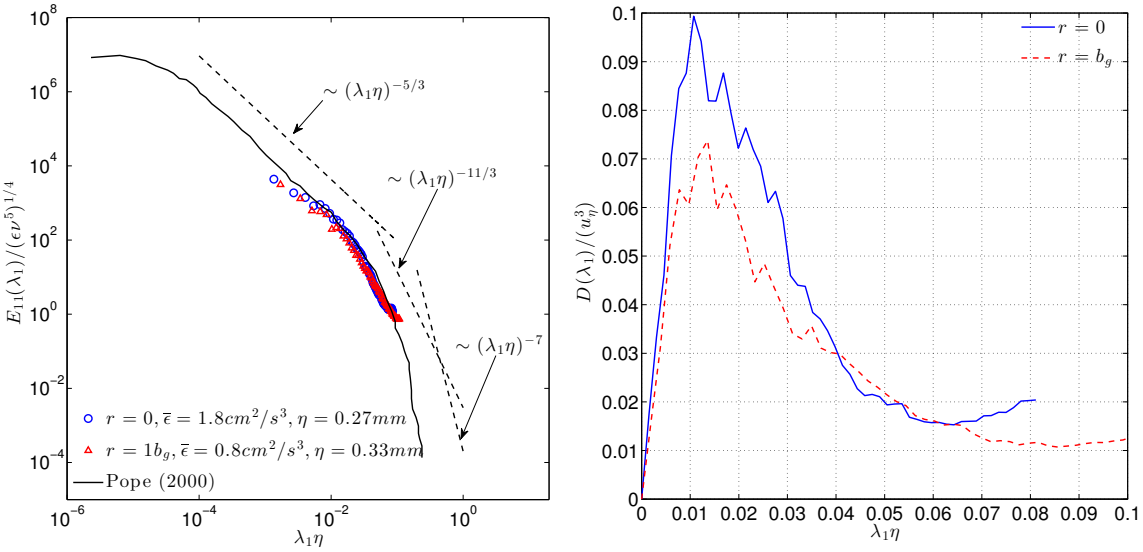

Figure 5.5: Normalized streamwise auto-spectral density function $E_{11}(\lambda_1)$ of a jet (left panel) and the corresponding dissipation spectrum $D(\lambda_1) = 2\nu\lambda_1^2 E_{11}(\lambda_1)$ (right panel); $u_\eta = (\nu\epsilon)^{1/4}$ = Kolmogorov velocity scale, $u_\eta = 0.37$cm/s and 0.3cm/s at $r = 0$ and $r = 1b_g$ respectively

According to Pope (2000), this represents about 75-80% of the total dissipation (see below).

Figure 5.6 shows the longitudinal (streamwise) cross-spectral density $E_{uv}(\lambda_1)$ obtained at various radial locations of the jet. It is normalized by the following scales (Pope 2000,): $L_S = \overline{\epsilon^{1/2}} S^{-3/2}$ and $u_S = (\bar{\epsilon}/S)^{1/2}$ where $S = \partial U/\partial r$ is the radial gradient of mean axial velocity and the required quantities are computed from measurements. Consistent with the tenets of local isotropy, there exists a range of $\lambda_1 L_S$ having a -7/3 spectral slope; while turbulent kinetic energy distributes as $\lambda_1^{-5/3}$ in the inertial subrange the anisotropy in turbulence is decaying faster. The data do not collapse onto each other under the normalization. A probable reason is that the fluid turbulence is not completely homogeneous in the streamwise direction albeit the slow decay ($\sim x^{-1}$) of the jet.

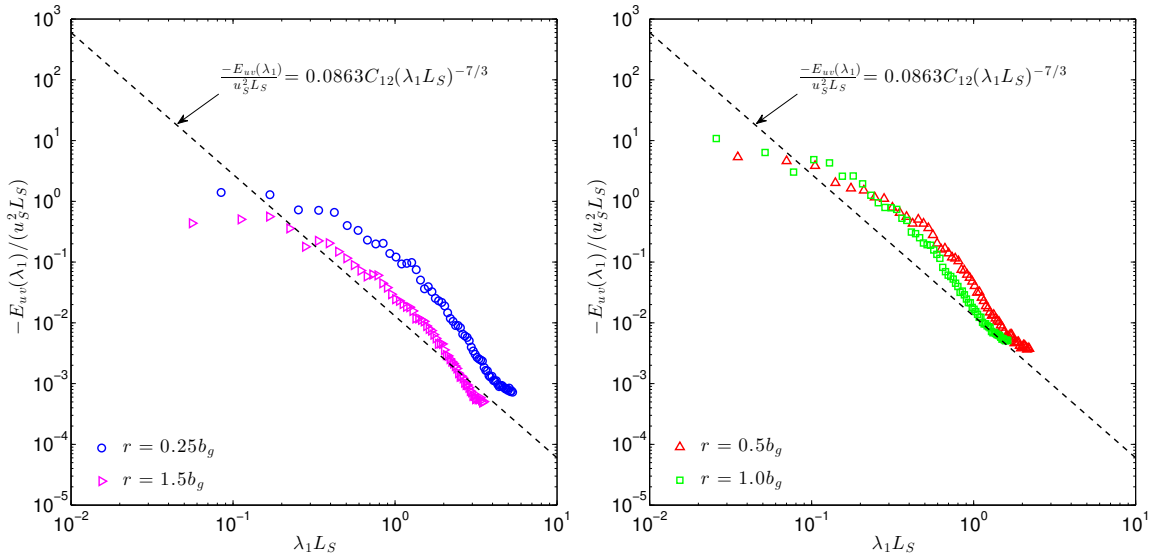

Figure 5.6: Normalized streamwise cross-spectral density function $E_{uv}(\lambda_1)$; $C_{12} = 0.15$, $(L_S,\ u_S) = (1.7\text{cm},\ 1.58\text{cm/s})$, $(0.71\text{cm},\ 1.09\text{cm/s})$, $(0.52\text{cm},\ 0.76\text{cm/s})$ and $(1.13\text{cm/s},\ 0.7\text{cm/s})$ for $r/b_g = 0.25$, 0.5, 1.0 and 1.5 respectively

Theoretically, the dissipation rate ϵ is given by the integral $\int_0^\infty 2\nu k^2 E(k) dk$ where $E(k)$ is the three-dimensional energy (auto-) spectrum. A model for $E(k)$ that compares well with experimental data obtained in many different turbulent flows is proposed in Pope (2000). Neglecting the contribution from the energy-containing range, the integral integrated up to the wavenumber k can be written as

$$\epsilon_{(0,k\eta)} = 2C\nu\epsilon^{2/3}\eta^{-4/3}\int_0^{k\eta}(k\eta)^{1/3} exp\{-\beta\{[(k\eta)^4 + c_\eta^4]^{1/4} - c_\eta\}\} d(k\eta) \qquad (5.1)$$

where $C = 1.5$, $\beta = 5.2$, $c_\eta = 0.4$ and $\epsilon = \epsilon_{(0,\infty)}$ = total dissipation rate. Figure 5.7 shows $\epsilon_{(0,k\eta)}$ as the fraction of total dissipation; to facilitate interpretation the abscissa is shown as $l/\eta = (k\eta/2\pi)^{-1}$, where l is a physical length and can be viewed as the smallest resolvable spatial scale by a given camera system. It can be seen that it is unnecessary to achieve spatial resolutions down to 1η in order to resolve ϵ;

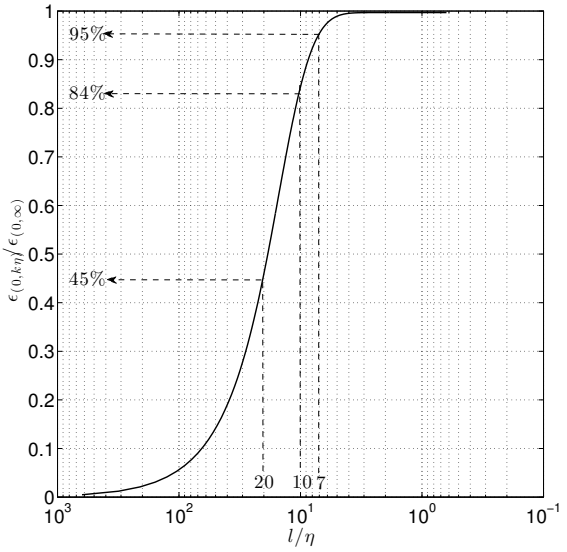

Figure 5.7: Cumulative dissipation rate $\epsilon_{(0,k\eta)}$ derived from the three-dimensional model energy spectrum $E(k)$ given in Pope (2000); l has a dimension of length [L]

at $l/\eta \approx 7$, 95% of the dissipation has already been captured. At about 18.5 times η, 50% of ϵ is resolved. The curve can be used to correct for insufficient spatial resolution. For instance, with $l/\eta = 10$, a factor of $1/0.84 = 1.19$ can be multiplied to the measurement to obtain the total dissipation rate. Such an adjustment is made to present data described in the next paragraph.

To compute $\bar{\epsilon}$ from 2D PIV data, the expression in Nimmo Smith, Katz & Osborn (2005) is used; the authors performed underwater 2D PIV measurements in the turbulent boundary layer at sea floor.

$$\bar{\epsilon} = 3\nu[\overline{(\frac{\partial u}{\partial x})^2} + \overline{(\frac{\partial v}{\partial r})^2} + \overline{(\frac{\partial u}{\partial r})^2} + \overline{(\frac{\partial v}{\partial x})^2} + 2(\overline{\frac{\partial u}{\partial r}\frac{\partial v}{\partial x}}) + \frac{2}{3}(\overline{\frac{\partial u}{\partial x}\frac{\partial v}{\partial r}})] \qquad (5.2)$$

The required spatial velocity gradients have been computed by spectral differentiation using Chebyshev polynomials. For this purpose, the open source Matlab code - *Chebfun* developed by Oxford's Numerical Analysis Group at Oxford Uni-

versity, United Kingdom, is used. The code is designed to achieve 15-digit accuracy, i.e. the number of decimal places of double floating point numbers, via an adaptive refinement strategy. More details can be found from the group's website (www.chebfun.org). The conceptual advantage of spectral differentiation is that no numerical grid is need as compared to finite differencing and the answer is exact. This eliminates error amplification and truncation error.

Figure 5.8 shows the computed time-averaged turbulent dissipation rate $\overline{\epsilon}$; the axial decay of centerline dissipation $\overline{\epsilon_c}$ is to the left whereas radial profiles of normalized $\overline{\epsilon}$ is to the right. Since $\overline{\epsilon_c}$ scales as U_c^3/b_g where $U_c \sim x^{-1}$ and $b_g \sim x$, $\overline{\epsilon_c}$ decays as x^{-4} which is borne out by the data. The radial profiles are self-similar with a uniform region for $|r/b_g| \leq 0.5$; for $x/D > 30$, $\overline{\epsilon_c} b_g/U_c^3 \approx 0.02$. Taking into account the 20-25% underestimation of ϵ mentioned above, the adjusted dissipation rate profiles are shown in the lower left panel of the figure; a factor of 4/3 has been multiplied to the measured values. Results from the direct numerical simulation DNS of Taub et al. (2013) on a turbulent round jet ($Re = 2000$) is plotted for comparison. A good agreement is seen for $x/D \sim 30$. The larger discrepancy for smaller x/D is possibly due to the fact that the DNS simulation reaches a fully self-similar state (at $x = 10D$, their figure 5) much earlier than present and previous experimental data. To further validate the correction method, measurements of a stronger jet with 2.1 times the original U_j were made for the same range of x/D. The jet width remained the same while $U_c(x)$ increased by a factor of $2.1^3 = 9.26$. This translates into a reduced η, which is about 57% of the original value (= 0.27mm at jet centerline), and the ratio l/η becomes $3.2/0.154 = 20.8$. Referring back to figure 5.7, approximately 40-45% of ϵ would have been resolved by the data of this strong jet. A prefactor of $1/0.4 = 2.5$ is applied to the measured values of ϵ and the result is shown in the lower right

panel in figure 5.8; a favorable agreement is achieved between the data of weak and strong jets and DNS. Finally, the non-dimensional dissipation rate C_ϵ at jet center-line computed using present data is shown in figure 5.9; according to Kolmogorov's hypothesis the mean energy dissipation rate is governed by properties of the large energy-containing scales and hence the relation $\overline{\epsilon_c} = C_\epsilon(\sqrt{\overline{u^2}})^3/L_{11}$ where L_{11} is the streamwise longitudinal integral scale. The proportionality constant C_ϵ is of order one and independent of viscosity in high Reynolds number flows. A value of 0.5 is derived from the data which lends support to the hypothesis and also agrees with other experimental datasets (Pearson, Krogstad & van de Water W. 2002).

Referring back to section 4, the bulk kinetic energy of the jet is given by the equation below.

$$\frac{0.703(0.106)}{z_1 z_2} = 6(\frac{D}{z^3})(0.0303)\frac{U_j}{\overline{W}}$$

Consider $z_1 = 18.7D$, $z_2 = 29.6D$, $z = \frac{z_1+z_2}{2} = 24.2D$ and the advection velocity $\overline{W} = W_c/2 = \frac{1}{2}6U_j(24.2)^{-1} = 3.77cm/s$ at z, the ratio between RHS and LHS equals to $0.8605/1.1126 = 0.773$, meaning that the measured dissipation is underestimated by 23%. This value compares favorably with the one ($3/4 = 0.75$) found from the integration of dissipation spectrum; the bulk energy analysis lends further support to the proposed correction method.

5.4 Single-phase round plume

Experiments on a turbulent round plume were also carried out using a salt water jet; the same nozzle was directed vertically downwards into the tank near the water surface. The buoyant jet had a density difference, $\triangle\rho/\rho_a = (g'_o/g)$, of 2.4%, a densimetric Froude number $Fr = W_j/\sqrt{g'_o D}$ of 3 and a jet-plume momentum length

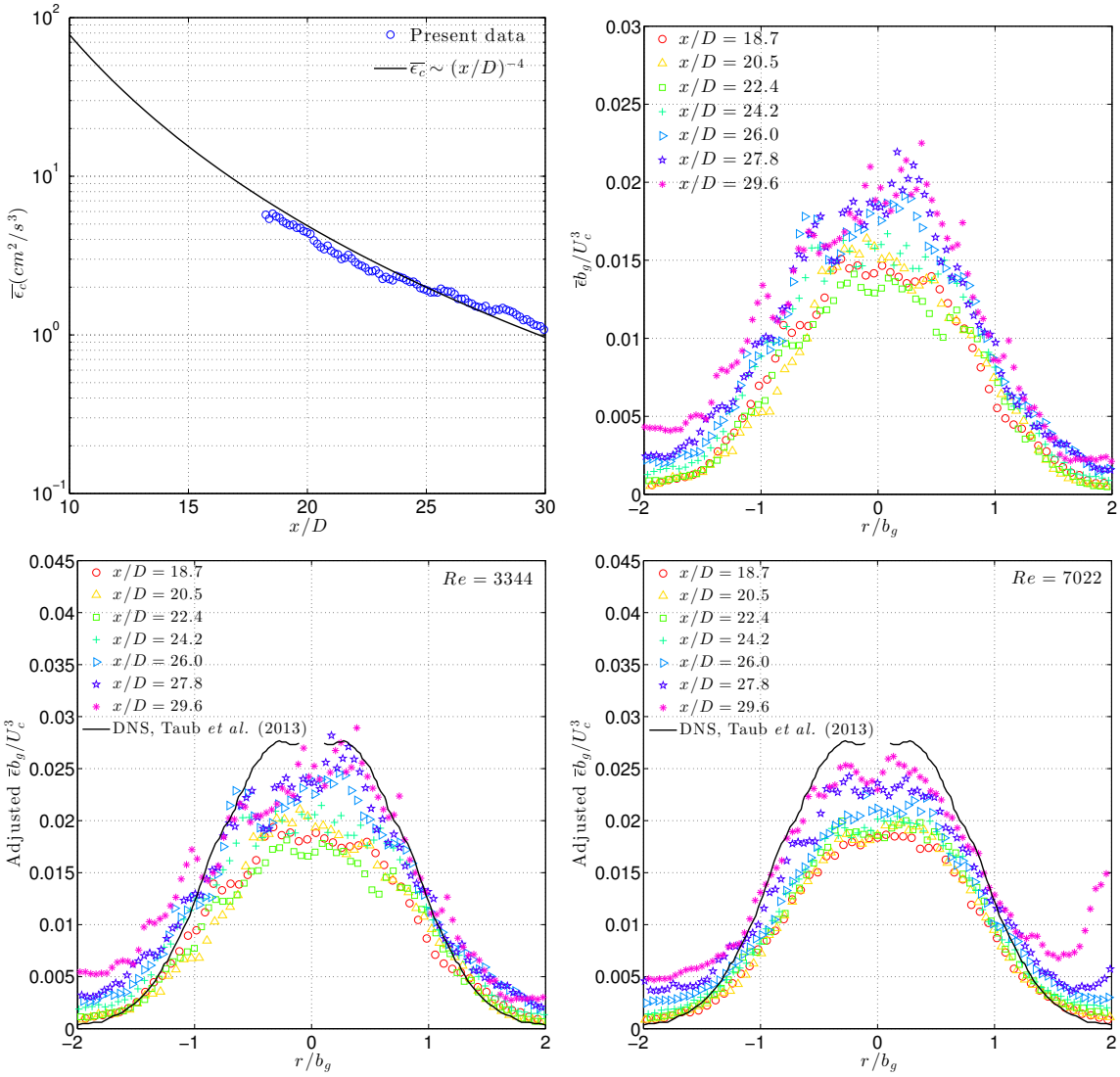

Figure 5.8: Decay of centerline time-averaged dissipation rate $\epsilon_c(x)$(top left panel), measured dissipation rate profiles (top right panel) and adjusted dissipation rate profiles; $Re = 3344$ (lower left panel) and $Re = 7022$ (lower right panel)

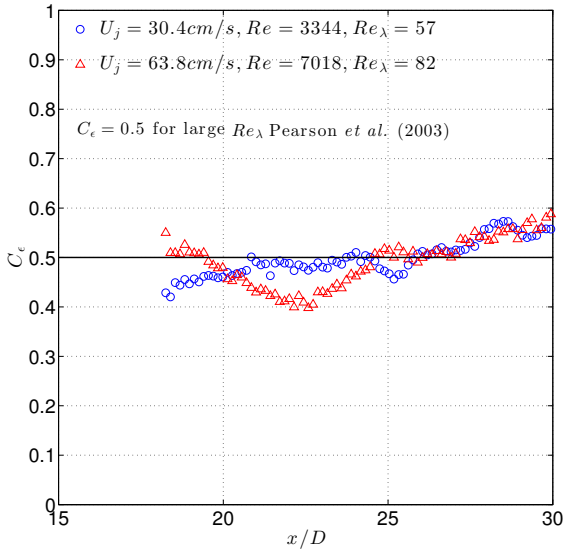

Figure 5.9: Non-dimensional mean energy dissipation rate at jet centerline $C_\epsilon = \overline{\epsilon_c} L_{11}/(\sqrt{\overline{v^2}})^3$; L_{11} = longitudinal (streamwise) integral length scale of axial velocity $= b_g/3$ (Pope (2000))

scale $l_M \sim FrD$ of 3cm. Temperature difference between source fluid and ambient water was less than 0.1^oC. The jet discharge velocity was 15.2cm/s. Results of the mean flow and turbulent stresses are shown in figure 5.10 and 5.11 where good agreement between present and published data can be seen. Figure 5.12 shows the measured $\overline{\epsilon}$. The centerline dissipation rate $\overline{\epsilon_c}$ evolves as z^{-2} since $W_c \sim z^{-1/3}$ and $b_g \sim z$; because of poorer laser light illumination at the edges of image only data in the central portion, 27cm $\leq z \leq$ 37cm, exhibit this behavior. Within this range, self-similarity of the normalized profiles is evident. Figure 5.13 shows the normalized profiles of TKE and adjusted $\overline{\epsilon}$ (a factor of 1/0.7 is applied to compensate for insufficient spatial resolution, the ratio $l/\eta \approx 13$); TKE have been approximated by $\frac{1}{2}(\overline{w^2} + 2\overline{u^2})$ where the missing out-of-plane stress $\overline{v^2}$ is taken as the same as $\overline{u^2}$. Black solid lines are double Gaussian fits to the data and the dotted lines are predictions from FLUENT (section 4) of a buoyant jet ($Fr = 5$); both experimental and numerical data are taken in the plume asymptotic regime ($z > 5l_M$). The two

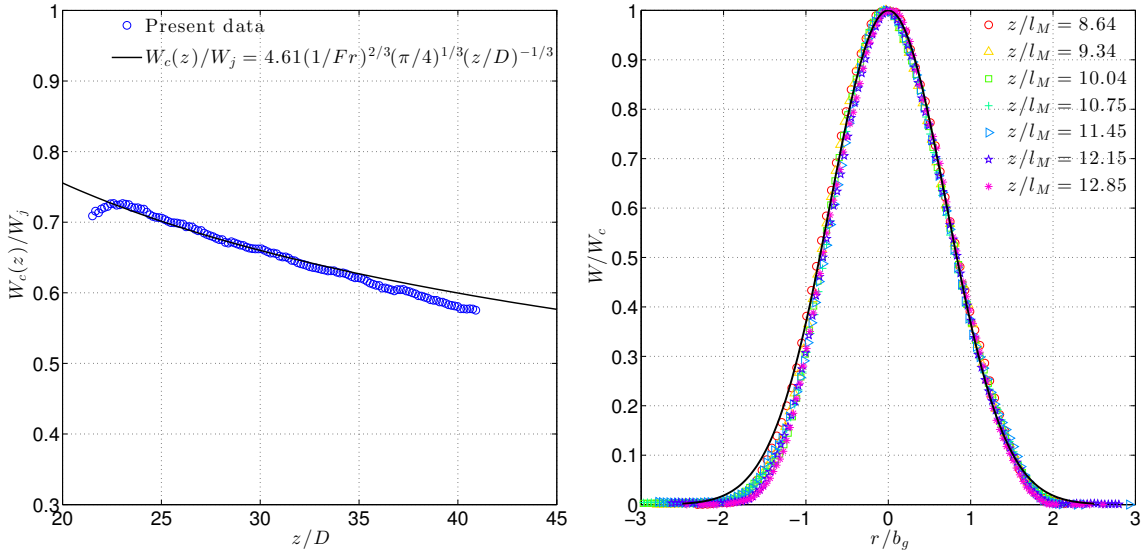

Figure 5.10: Decay of centerline axial velocity $W_c(z)$(left panel) and normalized axial velocity profile (right panel) in a plume; $W_j = 15.2$cm/s, $b_g = 0.104z$ and $Fr = 3$

datasets are essentially the same for TKE whereas the measured dissipation rate in plume core $|r/b_g| < 0.5$ is about 17% larger than predicted values. Recalling the bulk KE energy equation for a plume in section 4,

$$(\frac{1}{2}I_1 + C_{I_2}I_2)\beta = -2(C_{I_3}I_3) + \frac{CF_o}{\beta W_j^3 (C_1(\frac{\pi}{4})^{1/3}(\frac{1}{Fr})^{2/3})^3 D}$$

the ratio, RHS/LHS of the equation, is (-0.0507 + 0.1178)/0.0688 = 0.975; the energy budget is satisfied to within 2.5% with the PIV data (The constants are $(I_1, I_2, I_3) = (1.0472, 2.3032, 2.0511)$, $(C_{I_2}, C_{I_3}) = (0.060, 0.013)$, $(\beta, C_1) = (0.104, 4.61)$ and $F_o = 337.14\text{cm}^4/\text{s}^3$).

5.4.1 Vortical structures

A working definition of a vortex has been suggested by Robinson, Kline & Spalart (1989) as: "...[vortex] exists when instantaneous streamlines mapped onto a plane normal to the core exhibit a roughly circular or spiral pattern, when viewed in a

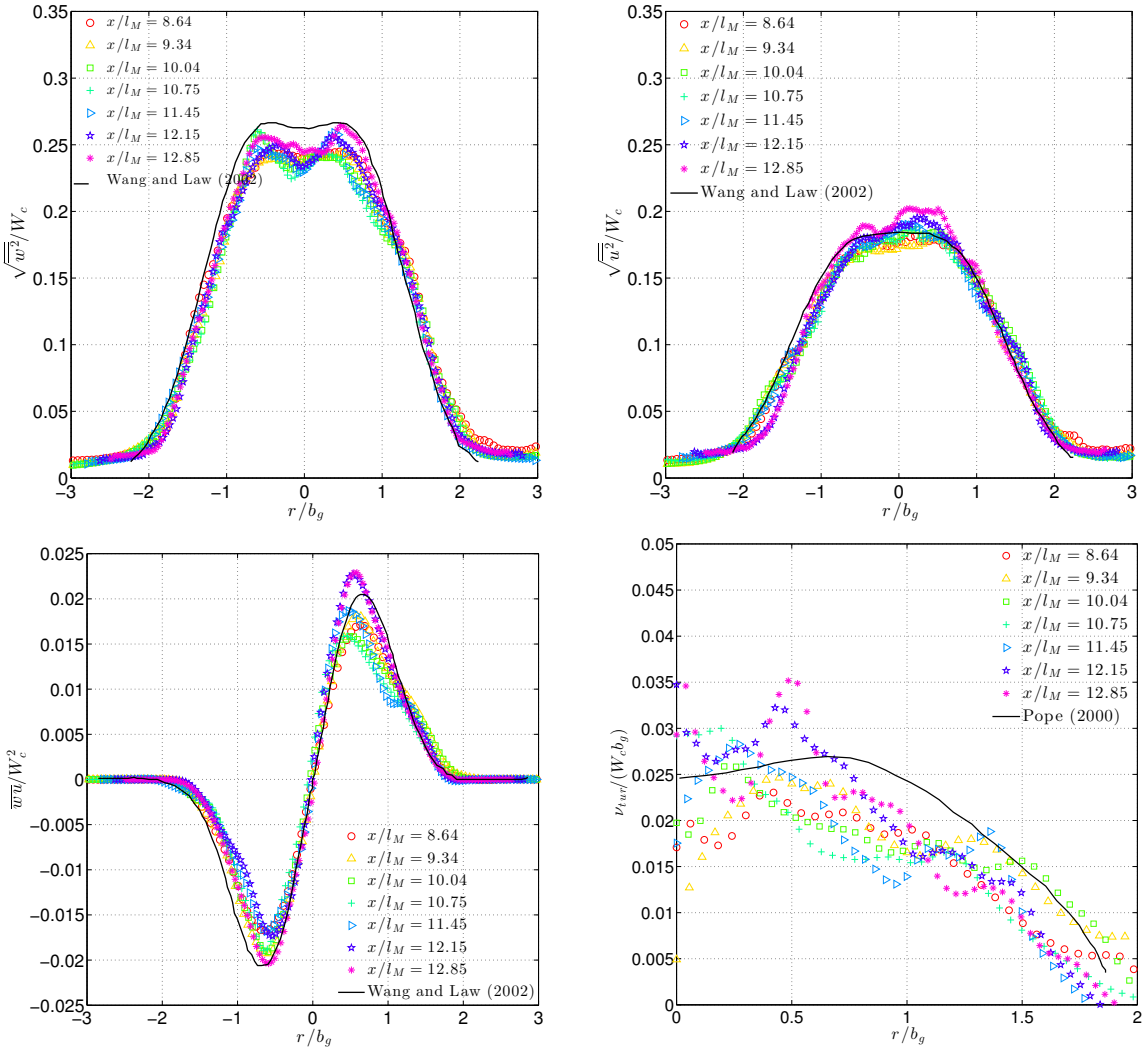

Figure 5.11: Measured turbulent stresses of a buoyant jet ($Fr = 3, D = 1.1$cm) by PIV; solid black lines are curve-fits to PIV data in Wang and Law (2002); Pope (2000) extracted hot wire anemometry (HWA) data from Hussein *et al.* (1994)

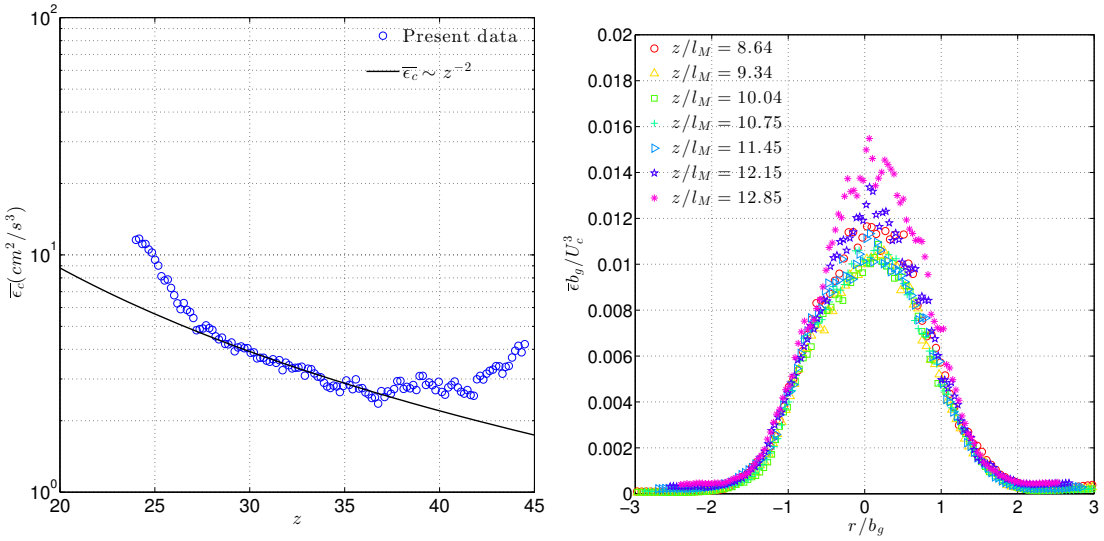

Figure 5.12: Measured turbulent dissipation rate of a buoyant jet ($Fr = 3, D = 1.1$cm) by PIV; centerline value (left panel) and radial profiles (right panel)

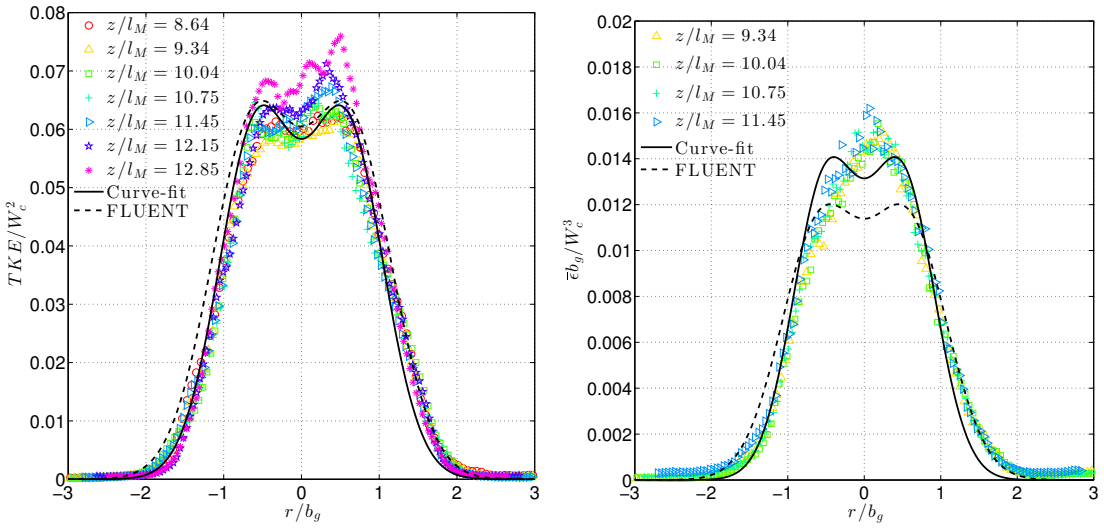

Figure 5.13: Measured TKE and adjusted dissipation rate of a buoyant jet ($Fr = 3, D = 1.1$cm) by PIV; TKE $= \frac{1}{2}(\overline{w^2} + 2\overline{u^2})$; solid black lines are double Gaussian fit to present data; dotted lines are simulation results by FLUENT of a buoyant jet in its asymptotic regime ($Fr = 5$)

reference frame moving with the center of the vortex core". Adrian, Christensen & Liu (2000) further elaborates on the second part of the definition and states that "If a turbulent field consists of large-scale motion with many small-scale vortices embedded within it, it will only be possible to recognize a vortex in terms of the foregoing definition if the velocity at the center of each small vortex is removed." While such definition is intuitively appealing, using it to search for vortices over a large dataset is impractical. A better, and conceptually more powerful, criterion is to use the swirl strength that was first proposed by Zhou, Adrian, Balachandar & Kendall (1999) in their study on open channel flows. The swirl strength will first be used to identify vortices and subsequently their associated spiraling fluid motions will be exposed by subtracting off their convection velocities. It should be aware that the PIV data is two-dimensional and therefore found vortices are only projections of actual three-dimensional structures onto the plume centerline (measurement) plane. Figure 5.14 shows such 3D structures in a turbulent round jet; they are visualized as iso-surfaces of the swirl strength and are derived from stereoscopic PIV data (Matsuda & Sakakibara 2005). A series of intermingled ring vortices can be seen in both streamwise-radial ($x - r$) and spanwise-radial ($y - z$) planes. The ring vortices appear to preferably arrange themselves in the spanwise direction and have sizes comparable to the jet radius. It can be expected that they would cut through the plume centerline plane at two locations and appear as two vortices of opposite vorticity. In an inviscid flow, both would have the same absolute vorticity because of conservation of angular momentum (second theorem of Helmholtz, see Batchelor 1967).

For the planar data, the swirl strength λ_{ci}^{+} is defined by the imaginary part of the pair of conjugated complex eigenvalues of the two-dimensional velocity gradient tensor

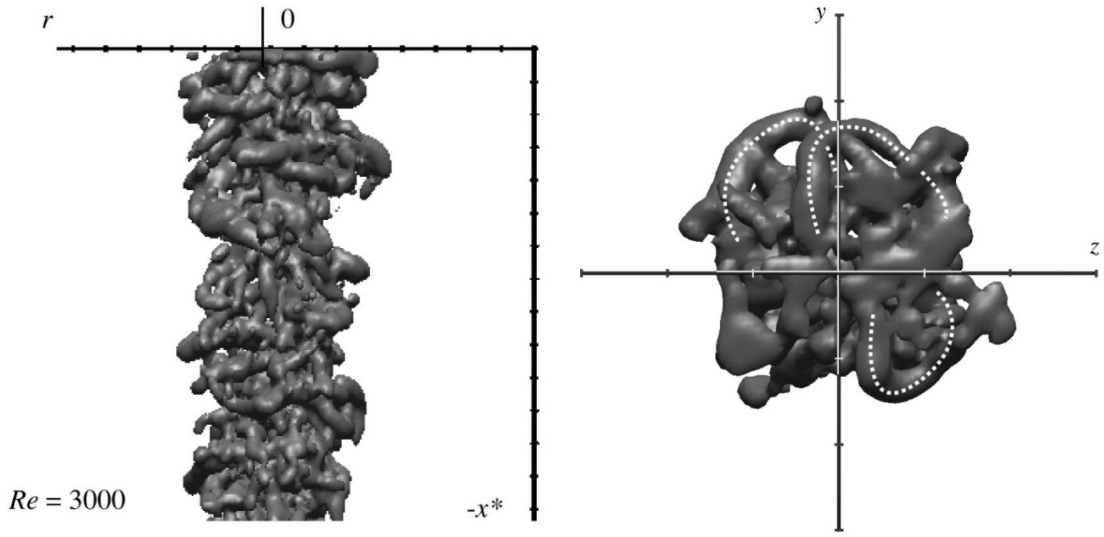

Figure 5.14: Vortical structures in a turbulent round jet ($Re = 3000, x = 30D$) captured by stereoscopic PIV, reprinted from Matsuda and Sakakibara (2005); structures are revealed by isosurfaces of swirl strength λ_{ci}; the streamwise-radial plane (left panel) and a horizontal jet cross-section (right panel)

$\nabla \tilde{\mathbf{u}}_{\mathbf{2D}}$ (Adrian et al. 2000). Only regions with significant spiraling motion, characteristic of a vortex, have complex eigenvalues. To distinguish between regions of positive and negative vorticity, the following definition is used

$$\lambda_{ci} = \lambda_{ci}^{+} \frac{\omega}{|\omega|} \tag{5.3}$$

where the out-of-plane vorticity ω is equal to $\frac{\partial \tilde{u}}{\partial z} - \frac{\partial \tilde{w}}{\partial r}$. The required velocity gradients have been evaluated by finite difference on a four-point stencil that is second-order accurate and minimizes random errors in a least-square sense (Table 6.2, Raffel, Willert, Wereley & Kompenhans 2007). Figure 5.15 shows the population statistics of computed λ_{ci}; it has the dimension of frequency $[\frac{1}{T}]$ and is normalized by b_g/W_c. It can be seen from the PDF that positive and negative values occur in equal proportion, reflecting the aforementioned generation of vortices with opposite magnitude of vorticity by the 3D structure in plume centerline plane. The cumulative density

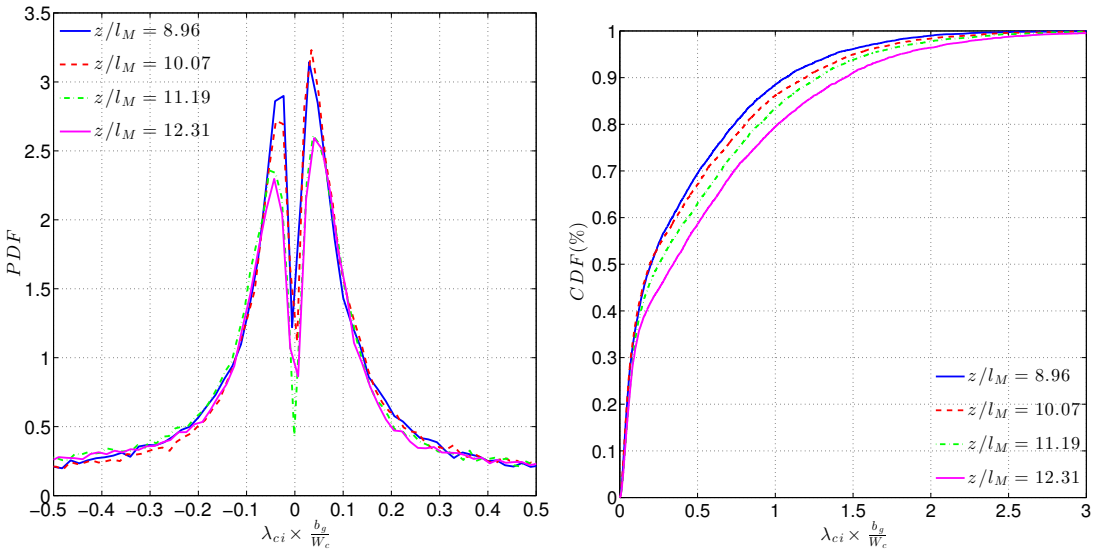

Figure 5.15: Population statistics of identified vortices by swirl strength λ_{ci}; W_c = 10cm/s and b_g = 35mm

function CDF on the right considers the absolute value $|\lambda_{ci}|$; over 95% of identified vortices have normalized swirl strength less than 2. Because of measurement and numerical errors, a threshold is needed to screen out unreliable values of λ_{ci}. The criterion used in Gao, Ortiz-Duenas & Longmire (2011) is adopted here; $|\lambda_{ci}|_{threshold}$ is set at 10% of the 99-percentile of swirl strength, which corresponds to $0.3W_c/b_g$. Referring back to the CDF, this threshold removes 45-50% of the initially computed λ_{ci}; this removal rate is common in studies of turbulent wall-bounded flows. Further, inspection on λ_{ci}-contours reveals the removed data to be mainly isolated spots that have no major impacts on large coherent vortices.

Apart from $|\lambda_{ci}|$, $|\omega|$ has also been used in the past to extract vortices. The latter suffers from the fact that high shear region also has high magnitudes of vorticity. Consider the simple case of a laminar one-dimensional flow with a linear velocity profile $\tilde{u} \sim y$ with a constant slope K, $\omega = -K$ whereas it can be shown that

the eigenvalues of $\nabla\tilde{\mathbf{u}}_{\mathbf{2D}}$ are real and equal to zero i.e. swirl strength is zero. It is clear that this simple flow has no turbulent vortices but $|\omega|$ would have suggested the otherwise. Thus, one advantage of using swirl strength is that this situation is completely avoided. Figure 5.16 shows maps of identified vortices at one particular time instant by $|\lambda_{ci}|$ and by $|\omega|$. To enhance readability, every other vector in each direction is plotted. The instantaneous 2D velocity field, after subtraction of the mean streamwise velocity field W, is also plotted to reveal the spiraling fluid motion around the vortices; the subtraction serves to remove local convection velocity of vortices, a procedure known as Reynolds-decomposition in Adrian et al. (2000). From the figure, it can be seen that both criteria extract similar number of vortices; for example, vortices in red square brackets and their associated spiraling fluid motions. A closer inspection on the contours reveals that $|\lambda_{ci}|$ gives tighter and well-defined vortices than $|\omega|$; in the dotted box A, the surrounding fluid motions support the existence of two vortices that are only identifiable by the former criterion. In terms of sizes, most vortices are between 5-7mm big and their distribution is rather uniform across the plume. A radial profile of mean vortex size will be given in the next section.

5.4.2 Vortical properties

Two properties of the vortices are of interest (i) linear dimension L (size) and (ii) circulation Γ. Procedures performed to calculate these quantities involve the following steps. *Step one*: Construct a map of swirl strength from each instantaneous velocity field and then apply the threshold, $|\lambda_{ci}|_{threshold}$. *Step two*: Convert the swirl strength map into a binary map; a point (x, y) is assigned the value one if its $\lambda_{ci} \neq 0$, otherwise, it is given a zero. *Step three*: Find and label the locations/pixels occupied by each vortex; this process is called *segmentation* in image

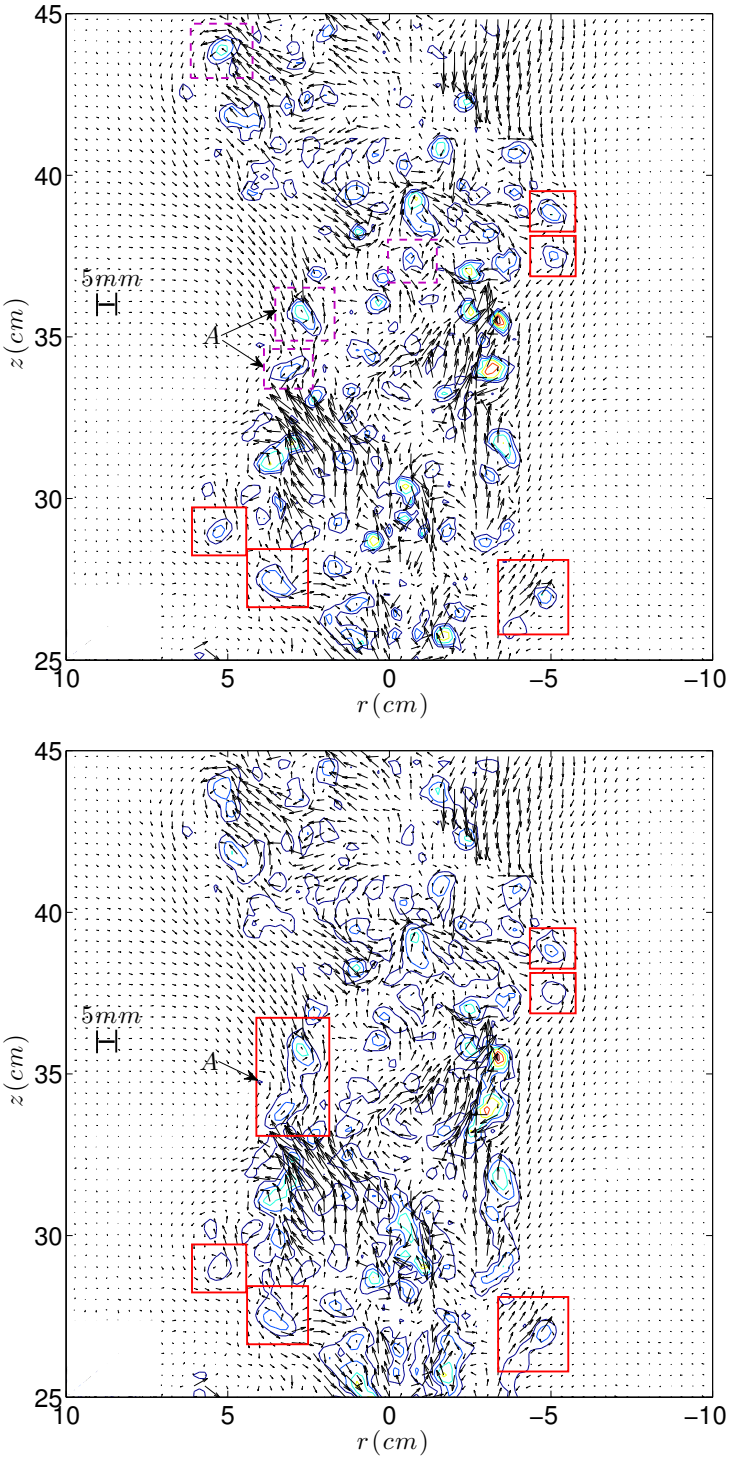

Figure 5.16: An example of identified vortices in a buoyant jet ($Fr = 3$); by absolute swirl strength $|\lambda_{ci}|$ (upper panel) and by absolute vorticity $|\omega|$ (lower panel); the instantaneous velocity field, after subtraction of the mean streamwise velocity W, is overlaid on the contours of $|\lambda_{ci}|$ and $|\omega|$; some identified vortices are indicated inside square brackets

processing and is here done by the Matlab function bwboundaries.m. The outcome is an index matrix $I(x,y)$ whose entries are integers $i \in [1,N]$ where N is the total number of identified vortices. $I(x,y) = i$ for the group of (x,y) belonging to vortex i. *Step four*: Extract corresponding values from the map of vorticity based on $I(x,y)$. It should be emphasized that results obtained in this manner is conditioned on λ_{ci}. A different set of results may arise had the vortices been extracted by other criterion, such as the second invariant, Q, of $\nabla\tilde{\mathbf{u}}_{\mathbf{2D}}$ and the Hessian of pressure (Gao et al. 2011). No systematic test was done to investigate and compare these other possibilities; the reliability of swirl strength has been well demonstrated in the cited publications. The area occupied by one velocity vector is given by $(8\text{pixels} \times 0.021\text{cm/pixel})^2 = 0.0282\text{cm}^2$ since the final iterative PIV pass is on 16-by-16 pixels windows with a 50% overlap. L and Γ of each vortex are then calculated by the following formulae, $L_i = \sqrt{\sum_{x,y}(I(x,y)/i)\delta_{ij}(x,y) \times 0.0282}$ and $\Gamma_i = \int \omega dA_i \approx \sum_{x,y} \omega(x,y)(I(x,y)/i)\delta_{ij}(x,y) \times 0.0282$ where δ_{ij} is the Kronecker delta; index j equals i whenever $I(x,y)/i = 1$. When calculating radial distribution of L, a vortex is assigned to a radial position based on its geometric center i.e. without regard to its vorticity distribution. This simplification appears to be sufficiently accurate given the approximately concentric $\omega(x,y)$-contours seen in figure 5.16.

The left panel of figure 5.17 shows the PDF of L. It is seen that a great majority of vortices measures between 4-12mm big, consistent with the observations in figure 5.16. The time and ensemble averaged $\overline{< L >}$ is shown in the right panel; <> refers to average in streamwise direction. First, the mean vortex dimension equals to $0.2b_g$ and is uniform across the plume for $|r/b_g| \leq 2$. The maximum size is also uniform and is 2.5 times the mean value, $0.5b_g$. These values can be compared to the stream-

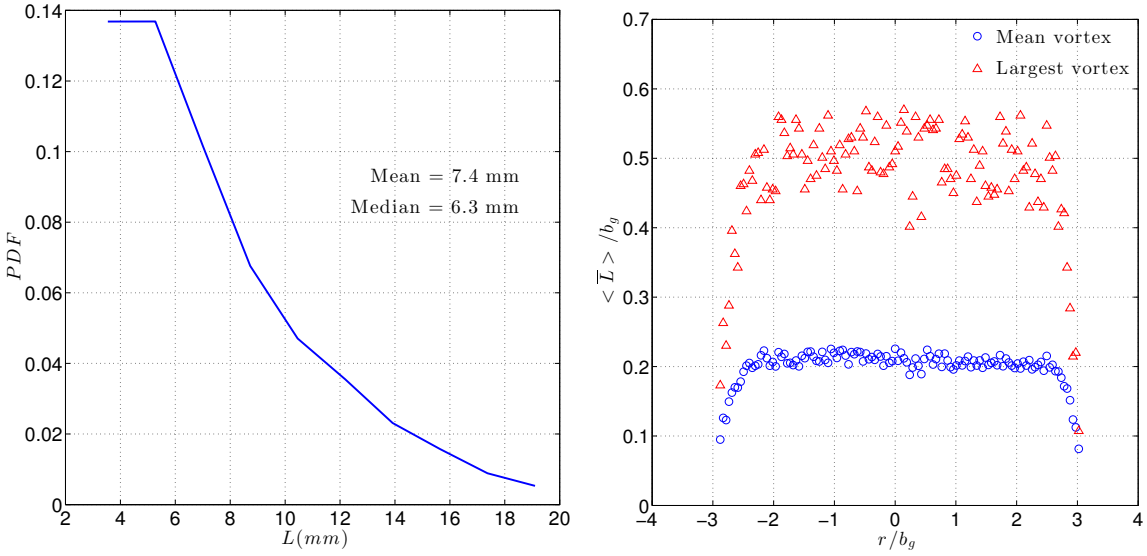

Figure 5.17: Distribution of vortex size L in a buoyant jet ($Fr = 3$) as identified by swirl strength λ_{ci}; population statistics (left panel) and radial profiles (right); $23 < z/D < 41$ and $b_g = 35$mm

wise and radial integral length scales evaluated from two-point spatial correlation functions; $L_{11} = 0.59b_g$ and $L_{22} = 0.25b_g$ (p.109, Pope 2000). It appears that the mean vortex size corresponds to L_{22} and the largest vortex is responsible for large streamwise correlation L_{11}. This uniformity of vortex size supports the well-known constancy of mixing length across jets/plumes in eddy-viscosity models (Pope 2000). Second, when compared to the data of air-water bubble plumes in Duncan et al. (2009), it is found that vortices, on average, are only half as big ($0.105b_g$) in the two-phase flow. Their maximum size is, however, comparable to the plume value ($0.45b_g$ *Vs* $0.5b_g$). The reduction of mean size is consistent with the expectation that growth of turbulent vortices is constrained by the diameter of bodies in a multi-body flow (Nepf 2012). Notwithstanding this fact is that the largest vortices are still originated from the global lateral spread of the plume and since both flows have almost the same spreading rate it is not surprising to see their largest vortices have a comparable size.

Figure 5.18 shows the radial profile of $\overline{<\Gamma>}$ in which its antisymmetry about plume center is evident. The profile peaks at the same radial position ($r/b_g \sim \pm 0.55$) as the maximum Reynolds shear stress $\overline{wu}$ (figure 5.11).The associated circulation of the mean-size vortex and the maximum-size vortex is plotted in figure 5.19. In the left panel it is seen that positive and negative values of Γ (or ω) exist in equal proportion which reflects the 3D ring structures of the plume. On average, mean-size vortices have an absolute $|\Gamma|$ of $3\text{cm}^2/\text{s}$ whilst the largest vortices have a value of $15\text{cm}^2/\text{s}$, giving a ratio of five. Since the area ratio ($\approx 14^2/7^2$) is about four, the average absolute vorticity inside the largest vortices must be 1.25 times that of the mean-size vortex, showing that regions of high vorticity need not be small. As a final comparison, the PDFs of Γ obtained in a round plume (this study) and a round jet (Agrawal & Prasad 2002) are plotted in figure 5.20; the latter dataset were obtained by 2D PIV. The jet had a Reynolds number of 4500 and measurements were taken between 175 to 263 jet diameters downstream, i.e. well in the asymptotic state. The authors used a different approach to identify vortices; instantaneous velocity field was first high-pass filtered to get rid of large, mean-flow like structures and vortices were subsequently extracted from the high-passed field by searching for closed streamlines. Using W_c and b_g to normalize Γ, the dependence of results on experimental conditions is removed and since both datasets are obtained in their respective asymptotic regime the results can be directly compared. Over the whole interval $-0.4 < \Gamma/W_c b_g < 0.4$, the PDFs are seen to be very similar despite more frequent episodes of large circulations appear to occur in the plume. A close-up on the interval $-0.1 < \Gamma/W_c b_g < 0.1$ is shown in the inset of figure. For the plume, peaks occur at $\Gamma/W_c b_g = \pm 0.02$ while they occur at ± 0.025 for the jet. Considering the differences in the identification of vortex and the overall agreement among PDFs, it can be said that statistics of normalized Γ are essentially the same in both flows.

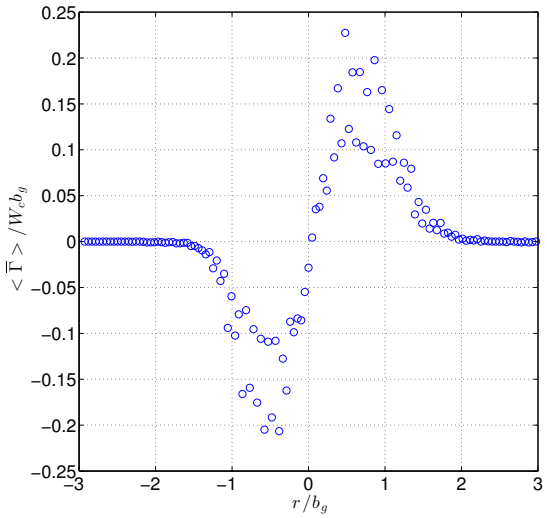

Figure 5.18: Time and ensemble-averaged circulation $\overline{<\Gamma>}$ across a buoyant jet ($Fr = 3$); $23 < z/D < 41$, $W_c = 10$cm/s and $b_g = 35$mm

Because turbulent vortices are thought to be generated by fluid instabilities, which in a plume there are two sources, buoyancy and velocity shear, while only shear exists in a jet, this experimental fact supports the understanding that the role of plume buoyancy to fluid turbulence is indirectly through its creation of mean velocity field (e.g. Wang & Law 2002).

5.5 Residual flow field behind round bubble plumes

To give a general impression of the unsteady (decaying) flow field left behind a bubble plume, this section begins with two such snapshots in figure 5.21; one of the plume core and the other of plume edge. The areal-averaged velocities, $< W >$ and $< U >$, have been subtracted from instantaneous flow fields to expose the turbulent fluctuations. The vectors have been scaled using the same ruler such that they can be directly compared among the two plots. As can be expected, velocities inside the core are higher than those near the edge. Velocity field of the core appears wavy with undulations that change rapidly their amplitudes and directions. In contrast, that of the plume edge has much weaker undulations and the flow is primarily aligned to

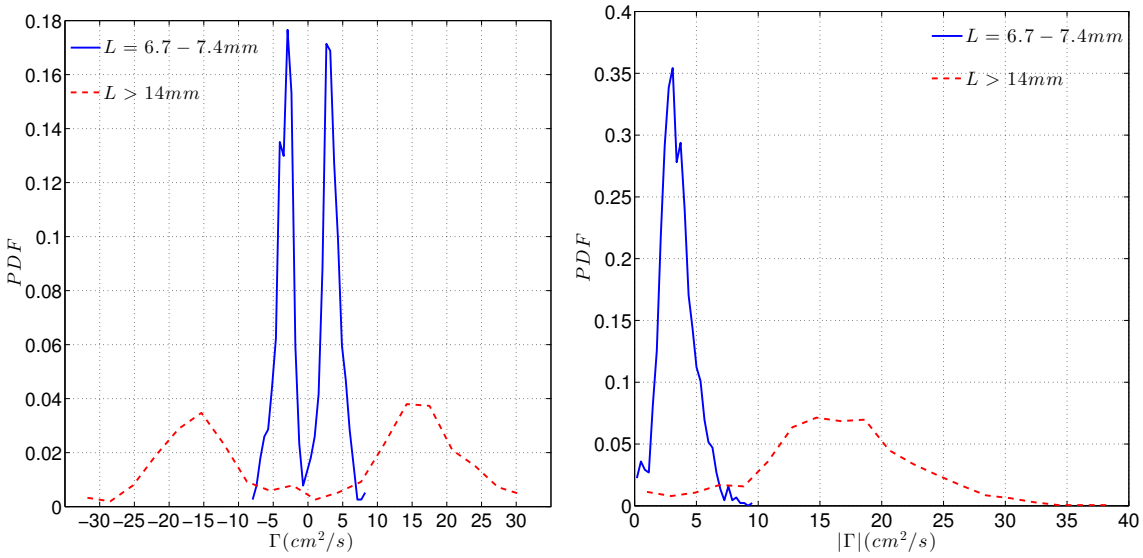

Figure 5.19: Population statistics of the circulation Γ of identified vortices in a buoyant jet ($Fr = 3$); mean vortex size = 7mm and maximum vortex size = 17.5mm

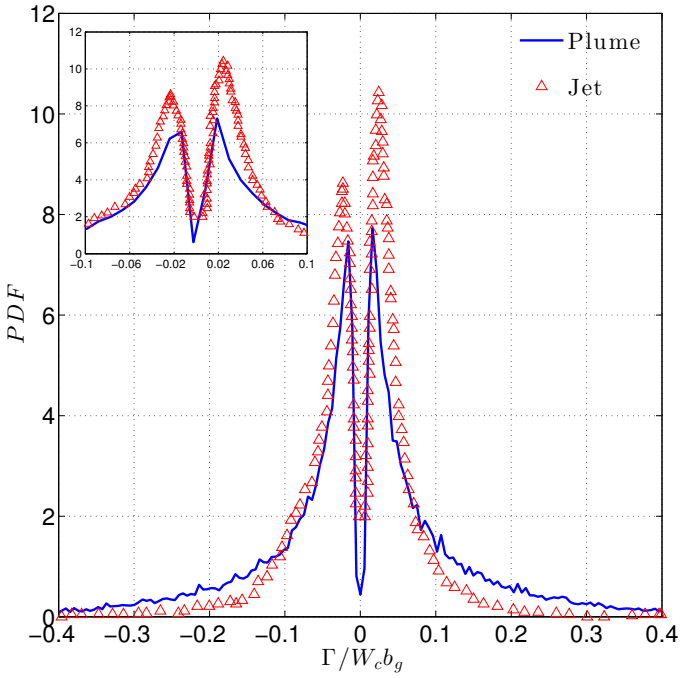

Figure 5.20: Comparison of Γ-population statistics between a plume (present study) and a jet ($Re = 4500$), both in their own asymptotic state; jet data are extracted from Argrawal and Prasad (2002)

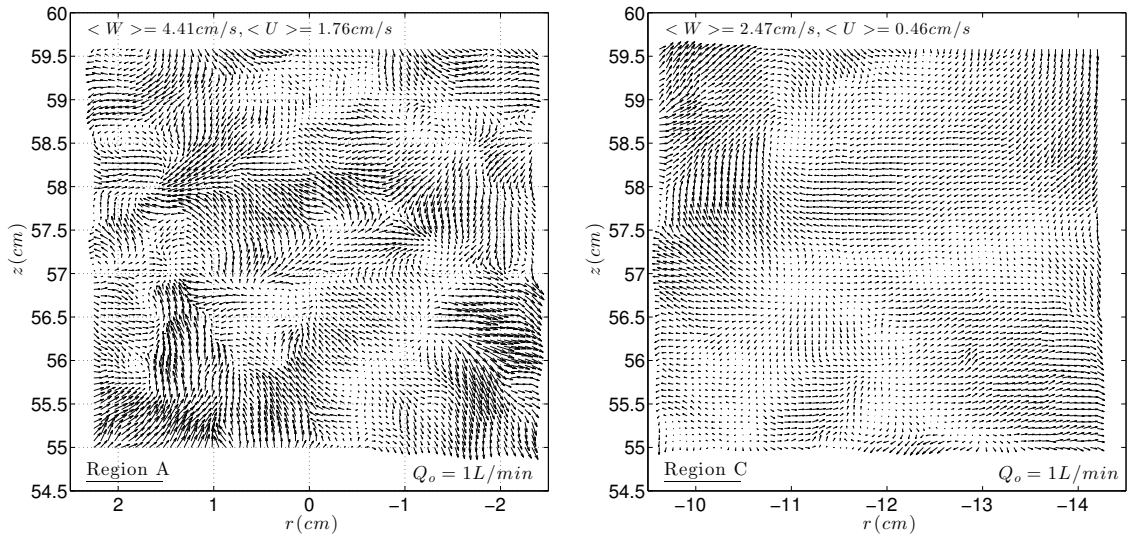

Figure 5.21: Snapshots of turbulent velocity field in the residual flow of a bubble plume; plume core (left panel) and plume edge (right panel); $< W >$ and $< U >$ are areal-averaged velocities that have been subtracted from the instantaneous flow field

the vertical. Any embedded vortices or structures would therefore be larger in the core as their stronger vorticity interact with the surrounding velocity field via the Biot-Savart law (e.g. Batchelor 1967). This expectation is supported by measured distribution of vortex size in the next section.

5.5.1 Vortical properties

Different from the previous dataset of a single-phase plume, the FOV here is a 4.5cm by 4.5cm square section and the window size of the final iterative PIV pass is 32pix by 32pix, and hence, each velocity vector occupies an area $(16 \times 0.0045)^2 = 0.005184 cm^2$. The same procedure described in section 5.4.2 has been used to extract vortices out of the instantaneous velocity fields; $|\lambda_{ci}|_{threshold} = 0.4 \text{s}^{-1}$. Figure 5.22 shows an example of the plume core, region A, for $Q_o = 1$L/min and results by both swirl strength and vorticity are again shown. The superior performance of λ_{ci} in defining a vortex can be seen. There are areas simultaneously having high vorticity and zero swirl strength (white areas in left panel); velocity shear is high in these regions. Vortices

are between 2 to 6mm large. It also appears that the spacing between vortices in a bubble plume is smaller than in a single-phase plume, see figure 5.16. The PDFs of vortex size for all Q_o are plotted in figure 5.23 where the equivalent diameter d_e is used to facilitate a comparison with the PDF of bubble diameters (figure 2.2). First, all PDFs collapse onto one curve in which d_e mostly falls between 2 to 8mm. A significant portion, 73%, of d_e lies between 2-4mm which is also the range of bubble diameters measured. This reflects a constrained turbulent vortex growth due to the presence of bubble wakes. Second, the mean vortex linear dimension L is equal to $0.06b_g$ and is uniform across the plume core. Recalling the results in previous section, the ratio of L formed between the data obtained here, Duncan et al. (2009) and the single-phase plume is $1 : \frac{0.105}{0.06} : \frac{0.2}{0.06}$ = 1:1.75:3.33; the present bubble plume data is only 60% of that in Duncan et al. (2009). This difference maybe caused by a larger vector spacing, 1.2mm, in their PIV experiments than the present value of 0.72mm. On the other hand, the ratio of maximum L formed from the three datasets is $1 : \frac{0.45}{0.16} : \frac{0.5}{0.16}$ = 1:2.81:3.13; Duncan's result would have predicted a maximum value of 0.45(6.27cm) = 2.82cm. This prediction is at odds with the observations in figure 5.22; the present spatial resolution (0.72mm) is more than adequate to capture such a large vortex had there been one.

Moving outside the plume core, smaller vortices are more frequently observed; figure 5.24 shows an example for Q_o = 1L/min on the interval $r \in [-10, 14]$cm, region C. Except for the few largest ones, majority of the vortices have size comparable to the bubble diameter d_{50} = 2.4mm. Inspection on the PDFs of equivalent diameter in figure 5.25 reveals that over 90% of the diameters is smaller than 4mm; the value is 73% in the plume core. Indeed, the mean vortex size L is about 20% smaller, $0.05b_g$ *Vs* $0.06b_g$. Maximum L, however, remains similar albeit a larger scatter in

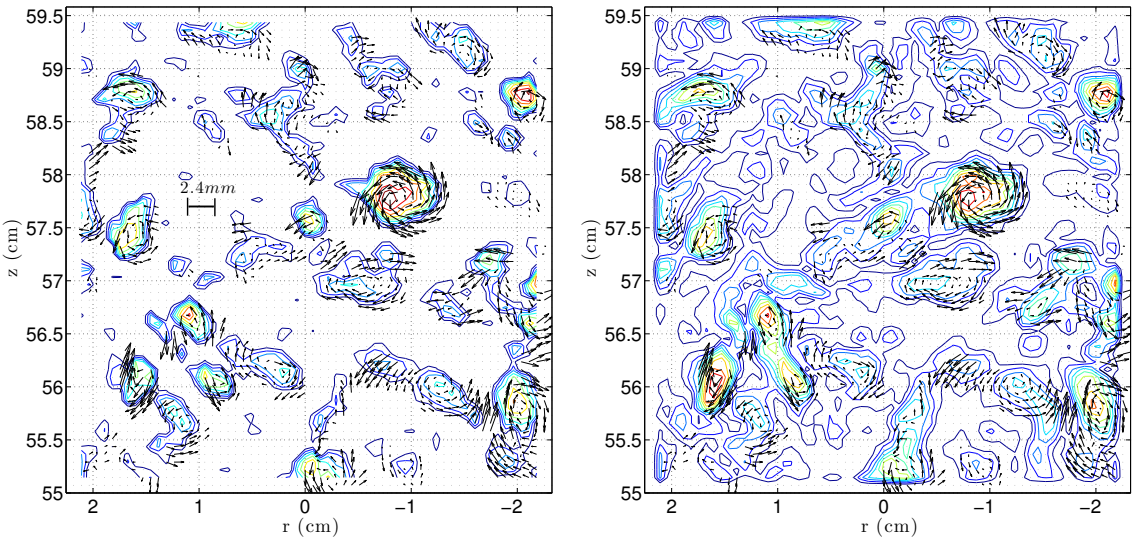

Figure 5.22: An example of identified vortices in the core of a bubble plume ($Q_o = 1L/min, D = 13.6cm$); by $|\lambda_{ci}|$ (left panel) and by $|\omega|$ (right panel)

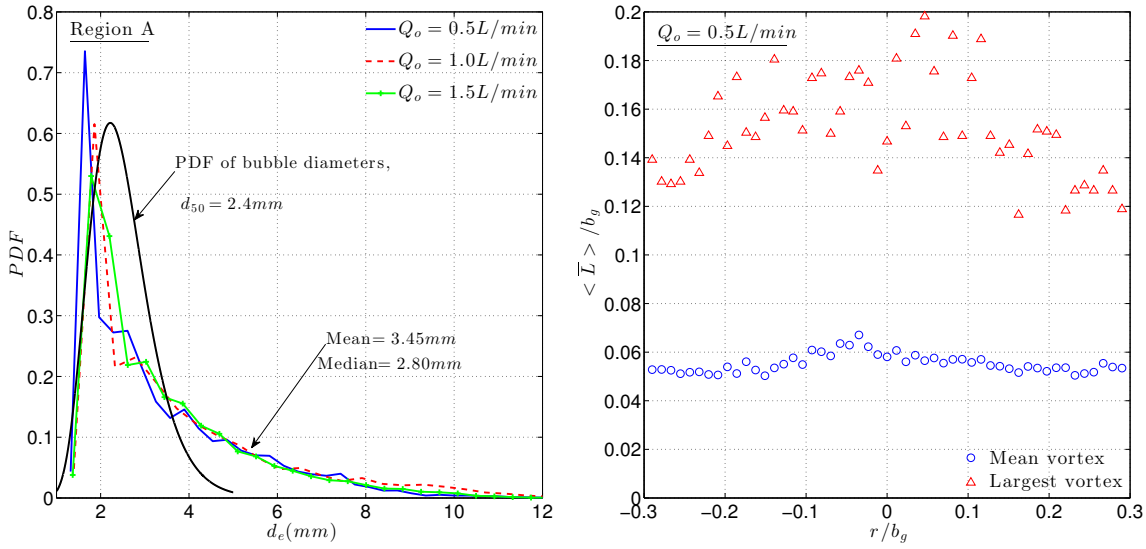

Figure 5.23: Distribution of vortex size in the core of bubble plumes as identified by swirl strength $|\lambda_{ci}|$; population statistics (left panel) and radial profiles (right); $b_g = 62.7$mm

the data. These observations suggest that despite a higher degree of wake-to-wake interactions in the core turbulent vortices would still pair-up and grow in size on the average. The very large vortices at plume edge may have been the result of their lateral migration from the core. And, it is clear that the overall distribution of sizes is set by that of the bubble diameters.

Bubbles can break into smaller fragments by turbulence and velocity gradients in a given flow via turbulent fragmentation (Deane & Stokes 2002). The mechanism by which this occur is when the differential pressure forces across the bubble exceed the restoring forces of surface tension. The Hinze scale a_H defines the critical radius above which fragmentation would occur and is given by the following expression.

$$a_H = 2^{-8/5}\epsilon^{2/5}(\gamma We_c/\rho)^{3/5} \tag{5.4}$$

where ϵ = time-averaged turbulent dissipation rate, γ = fluid surface surface tension, $We_c = 4.7$ = critical Weber number (Deane & Stokes 2002) and ρ = fluid density. For dispersed air bubbles in water at about 20 degree Celsius, $\gamma \approx 72 \times 10^{-3}$N/m and $\rho = 998.2$kg/m^3. The averaged dissipation rate can be estimated from the results in section 2, $\epsilon \approx 0.05 W_c^3/b_g = 0.05(0.25^3/0.114/0.5) = 0.0137$m^2/s^3. The Hinze scale is therefore 15.2mm; in other words, bubbles with diameter larger than about 30mm are likely to breakup. Referring back to the pdf of observed bubble diameters, $2a_H$ is seen to be larger and hence the size of bubbles are stable under fluid shear and turbulence.

5.5.2 Subgrid scale (SGS) dissipation

The PIV data can be used to estimate subgrid-scale (SGS) dissipation or energy flux from resolved spatial scales to unresolved ones, which is a key parameter that

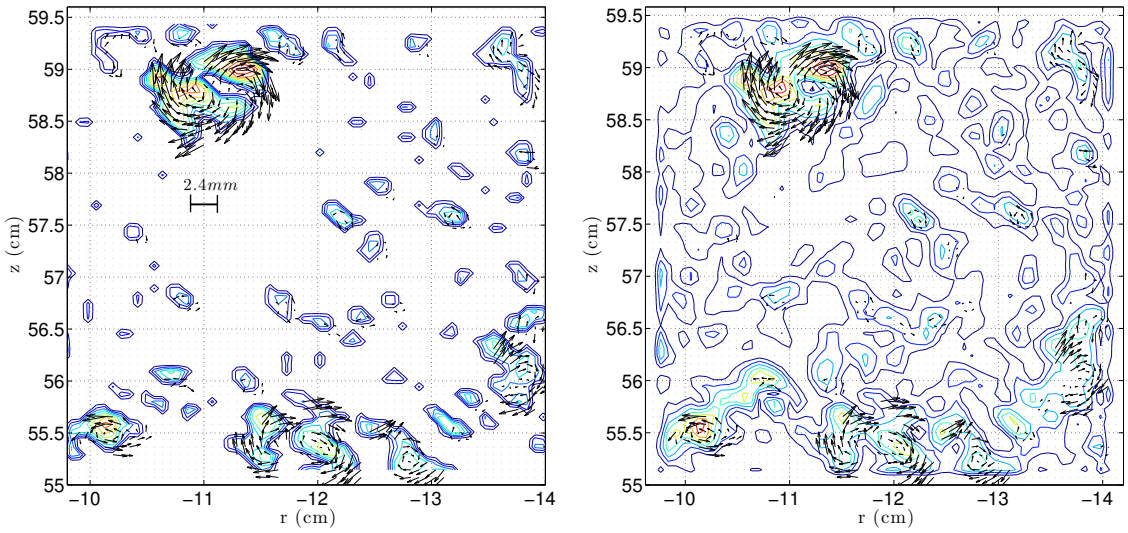

Figure 5.24: An example of identified vortices in the edge of a bubble plume ($Q_o = 1L/min, D = 13.6cm$); by $|\lambda_{ci}|$ (left panel) and by $|\omega|$ (right panel)

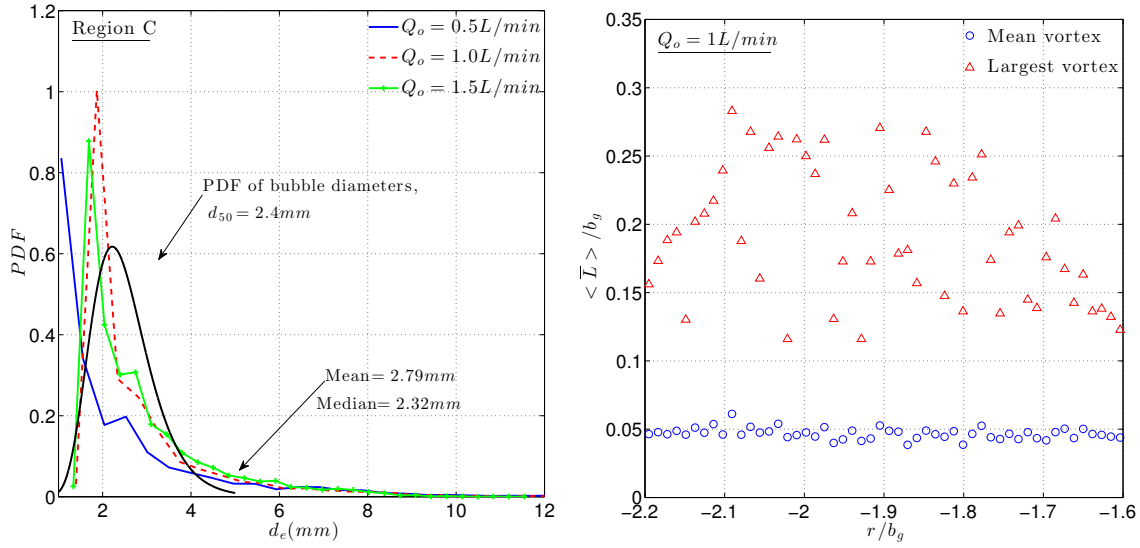

Figure 5.25: Distribution of vortex size in the edge of bubble plumes as identified by swirl strength $|\lambda_{ci}|$; population statistics (left panel) and radial profiles (right); $b_g = 62.7$mm

SGS stress models in large eddy simulation (LES) attempt to reproduce. It is computed here to elucidate the direction of energy transfer, i.e. to determine if the usual Kolmogorov-forward cascade picture is seen (Davidson 2015) or would a backward cascade that transfers energy from small to large scales sometimes occur. It is emphasized that the overall cascade must be forward as fluid energy does not grow without bound in nature. In LES, the Navier-Stokes equations after spatial filtering over a scale $\triangle$ produce the subgrid-scale stress tensor $\tau_{ij} = \widetilde{u_i u_j} - \tilde{u}_i \tilde{u}_j$ (Pope 2000); note the change of notation in this section, tilde represents a spatial filtering on $\triangle$ and u_i, u_j are instantaneous velocity components. The instantaneous subgrid-scale dissipation ϵ_{SG} is given by $-\tau_{ij}\widetilde{S_{ij}}$ where $\widetilde{S_{ij}} = \frac{1}{2}(\frac{\partial \tilde{u_i}}{\partial x_j} + \frac{\partial \tilde{u_j}}{\partial x_i})$ is the filtered rate-of-strain. A theoretical result for homogeneous, isotropic turbulence is that the ensemble averaged SGS dissipation, $< \epsilon_{SG} >$, is almost equal to the total viscous dissipation ϵ (Pope 2000). To compute ϵ_{SG} from the planar PIV data, the following equation proposed by Nimmo Smith et al. (2005) is used.

$$\epsilon_{SG} = -\tau_{ij}\widetilde{S_{ij}} \approx= -\frac{1}{2}(\tau_{11}\widetilde{S_{11}} + \tau_{33}\widetilde{S_{33}} - \tau_{11}\widetilde{S_{33}} - \tau_{33}\widetilde{S_{11}} + 12\tau_{13}\widetilde{S_{13}}) \tag{5.5}$$

Different from ϵ, values of instantaneous ϵ_{SG} can be either positive or negative. A positive value signifies energy flux from large to small scales whereas a negative value signifies a backward energy transfer from small to large scales. These concepts are first discussed with the single-phase plume dataset.

Figure 5.26 shows a typical spatial map of $\epsilon_{SG}(\mathbf{x}, t)$ in a single-phase plume at one particular time. The results are that of a 2D box filter of size 20-by-20 vector spacings and since the Kolmogorov length scale η is 0.22mm this corresponds

to an area of 144η-by-144η. To distinguish between regions of forward and backward energy cascade, locations (pixels) with $\epsilon_{SG}(\mathbf{x},t) > 0$ are colored blue and those with $\epsilon_{SG}(\mathbf{x},t) < 0$ are colored red; white regions are areas with $|\epsilon_{SG}(\mathbf{x},t)| < |\epsilon_{SG}(\mathbf{x},t)|_{threshold} = 1\text{cm}^2/\text{s}^3$ that are deemed to have negligible energy transfer. Such thresholding is need due to measurement and numerical errors. Contours of $\epsilon_{SG}(\mathbf{x},t)$ are plotted in the right panel. First, it can be noticed that energy transfer, hence dissipation, is highly intermittent in space and there are more areas having a forward cascade. Second, in terms of magnitude, the energy flux from small to large scale is much weaker than that in the opposite direction. Third, it appears that both forward and backward cascade co-exist in a plume, and perhaps in other turbulent flows as well, in spite of the classical isotropic $-5/3$-spectral slope seen in its velocity spectra. An overall cascading direction can be obtained from the areal-average $< \cdot >$ of $\epsilon_{SG}(\mathbf{x},t)$, which is plotted as $< \epsilon_{SG}(t) >$, a function of time, in figure 5.27. Results for three different box filter size $\triangle$ are shown. It is clear that the overall direction is forward at all times, lending support to the $-5/3$ slope. The result for different filter size represents the energy flux from the scale of $\triangle$ to scales smaller than itself. For $\triangle = 10$ and 20, $< \epsilon_{SG}(t) >$ is almost identical, meaning that these two scales carry the same amount of energy flux and belongs to the inertial subrange, i.e. in the spectral energy transfer pipeline (chapter 6, Pope 2000). The smallest filter size $\triangle = 5$, however, shows noticeable discrepancies. This is because it has stepped inside the dissipative range where fluid energy is removed by viscosity; it has already been shown in an early part of this section that the peak of dissipation spectrum occurs at a spatial scale of 50η. These results are all consistent with the classical Kolmogorov-Richardson phenomenology for turbulence (Davidson 2015). In LES, using a filter size comparable to the dissipative scales is rare since it would mean almost all scales are resolved in the simulations which renders LES into DNS and

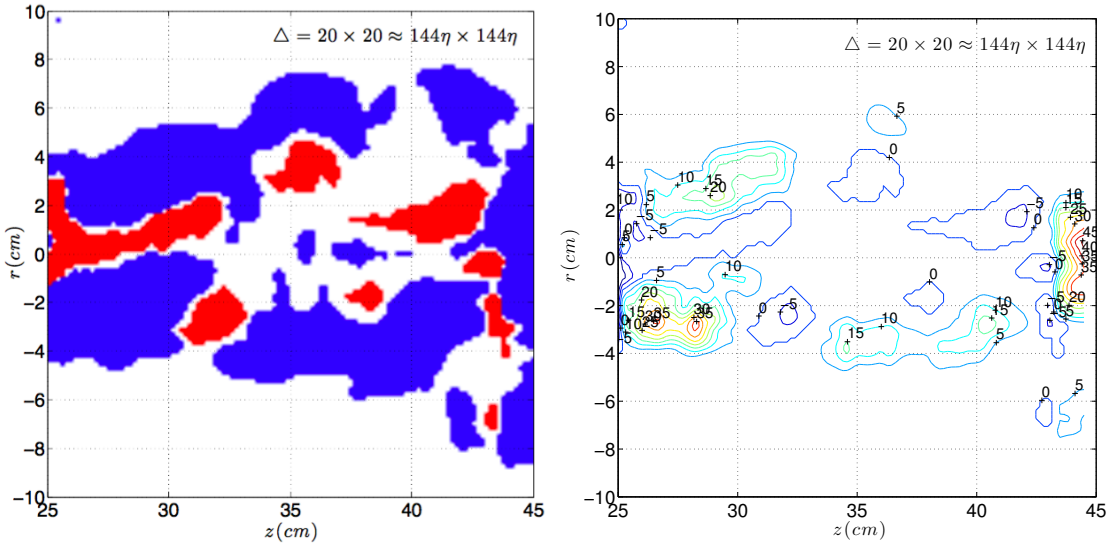

Figure 5.26: Instantaneous subgrid scale dissipation $\epsilon_{SG}(\mathbf{x}, t)$, calculated with a box filter $\triangle = 20 \times 20 = 144\eta \times 144\eta$, in a buoyant jet ($Fr = 3, 5 l_M = 15$cm); direction of energy cascade (left panel), forward (blue) and backward (red); contours of ϵ_{SG} (right panel)

loses its computational advantage. In terms of vortical structures inside the plume, the spiraling fluid motion associated with each identified vortex is plotted above the contours of $|\epsilon_{SG}(\mathbf{x}, t)|$ in figure 5.28. As can be expected, there is a high correlation between vortices and dissipation; stronger vortices are more dissipative.

Figure 5.29 shows the areal-averaged $< \epsilon_{SG}(t) >$ of the residual flow field behind a bubble plume ($Q_o = 1$L/min). A drastic difference with the results of a single-phase plume can be seen in the core and the edge; backward cascade is common and occurs intermittently (in time) over a range of spatial scales, 3.6-28.8mm (FOV is a 4.6cm square). To gain further insights, spatial maps of $\epsilon_{SG}(\mathbf{x}, t)$ at two times, $t = 0.65$s and $t = 2$s, are plotted in figure 5.30 and 5.31. The former corresponds to a negative maximum of $< \epsilon_{SG}(t) >$ whereas the latter corresponds to $< \epsilon_{SG}(t) > \approx 0$. Results of two filter size are shown and, similar to earlier plots, the spiraling fluid motion

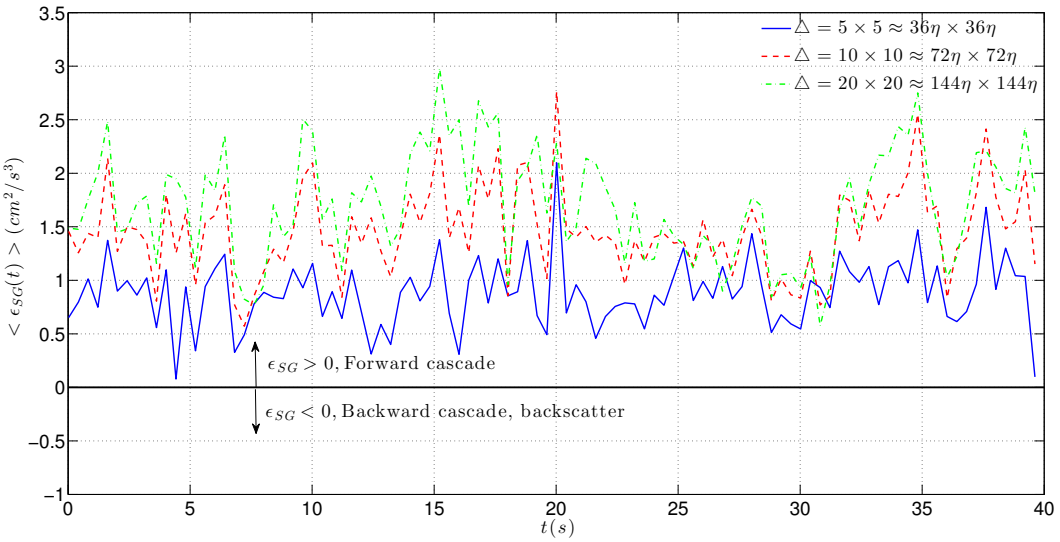

Figure 5.27: Areal-averaged instantaneous subgrid scale dissipation $< \epsilon_{SG}(t) >$ in a buoyant jet ($Fr = 3, 5 l_M = 15$cm); results from different box filters of various sizes

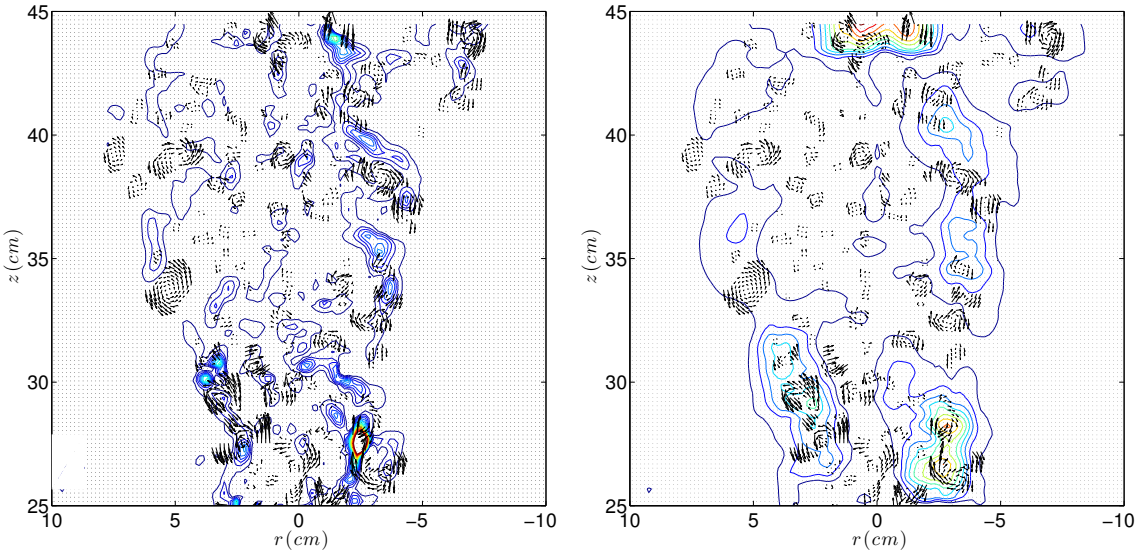

Figure 5.28: Instantaneous subgrid scale dissipation (absolute magnitude) $|\epsilon_{SG}(\mathbf{x}, t)|$ overlaid with the velocity field of identified vortices in a buoyant jet ($Fr = 3, 5 l_M = 15$cm); box filter $\triangle = 5 \times 5 = 36\eta \times 36\eta$ (left panel) and $\triangle = 20 \times 20 = 144\eta \times 144\eta$ (right panel)

of identified vortices is included in the figures; the high correlation between vortex motion and SGS dissipation (energy flux) should be noted. At $t = 2$s, negative energy fluxes (backward cascade, in different shades of blue) occupy similar area to that of positive fluxes (forward cascade, in different shades of red) and the magnitudes of both are comparable, in contrast to the dominance of forward cascade in the single-phase plume. Also, regions of high magnitudes of forward and backward cascade appear to pair-up. A completely different situation occurs at $t = 0.65$s where it can be seen that backward cascade occupies a larger area and is of higher magnitudes than its surrounding forward counterparts. The situation is very similar for both filter size. Similar results are found for the other two flowrates, $Q_o = 0.5$ and 1.5L/min.

5.5.3 Auto-spectral density function - velocity spectrum

Figure 5.32 shows the auto-spectral density function $E_{ii}(\lambda_1)$ of the residual flow for all three air flowrates. First, at the plume core (region A), E_{ww} and E_{uu} have a distinctive -8/3-spectral slope for the range of λ_1 between 300-1000m^{-1}, i.e. 3-10mm. Referring back to the distribution of vortex diameters d_e in figure 5.23, this range of spatial scales (λ_1) agrees that of d_e. Together with the spatial maps of $\epsilon_{SG}(\mathbf{x}, t)$, it is then apparaent that vortices shed behind bubbles, which are associated with large magnitudes of both forward and backward cascade, are plausible explanation to the observed -8/3 or -3 spectral slope in bubbly flows. Second, at the plume edge (region C), both velocity spectra show the classic -5/3-spectral slope, indicating that the turbulent characteristics of external flow is different from the core and majority of the vortices is probably not originated from the bubbles.

5.6 Summary and discussions

This section has investigated experimentally the unsteady turbulent properties of the residual flow left behind a bubble plume after an abrupt shut-off of gas inflow. The

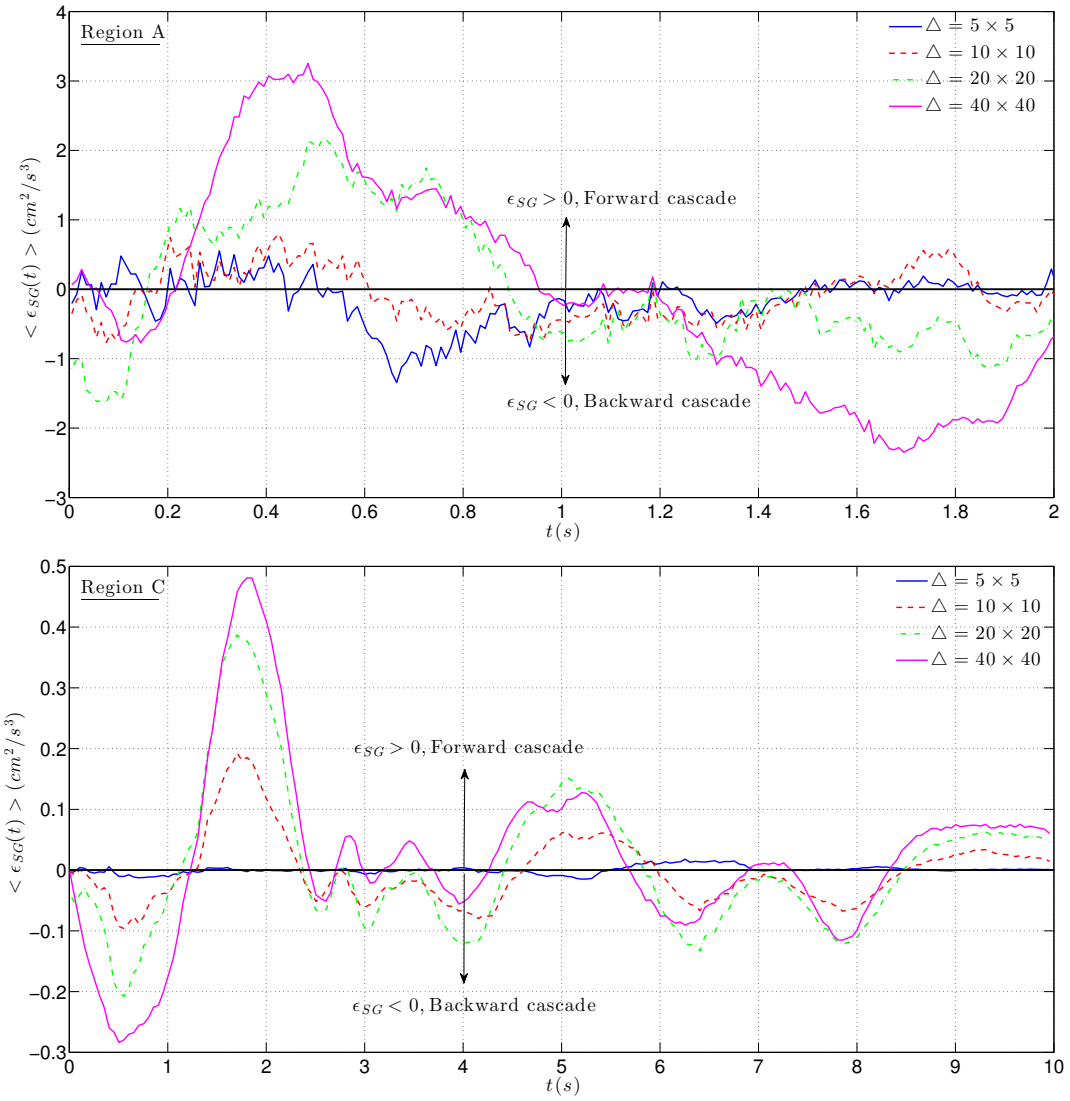

Figure 5.29: Areal-averaged instantaneous subgrid scale dissipation $< \epsilon_{SG}(t) >$ in a bubble plume (Q_o = 1L/min); plume core (upper panel) and plume edge (lower panel)

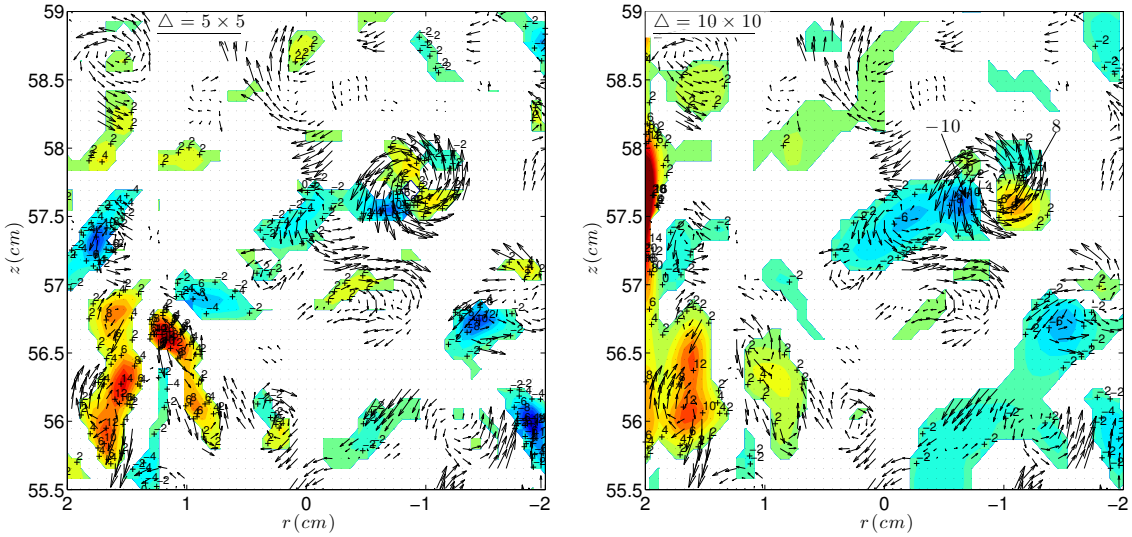

Figure 5.30: Maps of instantaneous $\epsilon_{SG}(\mathbf{x}, t)$ in the plume core (region A) at $t = 2$s in figure 5.29; two box filter sizes, $\triangle = 5 \times 5$ (left panel) and $\triangle = 10 \times 10$ (right panel)

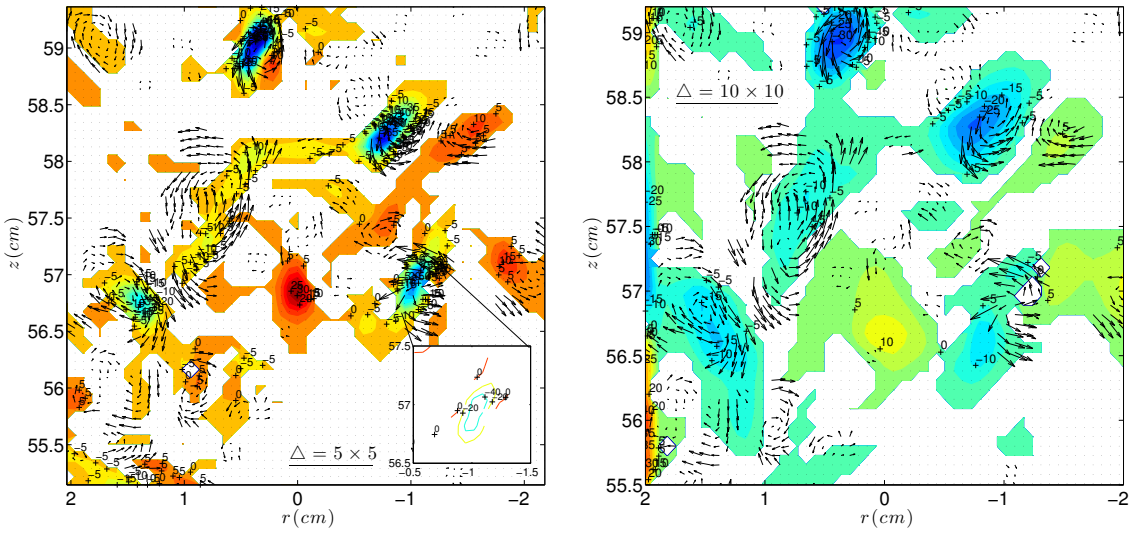

Figure 5.31: Maps of instantaneous $\epsilon_{SG}(\mathbf{x}, t)$ in the plume core (region A) at $t = 0.65$s in figure 5.29; two box filter sizes, $\triangle = 5 \times 5$ (left panel) and $\triangle = 10 \times 10$ (right panel)

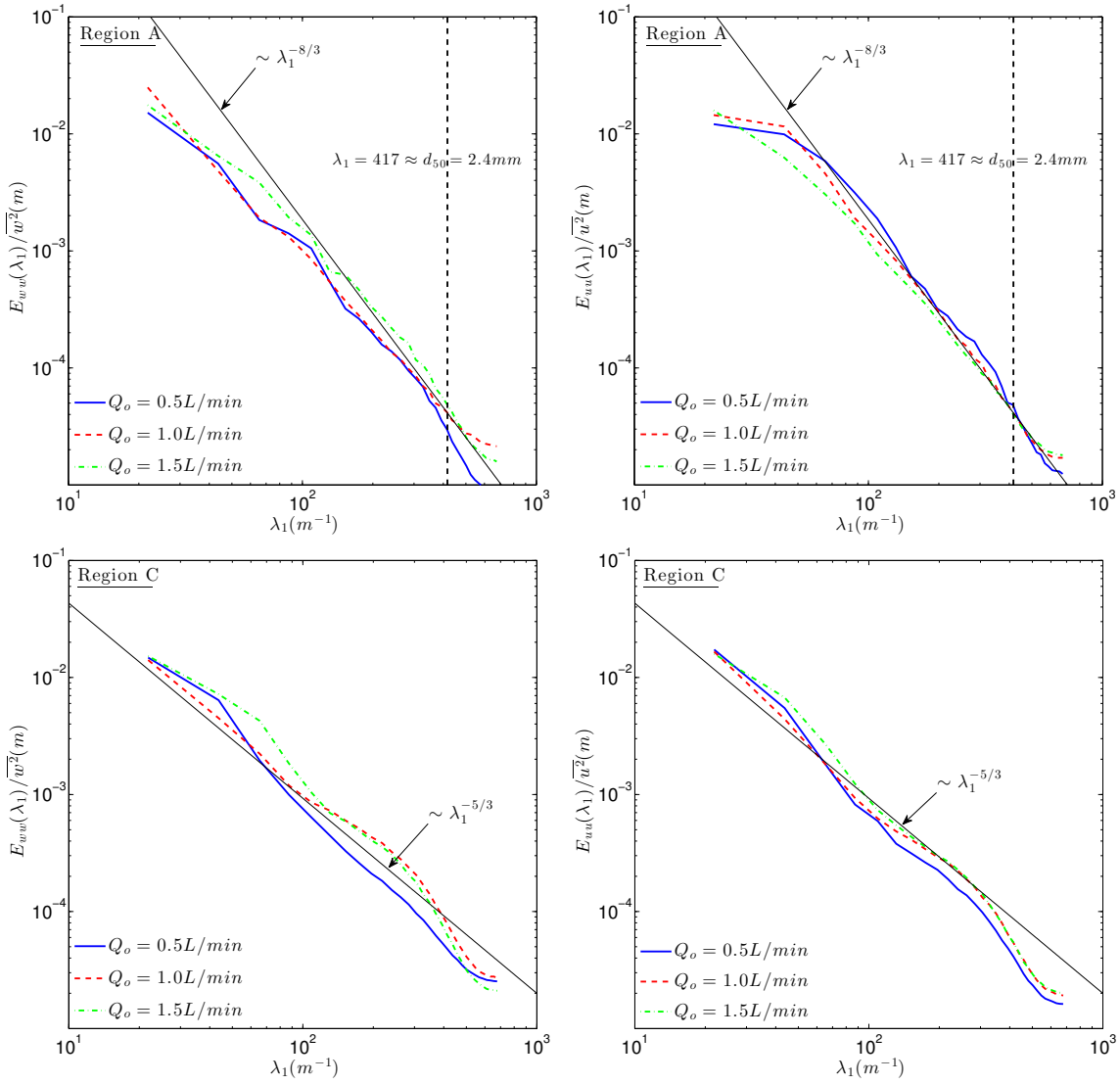

Figure 5.32: Auto-spectral density function $E_{ii}(\lambda_1)$ in the residual flow behind a bubble plume; plume core (upper panel) and plume edge (lower panel)

residual flow is considered as a proxy to the flow inside a steady bubble plume whose measurements pose challenges to optical techniques such as PIV and laser-induced fluorescence (LIF). Two single-phase jet/plume experiments have been carried out to test the chosen parameters of the PIV system and to provide a basis for comparison with the results of residual flow. A correction method for under-resolved mean-square velocity gradients in the calculation of turbulent dissipation rate is proposed and obtained data for the single-phase flows are shown to satisfy (to within $\pm 5\%$) the bulk kinetic energy balance equation presented in section 4.

Properties of turbulence have been extracted from the instantaneous velocity field by swirl strength, which identifies vortices, and by subgrid scale energy flux which elucidates energy transfer at different spatial scales. A comparison with the single-phase plume reveals the following, in the bubble plume: (i) turbulent vortices are smaller and their growth is constrained by bubble diameters; on average they are only half as big (ii) backward energy cascade is common and it can have magnitudes comparable to forward cascade and (iii) the distinctive -8/3 or -3 spectral slope seen in the velocity spectra of bubbly flows can be explained by the large backward energy cascade. For (iii), it is mentioned at the beginning of this section that the one-dimensional theoretical model by Risso (2011) predicts the existence of a -3 slope over the range of wavenumbers defined by the maximum and minimum diameters of bubbles. Present experimental results and those of Lance & Bataille (1991) and Riboux et al. (2010) confirm with this prediction. More significantly, its existence in both bubble plume and bubble column suggests that the interaction of bubble wakes is similar in the two flows and is largely independent of fluid shear.

6. CONCLUSIONS

6.1 Summary of present findings

In section 2, fluid turbulence in the two-phase air-water bubble plume has been investigated experimentally in this dissertation. Experiments were performed in a $1m^3$ cubic water tank. The ambient water was initially motionless and unstratified. Air bubbles, with a median diameter $d_{50} = 2.4$mm, were released through an aquarium airstone positioned at the center of tank bottom face (figure 2.1). The required three-dimensional velocity field was measured by a new generation of acoustic Doppler velocimeter (ADV) - the Nortek *Vectrino II* with profiling capability (Craig et al. 2011). A budget of the turbulent kinetic energy across the plume was performed with the data. Major findings are,

1. Contrary to the common belief that single-point ADVs are not capable of measurements in bubbly flows, fluid velocities registered by *Vectrino II* have been shown heuristically to be physical. The so-called non-physical "spikes" that occur in a time series are either caused by return fluid flow due to rising bubbles or bubble wakes. At the center of bubble plumes, these two components account for 20-25% of the total data while the bulk entrained flow accounts for the remaining 75-80%. Their contributions decrease steadily away from plume center and account for 5-7.5% near plume edge ($r/b_g = 1$). Capturing these large velocity fluctuations are important in performing a TKE budget.

2. Mean flow data establish the existence of an asymptotic regime when $z/D > 8$, D is the dynamic length scale defined in equation (2.1), with an entrainment coefficient of 0.095 and a densimetric Froude number of 1.63. The present

laboratory scale data also corroborate well with published data of large scale bubble plumes when the slip velocity u_s and D are used to non-dimensionlized relevant quantities; the combined dataset spans $0.01 < z/D < 11$. Turbulent stresses are highly anisotropic inside a bubble plume; vertical turbulent intensity $\sqrt{\overline{w^2}}$ is 2.2-2.6 times the horizontal one $\sqrt{\overline{u^2}}$. Similar to other single-phase shear layer flows (e.g. jet, wakes), stress profiles show a off-center peak at $r/b_g \sim 0.55$, indicating intense TKE production near plume edges.

3. Based on the analysis in section 4 and measured profiles of TKE and dissipation rate ϵ, the bulk kinetic energy balance, after correction for underestimated ϵ, is satisfied to within 11% in the plume asymptotic regime ($z/D > 8$). TKE production by bubbles is parametrized as $P_B = C_B \alpha_g [\frac{3}{4}\frac{C_D}{d_{50}}(\overline{w_g - w_l})^2](\overline{w_g - w_l})$ which is essentially the work done by bubble drag; the coefficient $C_B < 1$ assigns a fraction of work done to production. From the budget, C_B is found to 0.55-0.60.

In section 3, the development of an interpolation method for missing data in velocity time series of fluid turbulence is proposed; its aim is to preserve the magnitude and shape of auto-spectral density function. The method is applicable to any datasets that follow a *signal + white noise* model; examples include ADV and PIV. It is based on the observation that a first-order autoregressive AR(1) model is a good proxy for classic turbulent flows i.e. with the -5/3 isotropic slope in their spectra. The AR(1) model can be used to predict the values of missing data; in the terminology of time-series modeling this is known as *in-sample forecasting*. Under this framework, the zeroth-order sample and hold (S&H) interpolation has been shown to be the limiting case of an AR(1) process when the sampling (data) interval is much smaller than the flow integral time scale; the theoretical underpinning of S&H is shown for the

first time. When the data interval is not sufficiently small, S&H is not adequate and the AR(1) model must be used. Extension to cases showing non-classic behavior, e.g. -8/3-spectral slope in multiphase flows, has been demonstrated to be equally successful with a set numerical simulations.

In section 4, a balance equation of bulk kinetic energy (KE) in the flow of a single phase jet/plume is derived using the jet/plume integral framework. The derivation is first motivated by considering the change of KE over a time interval $\triangle t$ of a Lagrangian element moving along the jet axis. The connection to Eulerian laboratory measurements is then explained and validity of the equation is tested using PIV data of a jet (section 5) and FLUENT simulation results of a plume. Extension to the two-phase bubble plume is illustrated and the balance is found to be satisfied to within 11% with the measurements in section 2.

In section 5, residual flow field behind a bubble plume has been investigated using particle image velocimetry (PIV). Congruent with reported data of homogeneous bubble swarms, a distinctive -8/3 (slightly milder than -3) spectral slope is observed in the plume core for both vertical (streamwise) and horizontal (radial) auto-spectral density functions (velocity spectra), indicating the similarity of large-scale wake structures behind bubbles in both flows. The spectra, when normalized by their respective variance, collapse onto each other which means that they are not dependent on air void fraction. A combined analysis of vortical structures and sub-grid scale energy flux reveals that the vortices are accompanied by strong backward energy cascade that can at times occupy a large fraction of the measurement area, i.e plume volume. It is believed that this is the cause of the -8/3 or -3 spectral slope observed in bubbly flows. Further, the size of vortices is constrained by that

of the bubbles and their average value is only half as big as the vortices found in a single-phase plume. Nonetheless, a small growth in vortex size is still discernible in the plume core where interactions of bubble wakes are strong.

6.2 Recommendations for future work

1. Extend the range of laboratory data beyond $z/D > 10$: Bubble plumes of very small air inflow are used to mix fluids in the chemical industries. They behave differently than those in present experiments, oil spills and aerators used in lake destratification. Such weak plumes have been the subject in Leitch & Baines (1989) where bubbles appear to rise individually without interactions. Their measurements, however, demonstrated that the induced vertical liquid flow is considerable and a liquid volume flux does exist. Mixing brought by turbulent transport is not negligible. When related back to the oil spill problem, a weak plume most probably exists in the water surface layer where $z/D > 10$. If a plume flow is present, it will have implications to aftermath mitigation.

2. Tracer mass transport inside a bubble plume: Measurement of tracer mass flux is required to quantify diffusive flux across a fluid-droplet interface which is important in the modeling of droplet dissolution and chemical transformation; all of them depend on gradients of mass concentration. On a macroscopic scale, a relatively simple dye experiment can be made to estimate a Fickian-type diffusion coefficient by taking into account two sources of diffusion. The first one is the usual turbulent diffusion whereas the second one is the mechanical diffusion due to flow through a random array of bodies. The latter can be visualized in a reference frame moving with the bubbles; the bubble array can be considered fixed in space as a first approximation. This approach has been applied successfully to canopy flow in vegetated channels (Nepf 1999).

3. Direct numerical simulations (DNS) of bubble plumes: As mentioned in section 2, present data on mean and turbulent stresses for $Q_o = 0.5$L/min have been compared to the predictions from a LES model (Fraga et al. 2015); the simulations adopted a Eulerian-Lagrangian approach in which bubbles were represented as volume-less Lagrangian markers whose momentum exchange with the carrier fluid is two-way coupled via semi-empirical correlations. The comparison reveals that while mean vertical velocity, radial and shear stresses are accurately predicted, the vertical stress is largely under-predicted by a constant offset in the plume core where void fraction is high. Although anisotropy of turbulent stresses is also reproduced by the model, these results indicate that only some of the relevant (small) turbulent scales are resolved. To improve the predictions, DNS can be used to simulate the flow field surrounding each bubbles that is not currently available from LES.

REFERENCES

Adrian, R. (1997), 'Dynamic ranges of velocity and spatial resolution of particle image velocimetry', *Meas. Sci. Technol.* **8**, 1393–1398.

Adrian, R., Christensen, K. & Liu, Z.-C. (2000), 'Analysis and interpretation of instantaneous turbulent velocity fields', *Exp. Fluids* **29**, 275–290.

Adrian, R. & Yao, C. (1987), 'Power spectra of fluid velocities measured by laser doppler velocimetry', *Exp. Fluids* **5**, 17–28.

Agrawal, A. & Prasad, A. (2002), 'Properties of vortices in the self-similar turbulent jet', *Exp. Fluids* **33**, 565–577.

Asaeda, T. & Imberger, J. (1993), 'Structure of bubble plumes in linearly stratified environments', *J. Fluid Mech.* **249**, 35–57.

Bandara, U. & Yapa, P. (2011), 'Bubble sizes, breakup and coalescence in deepwater gas/oil plumes', *J. Hyd. Eng., ASCE* **137**(7), 729–738.

Batchelor, G. (1967), *An introduction to fluid dynamics*, Cambridge Mathematical Library, Cambridge University Press.

Bolotnov, I., Lahey Jr., R., Drew, D. & Jansen, K. (2008), 'Turbulent cascade modeling of single and bubbly two-phase turbulent flows', *Intl. J. Multiph. Flow* **34**, 1142–1151.

Bombardelli, F., Buscaglia, G., Rehmann, C., Rincon, L. & Garcia, M. (2007), 'Modeling and scaling of aeration bubble plumes: A two-phase flow analysis', *J. Hydraul. Res.* **45**(5), 617–630.

Cea, L., Puertas, J. & Pena, L. (2007), 'Velocity measurements on highly turbulent free surface flow', *Exp. Fluids* **42**, 333–348.

Cederwall, K. & Ditmars, J. (1970), Analysis of air-bubble plumes, Technical report KH-R-24, California Institute of Technology, Pasadena, California.

Chen, J. & Rodi, W. (1980), *Turbulent buoyant jets - a review of experimental data*, Vol. 4 of *HMT*, Pergamon Press.

Clift, R., Grace, J. & Weber, M. (1978), *Bubbles, drops and particles*, Academic Press, Inc., New York.

Craig, R., Loadman, C., Clement, B., Rusello, P. & Siegel, E. (2011), 'Characterization and testing of a new bistatic profiling acoustic doppler velocimete: The vectrino ii.', *IEES/OES Tenth Current, Waves, and Turbulence Measurement Workshop.*, Monterey, CA.

Crowe, C., Schwarzkopf, J., Sommerfeld, M. & Tsuji, Y. (2012), *Multiphase flows with droplets and particles*, 2nd edn, CRC Press.

Daubechies, I. (1990), 'The wavelet transform time-frequency localization and signal analysis', *IEEE, Trans. Inform. Theory* **36**(5), 961–1004.

Davidson, P. A. (2015), *Turbulence: An introduction to scientists and engineers*, 2nd edn, Oxford University Press.

Deane, G. & Stokes, M. (2002), 'Scale dependence of bubble creation mechanisms in breaking waves', *Nature* **418**.

Duncan, B., Seol, D.-G. & Socolofsky, S. (2009), 'Quantification of turbulence properties in bubble plumes using vortex identification methods', *Phys. Fluids* **21**(7), 075101.

Everson, R. & Sirovich, L. (1995), 'Karhunen-loeve procedure for gappy data', *J. Opt. Soc. Am. A* **12**(8), 1657–1664.

Fannelop, T. & Sjoen, K. (1980), 'Hydrodynamics of underwater blowouts', *Proc. AIAA 18th Aerospace Sci. Meeting*, Pasadena, California.

Farge, M. (1992), 'Wavelet transforms and their applications to turbulence', *Annu. Rev. Fluid Mech.* **24**, 395–457.

Feddersen, F. (2012), 'Scaling of surf zone turbulence', *Geophys. Res. Letters* **39**(L18613).

Fischer, H., List, E., Koh, R., Brooks, N. & Imberger, J. (1979), *Mixing in Inland and Coastal Waters*, Academic Press.

Fraga, B., Stoesser, T., Lai, C. & Socolofsky, S. (2015), 'An improved large-eddy simulation-based eulerian-lagrangian approach to predicut bubble plume dynamics', *Ocean Modell. (submitted)* .

Gao, Q., Ortiz-Duenas, C. & Longmire, E. (2011), 'Analysis of vortex population in turbulent wall-bounded flows', *J. Fluid Mech.* **678**, 87–123.

Garcia, C., Cantero, M., Nino, Y. & Garcia, M. (2005), 'Turbulence measurements with acoustic doppler velocimeters', *J. Hyd. Eng., ASCE* **131**(12), 1062–1073.

Gibson, M. (1963), 'Spectra of turbulence in a round jet', *J. Fluid Mech.* **15**(2), 161–173.

Goring, D. & Nikora, V. (2002), 'Despiking acoustic doppler velocimeter data', *J. Hyd. Eng., ASCE* **128**(1), 117–126.

Hill, R. (1996), 'Corrections to taylor's frozen turbulence', *Atmos. Res.* **40**, 153–175.

Horel, E. & Kennard, R. (1970), 'Ridge regression: Biased estimation for nonorthogonal problems', *Technometrics* **12**, 69–82.

Hurther, D. & Lemmin, U. (2001), 'A correction method for turbulence measurements with a 3d acoustic doppler velocity meter', *J. Atmos. Oceanic. Technol.* **18**, 446–458.

Hussein, H., Capp, S. & George, W. K. (1994), 'Velocity measurements in a high-reynolds number, momentum-conserving, axisymmetric, turbulent jet', *J. Fluid Mech.* **258**, 31–75.

Jirka, G. (2004), 'Integral model for turbulent buoyant jets in unbounded stratified flows. part 1: the single round jet.', *Env. Fluid Mech.* **4**, 1–56.

Jirka, G. & Harleman, D. (1979), 'Stability and mixing of a vertical plane buoyant jet in confined depth', *J. Fluid Mech.* **94**(2), 275–304.

Lai, A. & Lee, J. (2012*a*), 'Dynamic interaction of multiple buoyant jets', *J. Fluid Mech.* **708**, 539–575.

Lai, A., Zhao, B., Law, A. & Adams, E. (2013), 'Two-phase modeling of sediment clouds', *Env. Fluid Mech.* **13**, 435–463.

Lai, C. & Lee, J. (2012*b*), 'Mixing of inclined dense jets in stationary ambient', *J. Hydro-Environ. Res., IAHR-APD* **6**(1), 9–28.

Lance, M. & Bataille, J. (1991), 'Turbulence in the liquid phase of a uniform bubbly air-water flow', *J. Fluid Mech.* **222**, 95–118.

Lee, J. & Chu, V. (2003), *Turbulent jets and plumes - a Lagrangian approach*, Kluwer Academic.

Lee, J. & Kuang, C. (1999), 'Numerical simulations of turbulent bouyant jets', C. Wang, K. Lee & K. Ang, eds, *4th Asia-Pacific Conference on Computational Mechanics*, Elsevier, Singapore, pp. 651–656.

Leitch, A. & Baines, W. (1989), 'Liquid volume flux in a weak bubble plume', *J. Fluid Mech.* **205**, 77–98.

Lin, Y. & Linden, P. (2005), 'The entrainment due to a turbulent fountain at a denity interface', *J. Fluid Mech.* **542**, 25–52.

Lophaven, S., Nielsen, H. & Sondergaard, J. (2002), Aspects of the matlab toolbox dace, Tech. Rep. IMM-REP-2002-13, Technical University of Denmark.

Lumley, J. (1978), 'Computational modeling of turbulent flows', *Adv. Appl. Mech.* **18**(123-176).

Matsuda, T. & Sakakibara, J. (2005), 'On the vortical structure in a round jet', *Phys. Fluids* **17**(025106).

McDougall, T. (1978), 'Bubble plumes in stratified environments', *J. Fluid Mech.* **85**, 655–672.

Milgram, J. (1983), 'Mean flow in round bubble plumes', *J. Fluid Mech.* **133**, 345–376.

Milgram, J. & Van Houten, R. (1982), 'Plumes from sub-sea well blowouts', *Proc. of the 3rd Intl. Conf., BOSS*, Vol. I, pp. 659–684.

Morton, B., Taylor, G. & Turner, J. (1956), 'Turbulent gravitational convection from maintained and instantaneous sources', *Proc. R. Soc. London, Ser. A* **234**, 1–23.

Nepf, H. (1999), 'Drag, turbulence, and diffusion in flow through emergent vegetation', *Water Resour. Res.* **35**(2), 479–489.

Nepf, H. (2012), 'Flow and transport in regions with aquatic vegetation', *Annu. Rev. Fluid Mech.* **44**, 123–142.

Nezu, I. & Nakagawa, H. (1993), *Turbulence in Open-Channel Flows*, A.A. Balkema.

Nimmo Smith, W., Katz, J. & Osborn, T. (2005), 'On the structure of turbulence in the bottom boundary layer of the coastal ocean', *J. Phys. Oceanogr.* **35**, 72–93.

Nortek (2013), *Vectrino profiler - User manual*, Nortek AS.

Papanicolaou, P. & List, E. (1988), 'Investigations of round vertical buoyant jets', *J. Fluid Mech.* **195**, 341–391.

Pearson, B., Krogstad, P.-A. & van de Water W. (2002), 'Measuremenets of the turbulent energy dissipation rate', *Phys. Fluids* **14**(3), 1288–1290.

Pope, S. (2000), *Turbulent flow*, Cambridge University Press, New York.

Raffel, M., Willert, C., Wereley, S. & Kompenhans, J. (2007), *Particle image velocimetry - A practical guide*, second edn, Springer, New York.

Riboux, G., Legendre, D. & Risso, F. (2013), 'A model of bubble-induced turbulence based on large-scale wake interactions', *J. Fluid Mech.* **719**, 362–387.

Riboux, G., Risso, F. & Legendre, D. (2010), 'Experimental characterization of the agitation generated by bubbles rising at high reynolds number', *J. Fluid Mech.* **643**, 509–539.

Risso, F. (2011), 'Theoretical model for k^{-3} spectra in dispersed multiphase flows', *Phys. Fluids* **23**(1), 011701.

Robinson, S., Kline, S. & Spalart, P. (1989), 'Quasi-coherent structures in the turbulent boundary layer. part ii: verification and new information from a numerically simulated flat-plate boundary layer', S. Kline & N. Afgan, eds, *Near wall turbulence*, Zaric memorial conference, Hemisphere, New York, pp. 281–247.

Rodi, W. (1993), *Turbulence models and their application in hydraulics - A state of the art review*, 3rd edn, IAHR.

Seol, D.-G., Bhaumik, T., Bergmann, C. & Socolofsky, S. (2007), 'Particle image velocimetry measurements of the mean flow characteristics in a bubble plume', *J. Hyd. Eng., ASCE* **133**(6), 665–676.

Seol, D.-G., Duncan, B. & Socolofsky, S. (2009), 'Measurements of behavioral properties of entrained ambient water in stratified bubble plume', *J. Hyd. Eng., ASCE* **135**(11), 983–988.

Shih, T., Liou, W., A., S., Yang, Z. & Zhu, J. (1995), 'A new $k - \epsilon$ eddy viscosity model for high reynolds number turbulent flows', *Computer and fluids* **24**(3), 227–238.

Shrinivas, A. & Hunt, G. (2014), 'Unconfined turbulent entrainment across density interfaces', *J. Fluid Mech.* **757**, 573–598.

Shumway, R. & Stoffer, D. (2010), *Time series analysis and its applications: with R examples*, 3rd edn, Springer.

Simiano, M., Lakehal, D., Lance, M. & Yadigaroglu, L. (2009), 'Turbulent transport mechanisms in oscillating bubble plumes', *J. Fluid Mech.* **633**, 191–231.

Simiano, M., Zboray, R., de Cachard, F., Lakehal, D. & Yadigaroglu, L. (2006), 'Comprehensive experimental investigation of the hydrodyanmics of large-scale, three-dimensional bubble plumes', *Intl. J. Multiph. Flow* **32**(10), 1160–1181.

Socolofsky, S., Adams, E. & Sherwood, C. (2011), 'Formation dynamics of subsurface hydrocarbon intrusions following the deepwater horizon blowout', *Geophys. Res. Lett.* **38**(L09602).

Socolofsky, S., Bhaumik, T. & Seol, D.-G. (2008), 'Double-plume integral models for near-field mixing in multiphase plumes', *J. Hyd. Eng., ASCE* **134**(6), 772–783.

Taub, G., Lee, H., Balachandar, S. & Sherif, S. (2013), 'A direction numerical simulation study of higher order statistics in a turbulent round jet', *Phys. Fluids* **25**(115102), 1–19.

Tennekes, H. & Lumley, J. (1972), *A first course in turbulence*, MIT Press.

Torrence, C. & Compo, G. (1998), 'A practical guide to wavelet analysis', *Bull. Amer. Meteor. Soc.* **79**(1), 61–78.

Venturi, D. & Karniadakis, G. (2004), 'Gappy data and reconstruction procedures for flow past a cylinder', *J. Fluid Mech.* **519**, 315–336.

Voulgaris, G. & Trowbridge, J. (1998), 'Evaluation of the acoustic doppler velocimeter for turbulence measurements', *J. Atmos. Oceanic. Technol.* **15**, 272–289.

Wang, H. & Law, A. (2002), 'Second-order integral model for a round turbulent buoyant jet', *J. Fluid Mech.* **459**, 397–428.

Wüest, A., Brooks, N. & Imboden, D. (1992), 'Bubble plume modelling for lake restoration', *Water Resour. Res.* **28**(12), 3235–3250.

Westerweel, J. & Scarano, F. (2005), 'Universal outlier detection for piv data', *Exp. Fluids* **39**, 1096–1100.

Wygnanski, I. & Fiedler, H. (1967), 'Some measurements in the self-preserving jet', *J. Fluid Mech.* **38**(3), 577–612.

Zeldovich, Y. (1937), 'The asymptotic laws of freely-ascending convectiive flows', *Zh. Eksp. Teor. Fiz* **7**, 1463–1465 (in Russian).

Zheng, L., Yapa, P. & Chen, F. (2003), 'A model for simulating deepwater oil and gas blowouts - part i: Theory and model formulation', *J. Hydraul. Res.* **41**(4), 339–351.

Zhou, J., Adrian, R., Balachandar, S. & Kendall, T. (1999), 'Mechanisms for generating coherent packets of hairpin vortices in channel flow', *J. Fluid Mech.* **387**, 353–396.

APPENDIX A

CORRECTION FOR DOPPLER NOISE IN TURBULENT STATISTICS DERIVED FROM RAW ADV DATA

As mentioned in chapter 2 and 3, turbulent statistics are high-biased by Doppler noise σ_D inherent in ADV measurements. The degree of noise contamination is different for different quantities because of probe geometry. Let us now consider one of the ADV sampling cell. It has a unique probe geometry matrix $\mathbf{T}$ and the output Cartesian velocity $\tilde{\mathbf{u}}$ is related to the beam velocity $\tilde{\mathbf{b}}$ by,

$$\begin{bmatrix} \tilde{u_1} \\ \tilde{u_2} \\ \tilde{u_3} \\ \tilde{u_4} \end{bmatrix} = \begin{bmatrix} \tilde{w} \\ \tilde{v} \\ \tilde{u1} \\ \tilde{u2} \end{bmatrix} = \begin{bmatrix} T_{11}T_{12}T_{13}T_{14} \\ T_{21}T_{22}T_{23}T_{24} \\ T_{31}T_{32}T_{33}T_{34} \\ T_{41}T_{42}T_{43}T_{44} \end{bmatrix} \begin{bmatrix} \tilde{b_1} \\ \tilde{b_2} \\ \tilde{b_3} \\ \tilde{b_4} \end{bmatrix} \tag{A.1}$$

i.e. $\tilde{u_i} = T_{ij}\tilde{b_j}$ where summation over repeated indices is intended.

It has been demonstrated in Voulgaris & Trowbridge (1998) that $\tilde{b_j} = \tilde{b_{j,t}} + \tilde{\sigma_j}$ where $\{\tilde{b_{j,t}}\}$ are the true (unbiased) beam velocities and $\{\tilde{\sigma_j}\}$ are stochastic white noise processes with equal variances σ_D^2 that are also statistically uncorrelated with each other. It follows immediately that the time-averaged velocity U_i is unbiased.

Second-order statistics $\overline{u_i u_j}$

Using the definition $\overline{u_i u_j} = \overline{[(\tilde{u_i} - U_i)][(\tilde{u_j} - U_j)]}$, the relationship between true

$\overline{u_{i,t}u_{j,t}}$ and measured $\overline{u_iu_j}$ can be rigorously derived as the following.

$$\begin{bmatrix} \overline{u_t^2} \\ \overline{w_t^2} \\ \overline{v_{1,t}^2} \\ \overline{v_{2,t}^2} \\ \overline{u_t v_{1,t}} \\ \overline{u_t v_{2,t}} \\ \overline{v_{1,t} w_t} \\ \overline{v_{2,t} w_t} \end{bmatrix} = \begin{bmatrix} \overline{u^2} \\ \overline{w^2} \\ \overline{v_1^2} \\ \overline{v_2^2} \\ \overline{uv_1} \\ \overline{uv_2} \\ \overline{v_1 w} \\ \overline{v_2 w} \end{bmatrix} - \begin{bmatrix} T_{1j}T_{1j} \\ T_{2j}T_{2j} \\ T_{3j}T_{3j} \\ T_{4j}T_{4j} \\ T_{1j}T_{3j} \\ T_{1j}T_{4j} \\ T_{2j}T_{3j} \\ T_{2j}T_{4j} \end{bmatrix} \overline{\sigma_D^2} \tag{A.2}$$

The variance of the Doppler noise $\overline{\sigma_D^2}$ can be estimated from the spectra of the two independent $u1$ and $u2$ measurements (Hurther & Lemmin (2001)). Plugging in the values of T_{ij}, such as those in equation (2.3), the relative error due to noise for $\overline{u_t^2} : \overline{w_t^2} : \overline{v_{1,t}^2} : \overline{u_t v_{1,t}} \approx 20 : 20 : 1 : 0.05$; velocities that are perpendicular to the probe axis suffer much higher noise contamination whereas the shear stress is almost noise-free.

Third-order statistics $\overline{u_iu_ju_k}$

Similarly for the triple velocity correlation $\overline{u_iu_ju_k} = \overline{[(\tilde{u_i} - U_i)][(\tilde{u_j} - U_j)][(\tilde{u_k} - U_k)]}$, we get

$$\begin{bmatrix} \overline{u_t^3} \\ \overline{u_t v_{1,t}^2} \\ \overline{u_t w_t^2} \\ \overline{v_{1,t}^3} \\ \overline{v_{1,t} u_t^2} \\ \overline{v_{1,t} w_t^2} \end{bmatrix} = \begin{bmatrix} \overline{u^3} \\ \overline{u v_1^2} \\ \overline{u w^2} \\ \overline{v_1^3} \\ \overline{v_1 u^2} \\ \overline{v_1 w^2} \end{bmatrix} - \begin{bmatrix} T_{1j} T_{1j}^2 \\ T_{1j} T_{3j}^2 \\ T_{1j} T_{2j}^2 \\ T_{3j} T_{3j}^2 \\ T_{3j} T_{1j}^2 \\ T_{3j} T_{2j}^2 \end{bmatrix} \overline{\sigma_D^3} \tag{A.3}$$

This requires the skewness factor $\overline{\sigma_D^3}$ of the Doppler noise which cannot be evaluated as the probability density function of the stochastic noise is unknown, despite its variance can be calculated. In the lack of better information, a Gaussian pdf is assumed and hence $\overline{\sigma_D^3} = 0$ i.e. no corrections for third-order moments.

APPENDIX B

CURVE-FITS TO PROFILES OF TIME-AVERAGED TURBULENT QUANTITIES REQUIRED IN A TKE BUDGET

Curve-fits of the turbulent quantities required in the evaluation of the time-averaged TKE equation in chapter 2 are given. Similar to previous works on single-phase turbulent jets and plumes (e.g Hussein et al. 1994), the profiles are assumed to take on the separable form $F(z)G(r/b_g)$. In all cases, $F(z)$ is equal to certain power of the centerline velocity $W_c(z)$ whereas the shape function $G(r/b_g)$ is determined empirically from the data by means of a nonlinear least squares fit.

Second-order moments

. Streamwise stress $\overline{w^2} : 0.22W_c(z)^2G(r/b_g)$

. Out-of-plane stress $\overline{v^2} : 0.097W_c(z)^2G(r/b_g)$

. Radial stress $\overline{u^2} : 0.035W_c(z)^2G(r/b_g)$

. TKE $\frac{1}{2}(\overline{w^2+u^2+v^2}) : 0.18W_c(z)^2G(r/b_g)$

. Reynolds shear stress $\overline{wu} : W_c(z)^2[-0.0021+0.0857(r/b_g)^2]exp(-2.1276(r/b_g)^2)$

where $G(r/b_g) = exp(-\frac{(r-0.55b_g)^2}{(0.5b_g)^2}) + exp(-\frac{(r+0.55b_g)^2}{(0.5b_g)^2})$.

Third-order moments

. $\overline{ww^2} : W_c(z)^3[0.1080+1.6443(r/b_g)^2-12.8363(r/b_g)^4+14.5074(r/b_g)^6]exp(-4.7620(r/b_g)^2)$

. $\overline{wu^2} : W_c(z)^3[0.0096+0.0675(r/b_g)^2-0.0217(r/b_g)^4+0.8527(r/b_g)^6]exp(-5.1649(r/b_g)^2)$

. $\overline{wv^2}$: $W_c(z)^3[0.0287+0.3316(r/b_g)^2-0.5740(r/b_g)^4+5.8437(r/b_g)^6]exp(-5.6077(r/b_g)^2)$

. $\overline{uu^2}$: $W_c(z)^3[-0.0028+0.0354(r/b_g)^3+0.7710(r/b_g)^5-0.3208(r/b_g)^7]exp(-4.1522(r/b_g)^2)$

. $\overline{uw^2}$: $W_c(z)^3[-0.0008+0.0204(r/b_g)^3+0.0010(r/b_g)^5+0.0424(r/b_g)^7]exp(-3.901(r/b_g)^2)$

. $\overline{uv^2}$: $W_c(z)^3[-0.0013+0.0576(r/b_g)^3-0.2292(r/b_g)^5+0.1536(r/b_g)^7]exp(-3.5618(r/b_g)^2)$

Turbulent dissipation rate

. $\epsilon : 0.037\frac{W_c(z)^3}{b_g(z)}[exp(-\frac{(r-0.5b_g)^2}{(0.54b_g)^2}) + exp(-\frac{(r+0.5b_g)^2}{(0.54b_g)^2})]$

APPENDIX C

GENERATION OF TURBULENT SYNTHETIC TIME SERIES

The velocity signal $v(t)$ used in the *signal + noise* model for synthetic ADV time series (chapter 3) is generated based on the 1D wavenumber model spectrum E_{11} proposed by Pope (2000). The implementation details follow that of Garcia et al. (2005). A summary of the procedures is given below.

1. Specify inputs to E_{11} (i) energy-containing eddy length scale L; and (ii) Kolmogorov length scale η.

$$E_{11}(k_1) = C_o \epsilon^{2/3} k_1^{-5/3} \left(\frac{k_1 L}{\sqrt{(k_1 L)^2 + c_L}}\right)^{5/3+p_o} exp\{-\beta\{[(k_1\eta)^4 + c_\eta^4]^{1/4} - c_\eta\}\} \tag{C.1}$$

   where the model parameters are $C_o = 0.49$, $p_o = 0$ (default for a -5/3 spectral slope), $c_L = 6.78$, $c_\eta = 0.40$ and $\beta = 5.2$. The dissipation rate is uniquely specified by $\eta = \nu^3/\eta^4$.

2. To generate a random 1D turbulent velocity signal sampled at the frequency f_s and the duration T, the following equation is used. The convective velocity U_c is required to convert wavenumber to frequency (ii) i.e. Taylor's hypothesis.

$$v(t) = \sqrt{2} \sum_{i=1}^{N_s} A_i cos(f_i' t + \phi_i), t \in [0, T] \tag{C.2}$$

   where

   i amplitude of each sinusoidal component, $A_i = \sqrt{E_{11}(f_i) \triangle f}$

ii frequency-wavenumber conversion, $f_i = k_{1i}U_c$, $\triangle f = \triangle k_1 U_c$

iii perturbed frequency, $f_i' = f_i + \delta f$ for which δf is randomly uniformly distributed in $(-\alpha \triangle f/2, \alpha \triangle f/2)$. The parameter $\alpha = 0.05$ is known as the jitter parameter.

iv random phase angle ϕ_i is uniformly distributed in (0, 2π)

v number of sinusoidal components to include, N_s

3. To change the spectral slope i.e. different from the default -5/3, two modifications to Eq.(A1) are needed; (i) exponent of k_1 and (ii) value of p_o. For the -7/6 and -8/3 spectral slope considered here, these changes are (-7/6, -1/2) and (-8/3, 1) respectively.

APPENDIX D

AN ESTIMATE OF NOISE VARIANCE IN SIGNALS THAT FOLLOW AN ADDITIVE WHITE NOISE MODEL

Estimation of measurement errors is a routine made in every scientific enquires in which the errors are customarily considered as the sum of two separable components, (i) a systematic error and (ii) a random error. Systematic error causes a definite bias (either an overestimation or an underestimation but not the mixed of two) in the data that can usually be removed by a careful calibration of the measurement system. Random error, however, produces both over/underestimation and cannot be mended by calibration. It encapsulates the total effect of all unaccountable sources of random error within the measuring system and the environment that measurements are made. Being random and bias-free, its contribution to the average of a measured quantity is zero, i.e. mean quantities are unbiased. In this appendix, a simple method is proposed to estimate the variance (energy) of a random white noise superimposed on measured turbulent signals. The proposed method works with data that follow a simple additive *signal + noise* model. Examples in the research of fluid mechanics include acoustic Doppler velocimetry (ADV) and particle image velocimetry (PIV).

D.1 Methodology

The additive *signal + noise* model for N data points reads,

$$v_{i,m} = v_{i,t} + w_i, i = 1, 2, 3, ...N \tag{D.1}$$

where $v_{i,m}$ = measured value, $v_{i,t}$ = true value and $\{w_i\}$ = random white noise with $\overline{w_i} = 0$, $\overline{w_i^2} = \sigma_w^2$ and $\overline{w_i w_j} = 0$ for $i \neq j$ where the overbar indicates an ensemble

average. If we now consider a two-point moving average of $v_{i,m}$, the value of the smoothed data point $\widetilde{v_{i,m}}$ is given by,

$$\begin{aligned}\widetilde{v_{i,m}} &= \frac{1}{2}[v_{i,t} + v_{i+1,t}] + \frac{1}{2}[w_i + w_{i+1}] \\ &\approx v_{i,t} + \frac{1}{2}[w_i + w_{i+1}]\end{aligned} \tag{D.2}$$

The second line is obtained by assuming $v_{i,t} = v_{i+1,t}$ which is reasonable for data sampled at high frequencies and correlated turbulent signals. The crux of present method lies in difference between $v_{i,m}$ and $\widetilde{v_{i,m}}$,

$$w_{i,estimate} = v_{i,m} - \widetilde{v_{i,m}} = w_i - \frac{1}{2}[w_i + w_{i+1}] \tag{D.3}$$

This equation shows that the difference is a pointwise estimate of the white noise; if the $\frac{1}{2}[w_i + w_{i+1}]$ term equals to zero, the exact value of w_i is obtained. Because $\{w_i\}$ is white, neighboring noise terms are more likely to have an opposite sign than correlated signals, and hence, the cancellation does occur in practice. The variance of $w_{i,estimate}$ is given by,

$$\begin{aligned}\overline{w_{i,estimate}^2} &= \overline{[w_i - \frac{1}{2}[w_i + w_{i+1}]]^2} \\ &= \overline{[\frac{1}{2}[w_i - w_{i+1}]]^2} \\ &= \frac{1}{4}\overline{[w_i^2 + w_{i+1}^2 - 2w_i w_{i+1}]} \\ &= \frac{1}{4}\overline{[w_i^2 + w_{i+1}^2]} (\because \overline{w_i w_{i+1}} = 0) \\ &= \frac{1}{2}\overline{w_i^2} (\because \{w_i\} \text{is stationary})\end{aligned} \tag{D.4}$$

This estimate applies if no cancellations occur. In practice, $0.5\overline{w_i^2} \leq \overline{w_{i,estimate}^2} \leq \overline{w_i^2}$

and so the theoretical error upper bound of using $\overline{w^2_{i,estimate}}$ is two times the actual value.

D.2 Numerical study using synthetic time series

The above analysis relies on the assumption that $v_{i,t} = v_{i+1,t}$, which is only appropriate when the flow field is *frozen* during the time lapse between two neighboring data points. Quantitatively, this requires the ratio $\triangle t/I_t \ll 1$ where $\triangle t = 1/f_s$, $f_s =$ sampling frequency and $I_t =$ integral time scale. When this is not satisfied, the additional term $\frac{1}{2}[v_{i,t} - v_{i+1,t}]$ appears in $w_{i,estimate}$ and increases the error in $\overline{w^2_{i,estimate}}$. To study this decorrelation effect and the effect of signal-to-noise ratio (SNR) on the proposed method, a numerical study is carried out using synthetic time series of known true signals and white noise levels.

Synthetic time series are generated by using the one-dimensional wavenumber spectrum in Pope (2000) and the procedures described in Garcia et al. (2005). Turbulent signals of two values of I_t are used; 0.0910s and 0.0237s. Twenty four scenarios are studied over the following parameter space, $f_s = 25$, 50, 100, 200Hz and SNR = 5, 10 and 20. Table D.1 tabulates some properties of the synthetic signals.

Figure D.1 shows an example of the pointwise estimate $w_{i,estimate}$ as compared to w_i. It can be seen that the cancellation mentioned above only occurs infrequently. Figure D.2 shows the ratio $\overline{w^2_{i,estimate}}/\overline{w^2_{i,t}}$ as a function of $\triangle t/I_t$ and SNR. As discussed above, when the flow field is reasonably *frozen* we have $0.5 \leq \overline{w^2_{i,estimate}}/\overline{w^2_i} \leq 1$. This is reflected in the figure for $\triangle t/I_t \leq 0.05$. Further, in this region the effect of SNR is relatively weak. As $\triangle t/I_t$ increases, the decoration effect become more prominent where the proposed method overestimates the true noise variance. The

Case	I_t (s)	$\sqrt{\overline{v_{i,t}^2}}$ (cm/s)	$\sqrt{\overline{w_i^2}}$ (cm/s)	SNR
A	0.091	0.0435	0.0178	5
	0.091	0.0427	0.0128	10
	0.091	0.0411	0.0090	20
B	0.0237	0.0088	0.0036	5
	0.0237	0.0082	0.0025	10
	0.0237	0.0082	0.0018	20

Table D.1: Properties of synthetic time series studied; signal-to-noise ratio SNR = $\overline{v_{i,t}^2}/\overline{w_i^2}$

overestimation is more severe with higher values of SNR, e.g. at $\triangle t/I_t \sim 0.4$, the ratio is 4.1 for SNR = 20 compared to 1.45 when SNR = 5.

To correct for the under/overestimation, a correction factor f can be defined as the inverse of $\overline{w_{i,estimate}^2}/\overline{w_{i,t}^2}$. Then, $\overline{w_{i,t}^2} = f \times \overline{w_{i,estimate}^2}$. Figure D.3 shows f as a function of $\triangle t/I_t$ and SNR.

D.3 Application to real time series

In the actual measurement of turbulent flows, one only has the measured data without knowing the actual signal and noise. The proposed method can still be used to get a good estimate of $\overline{w_{i,t}^2}$. First, compute $\overline{w_{i,estimate}^2}$ from the measured data. The empirical SNR can then be computed by $\overline{v_{i,m}^2}/\overline{w_{i,estimate}^2}$. This SNR is different from the actual value but should be close to it. Second, calculate the correction factor f based on this value of SNR. Finally, obtain $\overline{w_{i,t}^2}$ as $f \times \overline{w_{i,estimate}^2}$.

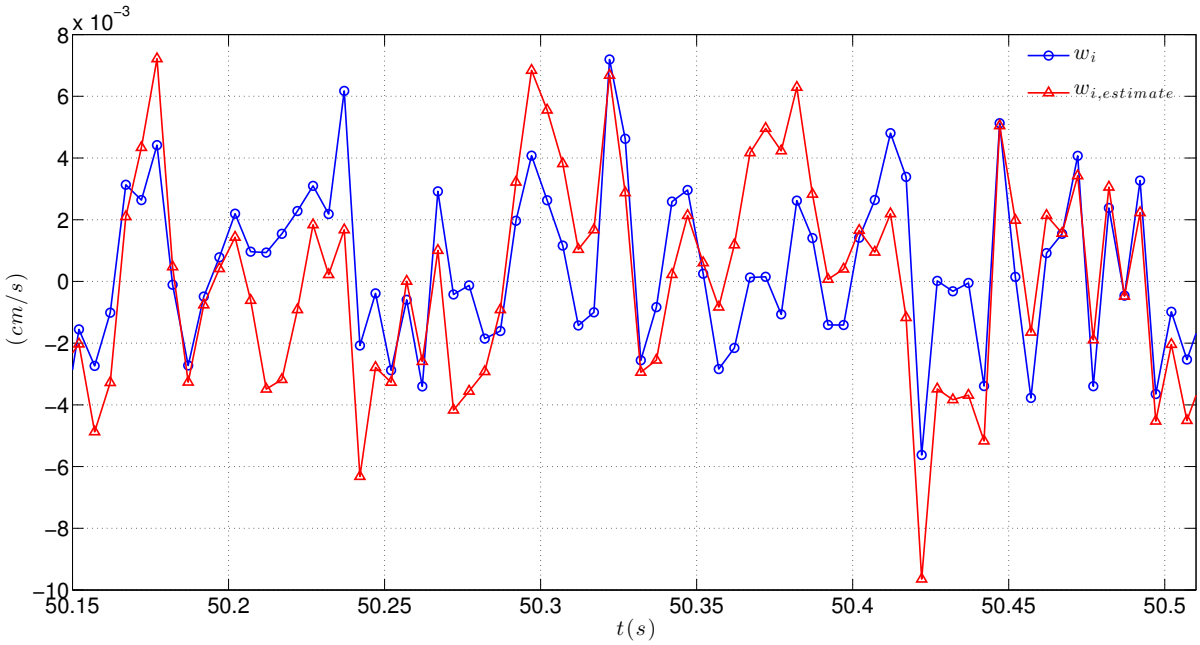

Figure D.1: A comparison between the pointwise estimate $w_{i,estimate}$ and the true noise w_i; Case B, $f_s = 200$Hz and SNR $= 20$

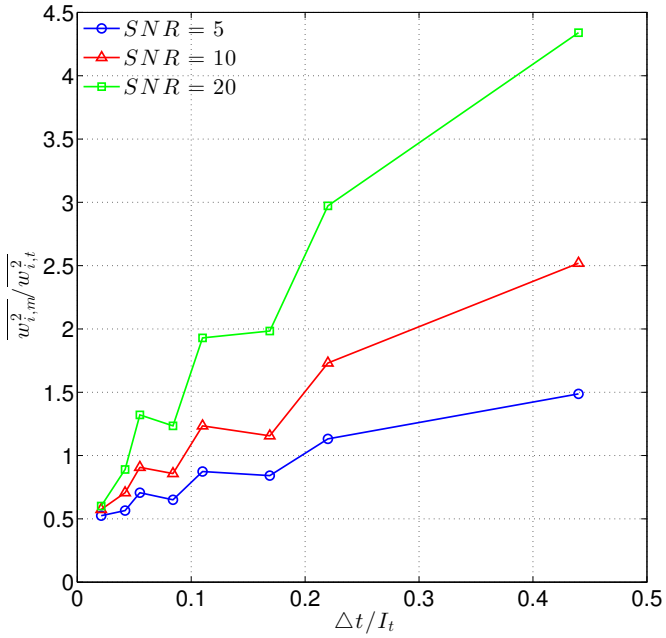

Figure D.2: Ratio of estimated noise variance to actual variance as a function of $\triangle t/I_t$ and SNR

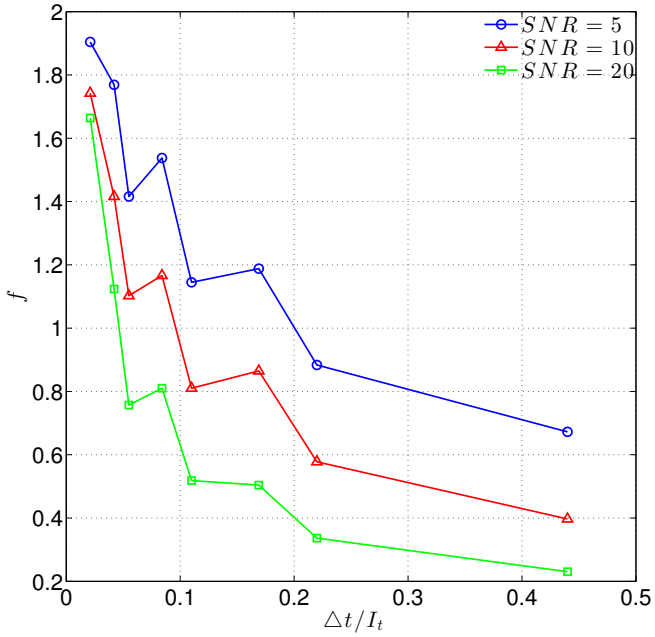

Figure D.3: Correction factor for $\overline{w^2_{i,estimate}}$ as a function of $\triangle t/I_t$ and SNR